NONEQUILIBRIUM HYPERSONIC AEROTHERMODYNAMICS USING THE DIRECT SIMULATION MONTE CARLO AND NAVIER-STOKES MODELS

by

Andrew J. Lofthouse, Major, USAF

A dissertation submitted in partial fulfillment
of the requirements for the degree of
Doctor of Philosophy
(Aerospace Engineering)
in The University of Michigan
2008

Doctoral Committee:

    Professor Iain D. Boyd, Chair
    Professor Kenneth G. Powell
    Professor Philip L. Roe
    Associate Professor Hong G. Im
    José A. Camberos, U. S. Air Force Research Laboratory

Report Documentation Page

1. REPORT DATE	2. REPORT TYPE	3. DATES COVERED
17 JAN 2008	**N/A**	**-**

4. TITLE AND SUBTITLE	5a. CONTRACT NUMBER
Nonequilibrium Hypersonic Aerothermodynamics Using The Direct Simulation Monte Carlo And Navier-Stokes Models	5b. GRANT NUMBER
	5c. PROGRAM ELEMENT NUMBER

6. AUTHOR(S)	5d. PROJECT NUMBER
	5e. TASK NUMBER
	5f. WORK UNIT NUMBER

7. PERFORMING ORGANIZATION NAME(S) AND ADDRESS(ES)	8. PERFORMING ORGANIZATION REPORT NUMBER
University of Michigan	**CIO8-0001**

9. SPONSORING/MONITORING AGENCY NAME(S) AND ADDRESS(ES)	10. SPONSOR/MONITOR'S ACRONYM(S)
The Department of the Air Force AFIT/ENEL, Bldg 16 2275 D Street WPAFB, OH 45433	11. SPONSOR/MONITOR'S REPORT NUMBER(S)

12. DISTRIBUTION/AVAILABILITY STATEMENT
Approved for public release, distribution unlimited

13. SUPPLEMENTARY NOTES
The original document contains color images.

14. ABSTRACT

15. SUBJECT TERMS

16. SECURITY CLASSIFICATION OF:			17. LIMITATION OF ABSTRACT	18. NUMBER OF PAGES	19a. NAME OF RESPONSIBLE PERSON
a. REPORT **unclassified**	b. ABSTRACT **unclassified**	c. THIS PAGE **unclassified**	**UU**	**261**	

There is a special room in Purgatory, reserved for CFDers, where they will be compelled to repeat, by hand, all of the unnecessary computations that they have ever placed on a computer.

Robert W. MacCormack

Doh!

Homer Simpson

Remember that you are very stupid, and that your sole claim to intelligence lies in how well you can work within this handicap.

Philip L. Roe

Genius is one percent inspiration and ninety-nine percent perspiration.

Thomas A. Edison

For my grandfather,
scientist and disciple of Christ.

ACKNOWLEDGEMENTS

The work presented here is the culmination of many years of work, and certainly wouldn't have been possible without the support of many people throughout my life and Air Force career.

I would first like to thank all of the fine people at the Air Force Institute of Technology (AFIT), and particularly Lt. Col. Monty Hughson, Lt. Col. Ray Maple, Maj. Jeff Bons and Maj. Jeff McMullan for their mentorship and support. I've learned valuable lessons from each of them.

I would like to thank my graduate committee for their willingness to serve. Prof. Iain Boyd has been a very able advisor from the very beginning, and his direction has been very profitable. Prof. Hong Im has a lock on a title coveted by Air Force officers the world over—PowerPoint Warrior! Who knew you could learn so much CFD from PowerPoint slides? I might just use some of that inspiration in my teaching duties at AFIT. It has been a privilege to work with Prof Philip Roe, and I owe him a debt of gratitude for his instruction in CFD, and for his wonderful British sense of humor! Although I never personally worked with Prof. Kenneth Powell, I certainly owe him my gratitude for overseeing the University's Center for Advanced Computing; many, many CPU cycles were expended in the course of this research, and, hopefully (for my sake in the afterlife!), these were not wasted CPU cycles. Finally, I am especially indebted to Dr. Jose Camberos of the Air Force Research Laboratory at Wright-Patterson AFB, OH. It was in his hypersonics course at AFIT (when I was a wee

First Lieutenant) that I was first exposed to nonequilibrium gas dynamics. When the time came to pursue further graduate work, it was due to his suggestion that I came to the University of Michigan to work with Prof. Boyd, a decision that I don't regret.

I also acknowledge the help I received over the years from several graduate students, particularly Tom Schwartzentruber, Jose Padilla, Jon Burt and Leo Scalabrin. Leo's ability to create the CFD code LeMANS with only three years of work is absolutely amazing. I couldn't have done this work without standing on the shoulders of giants.

I'm eternally indebted to my wife for her constant love and support. Since the day we met as undergraduate students, she has inspired and motivated me beyond mere academic mediocrity. During the past three years this support has continued. The satisfaction of completing this work would have been meaningless without having my family by my side throughout the entire process.

Finally, I owe my life and talents to God. Although I was not blessed with genius, I was blessed with sufficient wisdom and intelligence (I hope) to recognize my weaknesses so that I might, through hard work and the grace of God, achieve a measure of success in this life.

TABLE OF CONTENTS

LIST OF FIGURES

Figure

LIST OF TABLES

CHAPTER I

Introduction and Motivation

1.1 Introduction

Hypersonic flight vehicles are a current topic of interest in both civilian and military research. NASA is currently designing a Crew Transport Vehicle (CTV) [44, 69] and Crew Exploration Vehicle (CEV) [32] to replace the space shuttle; reentry vehicles are, by definition, hypersonic vehicles. Military requirements for reconnaissance and surveillance, as well as the mission of the United States Air Force to rapidly project power globally makes the design of a hypersonic plane that can quickly traverse the globe very attractive [102].

The design of hypersonic vehicles requires accurate prediction of the surface properties while in flight. These quantities are typically the heat flux, pressure and shear stress, from which the aerodynamic forces and moments can be calculated. These variables govern not only the aerodynamic performance of the vehicle, but also determine the selection and sizing of the thermal protection system (TPS), which protects the vehicle from the extreme temperatures encountered at hypersonic velocities.

The geometry of a vehicle, and in particular, the nose and the leading edges of wings and other aerodynamic surfaces, is a critical consideration in a vehicle's design. Aerodynamic heating is inversely proportional to the square root of the

1

radius at the stagnation point; hence, historically most vehicles have had blunted noses and leading edges to reduce the thermal loads to acceptable levels.

Recently, however, a class of materials, designated Ultra-High Temperature Ceramic (UHTC) composites, has been developed that can withstand temperatures as high as 3500 K [57, 78]. Materials such as these allow the use of much sharper leading edges. Sharp leading edges are important in the design of waveriders, a class of hypersonic vehicles that depend on the high pressures behind a shock wave to achieve a high lift-to-drag ratio [2]. These vehicles are designed theoretically with infinitely sharp leading edges in order that the shock stays attached. Manufacturability and thermal considerations then require a finite amount of blunting. Any blunting will detach the shock allowing spillage of high pressure gases around the leading edge, decreasing aerodynamic performance by as much as 20% [27]. Other vehicle designs, such as the experimental X-43A, also depend on sharp leading edges [97].

During its trajectory through an atmosphere, a hypersonic vehicle will experience vastly different flow regimes because the atmosphere's density varies as a function of altitude. Flight testing and reproduction of these varied flow conditions in ground-based laboratory facilities is both expensive and technically challenging. Hence, there is an extremely important role for computational models in the development of hypersonic vehicles.

1.2 Nonequilibrium Hypersonic Gas Flows

There are, generally speaking, three regimes in which hypersonic vehicles travel. They are classified as the continuum, continuum-transition and free-molecular regimes. Typically, the different regimes are distinguished by the Knudsen number,
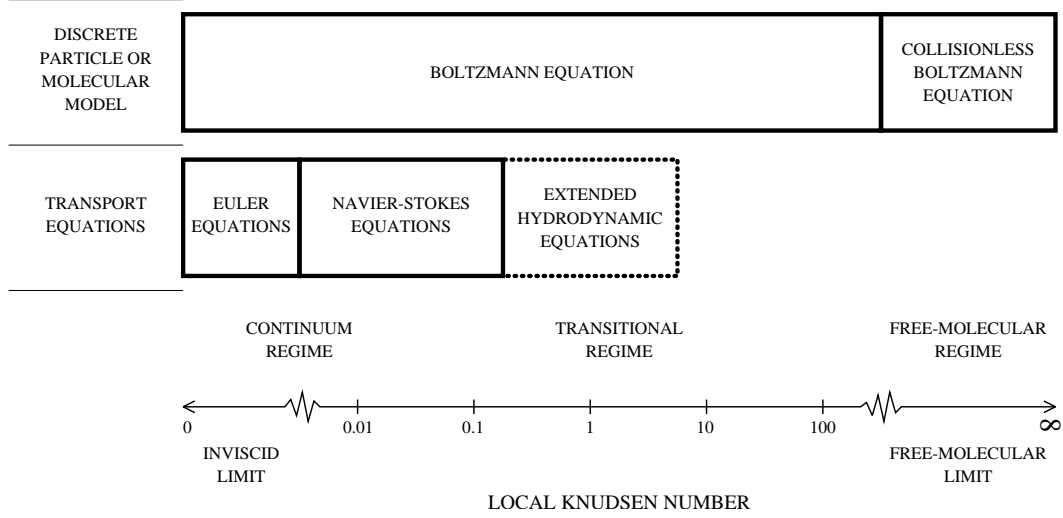
Figure 1.1: The Knudsen number limits on the mathematical models (from Ref. [14], after Ref. [4]).

defined as

$$\text{Kn} = \frac{\lambda}{L} \propto \frac{1}{\rho L}, \qquad (1.1)$$

where the mean free path, λ, of a gas is defined as the average distance a particle travels between successive collisions; L is a characteristic length and ρ is the density.

Figure 1.1 illustrates the different flow regimes, from the continuum ($\text{Kn} < 0.01$), through the transitional to the free-molecular ($\text{Kn} > 10$) regime. The Boltzmann equation is valid for all regimes, whereas the Navier-Stokes equations are valid only for those regimes near the continuum limit. Extended hydrodynamic equations, also known as higher-order moment equations, can be used further into the transitional regime than the Navier-Stokes equations. Methods based on these types of equations, however, are not as mature and are subject to significant limitations that prevent their use for hypersonic flows, as will be discussed in Chapter II.

At low altitudes, the atmospheric density is relatively high, and flows around hypersonic vehicles should be simulated using traditional Computational Fluid Dy-

namics (CFD) by solving either the Euler or preferably the Navier-Stokes equations. This is the continuum regime characterized by very large Reynolds numbers and very low Knudsen numbers. (Although CFD refers to techniques used to solve any set of conservation equations, the term will be used herein to refer only to methods used to solve the Navier-Stokes equations.)

At very high altitudes, at the edge of the atmosphere, the density is low such that there are very few collisions between the molecules and atoms in the flow around the vehicle. This is the rarefied flow regime and can be computed using the direct simulation Monte Carlo (DSMC) method [4], which has been shown to converge to solutions of the Boltzmann equation [95]. Generally speaking, CFD methods are about an order of magnitude faster than the DSMC method (although the DSMC method's computational cost decreases in more rarefied flows). However, the lack of collisions makes the physics of the Navier-Stokes equations invalid in rarefied regimes, which are characterized by a large Knudsen number. On a blunt body, a high-density fore-body flow can create a rarefied flow in the wake of the vehicle. In principle, the DSMC method can be applied to any dilute gas flow, but becomes prohibitively expensive for Knudsen numbers less than 0.001. Thus, it is attractive to find ways to increase the validity of CFD methods beyond the continuum regime.

One way to improve CFD modeling in the transition regime, that is, for lower density flows beyond the continuum regime and before the free molecular regime, is by replacing the typical no-slip boundary conditions with slip velocity and temperature jump boundary conditions. The addition of slip boundary conditions will not, however, eliminate all source of errors when using continuum methods for flows with large amounts of nonequilibrium.

Hybrid methods in which the computational domain is split between particle

(DSMC) and continuum (CFD) methods are another way to decrease computational cost while maintaining accuracy and are an area of active research [82].

The areas of the flow where the continuum hypothesis breaks down (or equivalently, where the flow is no longer in local thermodynamic equilibrium), can be quantified by the use of a continuum breakdown parameter [11].

1.3 Survey of Recent and Current Research

The DSMC and CFD methods have both been used for many years to model hypersonic, nonequilibrium gas flows, while advances in computing technology during the past several years, as well as more sophisticated models have enabled the modeling of more complex nonequilibrium phenomena [8, 42, 67, 70, 91, 104, 106, 108].

Some of the earliest work comparing DSMC and Navier-Stokes simulations is that of Moss and Bird [60], originally reported in 1984, in which DSMC solutions of the shuttle orbiter nose during re-entry were compared with viscous shock layer (VSL) solutions. Their work included a 5-species chemistry model, and the results showed that there was reasonably good agreement in flow solutions at the lower altitudes, which worsened as the flow became more rarefied.

The 1990's saw an increase in the use of DSMC, as well as additional comparisons between continuum and particle solvers. Only a representative sample of this work is described here.

Moss, et al. [59, 62] compared DSMC and CFD solutions of a Mach 20 flow of non-reacting and reacting nitrogen about a 70-deg blunted cone, for freestream Knudsen numbers of 0.001, 0.01 and 0.03. An emphasis was placed on the wake structure and afterbody heating. A three temperature model and slip boundary and no-slip boundary conditions were used for the Navier-Stokes solutions.

Olynick, et al. [64] compared DSMC and CFD solutions of the flow about the Fire II experimental re-entry vehicle. Freestream flow Knudsen numbers considered were about 0.0025 and 0.01. The solutions used a 5-species model for reacting air. Separate translational, rotational and vibrational energy equations, along with slip boundary conditions, were employed in the CFD computations. Special attention was paid to the submodels used in both DSMC and CFD to ensure compatibility. Emphasis was on the flow field solutions.

Candler, et al. [16] simulated the flow of a spherical blunt-body during re-entry using CFD and DSMC methods and compared the resulting radiative emissions from the flow field. Similar chemical kinetics and thermal relaxation models were used, where possible.

Research into developing hybrid DSMC-CFD methods also prompted additional comparisons between CFD and DSMC solutions. Boyd, et al. [11] computed solutions about a blunt sphere and for 1D shockwaves while Hash and Hassan [35] computed the flow about a 70-deg blunted cone.

Carlson, et al. [20] conducted CFD and DSMC simulations of a hemisphere in air for Mach 10 and 15. The flow was very near continuum, with Knudsen numbers of 0.02 and below. Different models of air chemistry (perfect gas, equilibrium air, 5-species) were used, as well as some vibrational nonequilibrium models. The emphasis was on the effect of thermochemical nonequilibrium on the field of view of a sensor.

More recently, work on comparing DSMC and CFD solutions has been concentrated on several validation cases for computational codes [107]. In particular, the NATO Research Technology Organization (RTO) Advanced Vehicle Technology Panel Working Group 10 (WG 10) coordinated several experiments to highlight six topical areas for CFD validation [96]. These areas included shock–shock interactions

and laminar hypersonic viscous–inviscid interactions [45]. Computational simulations for two experiments, Mach 12 and Mach 16 flows of nitrogen over a 25–55-deg double cone and a hollow cylinder flare, were solicited for a blind comparison for the 2001 AIAA Aerospace Sciences Meeting and Exhibit. Several DSMC [13, 58] and CFD [18, 28, 43] solutions were submitted.

Later, others compared CFD and DSMC solutions to these and similar experimental results [19, 55, 61, 72, 73, 100, 99]. Inger and Moss [39] also compared DSMC with theoretically derived expressions from the Navier-Stokes equations for the separation and reattachment streamline angles for the shock–boundary layer interaction.

In each of these validation cases, while the surface properties between CFD and DSMC were computed and compared with the experimental results, particular emphasis was on the size of the recirculation zone near the shock–boundary layer interaction.

Most recently, Boyd, et al. [12] and Ozawa, et al. [65] compared particle and continuum solutions with flight data for the Stardust atmospheric re-entry for near-continuum conditions (with a freestream Knudsen number of about 0.005). This data set is of particular interest considering the high velocities (about 12.6 km/s) attained during re-entry. This study focused on dissociation and ionization. Enormous differences were seen in basic flow property predictions between the two methods.

Jain and Hayes [40] developed an analytical method for engineering estimates of pressure, shear stress and heat transfer rates on vehicles of arbitrary shape for the hypersonic continuum through the transitional and free-molecular flow regimes. The method is applicable to sharp- and blunt-nosed bodies. Solutions are compared with DSMC and CFD solutions with reasonable accuracy.

There is, then, an abundant amount of research that has been performed, and

is still being done, to determine how accurate CFD solutions are compared with DSMC and experimental data. However, these studies are limited in several ways; for example, few studied cases for several different flow regimes or body geometry. In addition, as most are compared to experiment, they include complex thermochemical nonequilibrium effects. The addition of these complex models, while important, can mask fundamental differences that must be understood. Furthermore, while the surface properties are computed in some studies, the emphasis is usually placed on other flow properties, such as ionization species concentration and shock wave structure.

A quantitative link between a given level of continuum-breakdown and the accuracy of predicted surface quantities using CFD has not been presented in prior studies. Thus, there is a need for a more systematic, fundamental study to determine the effects of nonequilibrium on the surface properties of hypersonic vehicles. The goal of the present study is therefore to investigate this issue. Specifically, how are the critical hypersonic vehicle design surface properties of pressure, shear stress and heat transfer rate affected by failure of the continuum approach in certain regions of the flow field? For example, in hypersonic flow, the first place where continuum breakdown is observed is within the shock wave itself. It is well known that traditional, Navier-Stokes-based CFD cannot accurately predict hypersonic shock structure [17, 25]. It is not clear, however, whether local breakdown within the shock has a tangible impact on the rest of the flow field and the resulting surface properties.

1.4   Scope of Current Work

The research presented in this dissertation has several goals meant to address the limitations in the previous and current research efforts mentioned above. These goals are, specifically:

1. Start with the fundamentals. The present study, as a purely numerical study, will focus primarily on the fundamentals of nonequilibrium behavior and gradually increase the complexity, starting with a monatomic gas, argon, and progressing to a diatomic gas, nitrogen. The effects of each type of nonequilibrium on the surface properties will be quantified as the complexity increases.

2. Study many flow regimes, about blunt and sharp bodies. The current work will consider flow regimes from the continuum and into the transitional regime to quantify the effects of the degree of rarefaction; considering two different flow velocities to quantify the effects of larger Mach number; and considering two types of geometry, a cylinder and a wedge, to quantify differences due to blunt-body phenomena versus sharp leading-edge phenomena.

3. Evaluate the effectiveness of several types of CFD slip boundary conditions and compare the CFD slip values with the DSMC slip values. This research will evaluate the effectiveness of several CFD slip boundary conditions, including one only recently proposed [49], in predicting the surface properties of a hypersonic vehicle. The actual slip quantities predicted by these boundary conditions will also be compared with those extracted from the DSMC simulations for each flow condition.

4. Lay the foundation for further studies essential to the design of hybrid methods. Hybrid methods face two basic problems; determining the boundaries between the CFD and DSMC domains and passing information from one domain to the other. This research contributes to both of these areas. The chosen value for the continuum breakdown parameter's effectiveness in predicting differences will be shown by comparing the breakdown parameter value with the other flow properties. An effective hybrid design also requires that the different submodels used in both computational methods be equivalent as much as possible; thus information passed between both domains is also equivalent.

5. Show conclusively that flow property differences near the wall are concentrated in the Knudsen layer. Unique to this dissertation are the results that the differences between CFD and DSMC near the wall are concentrated mainly in the Knudsen layer, defined here as the region of flow 10 mean free paths or less from the wall surface.

An outline of this dissertation is as follows:

Chapter 2 presents a brief description of kinetic theory and the concepts of equilibrium and nonequilibrium gas dynamics and the equations governing gas flows. The chapter concludes with a brief description of the DSMC code MONACO and the CFD code LeMANS, which are used for the computational analyses in the remaining chapters.

Chapter 3 discusses the different submodels present in DSMC and CFD simulations. Such physical models include transport properties (such as viscosity), wall boundary conditions and vibrational relaxation. This chapter will discuss the relevant physical models and the manner in which they are treated in each simulation

method such that they are equivalent, as much as is possible.

Chapter 4 presents solutions obtained using both computational methods for a hypersonic flow about a cylinder. First, the case of a hypersonic flow of argon, a monatomic gas, is considered. The monatomic nature of argon eliminates the possibility of thermal nonequilibrium due to the nonexistence of internal energy modes. Then the case of a hypersonic flow of nitrogen, using the same physical geometry, is considered. The use of nitrogen, a diatomic gas, allows the investigation of the effects of thermal nonequilibrium in addition to the translational nonequilibrium present in the argon flow.

Chapter 5 considers the flow about a wedge with a sharp leading-edge. Again, solutions for flows of argon and nitrogen at Mach 10 and Mach 25 are computed and compared. The distinct physical phenomena associated with a sharp leading-edge flow are discussed.

Chapter 6 presents two-dimensional CFD solutions that are compared with experimental measurements of a hypersonic flow of nitrogen over a flat plate. Several different values for the accommodation coefficient are evaluated. In addition, the CFD solutions are also indirectly compared to DSMC solutions of the same flow. Thus, the relative accuracy of CFD and DSMC can be evaluated for a realistic flow.

The dissertation concludes with Chapter 7 in which some conclusions are drawn and future work is proposed.

CHAPTER II

Simulation of Hypersonic Gas Flows: Background and Theory

2.1   Introduction

The computational simulation of nonequilibrium hypersonic gas flows requires a basic understanding of the kinetic theory of gases, as well as the different methods used to model the varied phenomena present. This chapter begins by presenting a brief description of kinetic theory and the concepts of equilibrium and nonequilibrium gas dynamics. It then describes the equations governing gas flows, including the Boltzmann equation and the Navier-Stokes equations. The Boltzmann equation can be emulated using the direct simulation Monte Carlo (DSMC) method, while the Navier-Stokes equations can be solved numerically using Computational Fluid Dynamics (CFD) techniques. The chapter concludes with a brief description of the DSMC code MONACO and the CFD code LeMANS, which are used for the computational analyses in the remaining chapters.

2.2   Some Basics of Kinetic Theory

The discussion of the methods to follow requires some degree of knowledge in the kinetic theory of gases. This section is only meant to provide a short overview.

Monatomic gases (such as argon) and diatomic gases (such as nitrogen) are considered. For more details, the reader is directed to many texts on the subject, such as References [4, 31, 93].

Kinetic theory considers a gas flow on the molecular level. The individual gas molecules, or particles, are considered to be constantly moving about, colliding with other particles and any surfaces present. The properties of the flow depend only on the mass, size, position, velocity and internal energy of the particles. In this chapter, the mass of a particle is m; the size is defined as an effective particle diameter, d; the position is given as a vector position from the origin, x_i; and the velocity of an individual gas particle is denoted as a vector, c_i. The macroscopic thermodynamic properties, such as temperature, density and pressure, are derived by taking moments, or averages, of the individual particle properties.

The individual molecular velocity can be split into its random and average components as $c_i' = |c_i - \langle c_i \rangle|$ where $\langle c_i \rangle$ is the average velocity of the particles in the volume under consideration. The random velocity, c_i', is also known as the thermal velocity and the average velocity is known as the bulk velocity.

Each particle may have several energy modes. The translational energy is described by the random motion of the particles. Diatomic particles also possess internal energy due to rotation of the atoms around an axis, as well as vibration of the atoms along the internuclear axis.

The thermodynamic, or translational, temperature can be defined as a measure of the kinetic energy due to the random motion of the gas particles and is defined as

$$e_{tra} = \frac{1}{2}m\left(\langle c_1'^2 \rangle + \langle c_2'^2 \rangle + \langle c_3'^2 \rangle\right) = \frac{3}{2}\mathrm{k}T_{tra} \tag{2.1}$$

where e_{tra} is the average translational energy per particle and k is the Boltzmann con-

stant. Similarly, rotational and vibrational temperatures can be defined as measures of the internal rotational and vibrational energy of a diatomic gas

$$e_{rot} = kT_{rot}, \qquad (2.2)$$

$$e_{vib} = \frac{k\Theta_v}{\exp(\Theta_v/T_{vib}) - 1}, \qquad (2.3)$$

where e_{rot} and e_{vib} are the average rotational and vibrational energies per particle, and Θ_v is the characteristic vibrational temperature (the temperature at which the vibrational mode is significantly activated, approximately 3300 K for nitrogen). Here the assumption has been made that the rotational mode is fully activated at the temperatures of interest (the characteristic temperature of rotation for nitrogen is about 3 K), and that the vibrational energy can be modeled as a harmonic oscillator.

The rotational and vibrational energy modes are activated through the process of intermolecular collisions. As the molecules collide, energy is transferred from the translational mode to the rotational and vibrational modes, and vice-versa. The number of collisions required to activate the internal energy modes is dependent on the temperature of the flow. As the temperature increases, the collisions tend to be more energetic, and hence, the rotational and vibrational modes are activated with fewer collisions.

Figure 2.1 illustrates how the rotational and vibrational collision probabilities for nitrogen vary with temperature. Here, the rotational collision probabilities are obtained from Lordi and Mates experimental values [4] and the vibrational collision probabilities plotted are obtained from the Landau-Teller relaxation model as explained in Chapter III. The collision probability is the inverse of the collision number, or the number of collisions required on average to activate the internal energy modes. At lower temperatures—on the order of 100 K—the rotational collision
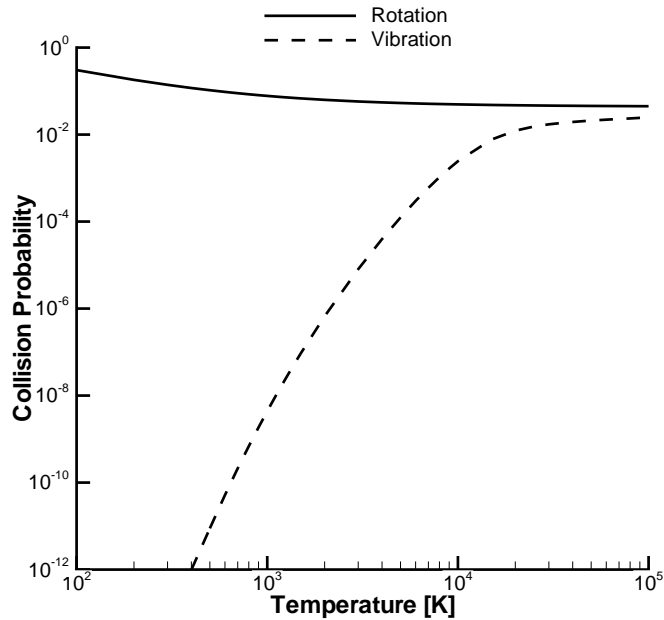
Figure 2.1: Probability that a collision will results in transfer of rotational and vibrational energy (for nitrogen).

probability is about 1/3. That is, about 3 collisions are required, on average, to activate the rotational modes. As the temperature increases, the rotational collision probability decreases and eventually remains constant at a value of about 0.045 (equivalent to a collision number of about 21).

Alternatively, the probability of vibrational energy exchange remains very small (below 10^{-3}, or a collision number of about 1000) until the temperature reaches about 5000 K. As the temperature increases, the vibrational collision probability increases dramatically and levels off at about 0.025 at 50,000 K. Thus, at such elevated temperatures, a larger number of collisions would result in vibrational energy exchange than at lower temperatures. It is important to note that the number of collisions required for vibrational activation decreases dramatically as the temperature increases, but the rotational modes still require far fewer collisions for activation

even at the higher temperatures.

An exact representation of a collision, or interaction of two or more particles, requires a detailed knowledge of the shape and orientation of the individual particles. For any realistic gas flow, this is impossible. Different models for the shape of the intermolecular force simplify the analysis. The hard-sphere model describes each gas particle as an elastic sphere with a specific size, defined as the diameter, d. There is no intermolecular force until the two molecules come into contact, at which point the repulsive force is infinite.

A significant weakness of the hard-sphere model is the fixed size, d. The total collision cross-section, σ_T, for the hard-sphere model is given by $\sigma_T = \pi d^2$. Experience has shown that the total collision cross-section is dependent on the relative speed between the molecules involved in the collision and it is important to reproduce this behavior to successfully model the temperature dependence of viscosity [4]. The average relative speed is dependent on temperature; hence, there is a temperature dependence to the average total collision cross-section, and the particle diameter.

Other models have been proposed that model the temperature dependence of the collision cross-section (and the viscosity) in a more realistic manner. Among these is the variable hard sphere (VHS) model [4]. A VHS particle has a diameter that is a function of the relative velocity of the collision partners. In many cases the function is an inverse power law, with the temperature dependence explicitly chosen to match experimental viscosity data.

In any realistic flow it is impossible to follow each individual molecule as it collides with other molecules and surfaces and describe its particular properties as a function of time. The use of a velocity distribution function (VDF) allows a probabilistic description of a particle's velocity and position. A VDF, denoted by $f = f(c_i, x_i, t)$, is

simply a probability density function in velocity-space; that is, it gives the probability that any particular particle will have a velocity that falls within the range $c_i + \Delta c$ at a particular location and time.

Once the VDF for a particular flow is known, the macroscopic properties can be obtained by taking moments of the VDF. The moment of a quantity, $Q(c_i)$, is defined as

$$\langle Q \rangle = \int_{-\infty}^{\infty} Q(c_i) f(c_i) \, \mathrm{d}c_i. \tag{2.4}$$

When $Q = c_i^n$ (where n is a power), then the average $\langle c_i^n \rangle$ is known as the nth-moment of the VDF.

2.3   Equilibrium and Nonequilibrium

Choosing a simulation method appropriate for a particular gas flow depends on whether or not there are significant equilibrium effects present. A precise definition of thermodynamic equilibrium will not be given here, but rather a few qualitative descriptions will be given to help in understanding the difference between equilibrium and nonequilibrium gas flows.

A gas in equilibrium can be thought of as one whose molecular properties are unchanging in time and space. This suggests that there are no gradients in molecular or macroscopic properties (velocity, temperature, mass density, etc). A gas in equilibrium will have a velocity distribution as given by Maxwell,

$$f_0 = \left(\frac{m}{2\pi kT} \right)^{3/2} \exp\left[-\frac{m}{2kT} \left(c'^2_1 + c'^2_2 + c'^2_3 \right) \right]. \tag{2.5}$$

A gas flow that is in complete thermodynamic equilibrium would have no interesting features present, and would, in fact, be completely at rest. The driving force behind flow features of interest are inherently nonequilibrium. However, if changes

in the gas that are due to nonequilibrium effects occur significantly rapidly such that the gas can be thought of as adjusting instantaneously to those changes, the flow is said to be in local thermodynamic equilibrium (LTE). Thus, although the gas is not at rest, the departure from the Maxwellian distribution 2.5 is everywhere small. The assumption of LTE implies that the effects of viscosity and thermal conductivity are negligible; that is, there is no transport of momentum or thermal energy due to velocity and temperature gradients.

In contrast, a gas in nonequilibrium will have gradients that allow for the transport within the gas of mass, momentum and/or energy. Mass flow is driven by species concentration gradients. A viscous fluid with velocity gradients will cause a transfer of momentum. Similarly, a gas with a temperature gradient will transport heat energy. Thermal nonequilibrium concerns internal energy modes of a diatomic gas, specifically the rotational and vibrational energy modes. Chemical nonequilibrium, present in a reacting flow, is beyond the scope of the current research and will not be discussed further here. Mass transport due to species concentration gradients is also neglected as only simple gases, comprising one species, are considered.

The transfer of momentum and energy is due to translational nonequilibrium and gives rise to the effects of viscosity and thermal conductivity. Rotational nonequilibrium is manifested in two different areas: the first concerns the so-called bulk viscosity; and the second a thermal nonequilibrium where the rotational temperature, as defined in Eq. 2.2, is not the same as the translational temperature, as defined in Eq. 2.1. Similarly, vibrational nonequilibrium is present in gas flows where the vibrational temperature, as defined in Eq. 2.3, is not equal to the translational temperature.

When nonequilibrium effects are present, the gas is driven towards equilibrium

through intermolecular collisions. The number of collisions required for gas molecules to equilibrate is dependent on the type of nonequilibrium present. Translational energy equilibrates with only a few collisions. Rotational energy requires on the order of ten collisions, while vibrational energy typically requires thousands of collisions to equilibrate.

The relaxation time is the time required for the gas to come to equilibrium. The distance traveled during that time by the bulk flow is the relaxation distance. Generally, the relaxation time is on the order of the mean collision time, and the relaxation distance is on the order of the mean free path [4].

The residence time of a gas particle can be defined as the amount of time taken for the gas particle to traverse a given flow feature, such as a velocity or temperature gradient. If the residence time is much longer than the relaxation time—that is, if the molecules undergo sufficient collisions to equilibrate to the local thermodynamic properties—then the flow is in equilibrium. However, if the residence time is short compared to the relaxation time, the gas particle will not reach equilibrium with the local thermodynamic conditions. Therefore, nonequilibrium effects can be expected in flow conditions with low residence times, or in flow conditions where relaxation times are large. These conditions are seen in areas of large gradients (such as in a shock wave or boundary layer) and in rarefied conditions (where the mean free path, and mean collision time, is large).

In a hypersonic flow, then, there are three main causes of significant nonequilibrium

- High velocities result in shorter residence times and larger gradients.

- High temperatures activate the vibrational energy modes, which are slower to

equilibrate than other energy modes.

- Many hypersonic vehicles fly in the upper, rarefied atmosphere. As the density decreases, the mean collision time increases and, thus, the relaxation time increases.

2.4   The Governing Equations of Gas Flows

This section describes the governing equations of gas flow, starting with the Boltzmann equation. The manner in which the Navier-Stokes equations can be derived from the Boltzmann equation is then briefly described. The resulting discussion highlights the strengths and weaknesses of each approach when used to model non-equilibrium gas flows.

2.4.1   The Boltzmann Equation

The Boltzmann equation, Eq. 2.6, describes the evolution in phase space (a combination of velocity and physical space) of the velocity distribution function of a particular gas flow [93]. There are two convective terms present; one models the convection in physical space due to the velocity, c_j; and the other the convection in velocity space due to accelerations caused by a force, F_j. The source term models the increase and decrease of particles of class c_i due to collisions.

$$\frac{\partial}{\partial t}[nf(c_i)] + c_j \frac{\partial}{\partial x_j}[nf(c_i)] + \frac{\partial}{\partial c_j}[F_j nf(c_i)] = \left\{ \frac{\partial}{\partial t}[nf(c_i)] \right\}_{coll} \qquad (2.6)$$

The form of the collision term depends on the particular molecular model considered. For a simple binary collision model, it can be written as

$$\left\{ \frac{\partial}{\partial t}[nf(c_i)] \right\}_{coll} = \int_{-\infty}^{\infty} \int_{0}^{4\pi} n^2[f(c_i')f(\zeta_i') - f(c_i)f(\zeta_i)]g\sigma \, d\Omega \, d\zeta_i, \qquad (2.7)$$

where σ is the differential collision cross-section, g is the relative velocity of the two colliding particles $(g = |c_i - \zeta_i|)$, and dΩ is the differential solid angle associated with the collision. Two types of collisions are considered. The first involves collisions between particles of class c_i with particles of class ζ_i. These collisions deplete the number of particles in class c_i. The second type of collisions is the inverse of the first; that is, collisions between particles of class c_i' and class ζ_i'. These collisions replenish the number of particles in class c_i. The total effect of these collisions on the VDF is found by integrating over all solid angles, and all collision pair velocities, ζ_i.

The Boltzmann equation is valid for all regimes of a gas flow, from the continuum to the rarefied regime, although it has been derived above to consider only binary collisions which would limit its validity to dilute gases. The main challenge in using the Boltzmann equation for modeling gas flows is the collision integral. Even assuming binary collisions only, the term is impossible (due to its nonlinear integral nature) to solve analytically and difficult to model numerically.

The Maxwellian VDF, given in Eq. 2.5 is a solution to the Boltzmann equation when the collision integral term is zero, and the flow is considered to be in LTE everywhere.

The Moment Equations

Moments of the velocity distribution function were defined in Eq. 2.4. Similarly, moments can be taken of the Boltzmann equation to give the moment equations, or equations of transfer,

$$\frac{\partial}{\partial t}(n\langle Q\rangle) + \frac{\partial}{\partial x_j}(n\langle c_j Q\rangle) - n\langle F_j\rangle\frac{\partial}{\partial c_j}(\langle Q\rangle) = \Delta[Q], \tag{2.8}$$

where $\Delta[Q]$ is the moment of the collision integral term.

It can be shown [93] that when the moment, $Q(c_i)$, is taken to be the mass,

momentum or energy per particle (m, mc_i or $mc_i^2/2$), the change in Q for the collision partners must remain zero, and, thus, $\Delta[Q] = 0$. Further simplifying the resulting set of equations gives the Euler equations. The Euler equations are then equivalent to the Maxwellian VDF when taking moments of the Boltzmann equation. The Euler equations are appropriate for modeling gas flows under the assumption of LTE.

The Chapman-Enskog Expansion

As mentioned, the Boltzmann equation has an equilibrium solution of $f = f_0$, where f_0 is the equilibrium, or Maxwellian, distribution function given in Eq. 2.5. Power-series solutions can be constructed for the Boltzmann equation. One well-known example is the Chapman-Enskog solution.

The Chapman-Enskog solution is obtained first by nondimensionalizing the Boltzmann equation in terms of a parameter ξ. It can be shown [93] that the parameter ξ is proportional to Kn $= \lambda/L$. Thus, for gas flows where Kn $<< 1$, this parameter will be small. As ξ approaches zero, f approaches f_0; this equation describes a small departure from equilibrium (a perturbation model). The Euler equations, the Navier-Stokes equations and the Burnett equations result from the Chapman-Enskog expansion of the distribution function for small departures from f_0.

As a power series, the VDF can be written as

$$\hat{f} = \hat{f}_0(1 + \xi\phi_1 + \xi^2\phi_2 + ...)$$

where $\hat{f}$ is the non-dimensional VDF.

The series is then usually truncated after one, two or three terms and substituted back into the Boltzmann equation, of which moments are taken. The resulting moment equations are the Euler equations (if only one term is kept), the Navier-Stokes equations (if two terms are kept) and the Burnett equations (if three terms

are kept).

2.4.2 The Navier-Stokes Equations

The Navier-Stokes equations (defined here as including the mass and energy conservation equations in addition to the momentum conservation equations) are typically used to describe gas flows in the continuum regime. As they can be derived from the Chapman-Enskog expansion of the Boltzmann equation (by keeping first-order terms), they are valid only for flows with small perturbations from equilibrium.

The Navier-Stokes equations for a simple gas and neglecting body forces can be written as [93]:

$$\frac{\partial \rho}{\partial t} + \frac{\partial}{\partial x_j}(\rho u_j) = 0 \tag{2.9}$$

$$\frac{\partial}{\partial t}(\rho u_i) + \frac{\partial}{\partial x_j}(\rho u_i u_j) = -\frac{\partial p}{\partial x_i} + \frac{\partial \tau_{ij}}{\partial x_j} \tag{2.10}$$

$$\frac{\partial}{\partial t}(\rho E) + \frac{\partial}{\partial x_i}(u_i \rho E) = -\frac{\partial}{\partial x_i}(u_i p) + \frac{\partial}{\partial x_i}(\tau_{ij} u_j) - \frac{\partial q_i}{\partial x_i} \tag{2.11}$$

where $E = e + \frac{1}{2}u_i u_i$ is the total energy per mass (e is the internal energy per mass, which includes the translational, rotational and vibrational energy), and τ_{ij} and q_i are the shear stress tensor and heat flux vector, respectively. (Note that $u_i = \langle c_i \rangle$.) In addition to τ_{ij} and q_i, which will be discussed shortly, another equation is required to close the set. Typically, an equation of state, such as the perfect gas law, is used.

The shear stress tensor and heat flux vectors arise due to translational nonequilibrium, and can be derived as

$$\tau_{ij} = \mu \left(\frac{\partial u_i}{\partial x_j} + \frac{\partial u_j}{\partial x_i} \right) - \mu_B \frac{\partial u_i}{\partial x_i} \tag{2.12}$$

$$q_i = -\kappa \frac{\partial T}{\partial x_i} \tag{2.13}$$

where μ is the coefficient of viscosity, μ_B is the bulk viscosity and κ is the coefficient of thermal conductivity. For a diatomic gas, similar expressions for the heat flux due

to rotational and vibrational energy are needed. Note that the Euler equations can be recovered from the Navier-Stokes equations above by setting τ_{ij} and q_i equal to zero.

Although the effects of the viscosity and thermal conductivity are due to translational nonequilibrium, the effect of bulk viscosity is due to rotational nonequilibrium [93]. For monatomic gases, then, it is equal to zero. Most conventional fluid dynamic analyses assume it is zero even for diatomic gases (Stokes' hypothesis).

The values of the coefficients of viscosity and thermal conductivity for a particular gas can also be derived from kinetic theory. Collision integral calculations are used to accurately determine their values across a wide range of temperatures [105].

The Navier-Stokes equations are only valid for the continuum regime (Kn < 0.01) with the no-slip boundary condition. Their validity can be extended to Kn < 0.1 by using slip boundary conditions, but for higher Knudsen numbers, they fail to accurately predict the flow.

Higher Order Moments and Extended Hydrodynamics

Additional information can be derived from the Boltzmann equation by retaining higher order terms of the Chapman-Enskog expansion. The Burnett equations result from retaining the first three terms of the expansion, and the super-Burnett equations result from retaining the first four terms. While the Burnett equations can give a more accurate description of the flow in nonequilibrium flows (such as the interior of shock waves [25]), there remain several significant hurdles to their practical implementation. Some of these include numerical stability and a failure to satisfy the second-law of thermodynamics [22]. Some researchers also contend that the Burnett equations cannot be used where the Navier-Stokes equations have already failed, as

they are also valid only for Knudsen numbers less than unity [33, 34].

Other attempts at deriving a general hydrodynamic approach for nonequilibrium gas flows include higher moment methods, of which Grad's method is one example. In this approach, higher order moments are taken of the Boltzmann equation and related to the lower order moments. A system of 20 equations can be obtained, which are then simplified to a set of 13 moment equations [31]. Sets of higher order moment equations can be obtained from the Boltzmann equation by considering Gaussian velocity distributions [47]. Numerical solutions of the 10- and 35-moment equations have been obtained for one-dimensional shocks [14]. However, the 10-moment equations do not include heat-transfer effects, while solutions to higher order moment equations, including the 13-, 14-, 20-, 21- and 35-moment equations, result in embedded discontinuities in the shock structure for inflow Mach numbers higher than about 5 or less [14, 41, 74, 101]. Thus, while these equations are valid for higher Knudsen number flows, their practical utility for hypersonic flows is limited.

2.5 Simulation Methods

The governing equations for gas flows (the Boltzmann equation and the Navier-Stokes equations) have now been reviewed in general. This section will describe two methods used to simulate gas flows; the direct simulation Monte Carlo method and Computational Fluid Dynamics.

2.5.1 The Direct Simulation Monte Carlo Method

Although the Boltzmann equation is valid for all flow regimes, it is impossible to solve analytically (except for extremely simple flows—although analytical solutions do exist for collisionless flows). Numerically solving the equation quickly becomes intractable due to its multi-dimensional nature (one in time, three in physical space

and three in velocity space) and the complexity of the collision integral term. The direct simulation Monte Carlo (DSMC) method [4] is a way to emulate the physical processes modeled by the Boltzmann equation. The DSMC method, similar to other Monte Carlo schemes, is a statistical approach. Instead of simulating each individual particle in a gas flow, a representative sample of particles is followed through the flow. Each particle has a specific position, velocity and internal energy (including rotational and vibrational). The intermolecular collisions are treated on a probabilistic rather than a deterministic basis and assume "molecular chaos" of dilute gas flows. The resulting process has been shown to converge to a solution of the Boltzmann equation [95].

A DSMC implementation can be briefly described as follows. A physical flow domain with appropriate boundaries is described. The computational domain is divided into cells used for selecting collision partners and over which the particle properties are averaged to obtain macroscopic properties. The physical domain is initialized with a number of representative computational particles with an initial position and velocity (according to an equilibrium VDF). The simulation then proceeds, stepping through time. At each time step

- The particles are moved according to the velocity and time step size.

- Boundary conditions, such as collisions with walls, inflow and outflow, are applied.

- Particle collisions are computed based on collision probabilities and molecular models.

- Macroscopic properties are evaluated by taking the averages of the properties of the individual particles.

This procedure implies certain assumptions and limitations. First, the time step must be small enough relative to the mean collision time such that the particle movements and the collision routines can be separated. Typical limits require a time step to be approximately 1/3 of the mean collision time. Second, the collision partners are chosen based on the particles in each cell. That is, each cell should be less than one mean free path in size—collision partners can then be randomly chosen from the particles in the each cell while maintaining physical accuracy. Third, each cell should contain sufficient particles such that the macroscopic averages are statistically meaningful—20 particles per cell is generally required.

DSMC is an attractive way to simulate complex, nonequilibrium flows. It has been shown to converge to solutions of the Boltzmann equation in the limit of an infinite number of particles [95]. Both the Boltzmann equation and DSMC are based on the same physical reasoning, and both require models to describe surface and intermolecular interactions. Nevertheless, it is easier to implement models that have been phenomenologically derived to agree with physical reality into DSMC, rather than into the mathematically rigorous Boltzmann equation [84]. However, the practical utility of DSMC is limited due to the computational cost. As the Knudsen number of a flow decreases, the number of cells (and, hence, particles) required increases. DSMC simulations of higher density flows are limited based on the computational resources available. Thus, DSMC is appropriate for the simulation of flows with all types of nonequilibrium in the transitional and rarefied regimes.

The Lattice Boltzmann Equation

The Lattice Boltzmann Equation is a "hyper-stylized version of the Boltzmann equation explicitly designed to solve fluid-dynamics problems" [87]. LBE methods

are suitable for flow conditions where considerable nonequilibrium effects are present, such as rarefied flows. However, these methods are not yet suitable for flows with strong compressibility and substantial heat transfer effects [87]; their applicability for hypersonic flows is thus limited.

2.5.2 Computational Fluid Dynamics

The Navier-Stokes equations can be solved analytically for simple flows, or, as is the case for Computational Fluid Dynamics (CFD) applications, solved numerically. (Strictly speaking, CFD techniques can be applied to any of the conservation equations previously mentioned, such as the Burnett or 13-moment equations; for this study, however, it should be noted that the term "CFD" refers to numerically solving the Navier-Stokes equations.) The finite-volume method is commonly used today [37, 38, 89].

A two-dimensional, finite volume method that considers a single species would solve the Navier-Stokes equations in conservative form as

$$\frac{\partial \mathbf{Q}}{\partial t} + \frac{\partial (\mathbf{E}_i - \mathbf{E}_v)}{\partial x} + \frac{\partial (\mathbf{F}_i - \mathbf{F}_v)}{\partial y} = \mathbf{S}. \tag{2.14}$$

Some degree of vibrational thermal nonequilibrium can be modeled using an additional energy equation for the vibrational modes [68]. The rotational modes are assumed to be in equilibrium with the translational modes and are modeled with one temperature, T; the vibrational modes are modeled with a vibrational temperature, T_{vib}. In this way, the vector of conserved variables, $\mathbf{Q}$, and the source vector, $\mathbf{S}$, are

given as

$$
\mathbf{Q} = \begin{bmatrix} \rho \\ \rho u \\ \rho v \\ \rho e \\ \rho e_v \end{bmatrix}, \ \mathbf{S} = \begin{bmatrix} 0 \\ 0 \\ 0 \\ 0 \\ \dot{w}_v \end{bmatrix},
$$

where ρ is the mass density, u and v are the bulk velocity in the x and y directions, e is the total energy and e_v is the vibrational energy per unit volume of the gas and $\dot{w}_v$ is the vibrational energy source term (modeled using the Landau-Teller model for vibrational relaxation [93]). The inviscid and viscous flux vectors in the x-direction are

$$
\mathbf{E}_i = \begin{bmatrix} \rho u \\ p + \rho u^2 \\ \rho u v \\ (\rho e + p)u \\ \rho e_v u \end{bmatrix}, \ \mathbf{E}_v = \begin{bmatrix} 0 \\ \tau_{xx} \\ \tau_{xy} \\ \tau_{xx}u + \tau_{xy}v - (q_{tr,x} + q_{v,x}) \\ -q_{v,x} \end{bmatrix}.
$$

The inviscid and viscous flux vectors in the y-direction are similar. The shear stress tensor and heat flux vector are evaluated assuming Newton's law of friction and Fourier's law, as given in equations 2.12 and 2.13, along with Stokes' hypothesis leading to $\mu_B = 0$. The system of equations is closed using the perfect gas law, $p = \rho R T$.

CFD has been used for many years to simulate gas flows in the continuum regime. With the use of additional equations, it can also successfully simulate vibrational (and chemical) nonequilibrium. Typical CFD methods do not include an additional rotational energy equation, nor can they accurately model the translational none-quilibrium present as the flow becomes more rarefied. The computational cost of a

CFD simulation is a function of the number of cells required, which is not explicitly dependent on the flow regime in question. Thus, CFD is appropriate for modeling high-temperature, high-speed gas flows in the continuum regime, with limited success in the slip and transitional regimes (with the slip boundary conditions).

2.6 Computational Codes

The remaining chapters describe numerical simulations of hypersonic gas flows obtained using the DSMC and CFD methods. The two codes used to obtain these results are MONACO (DSMC) and LeMANS (CFD), which are briefly described here.

2.6.1 MONACO

In this research, DSMC results are provided from the MONACO code [23], which is a general 2D/3D, object-oriented, cell-based, parallel implementation of the DSMC method. It has been applied to many hypersonic, rarefied flows [88]. Several different molecular models can be used, including the Variable Hard Sphere (VHS) and Variable Soft Sphere collision models [4, 46]. It also includes variable vibrational [92] and rotational [9] energy exchange probability models to model the temperature dependence of the rotational and vibrational collision probabilities. In cases where the cell sizes are larger than the local mean free path, the subcell method can be used to select particles for collisions [4] to ensure physical accuracy.

The current work uses the VHS model, the details of which are discussed in Chapter III.

2.6.2 LeMANS

The CFD results are obtained using the (Le) Michigan Aerothermodynamic Navier-Stokes (LeMANS) code, developed at the University of Michigan for the simulation of hypersonic reacting flow-fields [75, 76, 77]. LeMANS is a general 2D/3D, parallel, unstructured, finite-volume CFD code capable of simulating gases in thermal and chemical nonequilibrium. A modified Steger-Warming flux vector splitting scheme is implemented [54, 85]. The code is second-order in space and time, using a point- or line-implicit time integration scheme [75]. A two-temperature model [68] is used to account for the nonequilibrium between the vibrational and the translational-rotational modes, with the energy exchange rates modeled using the Landau-Teller model [93]. Standard finite-rate chemistry models for reacting air using 5 species, 7 species and 11 species allow atmospheric flow simulations in conditions causing dissociation and weak ionization [68]. Transport properties can be computed using Wilke's [103] and Blottner's [7] models. Different boundary conditions, including no-slip and slip velocity and temperature jump are enforced.

Details concerning the transport properties, the Landau-Teller model and the slip boundary conditions used in the current work are discussed in Chapter III.

A Note on Hybrid Methods

DSMC is an attractive and applicable method for simulating gas flows at large Knudsen numbers, although it becomes computationally expensive in the continuum regime. CFD works well for the continuum regime, but is inaccurate for higher Knudsen number flows. Many times, the gas flow around a hypersonic vehicle will fall into a range of flow regimes; for example, there might be a region of high density gas upstream of the vehicle where the continuum hypothesis holds, but downstream

in the wake the gas is sufficiently rarefied that the continuum hypothesis breaks down. Additionally, nonequilibrium effects tend to be concentrated in regions of large gradients, such as shock waves and boundary layers. Although DSMC could be used to simulate the entire domain, it is computationally expensive to do so.

A class of hybrid DSMC-CFD solvers has been proposed to solve this problem [36, 71, 80, 94]. In a hybrid method, the computational domain is divided into continuum and particle regions, with DSMC being used in the particle regions and CFD in the continuum regions. Two main problems are associated with this type of hybrid method. First is the problem of determining where the regions of equilibrium and nonequilibrium are located. This is usually accomplished through some type of continuum breakdown parameter [11], which is discussed in some detail in Chapter III. Second is the manner in which information is passed between the CFD and DSMC regions. Research continues in this area [79, 82, 80, 98].

CHAPTER III

Comparing Simulation Results from the DSMC and CFD Methods

3.1   Introduction

The direct simulation Monte Carlo (DSMC) method and the Computation Fluid Dynamics (CFD) method differ in their fundamental approach to simulating gas flows. Although these approaches are based on different assumptions regarding the amount of equilibrium present in the flow, each should give equivalent results in regimes where they are both valid. The goal of the current study, to determine the effects of nonequilibrium on the simulation results, requires that the physical models encapsulated within the framework of each method be treated in a similar manner. Thus it is assured that differences in the results are due to the fundamental differences of the methods, and their ability to capture nonequilibrium phenomena, and not due to differences in their treatment of the underlying physical models. Such physical models include transport properties (such as viscosity), wall boundary conditions and vibrational relaxation. This chapter will discuss the relevant physical models and the manner in which they are treated in each simulation method such that they are equivalent, as much as is possible.

As was discussed previously, the DSMC method is valid in regions of nonequil-

ibrium, while the CFD method is valid only for small departures from equilibrium. It is instructive to determine when and where the nonequilibrium present in a particular gas flow exceeds the capabilities of CFD. Therefore, methods appropriate for quantifying the amount of nonequilibrium present in a gas flow, in the form of a continuum breakdown parameter, are also discussed.

Much of the material of this chapter is also relevant when designing a hybrid code using both DSMC and CFD methods. In a hybrid code, it is critical that the physical models be treated in a consistent manner across the computational domain. It is also necessary to determine where in the computational domain DSMC should be used rather than CFD—the continuum breakdown parameter is used in that role in many hybrid methods.

3.2 Transport Properties

Even a small departure from LTE in a gas flow due to variations of macroscopic phenomena, such as species concentration, velocity and temperature, will give rise to the transfer of mass, momentum and energy, respectively. The molecular processes that govern the transfer of mass, momentum and energy result in the macroscopic properties of diffusion, viscosity and thermal conductivity [93]. As mentioned above, the goal of comparing DSMC and CFD simulations requires equivalent treatment of these transport properties. As all simulations treated herein involve only one gas species, the transport of mass via diffusion is not present and will not be treated further here.

3.2.1 Viscosity

All DSMC simulations presented here are generated using the variable hard sphere (VHS) model [4]. The viscosity can be calculated using the VHS model parameters.

Table 3.1: Variable hard sphere (VHS) model parameters for argon and nitrogen used in the computational simulations.

Species	ω	T_{ref} [K]	d_{ref} [m]
Ar	0.734	1000	3.595×10^{-10}
N$_2$	0.7	290	4.110×10^{-10}

Therefore, for the purposes of this study, LeMANS was modified to use a viscosity directly corresponding to the VHS model according to Eqs. 3.1 and 3.2 [81]:

$$\mu = \mu_{ref} \left(\frac{T}{T_{ref}} \right)^{\omega} \tag{3.1}$$

$$\mu_{ref} = \frac{15 \sqrt{\pi m k T_{ref}}}{2\pi d_{ref}^2 \left(5 - 2\omega\right) \left(7 - 2\omega\right)} \tag{3.2}$$

where μ is the viscosity, T is the temperature, ω is the VHS temperature exponent, m is the mass of one molecule of the gas, k is the Boltzmann constant and d is the molecular diameter. This model requires only that a reference temperature, T_{ref}, reference diameter, d_{ref} and the temperature exponent, ω, be specified for both DSMC and CFD and the viscosity treatment is equivalent, for a gas at or near equilibrium. The VHS parameters used in the current study are summarized in Table 3.1.

3.2.2 Thermal Conductivity

The thermal conductivity coefficient, κ, is related to the viscosity, μ, as

$$\text{Pr} = \frac{c_p \mu}{\kappa} \tag{3.3}$$

where Pr is the Prandtl number and c_p is the specific heat at constant pressure. From kinetic theory an equivalent form of the Prandtl number can be obtained, known as

Eucken's Relation [93],

$$\mathrm{Pr} = \frac{4\gamma}{9\gamma - 5} \tag{3.4}$$

from which the thermal conductivity coefficient is obtained as

$$\kappa = \frac{9\gamma - 5}{4\gamma - 4} \mathrm{R}\,\mu \quad . \tag{3.5}$$

The ratio of specific heats, γ, is related to the number of degrees of freedom, ξ, present in a particular gas species as

$$\gamma = \frac{\xi + 2}{\xi} \quad . \tag{3.6}$$

The use of Eqs. 3.5 and 3.6 in LeMANS ensures equivalent treatment of the thermal conductivity coefficient in both methods, for a gas at or near equilibrium.

3.3 Wall Boundary Conditions

Appropriate treatment of the boundary conditions, especially the wall boundary conditions, is critical when comparing solutions from DSMC and CFD. This section discusses the different wall boundary conditions implemented in MONACO and LeMANS.

3.3.1 Gas-Surface Interactions

When a gas molecule collides with a wall, it is reflected at a specific angle and velocity. In DSMC, this effect is modeled as if the particle were absorbed by the wall and then re-emitted from the wall, and results in two general types of interactions.

If the particle is reflected elastically, with a normal velocity component equal to the negative of the incoming normal velocity component, and with an unchanged tangential velocity component, the collision is said to be a specular interaction [66].

This boundary condition corresponds to an infinitely smooth, adiabatic wall. The wall shear stress and heat transfer rate in such a case are zero.

The other effect is when the particle collides with the wall, and is then re-emitted at a random angle and velocity corresponding to a Maxwellian velocity distribution in equilibrium with the wall. The colliding particle is thus thermally accommodated to the wall. This collision is said to be a diffuse interaction. This boundary condition corresponds to a rough wall held at a constant temperature. The wall shear stress and heat transfer rate are correspondingly non-zero.

Both of these conditions are theoretical in nature; in practice, particles collide with walls in both specular and diffuse interactions. The accommodation coefficient represents the fraction of incoming particles that are reflected diffusely. The remainder are reflected specularly. The accommodation coefficient is typically a function of the wall roughness, composition and the types of surface chemical reactions that might occur.

For the purposes of this study, only the case of a fully diffuse interaction is considered; that is, the accommodation coefficient is unity, and the walls are assumed to be isothermal, with all temperatures (translational, rotational and vibrational) being set to the constant wall temperature.

3.3.2 Velocity Slip and Temperature Jump

At sufficiently low Knudsen numbers to warrant the assumption of continuum flow, the velocity and temperature of the gas near the wall are in equilibrium with the wall. That is, the no-slip boundary conditions hold. As the flow becomes more rarefied, there are insufficient collisions near the wall to equilibrate the gas molecules to the wall, thus invalidating the no-slip conditions. This results in conditions known

as slip conditions where the velocity and temperature of the gas near the wall are not equal to the wall velocity and temperature. The slip conditions are inherent to the Boltzmann equation, and are thus handled transparently by the DSMC method. It is necessary, however, to extend the no-slip boundary conditions typically used in CFD to include the slip-conditions to improve its accuracy when used for more rarefied flows. This sections discusses several different types of slip boundary conditions implemented in the LeMANS code, as well as the method to extract slip quantities from MONACO simulations.

Slip Boundary Conditions in CFD

The slip boundary condition was first derived by Maxwell for a flat plate. The expression he derived for the velocity slip is shown in Eq. 3.7, as discussed in Ref. [48], where wall coordinates are used (n is normal to the wall and x is parallel to the wall):

$$U_s = A \left(\frac{2 - \sigma}{\sigma} \right) \lambda \frac{\partial u_x}{\partial n} + \frac{3}{4} \frac{\mu}{\rho T} \frac{\partial T}{\partial x} \tag{3.7}$$

where U_s is the velocity slip (assuming a stationary wall), A is a constant of proportionality, σ is the tangential momentum accommodation coefficient, λ is the mean free-path, u_x is the velocity in the x-direction, μ is the viscosity, ρ is the mass density and T is the temperature. For an isothermal wall, the temperature gradient can be neglected, giving the boundary condition in its simplest form as:

$$U_s = A \left(\frac{2 - \sigma}{\sigma} \right) \lambda \left. \frac{\partial u_x}{\partial n} \right|_{n=0}. \tag{3.8}$$

The mean free path, λ, is calculated from typical gas flow properties as [29]:

$$\lambda = \frac{2\mu}{\rho \bar{c}} = \frac{\mu}{\rho} \sqrt{\frac{\pi}{2RT}} \tag{3.9}$$

where μ is the viscosity, ρ is the mass density and $\bar{c}$ is the mean molecular speed. The boundary condition for the temperature jump is similar [30]:

$$T_0 - T_w = \frac{2 - \alpha}{\alpha} \frac{2\gamma}{(\gamma + 1)\,\mathrm{Pr}} \lambda \left. \frac{\partial T}{\partial n} \right|_{n=0} \tag{3.10}$$

where T_w is the wall temperature, T_0 is the temperature of the gas at the wall (and where $T_w - T_0$ is the temperature jump), α is the thermal accommodation coefficient, γ is the specific heat ratio, Pr is the Prandtl number, and T is the temperature. An equivalent mean free path can be adopted as

$$\lambda_T = \frac{4}{(\gamma + 1)} \frac{\kappa}{\rho \bar{c} c_v} = \frac{2}{(\gamma + 1)} \frac{\kappa}{\rho c_v} \sqrt{\frac{\pi}{2RT}} \tag{3.11}$$

to give a simpler form,

$$T_0 - T_w = \frac{2 - \alpha}{\alpha} \lambda_T \left. \frac{\partial T}{\partial n} \right|_{n=0}. \tag{3.12}$$

The simple Maxwell slip conditions are implemented in LeMANS as given by Eqs. 3.8 and 3.12.

The general form of the velocity slip has remained the same throughout many years of research; the difficulty is in determining the correct value for the constant, A, and the accommodation coefficients, σ and α. In effect, any change in A simply changes the value of the accommodation coefficient, which depends on the physical characteristics of the wall itself [86]. Many times these coefficients are determined empirically, while other times they are calculated from relations based on kinetic theory [83]. The most detailed boundary conditions require knowledge *a priori* of a good nonequilibrium solution for the flow considered. The current investigation seeks to find a good boundary condition that does not require *a priori* knowledge of any nonequilibrium solution, which would eliminate any advantage in using CFD over DSMC. For the purposes of this study, it is sufficient that the values for the
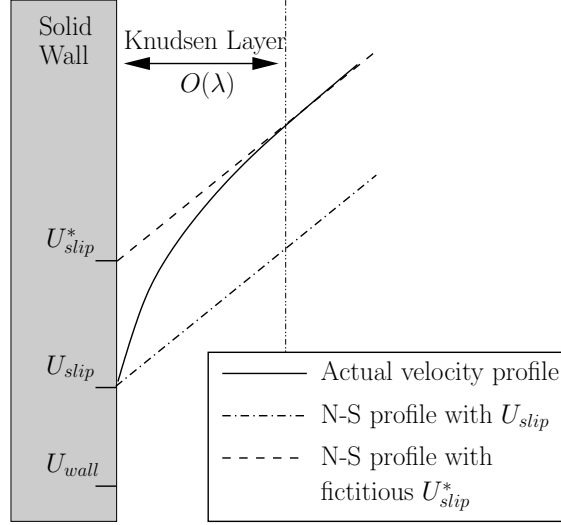
Figure 3.1: Velocity profiles in the Knudsen layer. The true velocity profile is compared to Navier-Stokes profiles with a true velocity slip and a fictitious velocity slip (after Ref. [49]).

accommodation coefficient be consistent between DSMC and CFD; therefore, an accommodation coefficient of unity is used.

The previous, simple slip boundary conditions were derived for small Knudsen numbers. Gökçen [29] showed that, for large Knudsen numbers, these simple slip boundary conditions converge to different values than those predicted by free molecular flow. He then proposed the general slip boundary conditions,

$$\alpha_a \left(a_\lambda - a_w \right) = 2\lambda_a \left. \frac{\partial a}{\partial n} \right|_{n=0} . \tag{3.13}$$

Here, a is either velocity or temperature, and λ_a is given by either Eq. 3.9 or 3.11. For small Knudsen numbers, this expression reduces to Eqs. 3.8 and 3.12 [30].

The Navier-Stokes (N-S) equations with no-slip boundary conditions fail in at least two different areas as the flow becomes more rarefied. The first area, the assumption of no-slip flow, is corrected through the use of the slip boundary conditions. However, the N-S equations also assume that the shear stress varies linearly with the

velocity gradient. Cercignani showed that this is not the case, and he computed the velocity profile near the wall, as discussed in [49]. Figure 3.1 illustrates the velocity profile near the wall in the Knudsen layer (which is defined as being on the order of one mean free-path from the wall). The velocity profiles corresponding to the N-S assumption of a shear stress that varies linearly with the velocity, with two different values of velocity slip, are shown in comparison to the actual velocity profile.

Here there are two choices one can make concerning the boundary conditions; use the actual velocity slip in which case the flow field away from the wall will not be accurate, or use a fictitious velocity slip (as shown in Figure 3.1). The fictitious slip will not accurately predict the flow near the wall (and hence may adversely affect the accuracy of drag and heat transfer rates) but will be more accurate in the region away from the wall.

To overcome this limitation, a correction to the velocity gradient was evaluated by Lockerby, et al. [49]. They proposed using a wall-function type of boundary condition for the velocity where the viscosity in the Knudsen layer is modified as

$$\mu = \frac{\mu}{\Psi},$$ (3.14)

where the wall-function,

$$\Psi\left(\frac{n}{\lambda}\right) \approx 1 + \frac{7}{10}\left(1 + \frac{n}{\lambda}\right)^{-3}$$ (3.15)

was derived from a curve-fit to Cercignani's Knudsen layer velocity profile. In Eq. 3.15, n is the distance from the wall and λ is the mean free-path.

This modification of the viscosity in the Knudsen layer is also used in connection with a simple slip boundary condition as given by Eq. 3.8 with $A = \sqrt{2/\pi}$. This approach is expected to allow the CFD method to accurately model the velocity profile in the Knudsen layer.

This new wall function has only been evaluated for isothermal flow conditions that are usually encountered in micro-flows [49]. Although there will be some change to the heat transfer rate coefficient (based on a constant Prandtl number), there might be other changes necessary to give the correct temperature profile in the Knudsen layer for the non-isothermal, hypersonic flows considered here. Nevertheless, it is instructive to investigate the possible improvement this wall function might afford. This slip condition is referenced herein as the Lockerby slip condition.

For cases involving a diatomic species that require a vibrational energy equation, a corresponding vibrational temperature jump is calculated in the same manner as the translational/rotational temperature jump, with the appropriate value for κ and c_v used when computing the mean free-path according to Eq. 3.11.

The CFD solutions with velocity slip and temperature jump boundary conditions assume a fully diffuse wall ($\sigma = 1$) that is also thermally accommodating ($\alpha = 1$). These assumptions correspond to the fully diffuse wall used in the DSMC simulations.

Slip Quantities in DSMC

While the DSMC method inherently includes the slip boundary conditions, it is necessary to extract this information from the simulation results. In MONACO, the velocity slip and temperature jump are calculated based on the particles that strike the surface, according to Eqs. 3.16 and 3.17, which are the relations used in Bird's DSMC implementation, DS2V[5, 6].

$$U_s = \frac{\sum \left((m/|U_n|)\, U_p \right)}{\sum \left(m/|U_n| \right)} \tag{3.16}$$

$$T_{tra,j} = \frac{1}{3R} \frac{\sum \left((m/|U_n|)\, (\|\mathbf{U}\|) \right) - \sum (m/|U_n|) U_s^2}{\sum \left(1/|U_n| \right)} - T_{tra,W} \tag{3.17}$$

where U_s is the velocity slip, U_n is the velocity normal to the wall, U_p is the velocity parallel to the wall, $||\mathbf{U}||$ is the velocity magnitude (includes all three components), $T_{tra,j}$ is the translational temperature jump, and $T_{tra,W}$ is the wall translational temperature and the summations are taken over all particles that strike the surface.

These relations include the somewhat counterintuitive use of the velocity component normal to the wall. This is due to the necessity of using wall fluxes, an inherently two-dimensional quantity, to derive a velocity slip and temperature jump, which are volume quantities. That is, only the properties of particles that hit the wall are considered, rather than those of all the particles in the cell adjacent to the wall. The probability that a particle in a cell will collide with the wall during a particular time step is proportional to its velocity component normal to the wall. Thus, the velocity slip and temperature jump quantities would be biased toward higher velocity particles if the summations were not weighted by the magnitude of the normal velocity component.

Corresponding quantities can be derived for the rotational and vibrational temperature jumps as

$$T_{rot,j} = \frac{1}{R} \frac{\sum (e_{rot}/|U_n|)}{\sum (1/|U_n|)} - T_{rot,W} \tag{3.18}$$

$$T_{vib,j} = \frac{\Theta_v}{\ln\left(\frac{R\Theta_v}{E_{vib}} + 1\right)} - T_{vib,W}, \quad E_{vib} = \frac{\sum (e_{vib}/|U_n|)}{\sum 1/|U_n|} \tag{3.19}$$

where e_{rot} and e_{vib} are the rotational and vibrational energies associated with each particle and Θ_v is the characteristic vibrational temperature.

A Note on Temperatures

As shown in Chapter II, LeMANS uses a two-temperature model (translational/rotational and vibrational) while MONACO tracks all three energy modes: trans-

lational, rotational and vibrational. Therefore, the proper way to compare simulation results for the temperatures is to average the DSMC translational and rotational temperatures according to the number of degrees of freedom of each mode ($\xi_{tra} = 3$ and $\xi_{rot} = 2$) as shown in Eq. 3.20 [4]. This averaged temperature is then equivalent to the translational/rotational temperature obtained from LeMANS.

$$T = \frac{3\,T_{tra} + 2\,T_{rot}}{5} \tag{3.20}$$

In the same way, the rotational and translational temperature jumps obtained from MONACO are averaged and then compared with the temperature jump predicted by LeMANS.

The vibrational temperature results obtained from each simulation method are compared directly.

3.4 Vibrational Relaxation

The rate of energy exchange between the translational and vibrational modes is inversely proportional to the vibrational relaxation time, τ_v. The Landau-Teller model is generally used to approximate the vibrational relaxation time [93]. Millikan and White [56] correlated experimental data with the Landau-Teller model to obtain an expression for the vibrational relaxation time as

$$\tau_{LT} = \frac{1}{p} \exp\left(\frac{A}{T^{1/3}} + B \right) \tag{3.21}$$

where p is the pressure, T is the temperature and A and B are constants that vary by species.

A correction proposed by Park [68] that is necessary for temperatures typically encountered at hypersonic speeds is given as

$$\tau_P = \frac{1}{n\bar{c}\sigma} \tag{3.22}$$

where n is the particle density, $\bar{c}$ is the mean molecular speed and σ is the vibrational collision cross section.

The vibrational relaxation time is then given in Eq. 3.23.

$$\tau_v = \tau_{LT} + \tau_P \tag{3.23}$$

The Landau-Teller model is a continuum model and can be directly implemented in a CFD code. The vibrational relaxation process in DSMC is governed by collision probabilities. The probability that a collision will result in an exchange of vibrational energy is given as

$$P = \frac{1}{\tau_v \nu} \tag{3.24}$$

where ν is the bi-molecular collision rate. This probability is then implemented in MONACO using discrete collision probabilities [10, 92] (with various corrections [53, 1]), which, when integrated over all collisions, is expected to correspond to the total probability as given in Eq. 3.24.

Proper comparison of the vibrational relaxation in both CFD and DSMC then requires the use of equivalent constants, A and B, in the Millikan and White correlation for vibrational relaxation time as well as equivalent Park correction parameters. The values for A and B for nitrogen are 220 and -24.80, respectively, for a pressure given in atm. For a pressure given in Pa, the value for B is -13.27. LeMANS uses the Millikan and White values in the Landau-Teller model, although with a different definition of B that corresponds directly to $B = $ -24.8. The current work uses a constant vibrational collision cross section, $\sigma = 5.81 \times 10^{-21}$ m², for both the CFD and DSMC simulations.

An additional correction to the vibrational collision probability in MONACO is necessary to achieve accurate results. A recent study compared the theoretical vi-

Table 3.2: Vibrational collision probability, P, in MONACO compared to theory for
N$_2$–N$_2$ collisions, with the correction factor [24].

Temperature (K)	MONACO	Theory	Correction Factor
5000	1.57×10^{-4}	1.24×10^{-4}	0.79
10000	1.71×10^{-3}	2.44×10^{-3}	1.43
15000	4.20×10^{-3}	7.68×10^{-3}	1.83
20000	6.76×10^{-3}	1.23×10^{-2}	1.82
25000	9.00×10^{-3}	1.53×10^{-2}	1.70
30000	1.08×10^{-2}	1.72×10^{-2}	1.59
35000	1.24×10^{-2}	1.85×10^{-2}	1.49
40000	1.38×10^{-2}	1.95×10^{-2}	1.41
45000	1.51×10^{-2}	2.03×10^{-2}	1.34
50000	1.61×10^{-2}	2.10×10^{-2}	1.30
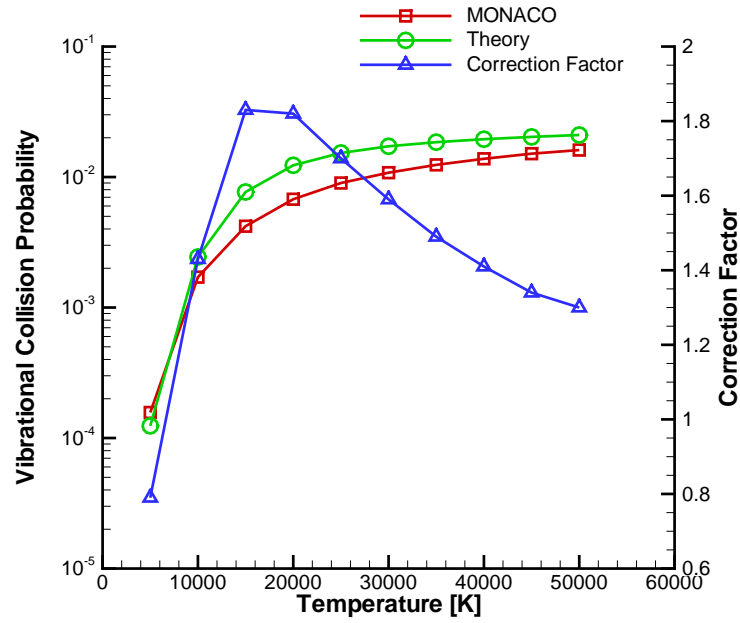
Figure 3.2: Vibrational collision probability for N$_2$–N$_2$ collisions in MONACO compared to theory, with the correction factor.

brational collision probability (Eq. 3.24) with that given by MONACO [24]. This study showed that, while remaining within a factor of 2, the overall probability seen in MONACO differed from the theoretical probability as shown in Table 3.2 and Figure 3.2 for N_2–N_2 collisions. The correction factor is the ratio of the theoretical vibrational collision probability to that of MONACO. The discrepancies between MONACO and the theoretical vibrational probability are most likely due to the method of analytical integration used in deriving the discrete collision probabilities used in the DSMC model [10]. It should be emphasized that this correction is obtained by comparing the vibrational collision probability in MONACO to the theoretical vibrational collision probability, and not to any CFD results.

In the present work, the vibrational collision probability is multiplied by a correction factor (as shown in the fourth column of Table 3.2) to better correspond to theory. The correction factor is chosen based on the maximum translational temperature in each case; for example, in a Mach 10 flow the maximum temperature is approximately 5,000 K, so the vibrational collision probability is multiplied by 0.79, while for a Mach 25 case the maximum temperature is approximately 25,000 and the vibrational collision probability is multiplied by 1.70.

3.5 Continuum Breakdown/Nonequilibrium Onset

The areas of the flow where the continuum hypothesis breaks down (or equivalently, where the flow is no longer in local thermodynamic equilibrium), can be quantified by the use of a continuum breakdown parameter. Several breakdown parameters have been proposed in the literature. Bird [3] proposed the parameter, P, for jet expansions:

$$P = \frac{U}{\rho\nu}\left|\frac{d\rho}{ds}\right| = M\sqrt{\frac{\pi\gamma}{8}}\frac{\gamma}{\rho}\left|\frac{d\rho}{ds}\right| \tag{3.25}$$

where U is the local velocity, ν is the collision frequency, M is the local Mach number, γ is the ratio of specific heats, and s is the distance along a streamline. Continuum breakdown is assumed when P is greater than 0.05.

Boyd, et al. [11] carried out extensive numerical investigation of one-dimensional normal shock waves and two-dimensional bow shocks comparing DSMC and CFD results to determine an appropriate breakdown parameter. They proposed the use of the gradient-length local Knudsen number,

$$\text{Kn}_{\text{GLL}} = \frac{\lambda}{Q} \left| \frac{dQ}{dl} \right| \tag{3.26}$$

where λ is the mean free-path, Q is some quantity of interest such as density, pressure, temperature or velocity magnitude, and the derivative is taken in the direction of the maximum gradient.

Other breakdown parameters that have been proposed include Tiwari's criterion [90],

$$||\Phi|| = \frac{1}{\rho R T} \left(\frac{2}{5} \frac{|q|^2}{R T} + \frac{1}{2} ||\tau||_E^2 \right)^{\frac{1}{2}} \tag{3.27}$$

where ρ is the mass density, R is the gas constant, T is the temperature, $||\tau||_E$ is the Euclidean norm of the stress tensor, τ, and q is the heat flux vector; and the parameter B [26],

$$B = max \left\{ \left| \tau_{ij}^* \right|, |q_i^*| \right\} \tag{3.28}$$

where τ_{ij}^* and q_i^* are the normalized stress tensor and heat flux vector, respectively. More recent work [15] has proposed the use of entropy generation rates to determine areas of nonequilibrium.

Further studies [98] have shown that Bird's parameter (based on density and other properties such as temperature and velocity magnitude) is inadequate in the stagnation region of hypersonic compressible flows. Of the alternatives, only the

gradient-length local Knudsen number, Kn_{GLL}, has been extensively tested for hypersonic compressible flows. Therefore this study will use Kn_{GLL}, computed using Eq. 3.26, as the breakdown parameter.

When calculating Kn_{GLL} based on velocity magnitude, the gradient is normalized by the maximum of the local velocity magnitude and the local speed of sound. It is generally assumed that continuum breakdown occurs whenever Kn_{GLL} is greater than 0.05.

CHAPTER IV

Hypersonic Flow about a Cylinder

4.1   Introduction

Hypersonic vehicles can be broadly classified as either blunt-body or sharp-leading-edge vehicles. The flows around each of these two types of vehicles are significantly different and highlight different physical phenomena. This chapter considers a hypersonic flow about a blunt-body; in this case a two-dimensional, 12-inch diameter cylinder as shown in Figure 4.1. Results from computational simulations are discussed.

First, the case of a hypersonic flow of argon, a monatomic gas, is considered. The monatomic nature of argon eliminates the possibility of thermal nonequilibrium due to the nonexistence of internal energy modes. The results from this part of the study will help to understand the effects of translational nonequilibrium on the flow field and surface property predictions, and will give a baseline to which further results can be compared. Then the case of a hypersonic flow of nitrogen, using the same physical geometry, is considered. The use of nitrogen, a diatomic gas, allows the investigation of the effects of thermal nonequilibrium in addition to the translational nonequilibrium present in the argon flow. It should be noted that only thermal nonequilibrium effects are considered; although the temperatures present, especially
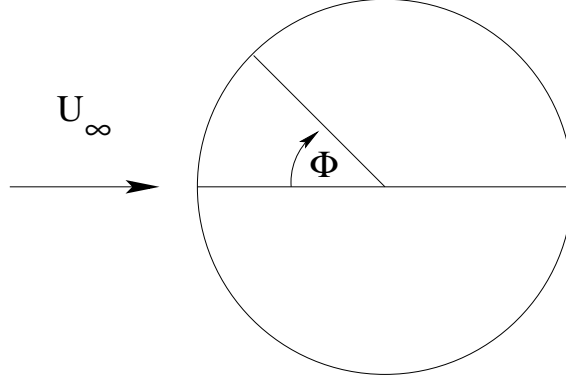
Figure 4.1: 2D cylinder geometry definition. Φ is the angle in degrees from the stagnation point.

at the higher velocities, are high enough that significant amounts of dissociation and ionization would be expected, no chemistry effects are considered.

The inflow boundary conditions are Mach 10 and Mach 25, and the free stream density of the flow is varied such that several different regimes are considered, from the continuum through the transitional to the rarefied regime, as shown in Table 4.1. Here, the global Knudsen number is calculated based on the cylinder diameter, using the hard-sphere model for the mean free-path, λ,

$$\lambda = \frac{1}{\sqrt{2}\pi d^2 n} \tag{4.1}$$

where d is the molecular diameter and n is the particle density. Note that in all cases the flow remains in the laminar regime, as shown by the small Reynolds number values.

Other relevant in-flow boundary conditions and the constant wall temperature are shown in Table 4.2.

Surface and flow field properties for this flow are presented from two different computational approaches. First, CFD results are obtained through solution of the Navier-Stokes equations, using the LeMANS code. Different boundary conditions,

Table 4.1: Flow regimes considered.

Kn_∞ [*]	n [particles/m^3]	ρ_∞ (Ar) [kg/m^3]	ρ_∞ (N$_2$) [kg/m^3]	Re [**]
0.002	2.124×10^{21}	1.408×10^{-4}	9.872×10^{-5}	20,000
0.01	4.247×10^{20}	2.818×10^{-5}	1.974×10^{-5}	4,000
0.05	8.494×10^{19}	5.636×10^{-6}	3.949×10^{-6}	800
0.25	1.699×10^{19}	1.127×10^{-6}	7.897×10^{-7}	160

[*] Based on hard-sphere mean free path.
[**] Based on cylinder diameter and Mach 25.

Table 4.2: Boundary conditions.

Mach	U_∞ (Ar) [m/s]	U_∞ (N$_2$) [m/s]	T_∞ [K]	T_{wall} [K]
10	2624	2883	200	500
25	6585	7208	200	1500

including no-slip and slip velocity and temperature jump are enforced, as discussed in Chapter III. Recall that the boundary conditions implemented are the no-slip conditions, the simple Maxwell slip conditions, the Gökçen slip conditions [29] and the Knudsen-layer correction to the standard slip conditions proposed by Lockerby, et al. [49].

In each case, a grid independence study is conducted to determine the final mesh resolution used. As the current study is most interested in the surface properties, the surface property profiles and integrated quantities are used to define a mesh-indendent solution. Successive solutions are generated as the number of nodes in the wall-normal direction in an area near the wall containing the boundary layer is doubled, and the number of nodes in the wall-parallel direction is doubled. A mesh-independent solution is defined as one for which the total drag and peak heat transfer rate change by 1% or less, and there is no discernable change in the overall surface property profiles of pressure, shear stress and heat flux.

Second, DSMC results are provided from the MONACO code for the same flow conditions. In general, the mesh used for the final solution for each case is adapted from previous solutions such that each cell size is on the order of a mean free path or smaller. The exceptions are the $\mathrm{Kn} = 0.002$ cases, where the cell size is approximately four times the mean free path, and the $\mathrm{Kn} = 0.01$ cases, where the cell sizes near the surface are on the order of two mean free paths in size. In these cases the subcell method is used to select particles for collisions to ensure physical accuracy [4].

Example meshes for both DSMC and CFD for the different flow regimes are shown in Figure 4.2.

It should be noted here that the DSMC solutions are assumed to be the more correct solutions, as discussed in Chapter II.

In the results that follow, the surface properties are presented in terms of non-dimensional coefficients,

$$C_P = \frac{p - p_\infty}{\frac{1}{2}\rho_\infty U_\infty^2} \tag{4.2}$$

$$C_F = \frac{\tau}{\frac{1}{2}\rho_\infty U_\infty^2} \tag{4.3}$$

$$C_H = \frac{q}{\frac{1}{2}\rho_\infty U_\infty^3} \tag{4.4}$$

where p is the pressure, τ is the shear stress, q is the heat transfer rate, p_∞ is the free stream pressure, ρ_∞ is the free stream density and U_∞ is the free stream velocity. The surface properties in each case are plotted as a function of the angle around the cylinder, with the stagnation point being located at an angle of zero (see Figure 4.1).

Along with the surface properties, the maximum value of $\mathrm{Kn_{GLL}}$ at the surface (based on the CFD solution) is plotted in each case. Note that the x-axis crosses the right y-axis at $\mathrm{Kn_{GLL,crit}} = 0.05$, thus only continuum breakdown parameter values above the critical value are shown in the figures.

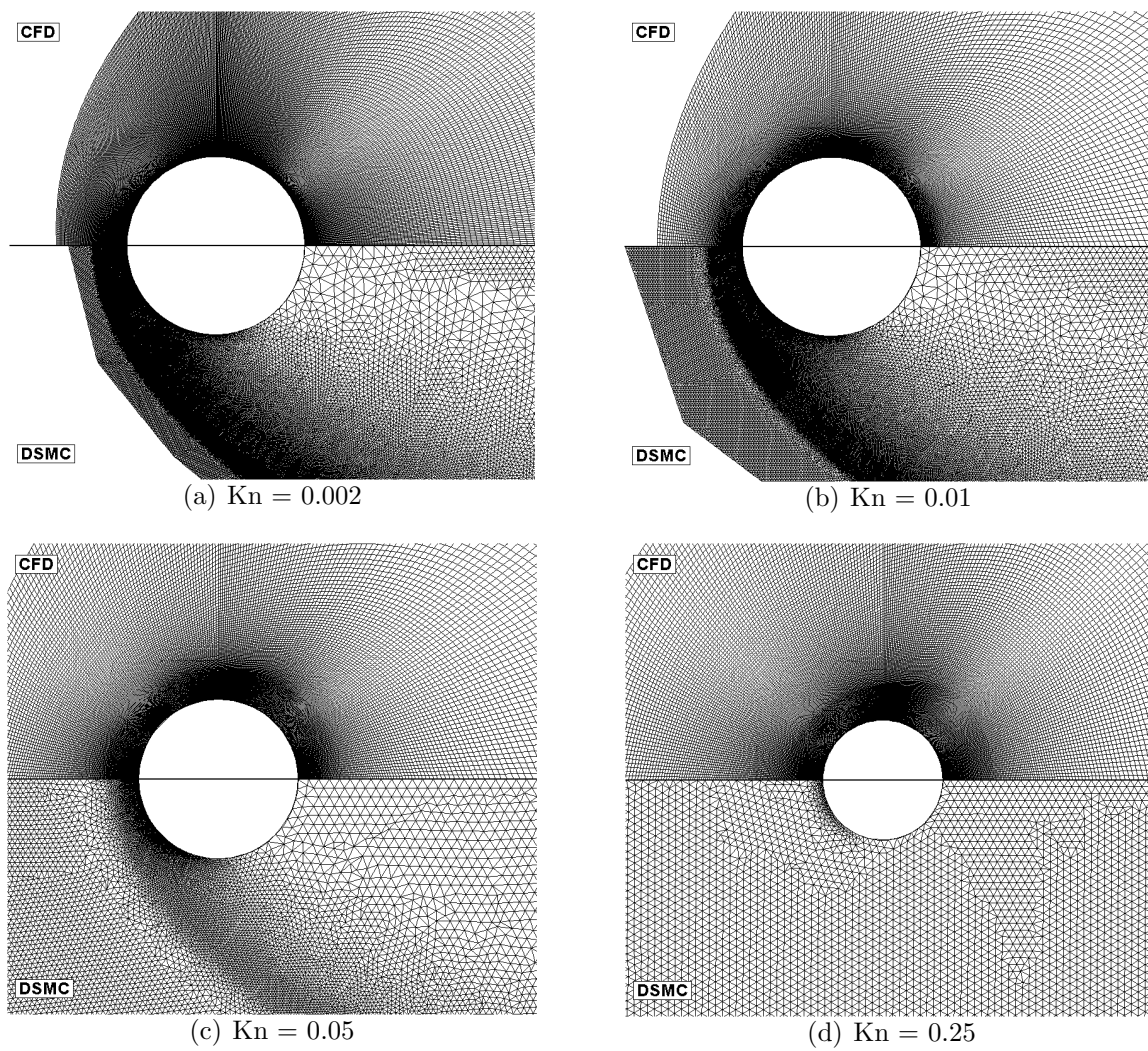(a) Kn = 0.002

(b) Kn = 0.01

(c) Kn = 0.05

(d) Kn = 0.25

Figure 4.2: Example meshes for both DSMC and CFD for a flow about a cylinder. Mach 10, nitrogen meshes are shown; others are similar.
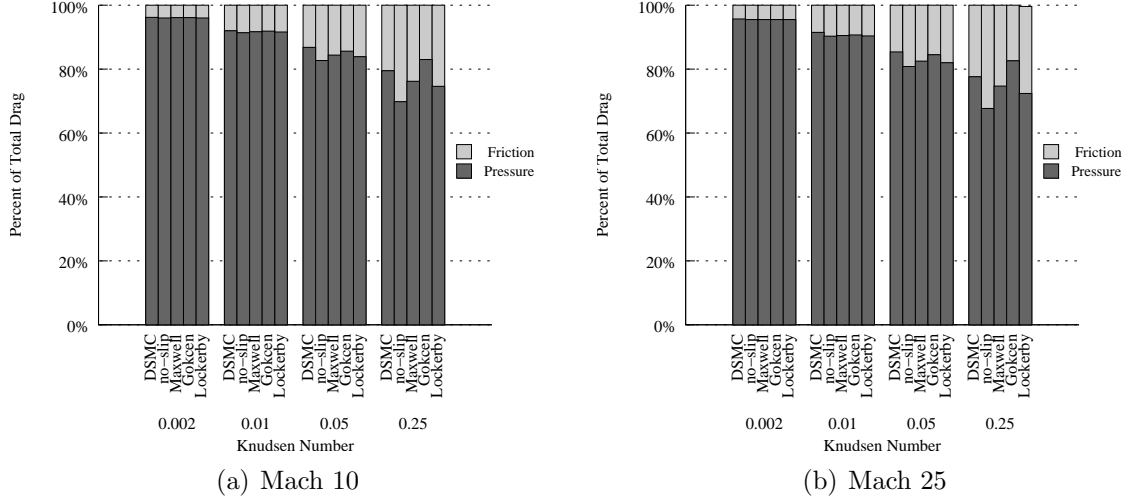
Figure 4.3: Percentage of total drag due to pressure and friction for a flow of argon about a cylinder.

4.2   Argon

The total drag and peak heat transfer rates predicted by both computational methods for a hypersonic flow of argon around the cylinder are summarized in Tables 4.3 and 4.4. The differences between CFD and DSMC are also shown graphically in Figures 4.4 and 4.5. Here, the peak heat transfer rate is obtained by averaging over the surface area within one degree of the stagnation point. For CFD, these quantities are calculated for each of the different boundary conditions implemented.

Figure 4.3 illustrates the percentage of total drag due to pressure and friction forces, for both DSMC and CFD. It is significant to note that as the Knudsen number increases, the percentage of total drag due to friction increases from about 5% at Kn = 0.002 to about 20% at Kn = 0.25. Also note that the vast majority of the drag is due to pressure forces. It is also significant to note, as shown in Figure 4.4, that the difference in predicted total drag between CFD and DSMC is due mostly to the differences predicted in the friction forces. Also, the large disagreement with the no-slip condition results is due to the increase in predicted friction drag.
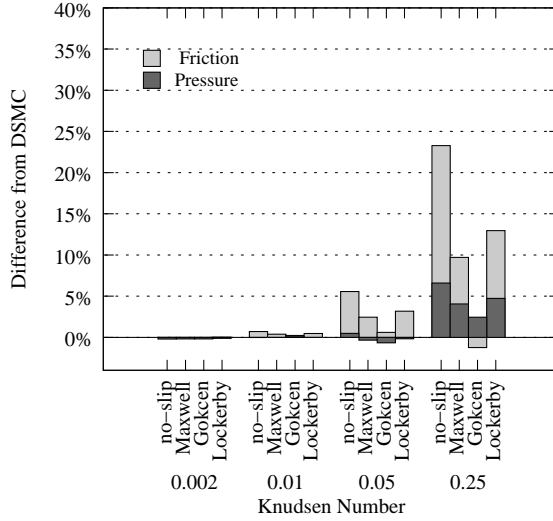
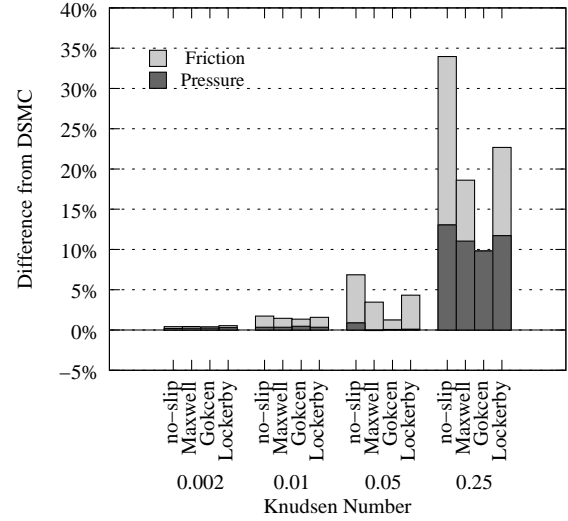Table 4.3: Total drag a for flow of argon about a cylinder.

Mach 10

Kn$_\infty$	Drag/Length [N/m] (% Difference)				
	DSMC	CFD			
		no-slip	Maxwell	Gökçen	Lockerby
0.002	187.6	187.5 (-0.1%)	187.4 (-0.1%)	187.4 (-0.1%)	187.6 (0.0%)
0.01	40.02	40.30 (0.7%)	40.17 (0.4%)	40.11 (0.2%)	40.20 (0.5%)
0.05	8.866	9.358 (5.6%)	9.082 (2.4%)	8.921 (0.6%)	9.148 (3.2%)
0.25	2.092	2.579 (23.3%)	2.296 (9.7%)	2.067 (-1.2%)	2.363 (12.9%)

Mach 25

Kn$_\infty$	Drag/Length [N/m] (% Difference)				
	DSMC	CFD			
		no-slip	Maxwell	Gökçen	Lockerby
0.002	1171	1176 (0.4%)	1176 (0.4%)	1176 (0.4%)	1177 (0.5%)
0.01	250.8	255.3 (1.8%)	254.5 (1.5%)	254.3 (1.4%)	254.8 (1.6%)
0.05	56.92	60.82 (6.9%)	58.89 (3.5%)	57.63 (1.3%)	59.38 (4.3%)
0.25	13.19	17.66 (34.0%)	15.64 (18.6%)	13.94 (5.7%)	16.18 (22.7%)

(a) Mach 10   (b) Mach 25

Figure 4.4: Total drag difference from DSMC for a flow of argon about a cylinder. Note that there is a negative contribution to total drag due to friction for the Mach 25, Kn = 0.25 case, bringing the total drag difference down to 5.7%.
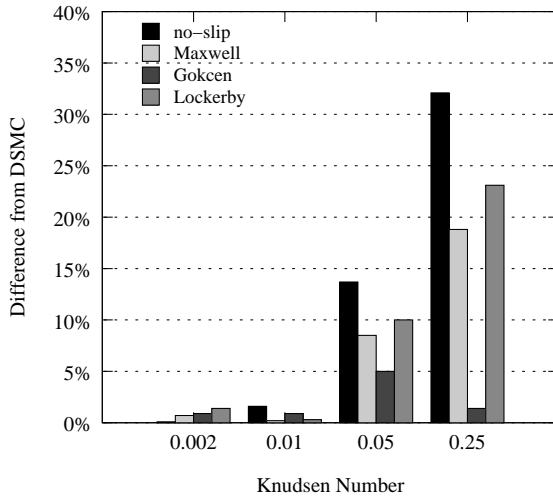
Table 4.4: Peak heat transfer rate for a flow of argon about a cylinder.

Mach 10

Kn_∞	Peak Heating [kW/m²] (% Difference)				
	DSMC	CFD			
		no-slip	Maxwell	Gökçen	Lockerby
0.002	89.80	89.84 (0.1%)	89.14 (-0.7%)	89.00 (-0.9%)	88.54 (-1.4%)
0.01	39.13	39.76 (1.6%)	39.06 (-0.2%)	38.77 (-0.9%)	39.23 (0.3%)
0.05	15.85	18.02 (13.7%)	17.20 (8.5%)	16.63 (5.0%)	17.43 (10.0%)
0.25	5.926	7.828 (32.1%)	7.040 (18.8%)	6.011 (1.4%)	7.296 (23.1%)

Mach 25

Kn_∞	Peak Heating [kW/m²] (% Difference)				
	DSMC	CFD			
		no-slip	Maxwell	Gökçen	Lockerby
0.002	1746	1763 (0.9%)	1750 (0.2%)	1746 (-0.1%)	1739 (-0.5%)
0.01	749.6	791.0 (5.5%)	771.1 (2.9%)	762.1 (1.7%)	774.8 (3.4%)
0.05	304.5	357.9 (17.1%)	339.5 (11.5%)	321.2 (5.5%)	345.0 (13.3%)
0.25	108.2	148.2 (37.0%)	133.4 (23.2%)	106.5 (-1.6%)	138.6 (28.0%)
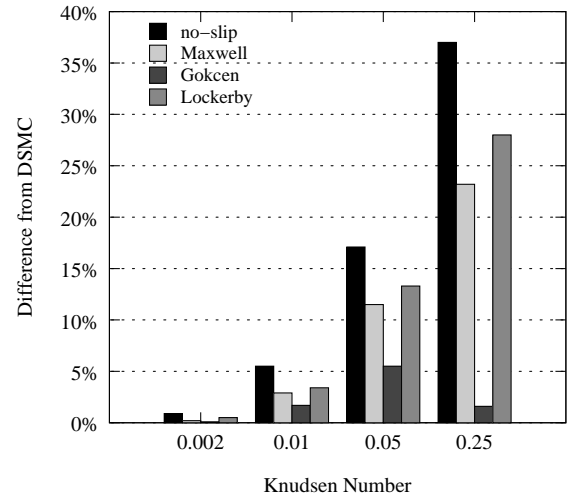
(a) Mach 10   (b) Mach 25

Figure 4.5: Peak heat transfer rate difference from DSMC for a flow of argon about a cylinder.

It is clear that the slip boundary conditions improve the agreement between the two simulation methods. While the difference in total drag is as high as 23.3% and 34.0% for the no-slip condition, the Gökçen slip boundary condition shows the best agreement, with the difference exceeding 5% only for the Mach 25, Kn = 0.25 case. Similar trends are noted for the peak heat transfer rate, with a 37% difference for the no-slip CFD solution, while the Gökçen slip solution remains near 2% or less for most of the cases and is 5% or greater only for the Kn = 0.05 cases.

There is also a slight improvement in drag and heat flux agreement between the Maxwell and Lockerby boundary conditions, where the only difference in the two boundary conditions is the inclusion in the Lockerby slip condition of the viscosity correction function within the Knudsen layer, and the use of a more correct value for the constant of proportionality, A, in Eq. 3.8. Surprisingly, it is the Maxwell boundary condition that shows better agreement with DSMC than the Lockerby boundary condition. This improvement is not as great as that achieved with the Gökçen boundary condition, but there is value in using this simple slip boundary condition.

Although there is very good agreement between the DSMC and Gökçen CFD results for the surface properties, there are still significant differences in flow properties (such as shock structure), as shown below.

Due to its better agreement with DSMC, all CFD results shown below are taken from the Gökçen CFD cases unless otherwise specified.

4.2.1 Continuum Breakdown

The breakdown parameter is calculated using both the CFD and the DSMC solutions according to Equation 3.26, with the derivative being taken in the direction

of the steepest gradient. For the case of a cylinder in a hypersonic flow of a simple gas, the only causes of breakdown to the continuum hypothesis expected are in regions of high gradients (such as the shock and boundary layer) and regions of rarefaction (such as in the wake). The amount of continuum breakdown is also expected to increase as the gas flow becomes more rarefied.

These trends are confirmed by the results that are shown in Figures 4.6 and 4.7, which illustrate the amount of continuum breakdown in the flow as it becomes more rarefied, for the Mach 10 and Mach 25 cases, respectively. The maximum gradient length local Knudsen number is computed from the DSMC (top) and CFD (bottom) solutions. Light gray regions correspond to $Kn_{GLL} < 0.05$, dark gray regions correspond to $Kn_{GLL} < 0.10$ and black regions correspond to $Kn_{GLL} > 0.10$.

In general, the flow experiences continuum breakdown in three areas; across the bow shock, in the boundary layer and in the wake region. The flow in the shock and boundary layer experiences very steep gradients in flow properties, while the wake region is more rarefied, thus leading to the breakdown of the continuum hypothesis.

At a Knudsen number of 0.002, the flow is within the continuum, no-slip regime. Nevertheless, there is still evidence of continuum breakdown in the shock, along the cylinder surface in the boundary layer and in the wake. Interestingly, DSMC predicts a larger degree of breakdown than does CFD. A Knudsen number of 0.01 is considered to be near the limit of the continuum, no-slip regime, with increased evidence of continuum breakdown. At a Knudsen number of 0.05, the flow is well within the slip regime with an associated increase in the regions of continuum breakdown. For a Knudsen number of 0.25, the flow would be considered outside of the slip regime and into the transition regime. Here, even the addition of slip boundary conditions is not expected to help the continuum CFD method's predictive capabilities very much.
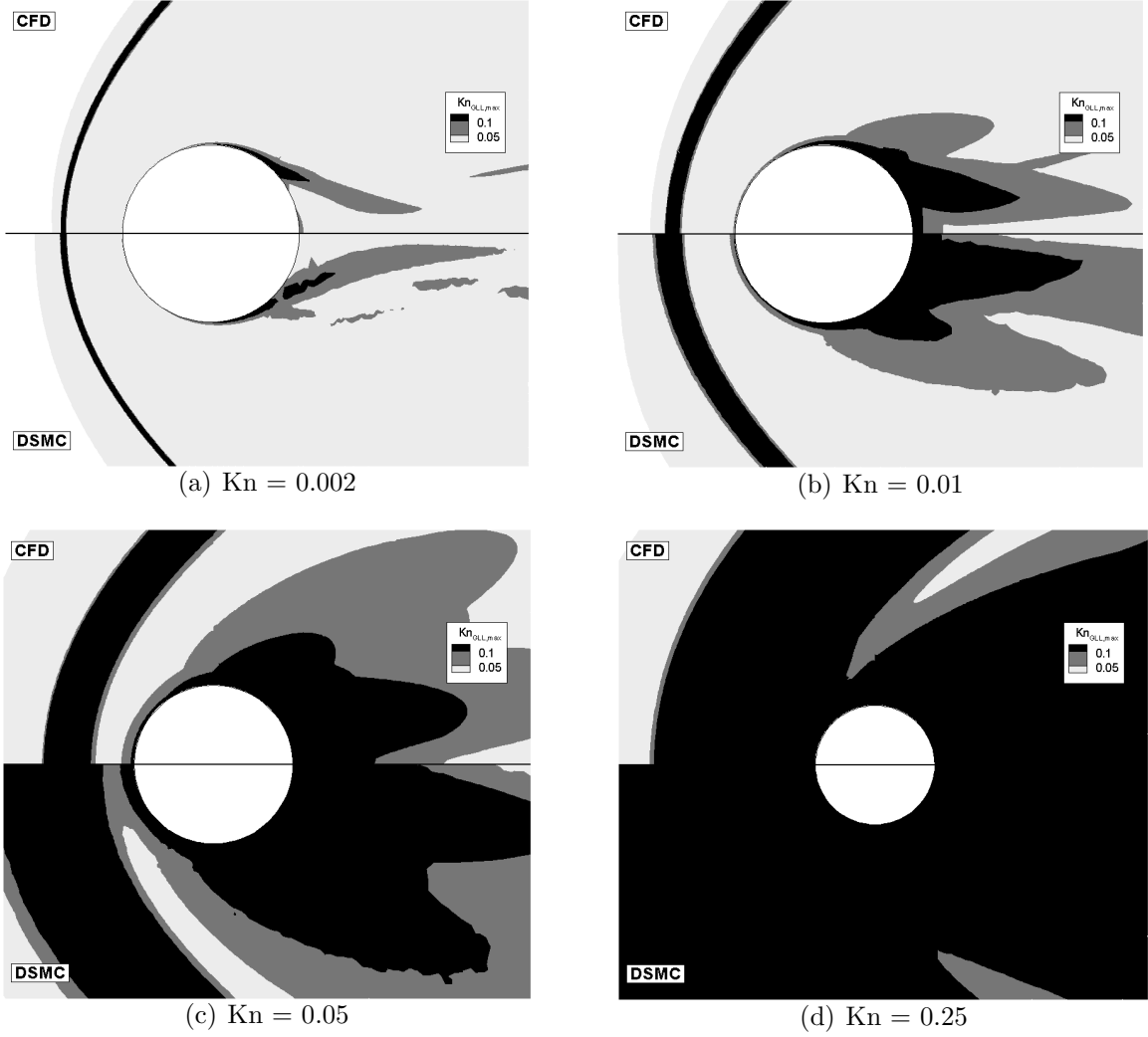
Figure 4.6: $\mathrm{Kn_{GLL}}$ field for a Mach 10 flow of argon about a cylinder. Light gray regions correspond to $\mathrm{Kn_{GLL}} < 0.05$, dark gray regions correspond to $\mathrm{Kn_{GLL}} < 0.10$ and black regions correspond to $\mathrm{Kn_{GLL}} > 0.10$

(a) Kn = 0.002

(b) Kn = 0.01
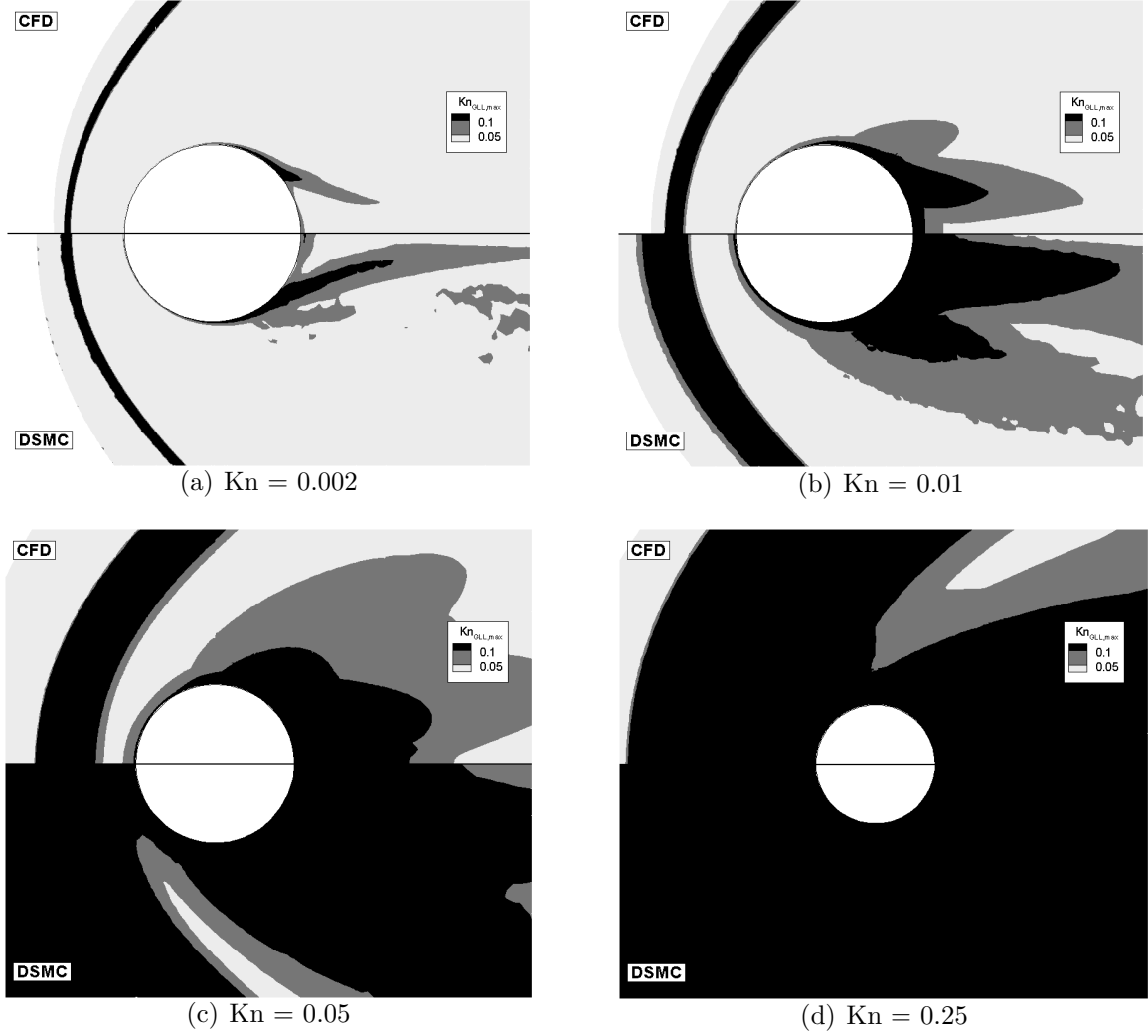
(c) Kn = 0.05

(d) Kn = 0.25

Figure 4.7: Kn_{GLL} field for a Mach 25 flow of argon about a cylinder. Light gray regions correspond to $Kn_{GLL} < 0.05$, dark gray regions correspond to $Kn_{GLL} < 0.10$ and black regions correspond to $Kn_{GLL} > 0.10$

Indeed, the plots of the breakdown parameter indicate that there are significant nonequilibrium effects across almost all of the flow domain.

Similar trends to those seen at Mach 10 are also present at Mach 25; the main difference being that continuum breakdown increases more rapidly as the flow becomes more rarefied. This is expected as the gradients in flow properties are expected to be more severe; as the flow velocity increases, the residence time of a fluid particle decreases, leaving less time for the properties to equilibrate to the local flow conditions.

Figures 4.6 and 4.7 can also give an idea of the relative efficiency of a hybrid CFD/DSMC method using $Kn_{GLL} > 0.05$ as an indicator of regions where the flow can no longer be accurately predicted by CFD. With such a design, the portions of the computational domain represented by the dark gray and black regions should be computed using DSMC. Initially, it would be necessary to base the interfaces according to the value of the continuum breakdown parameter predicted by CFD (top of sub-figures). As the solution progresses, the final interface locations should be determined by the more accurate, hybrid solution, which would correspond to the DSMC solution (shown at the bottom of each sub-figure). Hence, the final interfaces would be determined by the amount of continuum flow predicted by the DSMC solutions.

With this in mind, it can be seen that there would be very small portions of the computational domain requiring DSMC for the $Kn = 0.002$ and $Kn = 0.01$ cases, while for the $Kn = 0.05$ case only small portions remain in the CFD domain. The amount of continuum breakdown present in the $Kn = 0.25$ case implies that this would not be a likely candidate for a hybrid method; nearly the entire domain would require DSMC.

4.2.2 Flow Field Properties

The density ratio fields, where the density is normalized by the freestream density, can be seen in Figures 4.8 and 4.9. Note that the maximum density ratio behind the shock is about 4, agreeing with the theoretical limit for a monatomic gas in equilibrium and the results from the normal shock relations, $\rho/\rho_0 = 3.87$ (Mach 10) and $\rho/\rho_0 = 3.97$ (Mach 25). Overall agreement between CFD and DSMC is good, with some small differences in the shock structure at the higher Knudsen number conditions. Also note that as the freestream density decreases, the shock becomes much more diffuse.

The temperature fields predicted by both CFD and DSMC can be seen in Figures 4.10 and 4.11 for the Mach 10 and Mach 25 cases, respectively. The Kn = 0.002 temperature field exhibits the typical flow features found in a blunt body flow; namely, a fairly thin shockwave standing off from the body, a high temperature region following the shock (as the translational energy is converted into thermal energy with the decrease in velocity due to shock compression), a thermal boundary layer that gradually thickens around the cylinder, and a wake of lower temperature as the flow expands around the top of the cylinder. The maximum temperature behind the shock agrees with that from the normal shock relations, $T_{max} = 6,460$ K (Mach 10) and $T_{max} = 39,400$ K (Mach 25). The two simulation methods agree very well for the continuum flow here; the amount of nonequilibrium present in the flow seems to be adequately handled by the Navier-Stokes equations with no-slip boundary conditions. The Mach 25 case shows an increase in the maximum temperature as well as a slight increase in the shock thickness; however, for the presently considered simple gas, there are no other effects.

Although there is an increasing amount of nonequilibrium in the flow as the

(a) Kn = 0.002
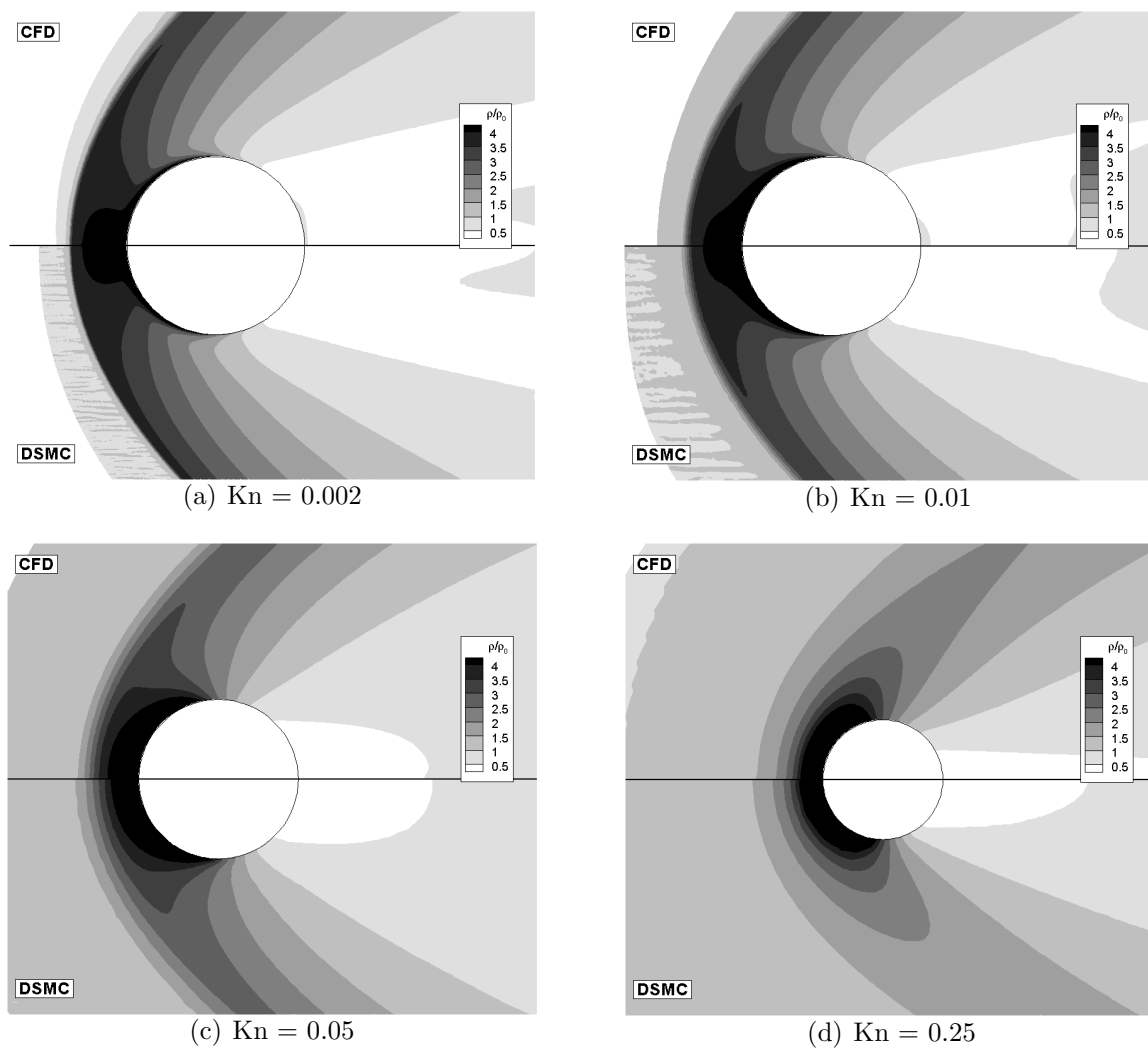
(b) Kn = 0.01

(c) Kn = 0.05

(d) Kn = 0.25

Figure 4.8: Density ratio field for a Mach 10 flow of argon about a cylinder. Density is normalized by the freestream density. The normal shock relations predict a density ratio of 3.87.
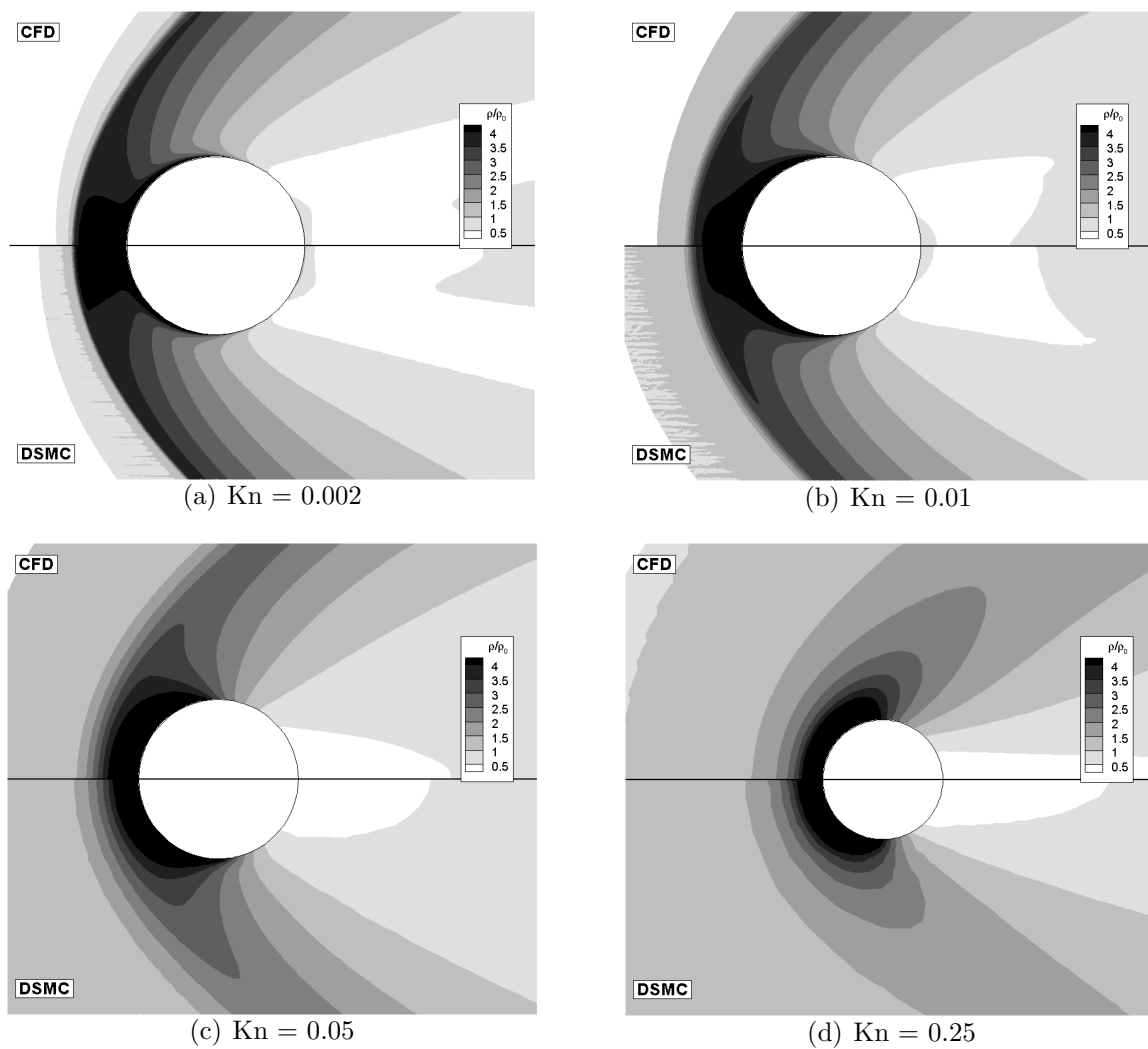
Figure 4.9: Density ratio field for a Mach 25 flow of argon about a cylinder. Density is normalized by the freestream density. The normal shock relations predict a density ratio of 3.97.
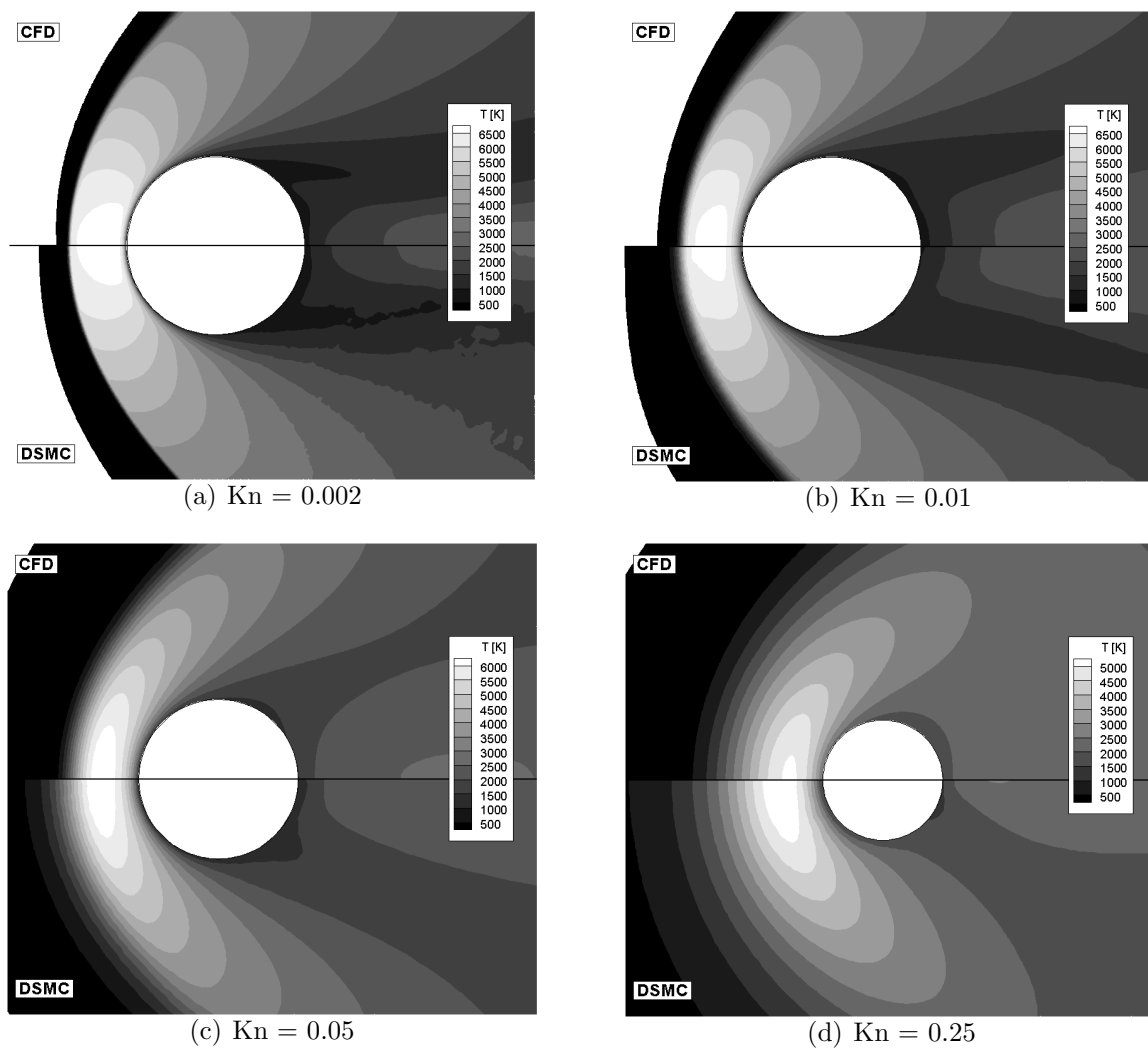
(a) Kn = 0.002

(b) Kn = 0.01

(c) Kn = 0.05

(d) Kn = 0.25

Figure 4.10: Temperature field for a Mach 10 flow of argon about a cylinder. The normal shock relations predict a post-shock temperature of 6,460 K.
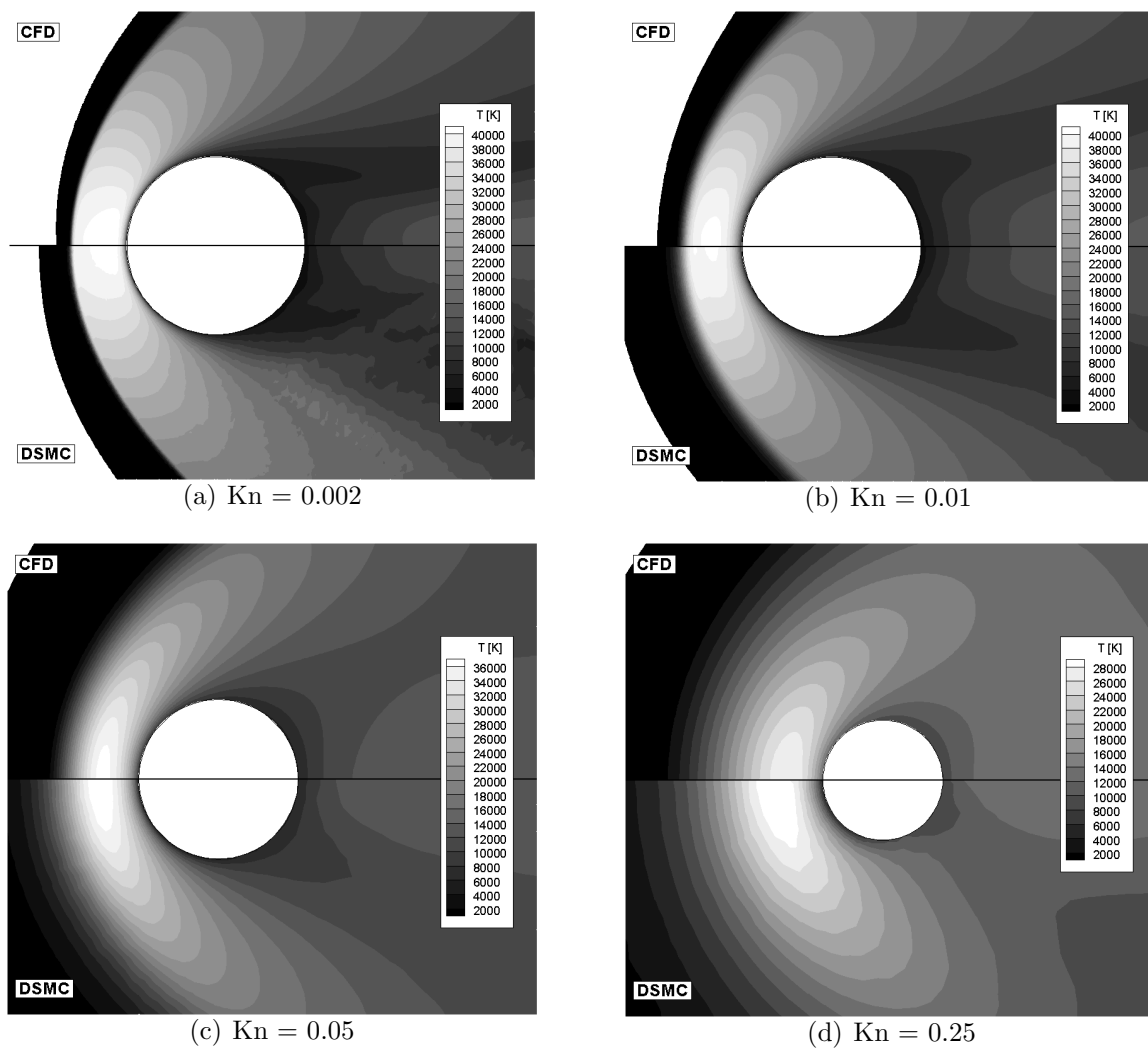
Figure 4.11: Temperature field for a Mach 25 flow of argon about a cylinder. The normal shock relations predict a post-shock temperature of 39,400 K.

density is decreased, the temperature fields in the Kn = 0.01 case still show fairly good agreement. There are, however, differences in the shock thickness, with DSMC predicting a more diffuse shock. (The Navier-Stokes equations are known to poorly predict the interior shock structure [25].) Disagreement is also seen in the wake, where the continuum hypothesis is expected to break down first. The shock standoff distance predicted by both methods is nearly the same as is the thermal boundary layer thickness at the stagnation point.

With the increase in nonequilibrium present in the Kn = 0.05 case, the differences between CFD and DSMC temperature field predictions are more pronounced, with even more differences for the higher Mach number. Most notable, the DSMC shock is much thicker, with a larger stand-off distance. The maximum temperature behind the shock has also decreased from the higher density cases, although both methods agree fairly well in their predictions of the peak temperature value and the thermal boundary layer thickness at the stagnation point. In the wake, some differences are expected with DSMC predicting lower temperatures.

There are major differences present for the Kn = 0.25 case, as would be expected considering the low density of the flow. There is a further decrease in the magnitude of the peak temperatures behind the shock, and DSMC predicts a higher temperature than CFD for the Mach 25 case. The shock thicknesses and stand-off distances are significantly different, as is the thermal boundary layer thickness, with DSMC predicting a more diffusive shock and boundary layer.

4.2.3 Stagnation Line

The temperatures predicted along the stagnation line are compared in Figures 4.12 and 4.13, again for Mach 10 and Mach 25 respectively. The maximum value of

Kn_{GLL} is also plotted against the right axis.

For Kn = 0.002, all of the CFD simulations agree with the DSMC results (although there is slight disagreement in the shock for the Mach 25 case). Figure 4.12(a) shows a typical stagnation line temperature distribution. The temperature is initially constant at the free stream value before increasing as the flow is compressed in the shock. The temperature then remains fairly constant through the shock layer before decreasing in the boundary layer to the wall temperature. Here, the only areas where there is a significant amount of continuum breakdown is in the shock, with a smaller amount in the boundary layer. For the Kn = 0.01 case, there is still good agreement between all CFD predictions and DSMC for the post-shock temperature distribution, although there is some disagreement in the shock itself. The peak value of the breakdown parameter is also higher than for the higher density case. The Kn = 0.05 case shows that the shock layer has now merged with the boundary layer. The post-shock temperatures are still in agreement, although there are differences among the CFD cases. The Kn = 0.25 case shows that the shock and the boundary layer have merged completely. The peak temperature is lower, and there are significant amounts of continuum breakdown from the shock all the way to the wall. There is also some significant disagreement between each of the CFD cases.

4.2.4   Surface Properties

The surface property distributions (pressure, shear stress and heat flux) for each of the cases is examined here. The surface pressure, in the form of a pressure coefficient, is shown in Figures 4.14 and 4.15. The surface pressure is the least sensitive to nonequilibrium of all the surface properties; all of the CFD solutions agree well with DSMC for all but the most rarefied conditions (Kn = 0.25), where the DSMC

(a) Kn = 0.002

(b) Kn = 0.01
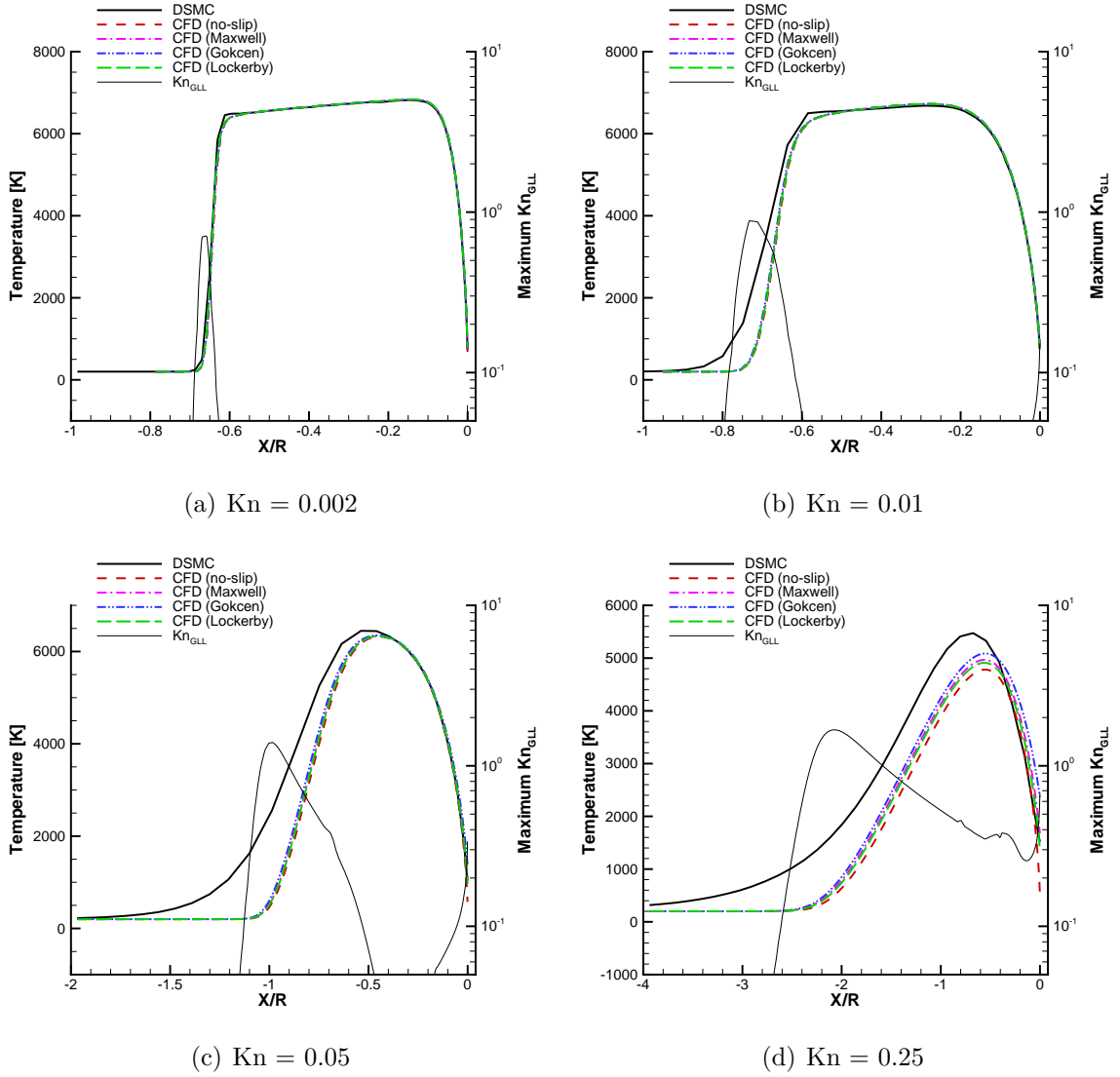
(c) Kn = 0.05

(d) Kn = 0.25

Figure 4.12: Temperature profiles along the stagnation line for a Mach 10 flow of argon about a cylinder. The maximum value of $Kn_{GLL,max}$ is plotted on the right axis. Flow is from left to right, and distance is normalized by the cylinder radius.
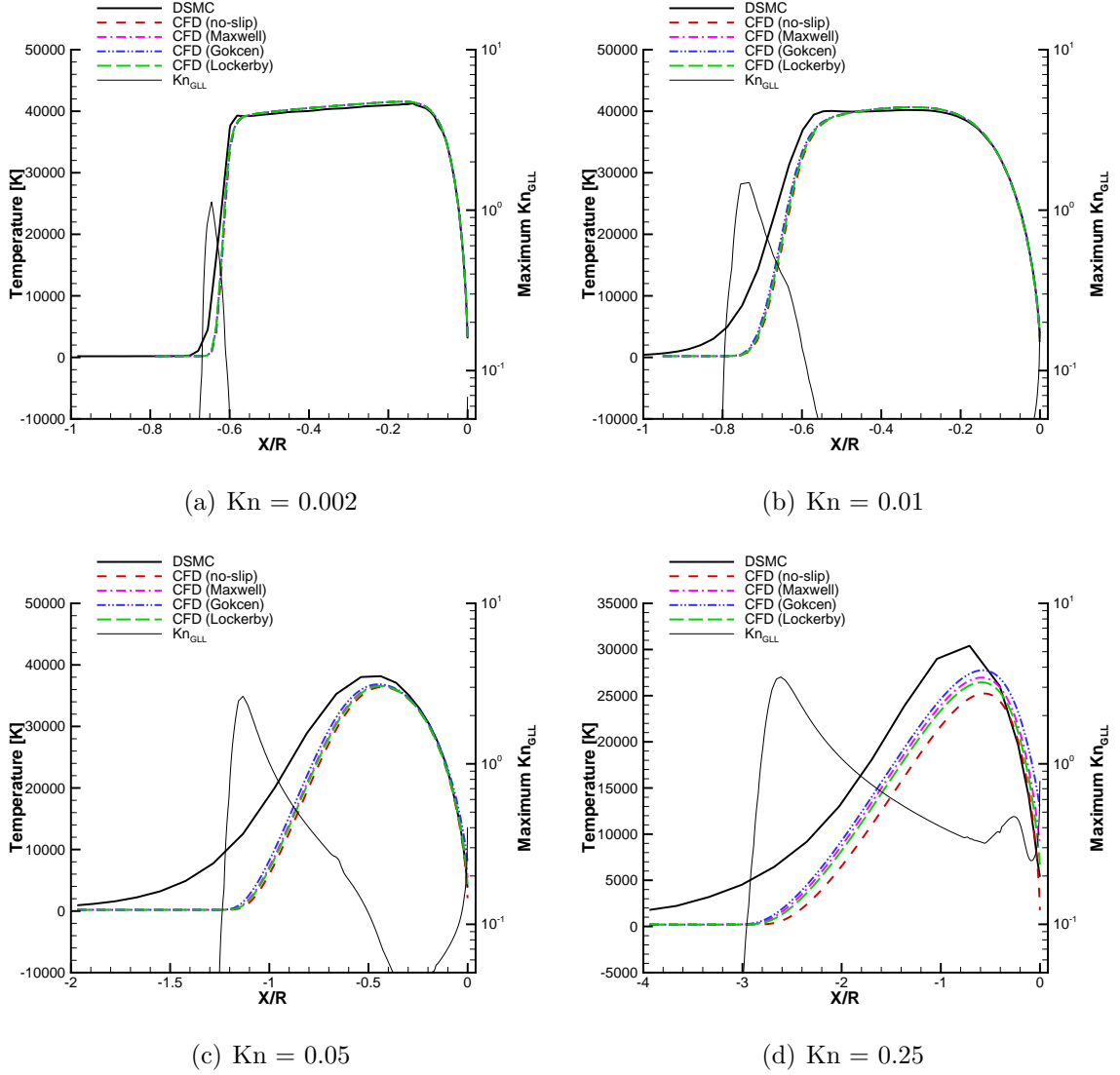
(a) Kn = 0.002

(b) Kn = 0.01

(c) Kn = 0.05

(d) Kn = 0.25

Figure 4.13: Temperature profiles along the stagnation line for a Mach 25 flow of argon about a cylinder. The maximum value of Kn_{GLL} is plotted on the right axis. Flow is from left to right; distance is normalized by the cylinder radius.

pressure is less than the CFD pressure near the fore-body (most likely due to the thinner shock predicted by CFD, which allows the CFD solution to approach the ideal jump condition more closely than the DSMC solution). The pressure tensor at this Knudsen number is also most likely non-isotropic, which would introduce errors into the CFD solution.

Also note that the maximum Kn_{GLL} near the surface is plotted against the right axis. The amount of continuum breakdown near the surface is highest in the wake, as expected, and the amount of continuum breakdown increases as the flow becomes more rarefied. Nevertheless, it is not until the complete merger of the shock and boundary layer in the $Kn = 0.25$ case that there is an effect on the pressure distribution. The Kn_{GLL} here is calculated from the Gökçen CFD solution; the no-slip CFD solution shows a much larger amount of continuum breakdown near the surface due to the larger gradients required to satisfy the no-slip condition.

The shear stress is the most sensitive of the surface properties to the amount of nonequilibrium in the flow, as seen in Figures 4.16 and 4.17. Notable shear stress differences are seen in the $Kn = 0.01$ case, and these become more pronounced as the density decreases. The best agreement with the DSMC solution is achieved with the Gökçen boundary conditions; this most certainly is the reason for the good agreement between the Gökçen CFD and DSMC predictions for total drag.

The heat transfer rate distributions are shown in Figures 4.18 and 4.19. Again, the slip boundary conditions improve the prediction capabilities of CFD, with the Gökçen condition showing the most agreement. Again, both computational methods agree well for the highest density cases and the agreement grows worse as the flow becomes more rarefied. The heat transfer rate does not seem to be sensitive to the amount of continuum breakdown near the surface as the amount of error between DSMC and
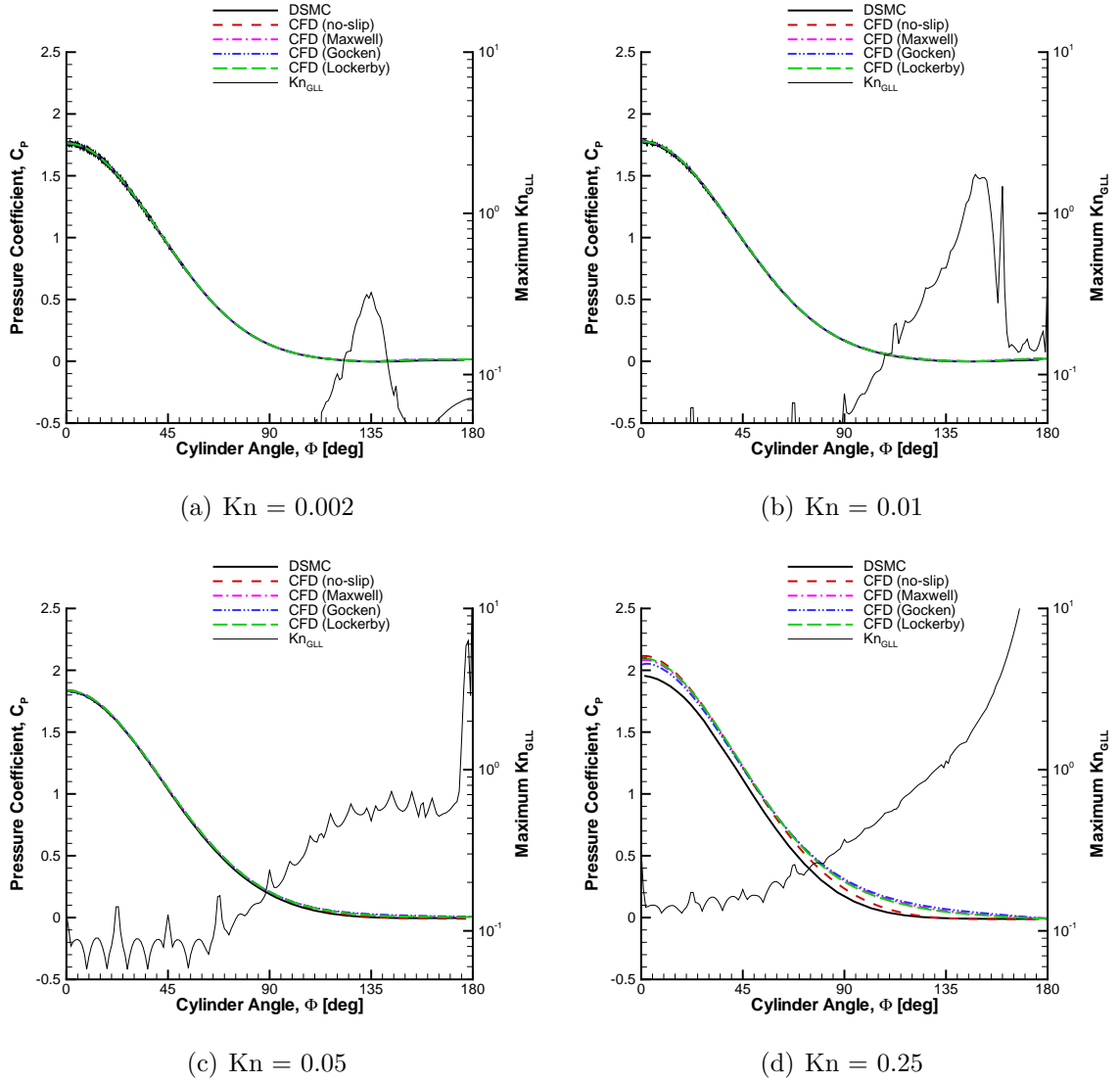
(a) Kn = 0.002

(b) Kn = 0.01
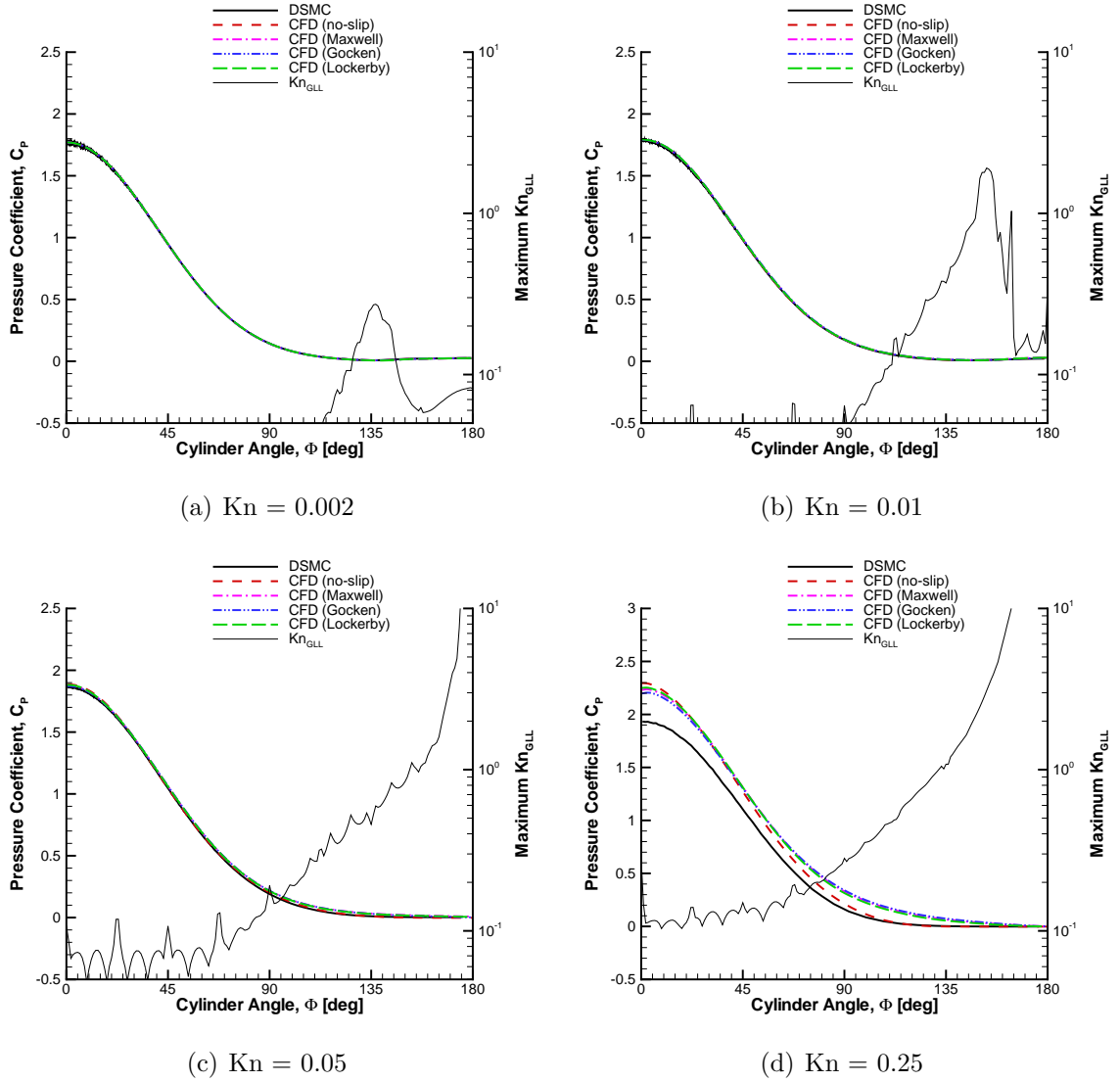
(c) Kn = 0.05

(d) Kn = 0.25

Figure 4.14: Surface pressure coefficient for a Mach 10 flow of argon about a cylinder. The maximum value of Kn_{GLL} near the surface is plotted on the right axis. Φ is the angle from the stagnation point.
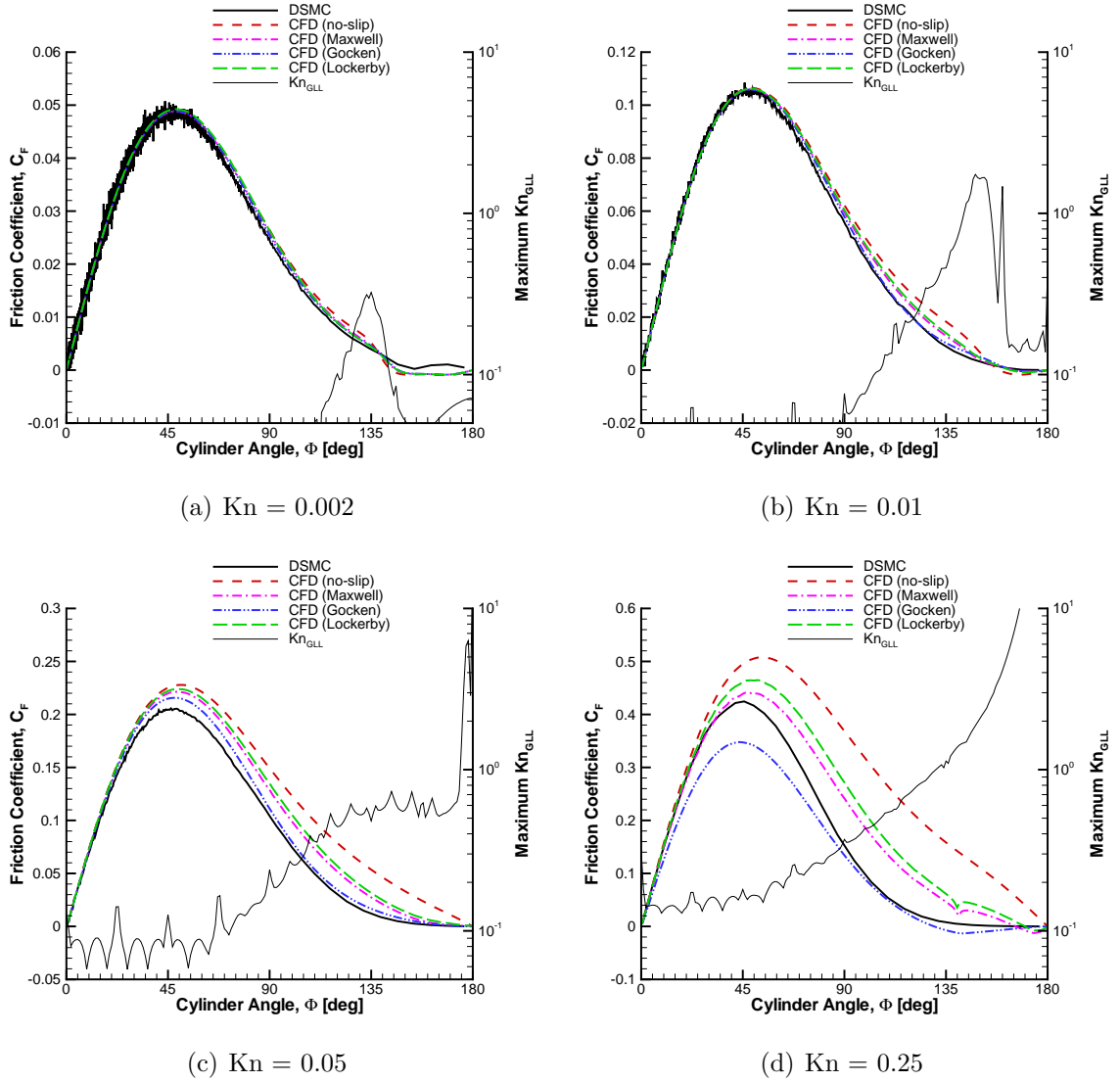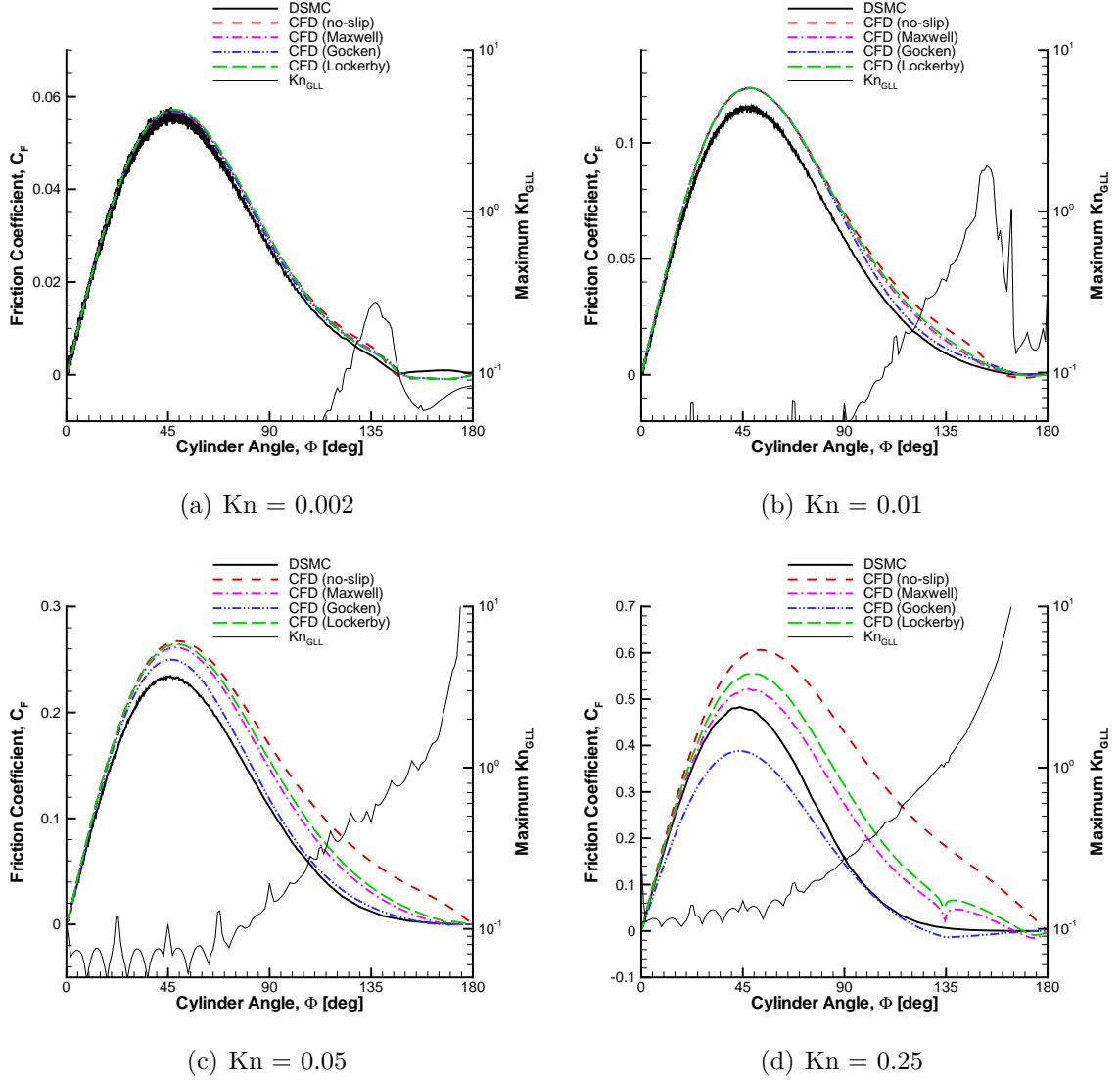
(a) Kn = 0.002

(b) Kn = 0.01

(c) Kn = 0.05

(d) Kn = 0.25

Figure 4.15: Surface pressure coefficient for a Mach 25 flow of argon about a cylinder. The maximum value of Kn_{GLL} near the surface is plotted on the right axis. Φ is the angle from the stagnation point.

(a) Kn = 0.002

(b) Kn = 0.01

(c) Kn = 0.05

(d) Kn = 0.25

Figure 4.16: Surface friction coefficient for a Mach 10 flow of argon about a cylinder. The maximum value of Kn_{GLL} near the surface is plotted on the right axis. Φ is the angle from the stagnation point.

(a) Kn = 0.002

(b) Kn = 0.01

(c) Kn = 0.05

(d) Kn = 0.25

Figure 4.17: Surface friction coefficient for a Mach 25 flow of argon about a cylinder. The maximum value of Kn_{GLL} near the surface is plotted on the right axis. Φ is the angle from the stagnation point.

CFD is very nearly constant along the entire surface; that is, the disagreement does not necessarily correlate with the higher values of Kn_{GLL} near the surface. This would suggest that errors in heat transfer rate in the CFD solutions are most likely caused by differences in the shock thickness, post-shock peak temperatures and thermal boundary layer thicknesses.

4.2.5   Flow Properties Along a Line at $\Phi = 90°$

The use of slip boundary conditions has been shown to improve the agreement in surface property prediction between DSMC and CFD. In this section, the agreement in flow properties is investigated. The surface properties that are most sensitive to nonequilibrium effects are the shear stress and heat flux. Therefore, the flow properties that are examined here are the temperature and velocity.

The temperature and the breakdown parameter values are plotted along a line normal to the surface at an angle of $90°$ in Figures 4.20 and 4.21, where the distance from the wall is normalized by the cylinder radius. A trend noted here is that the regions where values of Kn_{GLL} are highest are closest to the surface in the Knudsen layer, which is where a temperature jump is seen.

Very similar trends are seen with the velocity magnitude, which is plotted along the same line in Figures 4.22 and 4.23. Again, there are significant amount of non-equilibrium near the wall, with a velocity jump at the wall for the highest Knudsen number cases. Although the Gökçen CFD cases show the best agreement in surface property prediction, they do not necessarily show the best agreement in flow properties, particularly for the $Kn = 0.05$ cases.

For the $Kn = 0.002$ cases, there is very good agreement between all the CFD solutions and the DSMC solution, although there is a modest temperature jump near
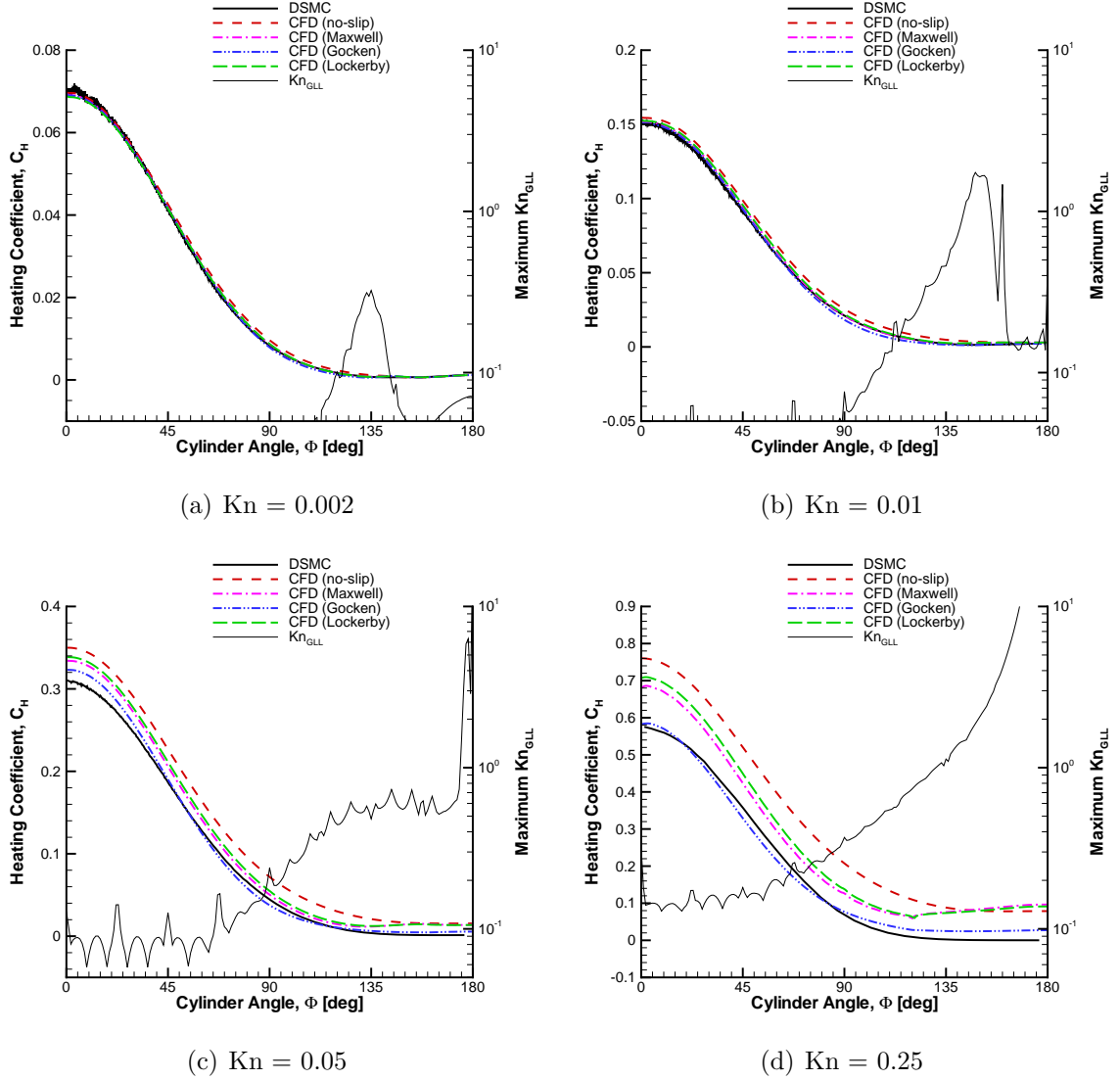
(a) Kn = 0.002

(b) Kn = 0.01
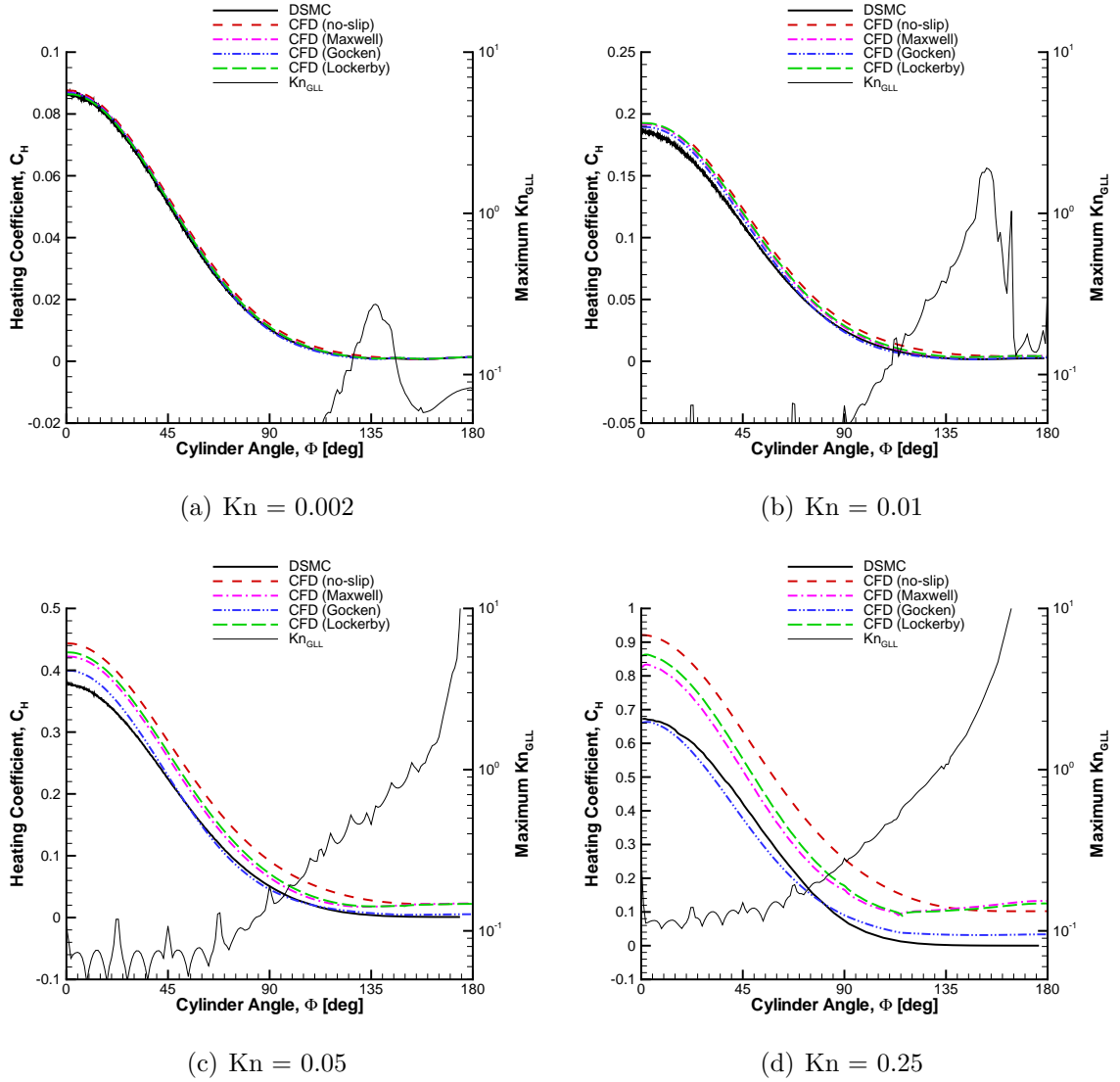
(c) Kn = 0.05

(d) Kn = 0.25

Figure 4.18: Surface heating coefficient for a Mach 10 flow of argon about a cylinder. The maximum value of Kn_{GLL} near the surface is plotted on the right axis. Φ is the angle from the stagnation point.
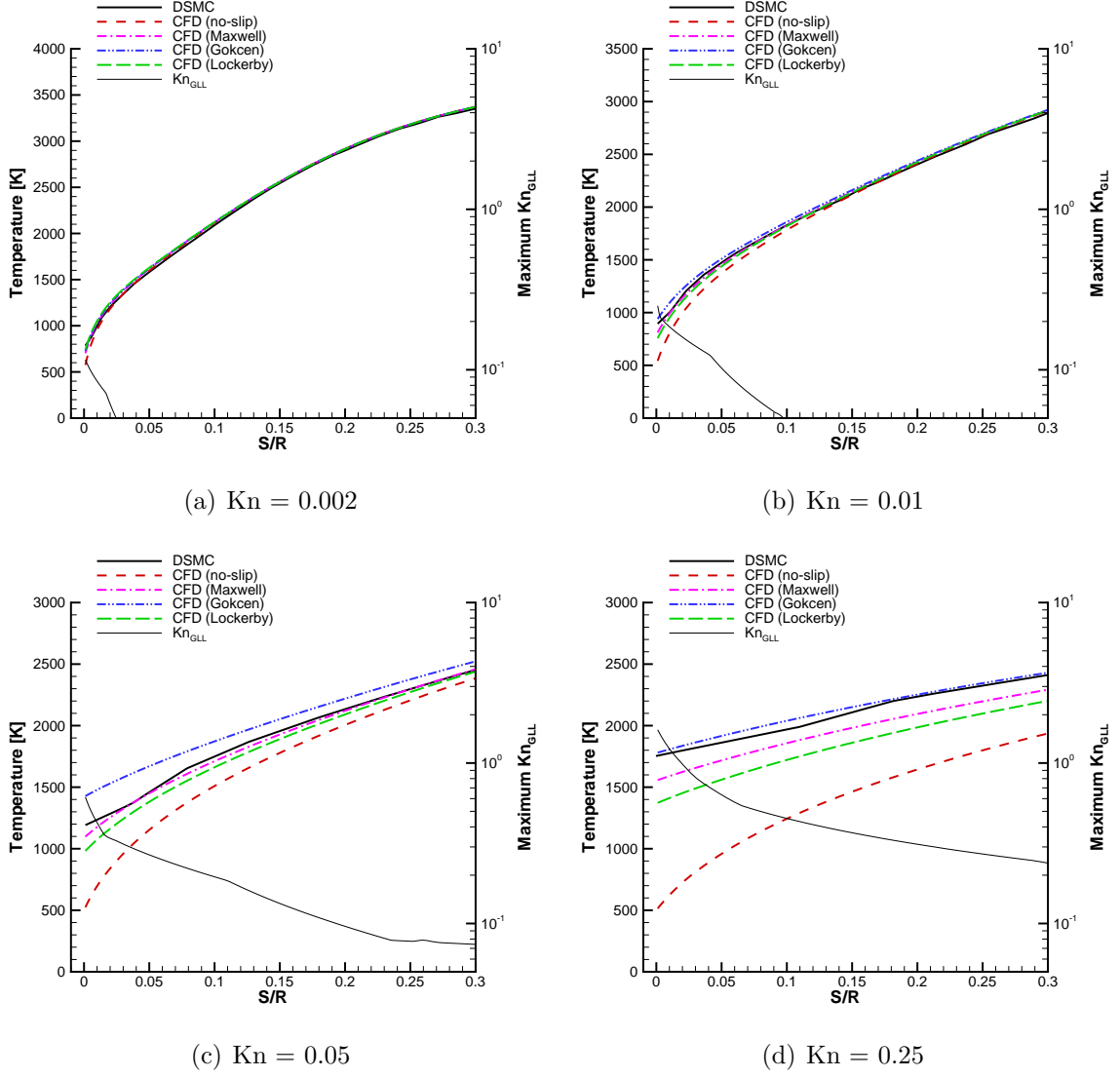
(a) Kn = 0.002

(b) Kn = 0.01

(c) Kn = 0.05

(d) Kn = 0.25

Figure 4.19: Surface heating coefficient for a Mach 25 flow of argon about a cylinder. The maximum value of Kn_{GLL} near the surface is plotted on the right axis. Φ is the angle from the stagnation point.
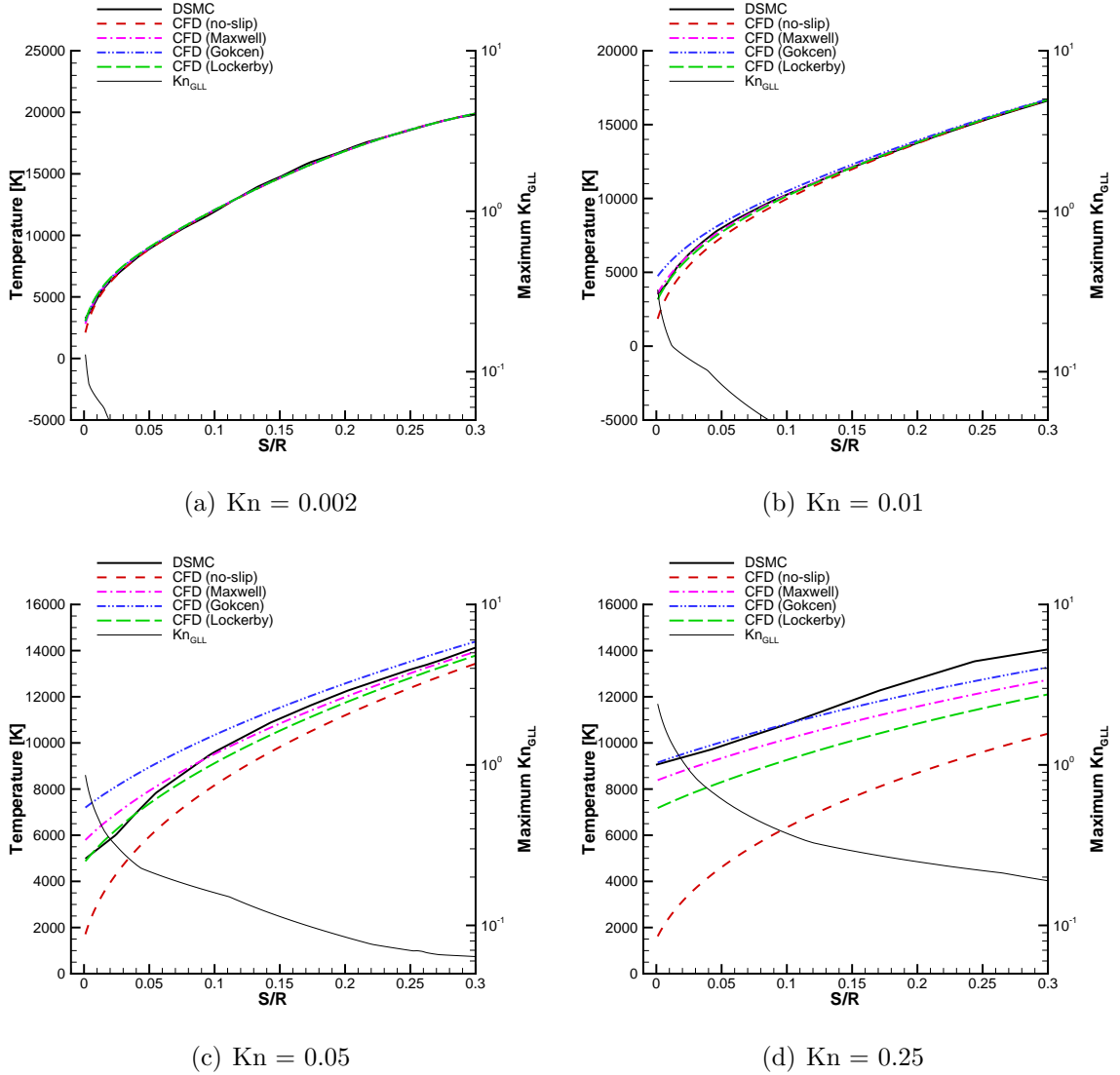
(a) Kn = 0.002

(b) Kn = 0.01

(c) Kn = 0.05

(d) Kn = 0.25

Figure 4.20: Temperature along a line normal to the body surface at $\Phi = 90°$ for a Mach 10 flow of argon about a cylinder. Distance is normalized by the cylinder radius and Φ is the angle from the stagnation point. Note that the wall temperature (at $S/R = 0$) is 500 K.
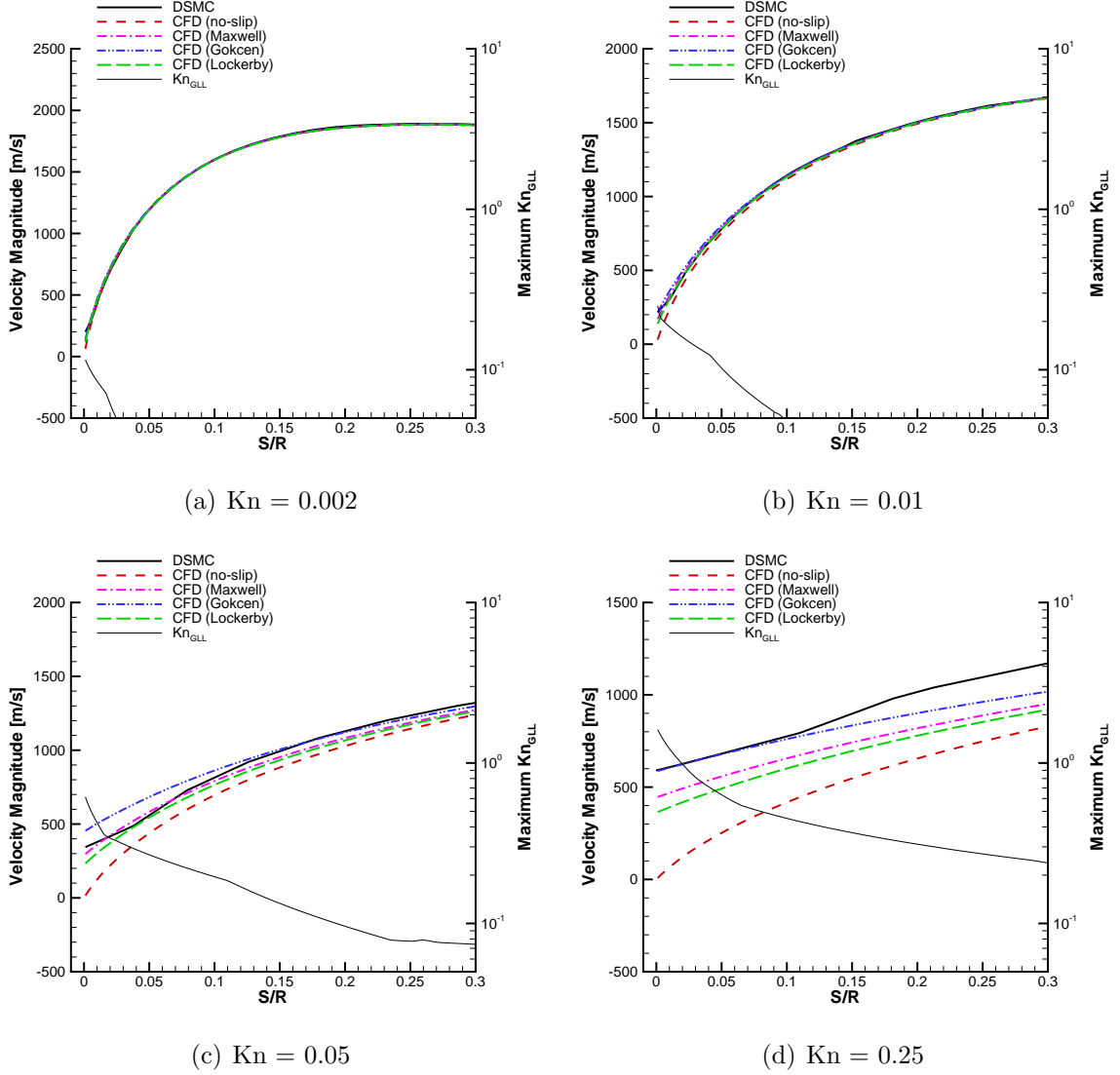
(a) Kn = 0.002

(b) Kn = 0.01

(c) Kn = 0.05

(d) Kn = 0.25
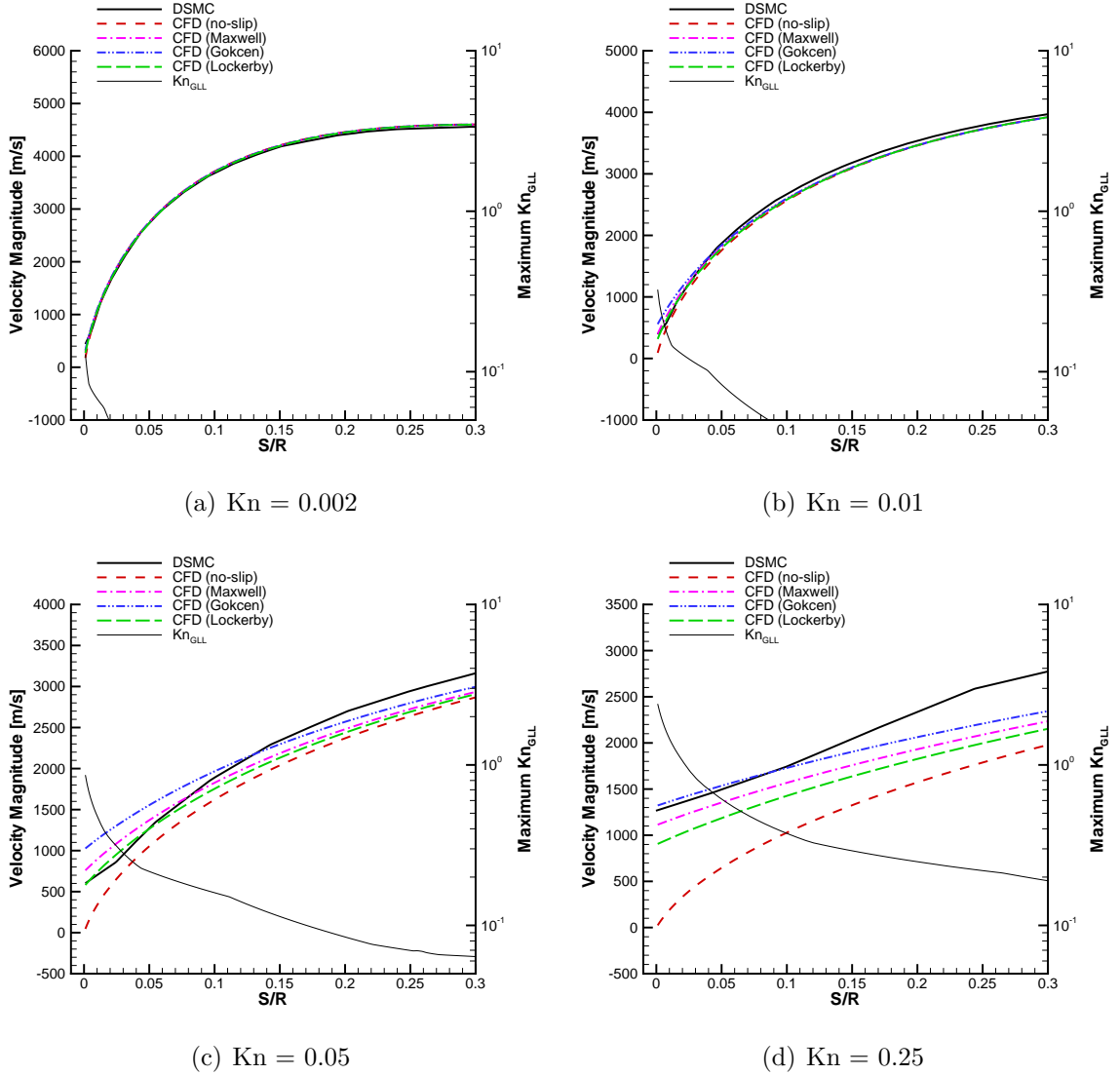
Figure 4.21: Temperature along a line normal to the body surface at $\Phi = 90°$ for a Mach 25 flow of argon about a cylinder. Distance is normalized by the cylinder radius and Φ is the angle from the stagnation point. Note that the wall temperature (at $S/R = 0$) is 1500 K.

(a) Kn = 0.002

(b) Kn = 0.01

(c) Kn = 0.05

(d) Kn = 0.25

Figure 4.22: Velocity magnitude along a line normal to the body surface at $\Phi = 90°$ for a Mach 10 flow of argon about a cylinder. Distance is normalized by the cylinder radius and Φ is the angle from the stagnation point. Note the non-zero velocity slip at the wall (at $S/R = 0$).

(a) Kn = 0.002

(b) Kn = 0.01

(c) Kn = 0.05

(d) Kn = 0.25

Figure 4.23: Velocity magnitude along a line normal to the body surface at $\Phi = 90°$ for a Mach 25 flow of argon about a cylinder. Distance is normalized by the cylinder radius and Φ is the angle from the stagnation point. Note the non-zero velocity slip at the wall (at $S/R = 0$).

the surface. There is very little nonequilibrium except near the wall. As the density decreases, there is more disagreement among the several CFD solutions, especially near the wall but the agreement improves extending out into the flow field. For the Kn = 0.05, Mach 10 case, the Maxwell CFD solution agrees best with DSMC, while for the Mach 25 case, the Lockerby solution agrees better near the wall. For the Kn = 0.25 case, the Gökçen solution shows the best agreement.

4.2.6   Slip Quantities

The Gökçen CFD predictions of the surface properties of pressure, shear stress and heat flux have been shown to agree best with DSMC. Here the velocity slip and temperature jump are examined.

The velocity slip for each simulation is seen in Figures 4.24 and 4.25. Although there are some differences in the actual peak velocity slip values (especially in the Mach 25 cases), the qualitative agreement is very good. Note that the Lockerby boundary conditions agree best with the DSMC data because of its use of the correct velocity slip at the wall rather than a fictitious slip used in the Maxwell slip conditions, as discussed in Chapter III. The Gökçen solution agrees least; it was derived specifically to match the wall properties of shear stress and heat flux at the wall rather than to accurately predict the velocity slip and temperature jump at the wall.

The temperature jump for each simulation is plotted in Figures 4.26 and 4.27. Here there is less agreement between CFD and DSMC, although the qualitative agreement at Kn = 0.002 is fair. Again, the Lockerby boundary conditions show the best agreement; DSMC and the Gökçen cases differ by more than 100%, and as much as 500%, at the stagnation point for the more rarefied cases.
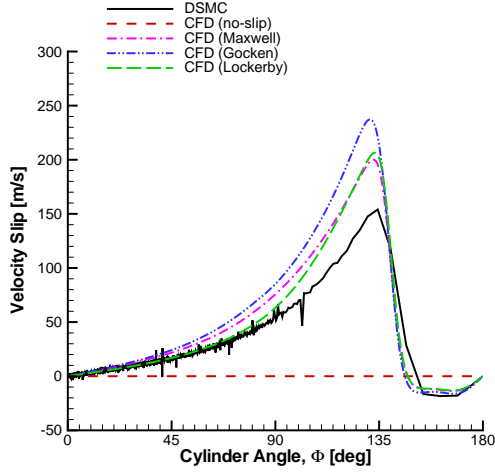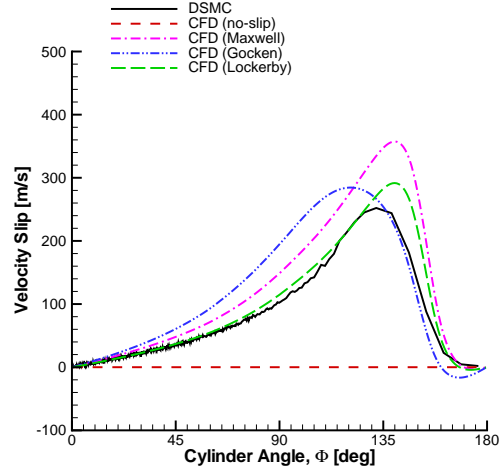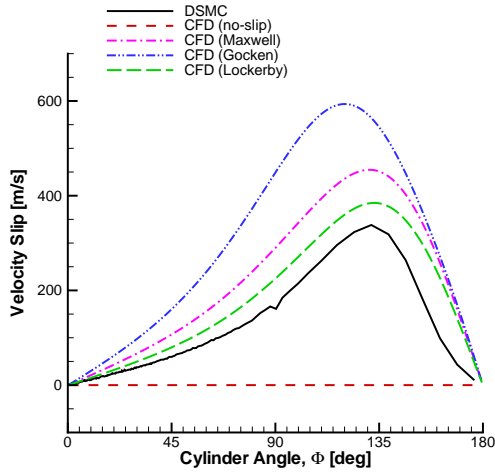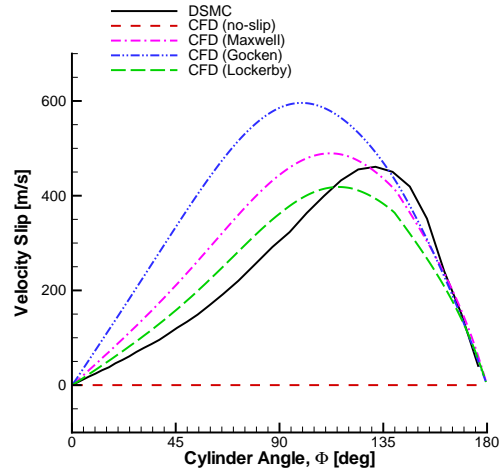
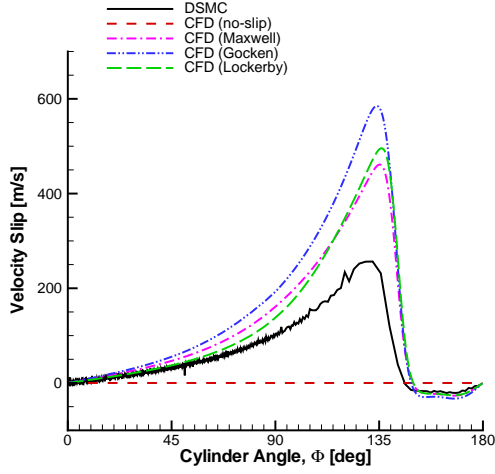Figure 4.24: Velocity slip for a Mach 10 flow of argon about a cylinder. Φ is the angle from the stagnation point.
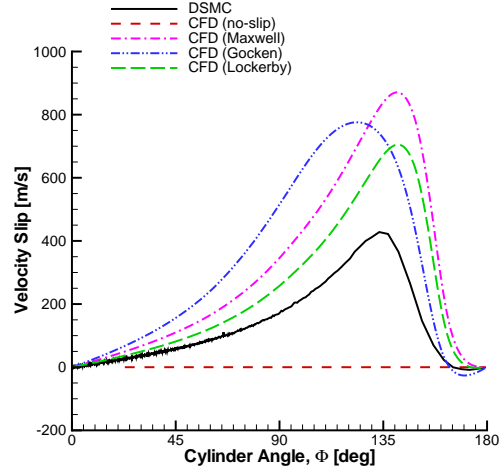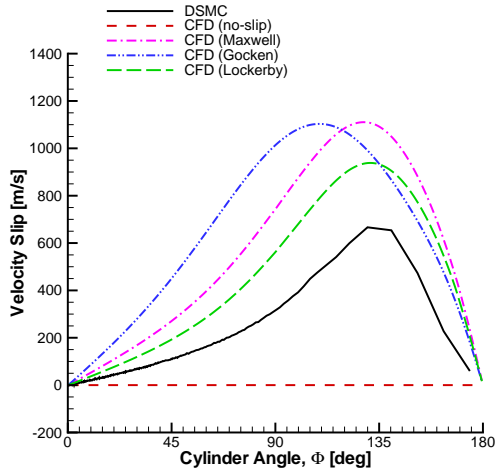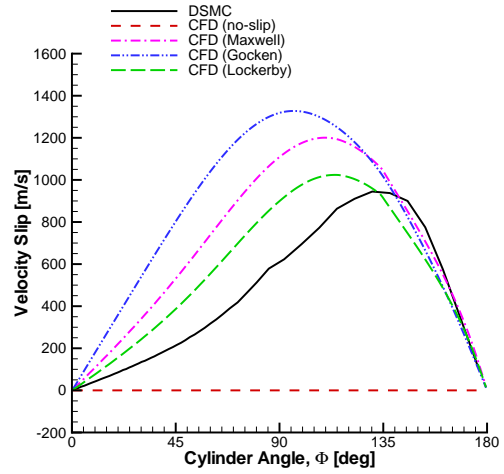
(a) Kn = 0.002

(b) Kn = 0.01

(c) Kn = 0.05

(d) Kn = 0.25

Figure 4.25: Velocity slip for a Mach 25 flow of argon about a cylinder. Φ is the angle from the stagnation point.
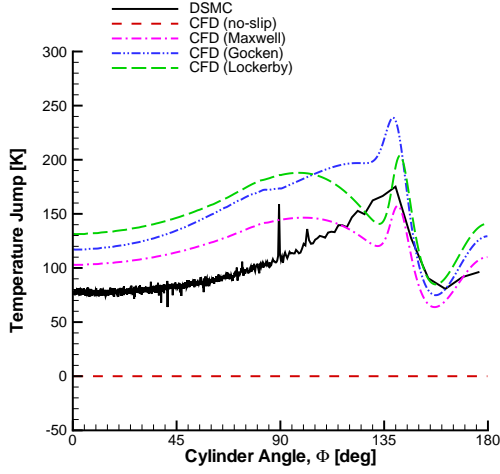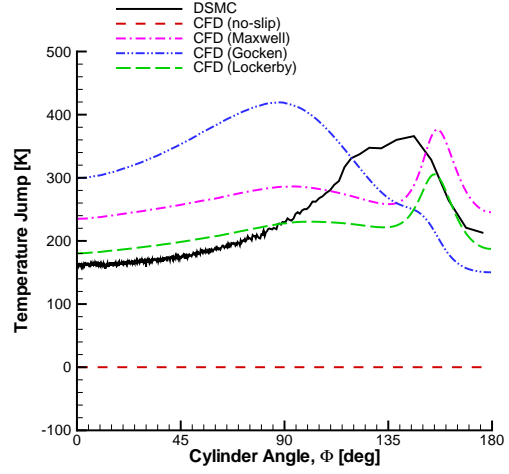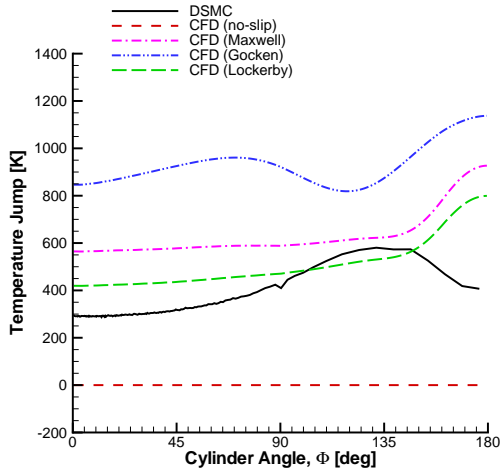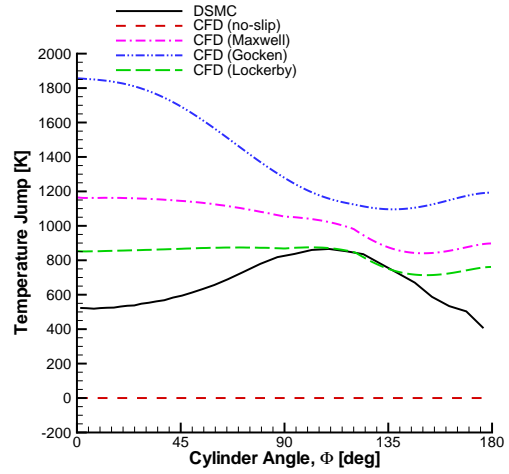
(a) Kn = 0.002

(b) Kn = 0.01

(c) Kn = 0.05

(d) Kn = 0.25

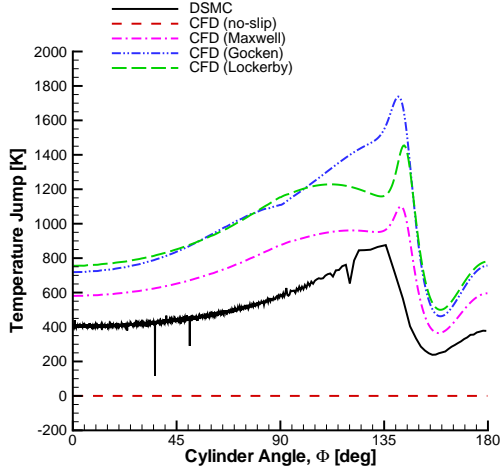Figure 4.26: Temperature jump for a Mach 10 flow of argon about a cylinder. Φ is the angle from the stagnation point.
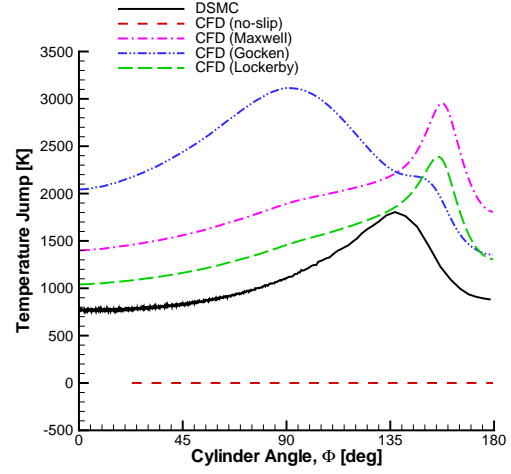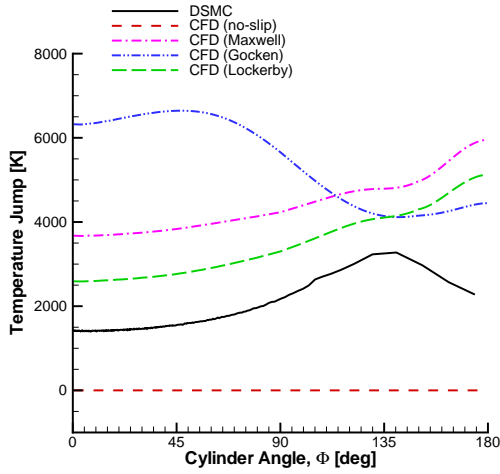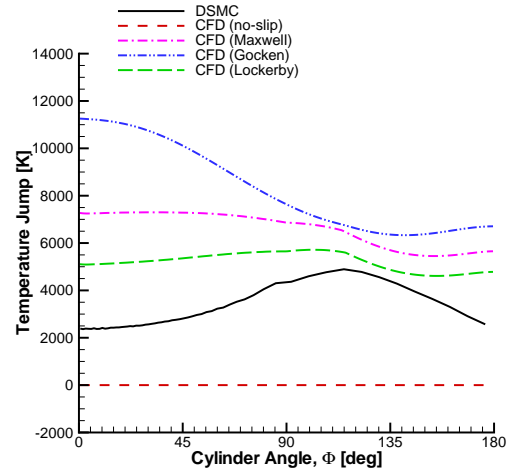
(a) Kn = 0.002

(b) Kn = 0.01

(c) Kn = 0.05

(d) Kn = 0.25

Figure 4.27: Temperature jump for a Mach 25 flow of argon about a cylinder. Φ is the angle from the stagnation point.

4.2.7 Comparison of Solutions Across the Knudsen Layer

Recall that the disagreements in flow properties are greatest near the wall, where there is more nonequilibrium than elsewhere. Here the simulations are analyzed to determine if those differences are actually concentrated in the Knudsen layer. The common definition of Knudsen layer is the portion of the flow on the order of one mean free-path (MFP) from the wall.

The analysis looks at data extracted from both DSMC and CFD solutions in four locations; along the stagnation line, along a line extending normal to the body at a point 45° from the stagnation point, along a line at 90° from the stagnation point, and along a line at 135° degrees (essentially in the wake). The following flow variables are examined: velocity magnitude, temperature, density and pressure. The number of MFPs from the wall is estimated by dividing the distance from the wall by the local MFP (from the DSMC solution). This is only an estimate due to the variation of the local MFP with location. The percent difference is obtained by using the DSMC value as the base; e.g. the percent difference in temperature is $100 \times (T_{CFD} - T_{DSMC})/T_{DSMC}$.

Figure 4.28 shows the results for temperature difference for the Mach 10, Kn = 0.01 case. Although there are still some differences between CFD and DSMC further from the wall, the locations where those differences are greater than 5% is concentrated in the region within 10 MFPs of the wall. This is seen most clearly in the Kn = 0.01 and Kn = 0.05 cases. Note that the Kn = 0.25 flow solutions diverge about 3 MFPs from the wall; this is due to flow differences in the shock.

Figure 4.29 shows similar results for the Mach 25 cases. Again, the regions where the differences are greater than 5% are within about 10 MFPs of the wall. For this higher velocity case, however, the Kn = 0.25 solutions do not reach better than 5%

(a) Kn = 0.002

(b) Kn = 0.01

(c) Kn = 0.05

(d) Kn = 0.25

Figure 4.28: Percent difference in temperature predicted in Knudsen layer along a line normal to the body surface at $\Phi = 90°$ for a Mach 10 flow of argon about a cylinder. Distance is normalized by the cylinder radius and Φ is the angle from the stagnation point. For Kn = 0.25, the shock starts about 3 MFPs from the wall.

agreement before reaching the shock.

Defining, then, the Knudsen layer as being of a thickness on the order of one MFP, i.e. it is 10 MFPs or less, the differences between CFD and DSMC are indeed concentrated in the Knudsen layer. This statement, however, does not apply near the shock, where there are also significant differences as the flow becomes more rarefied.

4.2.8 Free-Molecular Flow (Kn → ∞)

As the Knudsen number increases, the computational results for surface pressure, shear stress and heat transfer should approach the analytical results in the free-molecular, or collisionless, limit [31]. Figure 4.30 compares the non-dimensional surface properties obtained from the Mach 10 flow of argon DSMC simulations with those obtained analytically for free-molecular flow. As a further comparison of the DSMC implementation, a case is run for Kn = 100, which is essentially collisionless. It is evident that as the Knudsen number increases, the DSMC results do indeed approach the analytic results. In fact, for Kn = 100 the DSMC results are nearly identical to the analytical results.

4.2.9 Computational details

Some computational details of the simulations discussed here are given in Table 4.5. It should be noted that the Gökçen CFD cases generally took longer to converge than the other CFD cases.
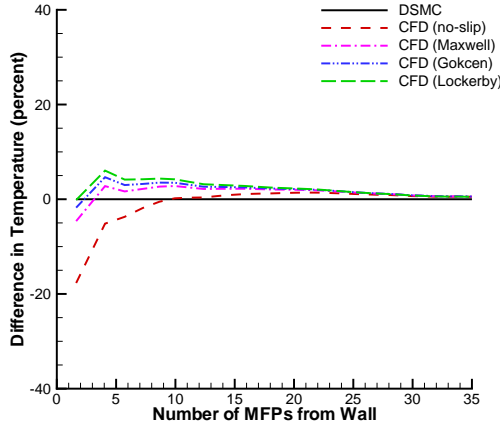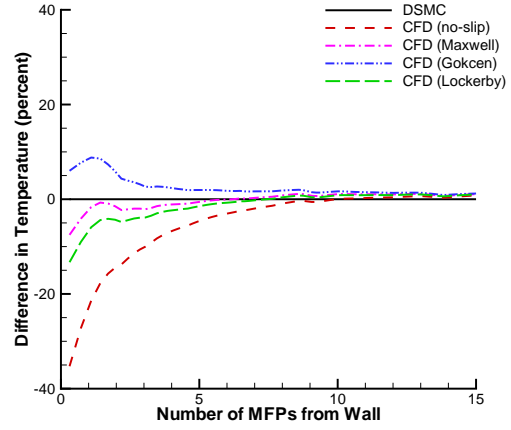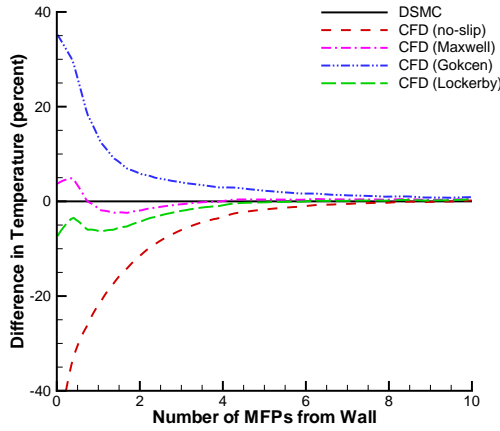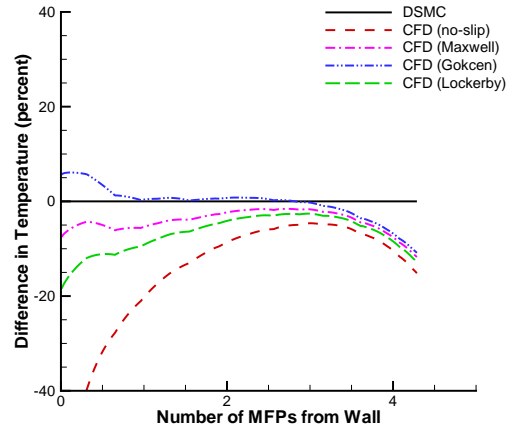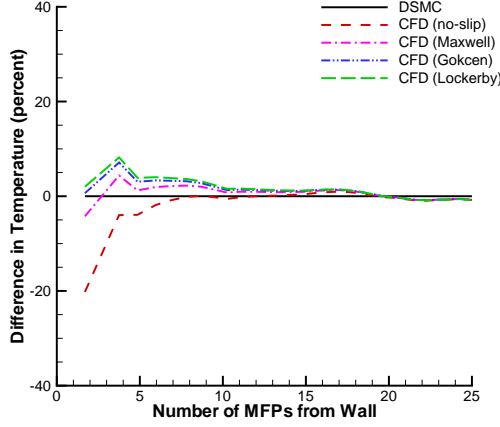
(a) Kn = 0.002
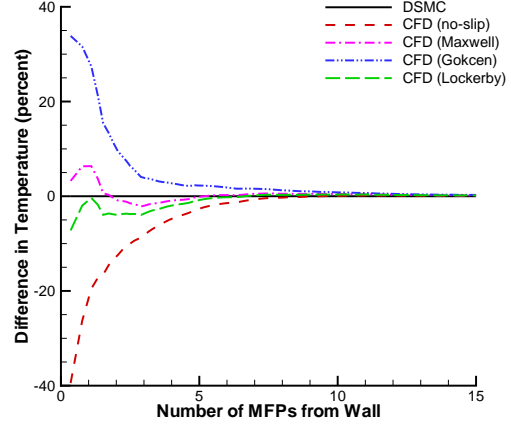
(b) Kn = 0.01
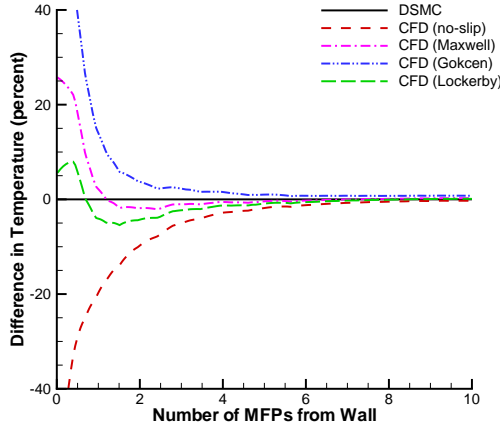
(c) Kn = 0.05
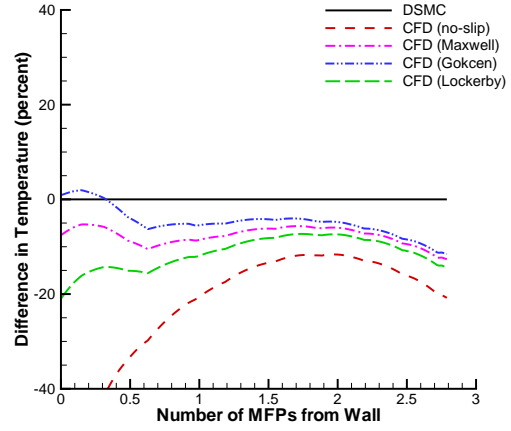
(d) Kn = 0.25

Figure 4.29: Percent difference in temperature predicted in Knudsen layer along a line normal to the body surface at $\Phi = 90°$ for a Mach 25 flow of argon about a cylinder. Distance is normalized by the cylinder radius and Φ is the angle from the stagnation point. For Kn = 0.25, the shock starts about 1.5 MFPs from the wall.

(a) Pressure

(b) Friction

(c) Heating
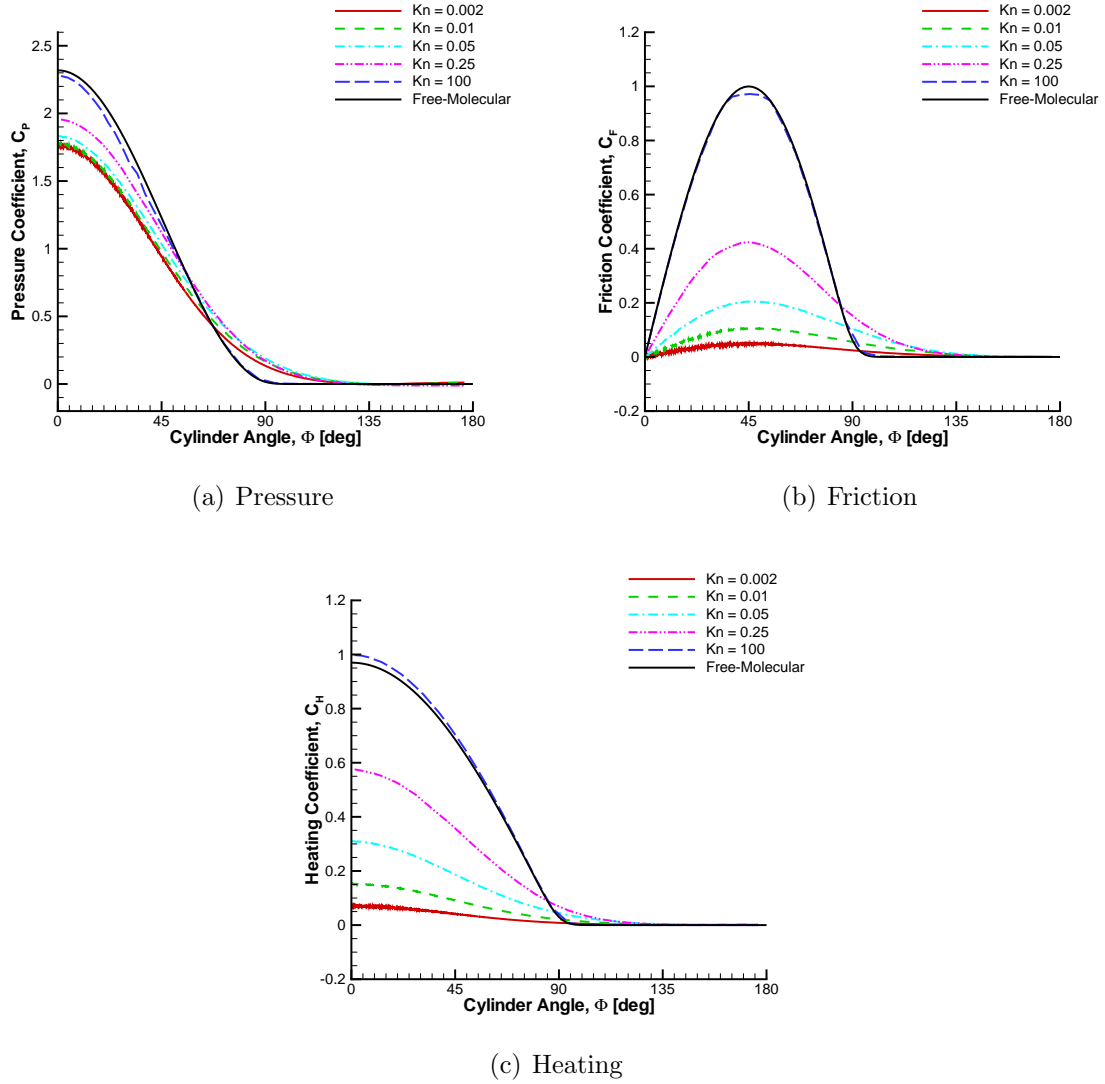
Figure 4.30: Comparisons of surface properties predicted by DSMC from the continuum to the free-molecular regimes. As the Knudsen number increases, the DSMC solutions tend toward the free-molecular analytical limits.

Table 4.5: Computational details for a flow of argon about a cylinder. Total CPU time is the wall time multiplied by the number of CPUs.

Mach 10

Kn_∞	DSMC				
	Cells	Particles	Time Steps	CPUs	Total CPU Time[*][hours]
0.002	394,250	287.0×10^6	1,050,000	128	57,186
0.01	68,497	26.8×10^6	430,000	32	1,827
0.05	18,818	7.1×10^6	430,000	32	499
0.25	24,452	8.2×10^6	290,000	32	387
Kn_∞	CFD				
	Cells		Iterations	CPUs	Total CPU Time[*][hours]
0.002	80,000		25,000	8	150
0.01	40,000		25,000	8	75
0.05	40,000		25,000	8	75
0.25	40,000		25,000	8	75

Mach 25

Kn_∞	DSMC				
	Cells	Particles	Time Steps	CPUs	Total CPU Time[*][hours]
0.002	102,626	75.1×10^6	420,000	64	5,047
0.01	71,997	37.7×10^6	300,000	32	1,793
0.05	22,523	13.1×10^6	200,000	16	429
0.25	18,395	6.2×10^6	200,000	8	198
Kn_∞	CFD				
	Cells		Iterations	CPUs	Total CPU Time[*][hours]
0.002	80,000		25,000	8	150
0.01	40,000		25,000	8	75
0.05	40,000		25,000	8	75
0.25	40,000		25,000	8	75

[*] Approximate

4.3 Nitrogen

The case of a hypersonic flow of nitrogen about a cylinder is now considered. Again, DSMC and CFD simulations are compared.

All temperature results from the DSMC simulations are obtained by averaging the translational and rotational temperatures, as shown in Eq. 3.20 unless otherwise noted.

Tables 4.6 and 4.7 compare the total drag and the peak heat transfer rate predicted by both computational methods. The differences between DSMC and CFD are also shown graphically in Figures 4.32 and 4.33. Here, the peak heat transfer rate is obtained by averaging over the surface area within one degree of the stagnation point. For CFD, these quantities are calculated for the no-slip boundary conditions; the Gökçen slip conditions [29], which gave the best agreement with DSMC for the surface properties; and the Lockerby wall-function slip conditions [49], which gave the best agreement with DSMC for the slip data.

Figure 4.31 illustrates the percentage of total drag due to pressure and friction forces, for both DSMC and CFD. As with argon, the percentage of total drag due to friction increases from about 5% at Kn = 0.002 to about 20% at Kn = 0.25 and the vast majority of the drag is due to pressure forces. That the difference in predicted total drag between CFD and DSMC is also due mostly to the differences predicted in the friction forces, as shown in Figure 4.32.

Although here a gas with internal degrees of freedom is considered, the additional possibility of thermodynamic nonequilibrium does not seem to significantly affect the surface properties, or the total drag and stagnation heat transfer. As with the flow of argon noted previously, the slip boundary conditions improve the agreement between

Table 4.6: Total drag for a flow of nitrogen about a cylinder.

Mach 10

| Kn_∞ | Drag/Length [N/m] (% Difference) | | | |
| | DSMC | CFD | | |
		no-slip	Gökçen	Lockerby
0.002	162.4	162.4 (0.0%)	162.2 (-0.2%)	162.4 (0.0%)
0.01	34.23	34.37 (0.4%)	34.17 (-0.2%)	34.32 (0.3%)
0.05	7.346	7.780 (5.9%)	7.456 (1.5%)	7.603 (3.5%)
0.25	1.714	2.056 (19.9%)	1.702 (-0.7%)	1.868 (9.0%)

Mach 25

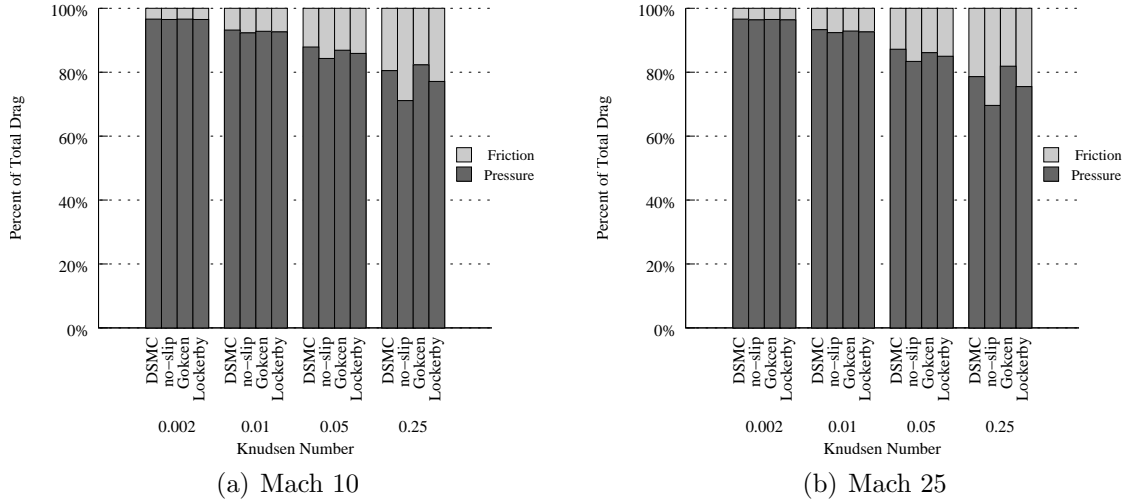| Kn_∞ | Drag/Length [N/m] (% Difference) | | | |
| | DSMC | CFD | | |
		no-slip	Gökçen	Lockerby
0.002	1020.	1022. (0.2%)	1021. (0.1%)	1022. (0.2%)
0.01	210.1	213.6 (1.7%)	212.7 (1.2%)	213.4 (1.6%)
0.05	46.36	49.00 (5.7%)	47.07 (1.5%)	48.02 (3.6%)
0.25	10.94	13.5 (23.4%)	11.25 (2.8%)	12.21 (11.6%)

(a) Mach 10   (b) Mach 25

Figure 4.31: Percentage of total drag due to pressure and friction forces for a flow of nitrogen about a cylinder.

Table 4.7: Peak heat transfer rate for a flow of nitrogen about a cylinder.

Mach 10

Kn_∞	Peak Heating [kW/m^2] (% Difference)			
	DSMC	CFD		
		no-slip	Gökçen	Lockerby
0.002	69.88	69.14 (-1.1%)	68.74 (-1.6%)	68.62 (-1.8%)
0.01	31.20	31.01 (-0.6%)	30.55 (-2.1%)	30.55 (-2.1%)
0.05	13.28	14.50 (9.2%)	13.85 (4.3%)	14.09 (6.1%)
0.25	5.173	6.380 (23.3%)	5.508 (6.5%)	6.034 (16.6%)

Mach 25

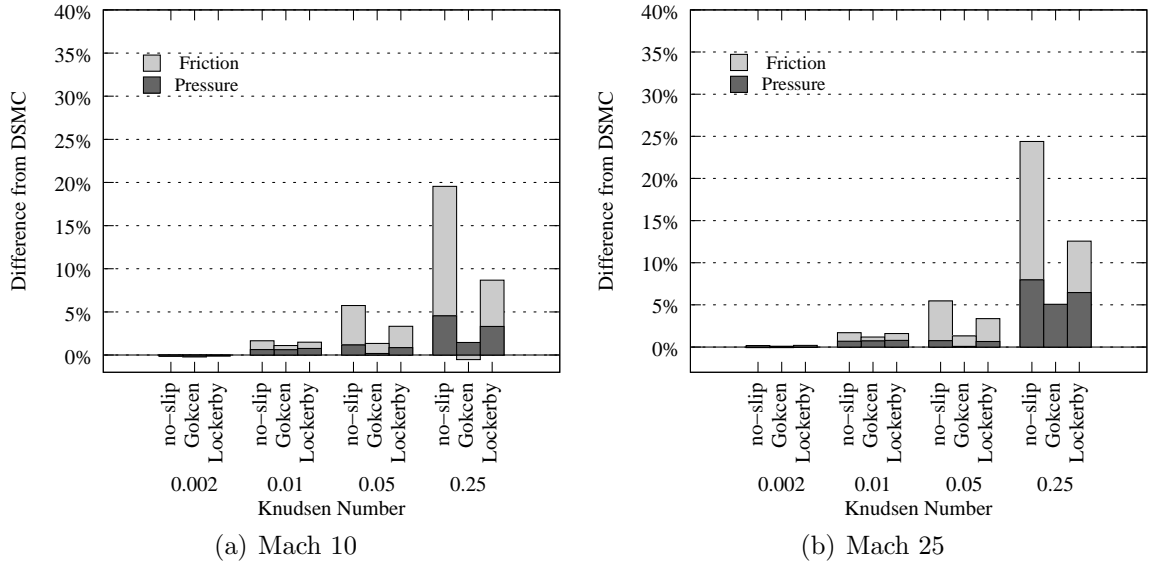| Kn_∞	Peak Heating [kW/m^2] (% Difference)			
	DSMC	CFD		
		no-slip	Gökçen	Lockerby
0.002	1348.	1309. (-2.9%)	1303. (-3.3%)	1302. (-3.4%)
0.01	585.0	586.3 (0.2%)	579.7 (-0.9%)	579.4 (-1.0%)
0.05	258.1	281.7 (9.1%)	268.6 (4.1%)	274.6 (6.4%)
0.25	91.87	118.3 (28.8%)	99.10 (7.9%)	111.6 (21.5%)

(a) Mach 10

(b) Mach 25

Figure 4.32: Total drag difference from DSMC for flow of nitrogen about a cylinder. Note that there is a negative contribution to total drag due to friction for the Kn = 0.25, Mach 25 case, bringing the total drag difference down to 2.8%.
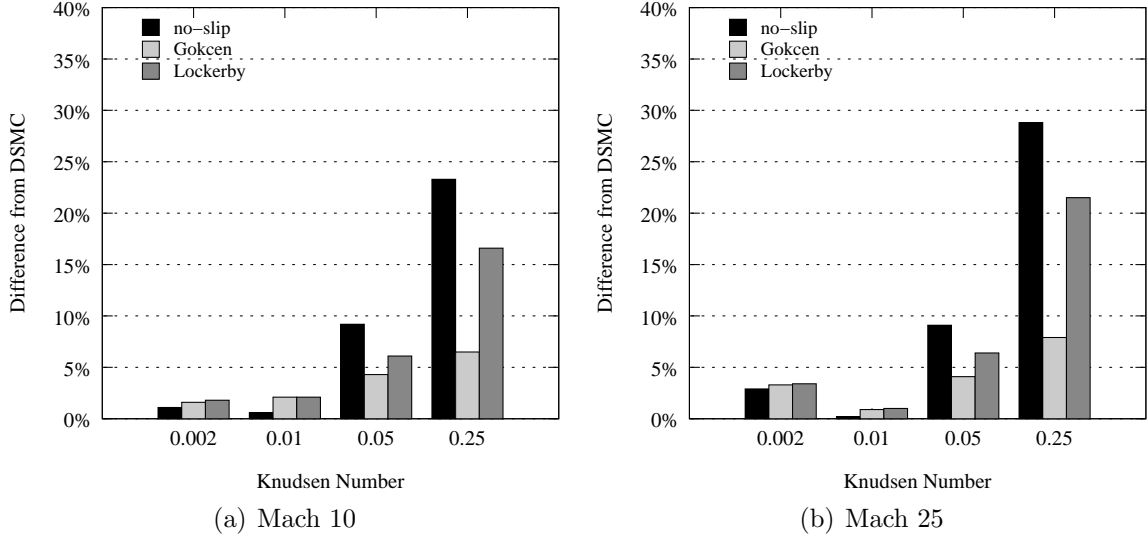
Figure 4.33: Peak heat transfer rate difference from DSMC for flow of nitrogen about a cylinder.

the two simulation methods, with the Gökçen slip boundary conditions showing the best agreement. In some cases, there is better agreement with the nitrogen cases than with the argon cases; for example, for the Mach 10, Kn = 0.25 case, the total drag computed using the Gökçen boundary conditions is within 3% of the DSMC solution with nitrogen, although it is just over 5% when using argon.

The peak heat transfer rates also show similar trends for nitrogen as with argon, although here the largest difference seen in the nitrogen results using the Gökçen boundary conditions is 8%, compared to about 6% with argon. The Mach 25 heat transfer results show a larger difference when considering nitrogen. The relatively large differences for the Mach 25, Kn = 0.002 case are most likely due to computational artifacts, rather than complexity due to the nonequilibrium nature of the flow, as will be discussed below.

Overall, however, the current results for nitrogen are very similar to those for argon. The Gökçen conditions give the best results, with total drag being within 3% of the DSMC results, and the peak heating rates being within about 5%.

Again, given that the Gökçen condition shows the best agreement with the DSMC solutions, the CFD field results shown below are taken from the Gökçen CFD case.

4.3.1 Continuum Breakdown

The breakdown parameter is again calculated using both the CFD and the DSMC solutions. As before, the only causes of breakdown to the continuum hypothesis expected here are in regions of high gradients (such as the shock and boundary layer) and regions of rarefaction (such as in the wake). Thermal nonequilibrium is expected to be higher in regions where the breakdown parameter values are highest; thus, the nonequilibrium between translational and rotational modes is expected in the shock wave, and the wake. As the flow becomes more rarefied in the higher Knudsen-number cases, the degree of thermal nonequilibrium is expected to increase.

Figures 4.34 and 4.35 illustrate the amount of continuum breakdown in the flow as it becomes more rarefied. As with the argon flow, the maximum gradient length local Knudsen number is computed from the DSMC (top) and CFD (bottom) solutions. Light gray regions correspond to $Kn_{GLL} < 0.05$, dark gray regions correspond to $Kn_{GLL} < 0.10$ and black regions correspond to $Kn_{GLL} > 0.10$. Continuum breakdown is expected in the same regions of the flow, namely in the shock region, in a thin boundary layer along the surface and in a region of flow expansion around the top of the cylinder. The additional thermal nonequilibrium present due to internal degrees of freedom does not affect the amount of continuum breakdown predicted by the breakdown parameter.

4.3.2 Flow Field Properties

The density ratio fields, where the density is normalized by the freestream density, can be seen in Figures 4.36 and 4.37. Note that the maximum density ratio behind the

(a) Kn = 0.002

(b) Kn = 0.01

(c) Kn = 0.05

(d) Kn = 0.25

Figure 4.34: Kn_{GLL} field for a Mach 10 flow of nitrogen about a cylinder. Light gray regions correspond to $Kn_{GLL} < 0.05$, dark gray regions correspond to $Kn_{GLL} < 0.10$ and black regions correspond to $Kn_{GLL} > 0.10$.
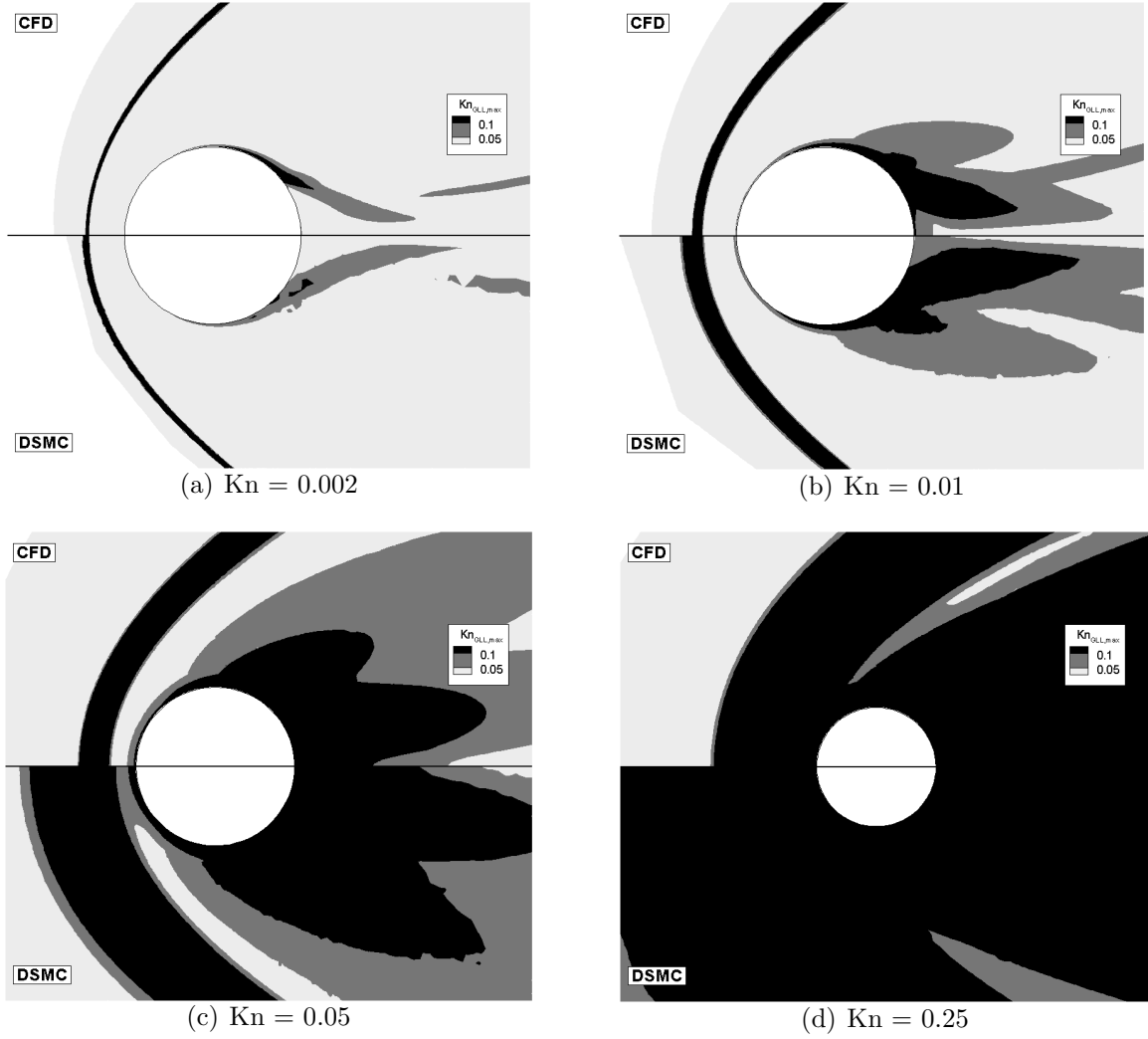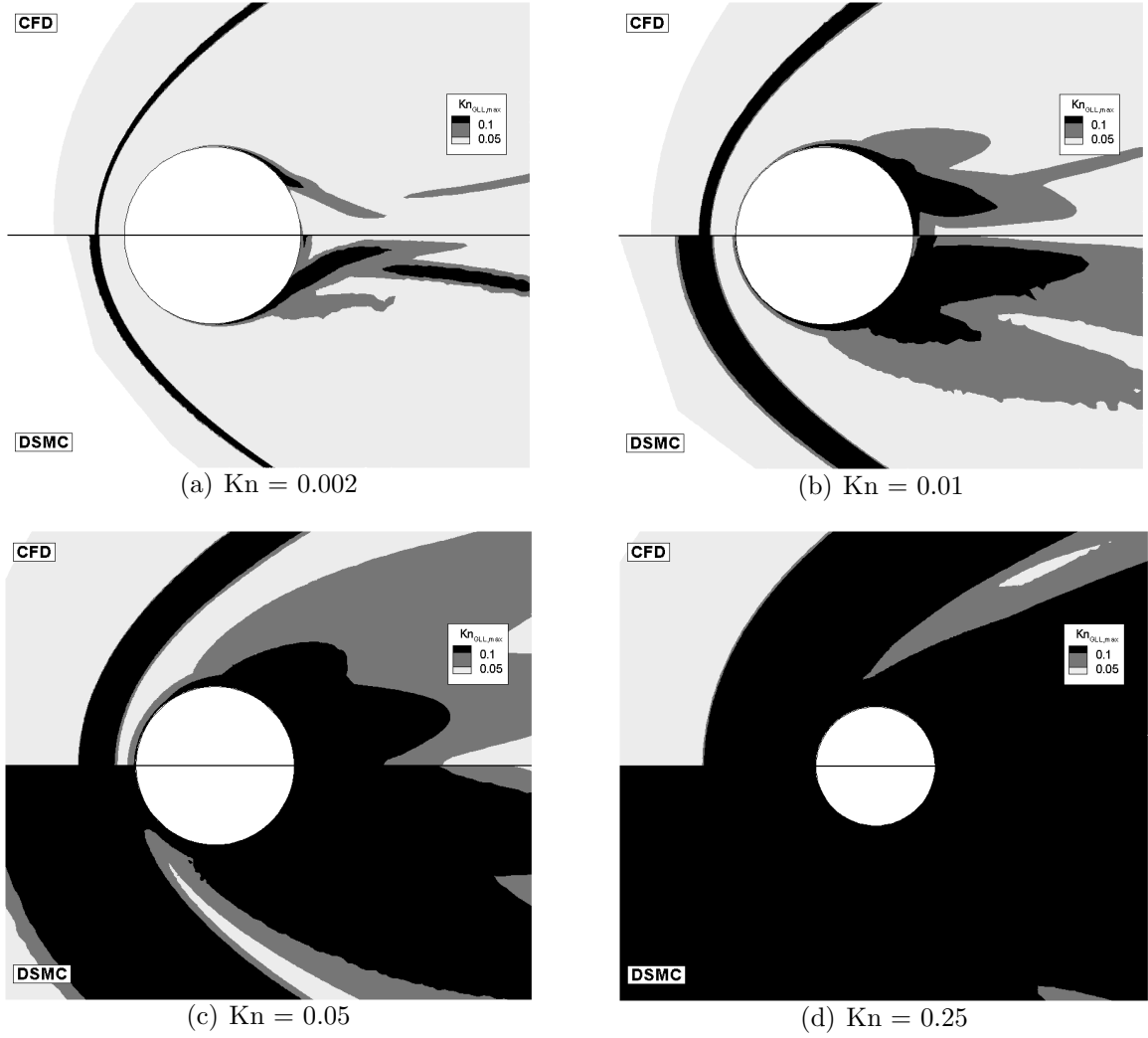
Figure 4.35: Kn_{GLL} field for a Mach 25 flow of nitrogen about a cylinder. Light gray regions correspond to $Kn_{GLL} < 0.05$, dark gray regions correspond to $Kn_{GLL} < 0.10$ and black regions correspond to $Kn_{GLL} > 0.10$.
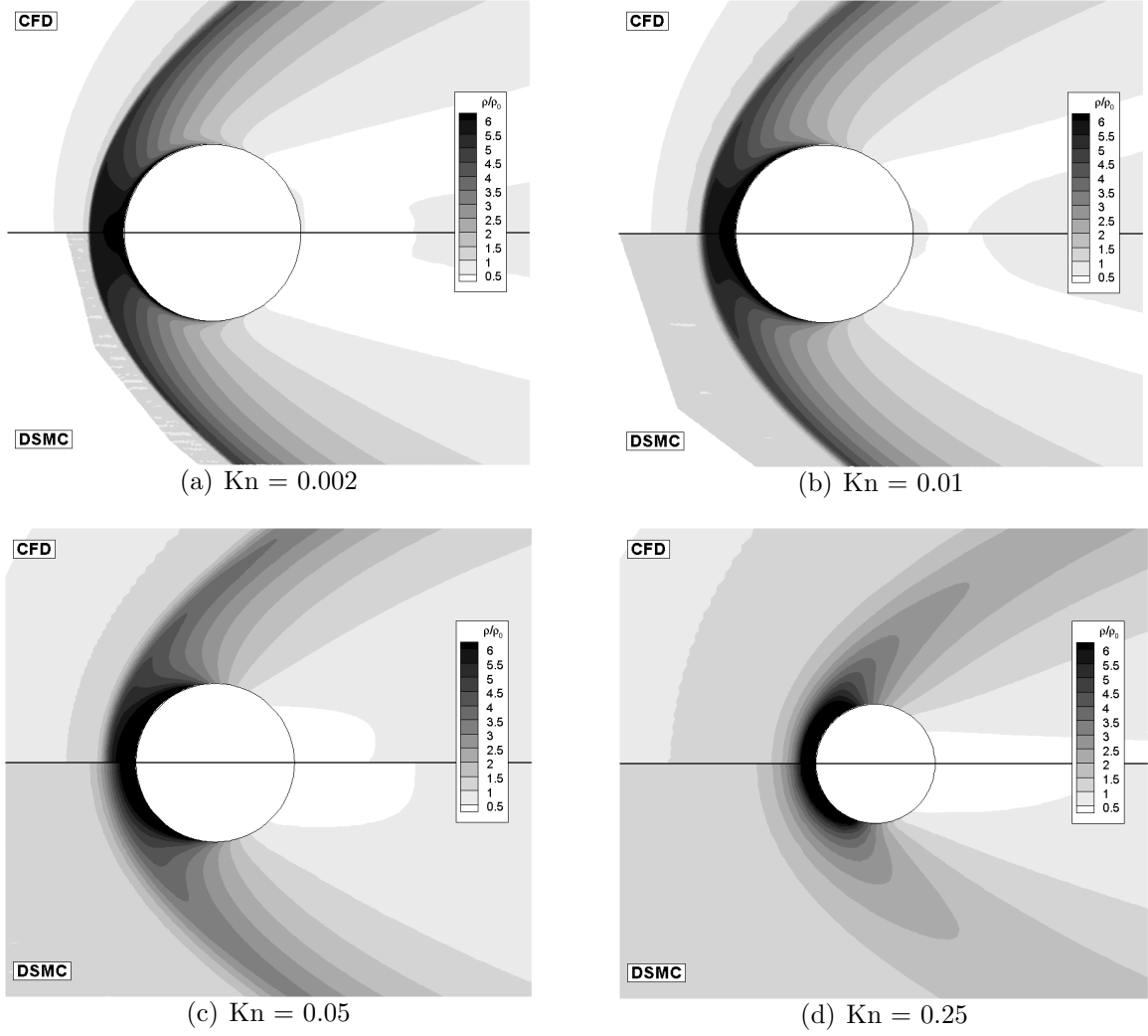
Figure 4.36: Density ratio field for a Mach 10 flow of nitrogen about a cylinder. The normal shock relations predict a density ratio of 5.71.

shock is about 6, agreeing with the theoretical limit for a diatomic gas in equilibrium and the results of the normal shock relations, $\rho/\rho_0 = 5.87$ (Mach 10) and $\rho/\rho_0 = 5.95$ (Mach 25). Overall agreement between CFD and DSMC is good, with some small differences in the shock structure at the higher Knudsen number conditions. As with argon, as the freestream density decreases, the shock becomes much more diffuse.

The translational/rotational temperature fields are seen in Figures 4.38 and 4.39. The temperature results for the Mach 10 flows are very similar to those seen above with the argon flow. However, the Mach 25 results exhibit some significant differ-

(a) Kn = 0.002
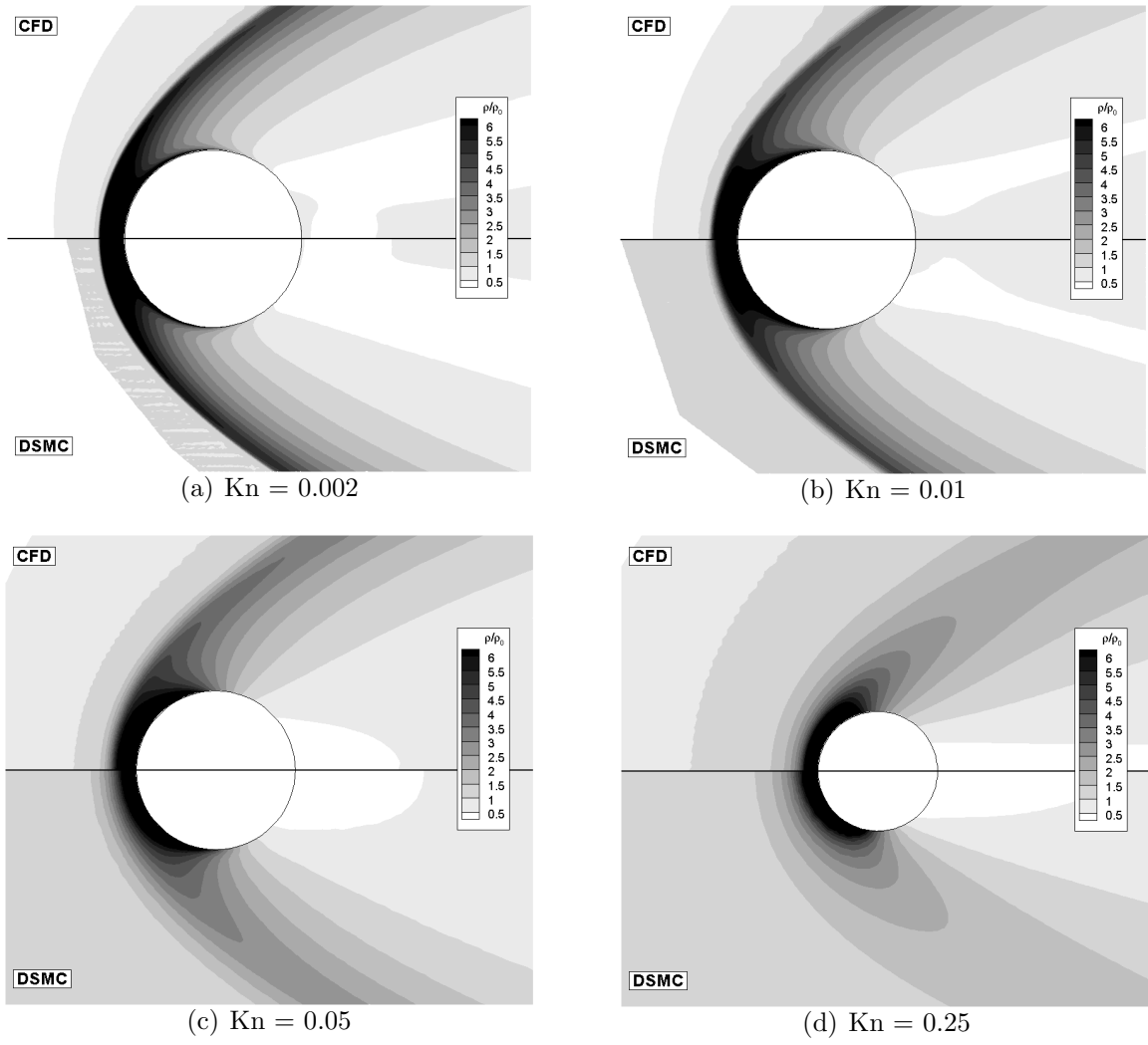
(b) Kn = 0.01

(c) Kn = 0.05

(d) Kn = 0.25

Figure 4.37: Density ratio field for a Mach 25 flow of argon about a cylinder. The normal shock relations predict a density ratio of 5.95.

ences. Although the CFD and DSMC methods agree well for Kn = 0.002, the peak temperature seen in the narrow band immediately behind the shock in Figure 4.39(a) shows the effects of vibrational energy excitation; that is, as the translational and rotational temperatures rise, energy is transferred into the vibrational mode, decreasing the translational temperature. This will be seen more clearly in the temperature profiles along the stagnation line that are examined below. The Kn = 0.01 cases also show some effect of the vibrational energy excitation, and the CFD solution no longer agrees with the DSMC solution. The Kn = 0.05 and Kn = 0.25 cases again show large differences, with the DSMC shocks being much more diffuse, the DSMC thermal boundary layer being much thicker, and the DSMC temperature in the wake being lower. In each of these cases the differences are more extreme than was noted for the argon flow.

The vibrational temperature fields can be seen in Figures 4.40 and 4.41. Here it can be seen that, for the Mach 10 cases, the amount of vibrational excitation is minimal. The peak translational/rotational temperatures seen in the Kn = 0.002 case is around 4000 K, while the vibrational temperature peaks at about 1200 K. While CFD and DSMC are in good agreement for the vibrational temperature field in the fore-body region, CFD predicts higher vibrational temperatures in the wake. As the flow becomes more rarefied, the level of vibrational excitation decreases as there are fewer collisions with which to equilibrate the vibrational and translational energy modes. For the Kn = 0.05 and Kn = 0.25 cases, the vibrational temperature does not exceed the wall temperature value of 500 K, and most, if not all, of the vibrational excitation is due to the wall boundary condition.

The Mach 25 cases show a larger amount of vibrational excitation, as expected, due to the much higher temperatures. The peak translational/rotational temperature

(a) Kn = 0.002

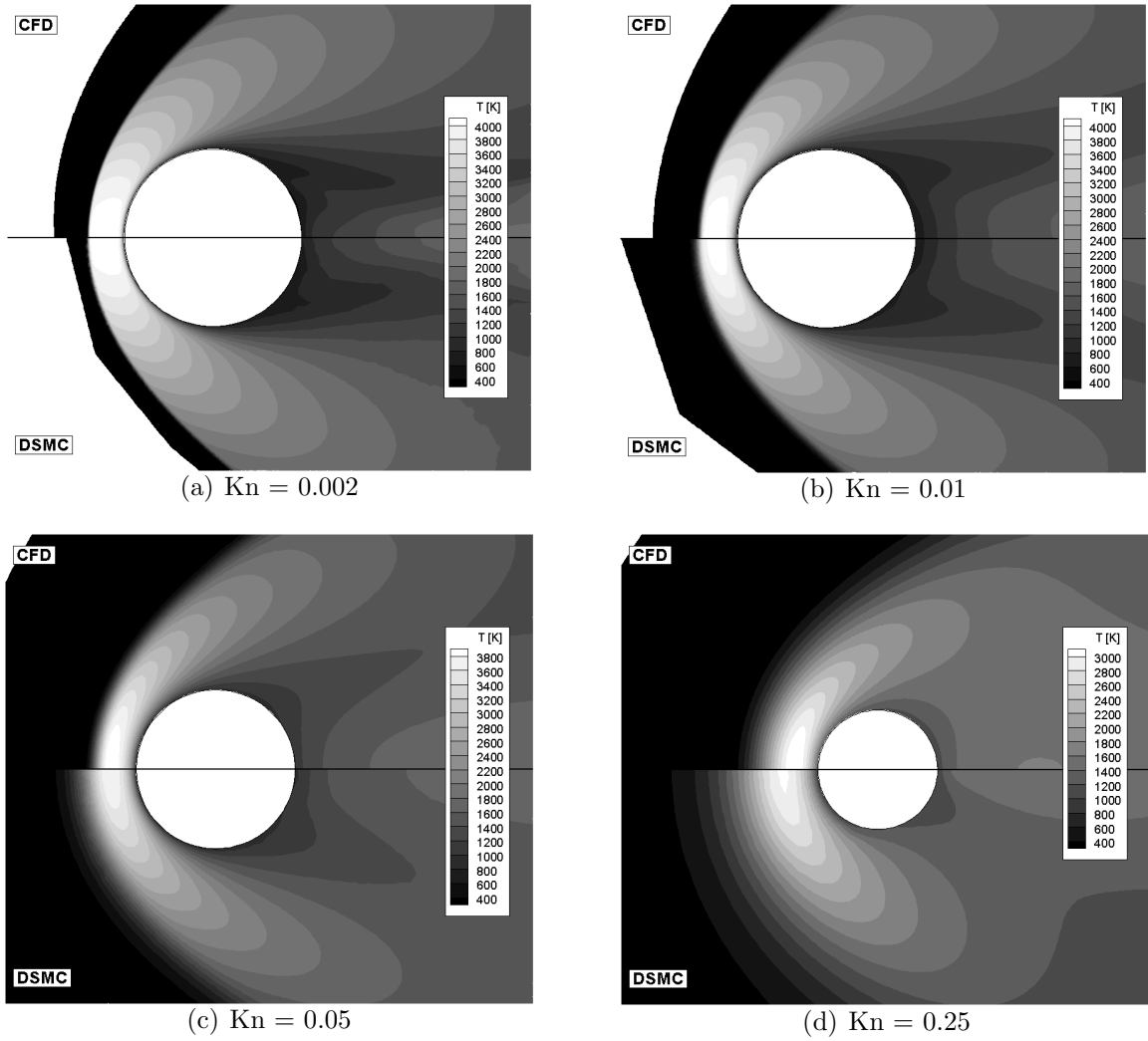(b) Kn = 0.01

(c) Kn = 0.05

(d) Kn = 0.25

Figure 4.38: Translational/rotational temperature field for a Mach 10 flow of nitrogen about a cylinder. The normal shock relations predict a post-shock temperature of 4,078 K.

(a) Kn = 0.002

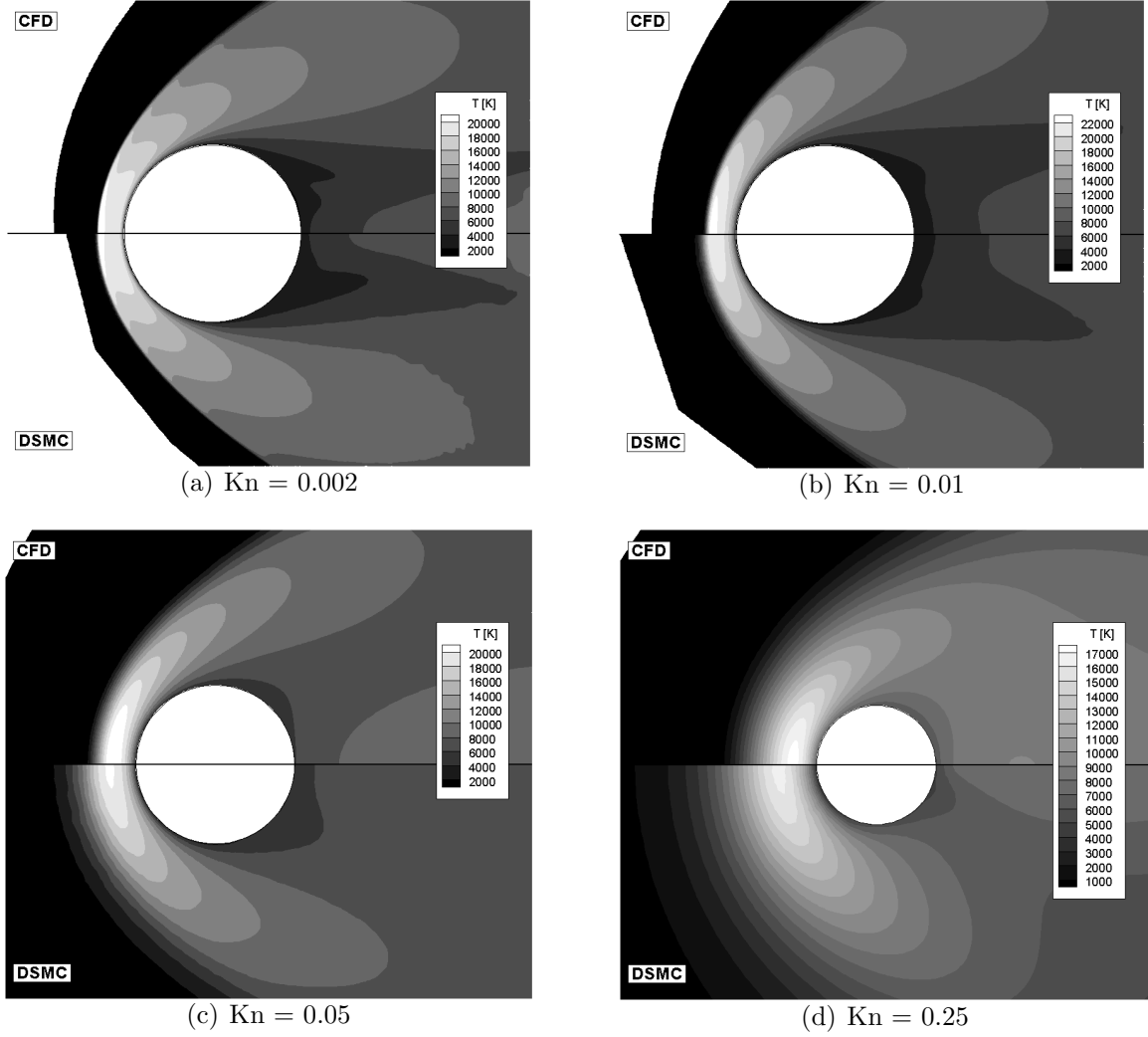(b) Kn = 0.01

(c) Kn = 0.05

(d) Kn = 0.25

Figure 4.39: Translational/rotational temperature field for a Mach 25 flow of nitrogen about a cylinder. The effects of vibrational nonequilibrium can be seen in the narrow band of high temperature directly behind the gas, as energy is transferred from the translational/rotational modes to the vibrational mode. The normal shock relations give a post-shock temperature of 24,500 K, which is slightly higher than the maximum temperature in the simulations.
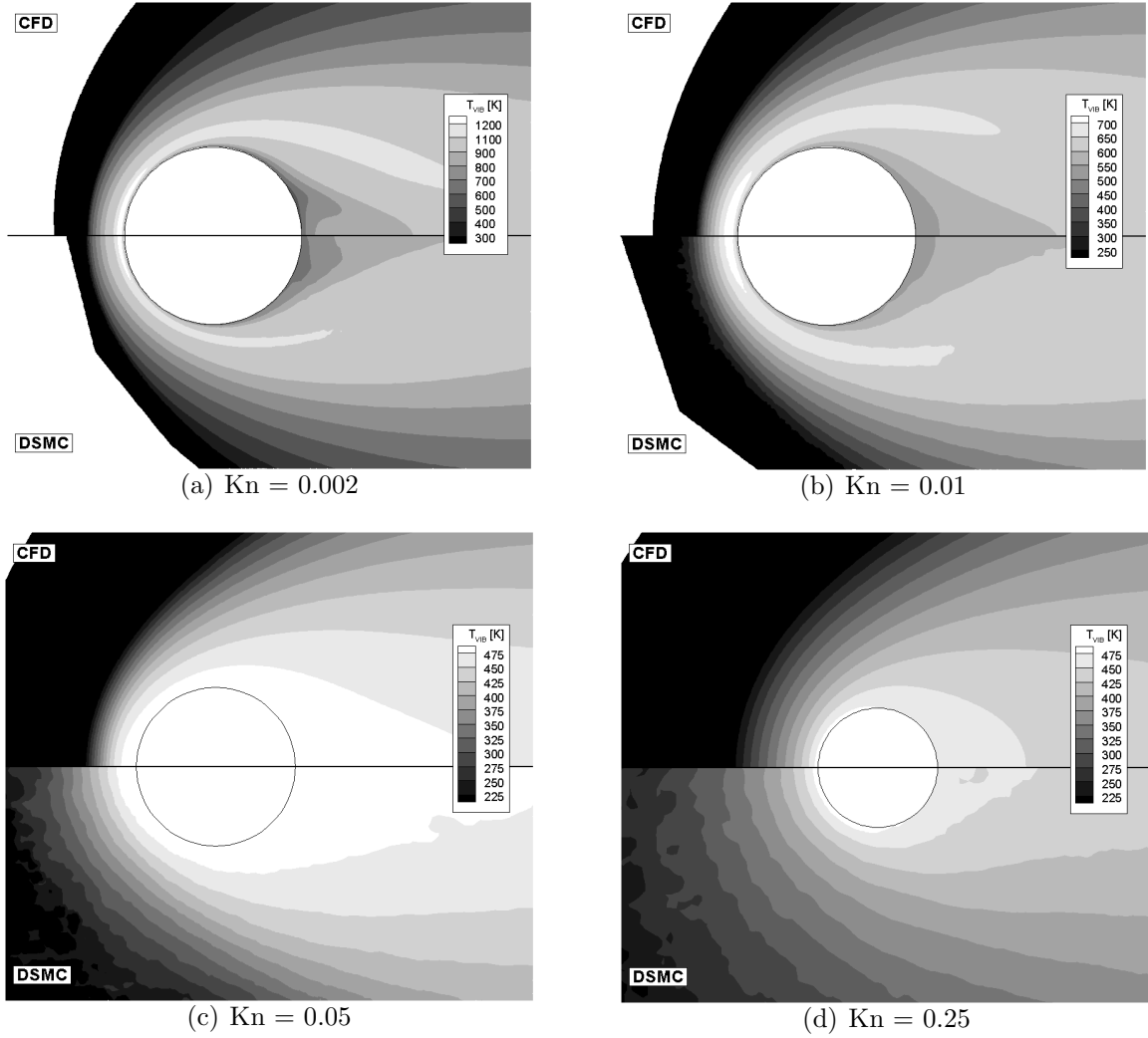
Figure 4.40: Vibrational temperature field for a Mach 10 flow of nitrogen about a cylinder. The vibrational energy modes are activated in significant amounts only for the lower Knudsen number cases. For the higher Knudsen number cases, the vibrational modes are activated mostly by the cylinder surface, where the vibrational temperature is 500 K.

(a) Kn = 0.002

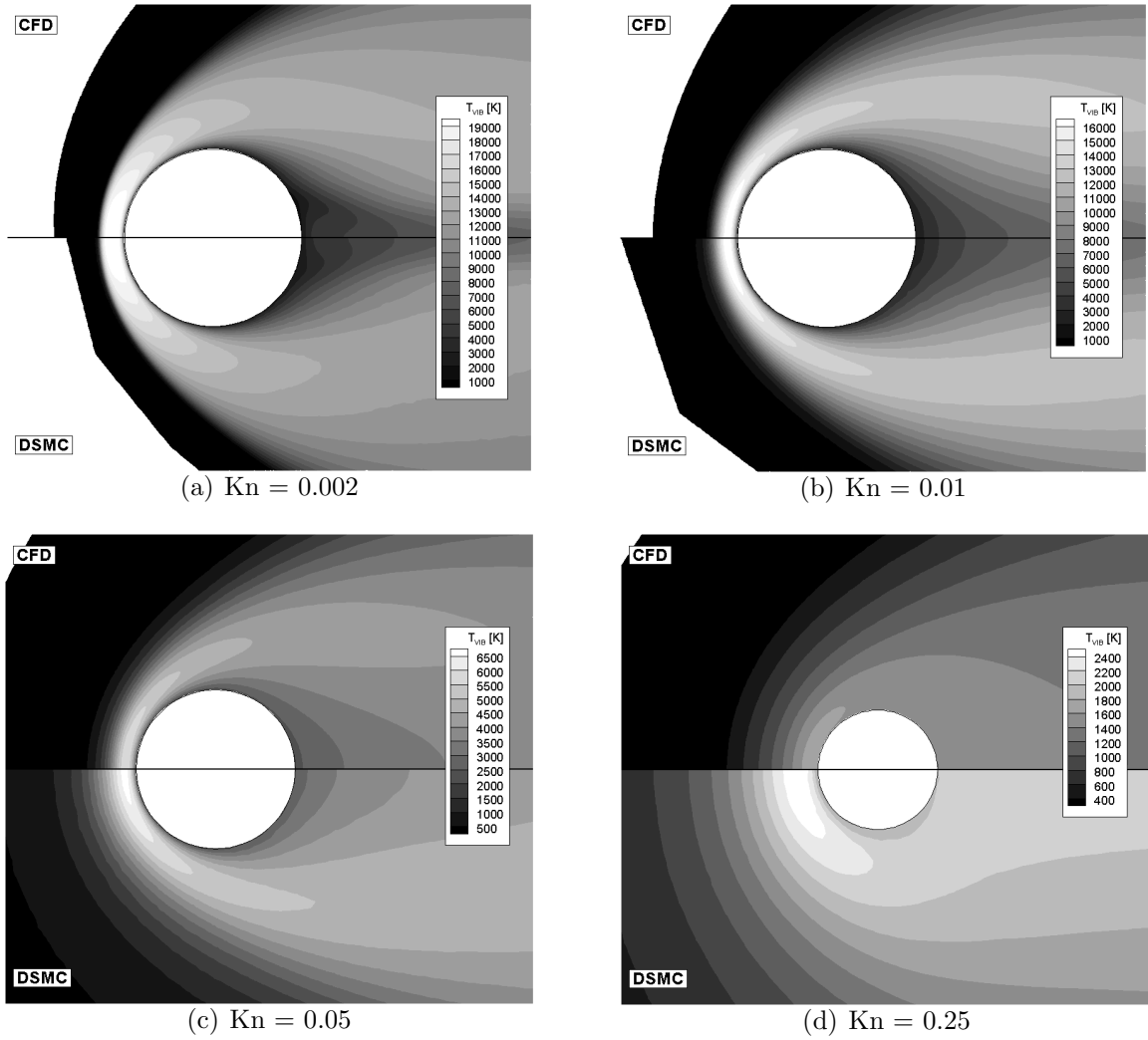(b) Kn = 0.01

(c) Kn = 0.05

(d) Kn = 0.25

Figure 4.41: Vibrational temperature field for a Mach 25 flow of nitrogen about a cylinder. The vibrational energy modes are much more significant than at Mach 10 due to the higher temperatures at Mach 25. Note that the vibrational temperature at the wall is 1500 K.

for the Kn = 0.002 case is around 20,000 K, and the peak vibrational temperature is very nearly the same; thus, there are sufficient collisions such that the different energy modes very nearly reach equilibrium. Again, the two computational methods agree well in their predictions for vibrational temperature for this and the Kn = 0.01 case. The CFD solutions significantly under-predict the amount of vibrational excitation for the more rarefied cases. DSMC predicts a significant amount of vibrational excitation within the shock for the Kn = 0.25 case, while that in the CFD solution is mostly due to the wall boundary conditions.

4.3.3   Stagnation Line Properties

The temperature profiles along the stagnation line for the Mach 10 cases are shown in Figure 4.42. Here, the translational, rotational, vibrational temperatures and the averaged translational/rotational temperature from the DSMC solutions are compared with the translational/rotational and vibrational temperatures from the Gökçen CFD solutions. The Kn = 0.002 case shows that there is very little nonequilibrium except in the shock. In the shock, there is a slight peak in translational temperature prior to equilibrating with the rotational mode. (This effect is seen more clearly in the Kn = 0.01 case.) The averaged DSMC temperature and the CFD temperature agree very well, although there is a small amount of translational-rotational nonequilibrium. There is also a significant amount of vibrational nonequilibrium as the temperatures are not high enough to significantly excite the vibrational mode. The two-temperature model of LeMANS is able to model this nonequilibrium very satisfactorily.

As the flow becomes more rarefied, the amount of translational/rotational nonequilibrium in the shock increases. For the Kn = 0.01 case, however, these two energy

(a) Kn = 0.002

(b) Kn = 0.01

(c) Kn = 0.05

(d) Kn = 0.25

Figure 4.42: Temperature profiles along the stagnation line for a Mach 10 flow of nitrogen about a cylinder. Flow is from left to right, with the distance normalized by the cylinder radius. The translational and rotational temperatures from DSMC are shown along with the averaged translational/rotational temperature.

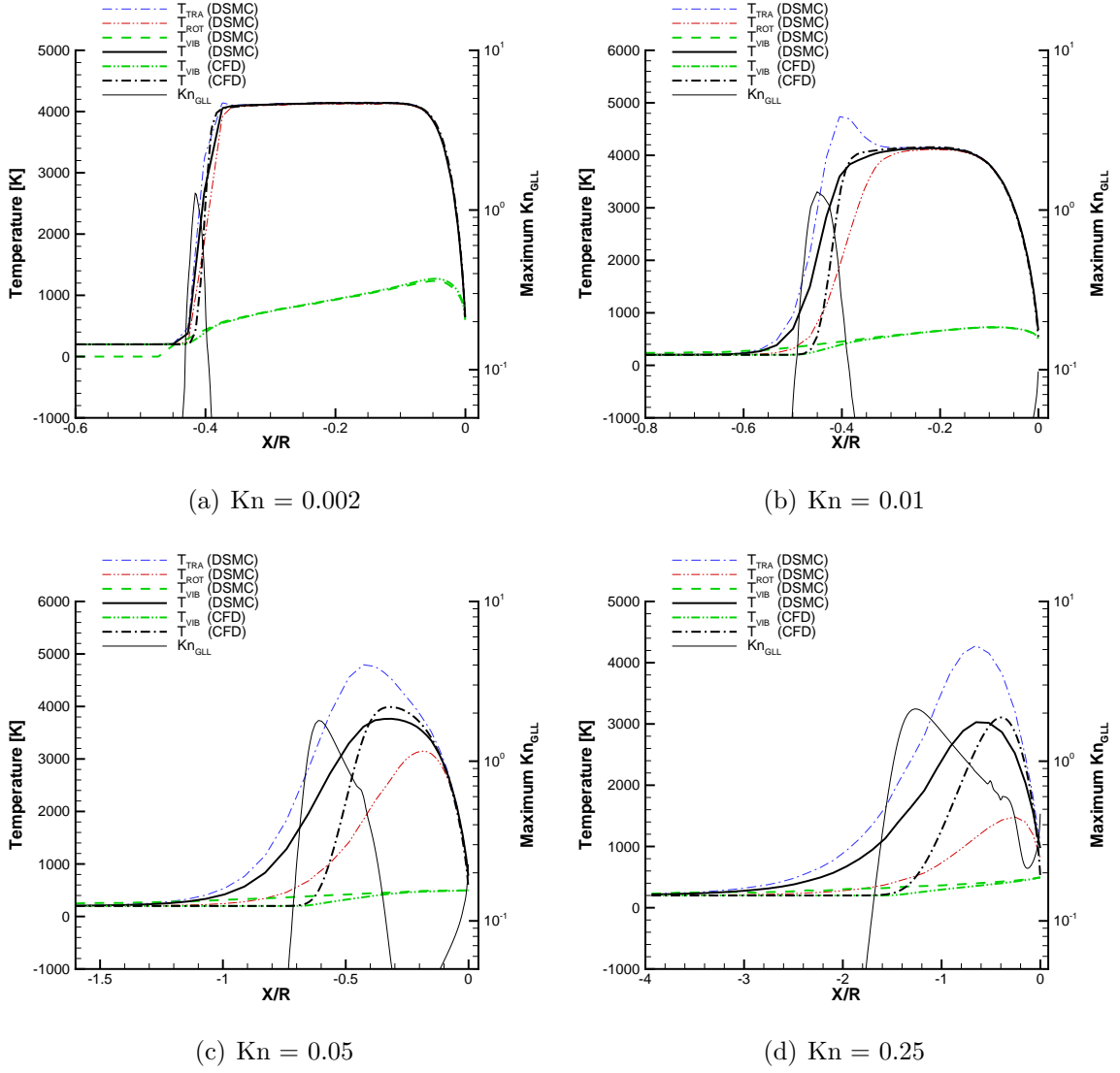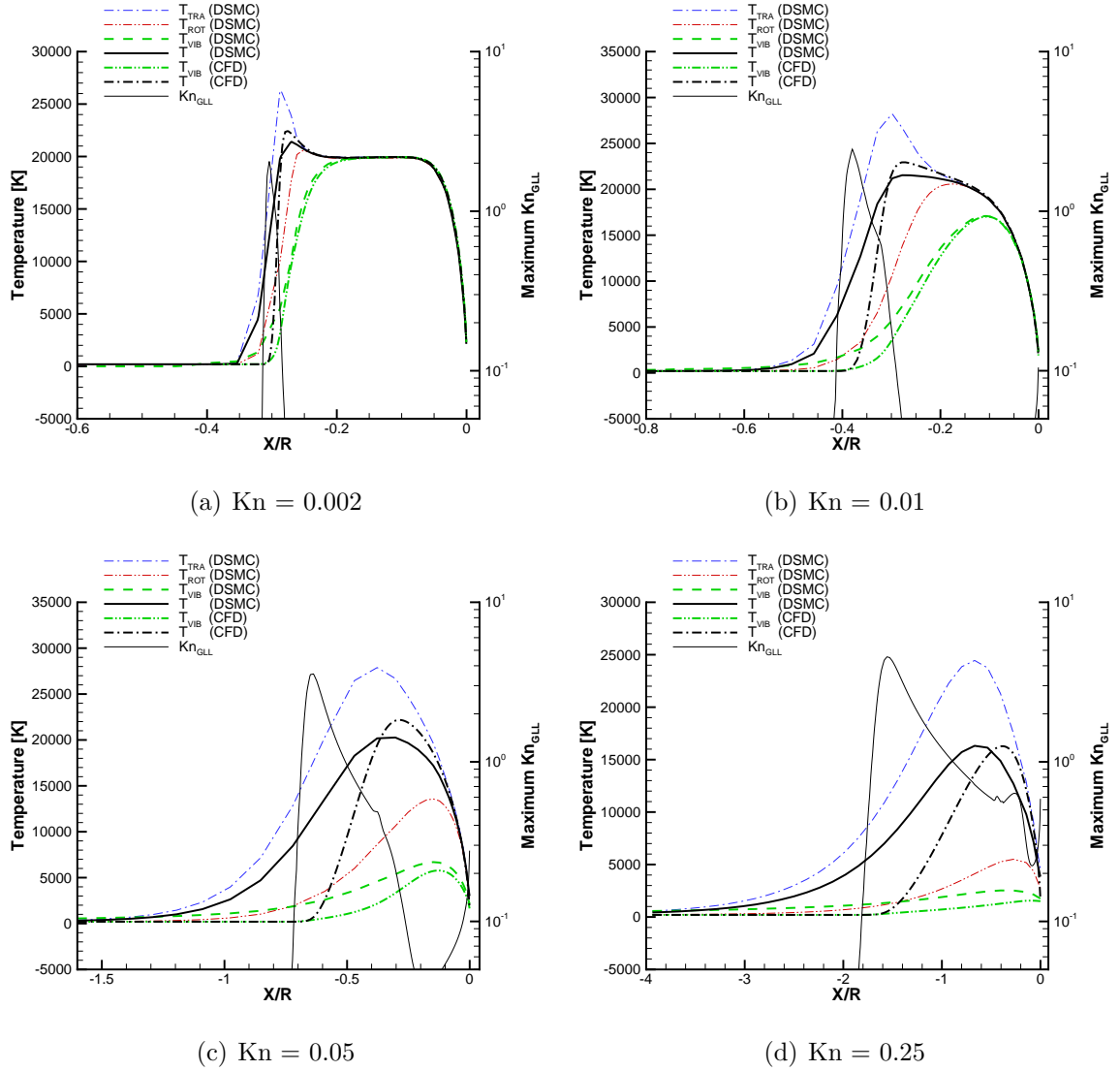(a) Kn = 0.002

(b) Kn = 0.01

(c) Kn = 0.05

(d) Kn = 0.25

Figure 4.43: Temperature profiles along the stagnation line for a Mach 25 flow of nitrogen about a cylinder. Flow is from left to right with the distance normalized by the cylinder radius.

modes are quickly brought back into equilibrium after the shock. For the $Kn = 0.05$

and $Kn = 0.25$ cases, however, there are too few collisions for the translational and

rotational modes to equilibrate prior to reaching the boundary layer (for $Kn = 0.05$)

or the wall (for $Kn = 0.25$). The vibrational temperature profiles for these last two

cases strongly imply that most, if not all, of the vibrational excitation is due to the

wall boundary conditions.

The Mach 25 temperature profiles are seen in Figure 4.42. The additional vibra-

tional excitation due to the high temperatures in the post-shock region is clearly

shown. There is additional translational-rotational nonequilibrium, even in the

$Kn = 0.002$ case. However, all temperatures, including the vibrational temperature,

equilibrate prior to the boundary layer. Similar trends as with Mach 10 are noted

for the more rarefied cases. Note, however, that CFD under-predicts the vibrational

temperature in the $Kn = 0.05$ and $Kn = 0.25$ cases.

4.3.4   Surface Properties

The surface properties for the flow of nitrogen about the cylinder are examined in

this section. Interestingly, there is no significant difference between the trends seen

here and those noted for the argon cases, notwithstanding the additional thermal

nonequilibrium present in the flows. At most, the surface property predictions (in

terms of the total drag and peak heat transfer rate) differ by a few percentage points

more than they did for the simple gas cases.

The surface pressure distributions, shown in Figures 4.44 and 4.45 are very similar

to those for argon. In particular, all of the simulations agree very well, except for

the $Kn = 0.25$ cases, where CFD predicts a higher pressure than DSMC.

The surface shear stress distributions are seen in Figures 4.46 and 4.47. Again,

(a) Kn = 0.002

(b) Kn = 0.01

(c) Kn = 0.05

(d) Kn = 0.25

Figure 4.44: Surface pressure coefficient for a Mach 10 flow of nitrogen about a cylinder. The maximum Kn_{GLL} near the surface is plotted on the right axis. Φ is the angle from the stagnation point.
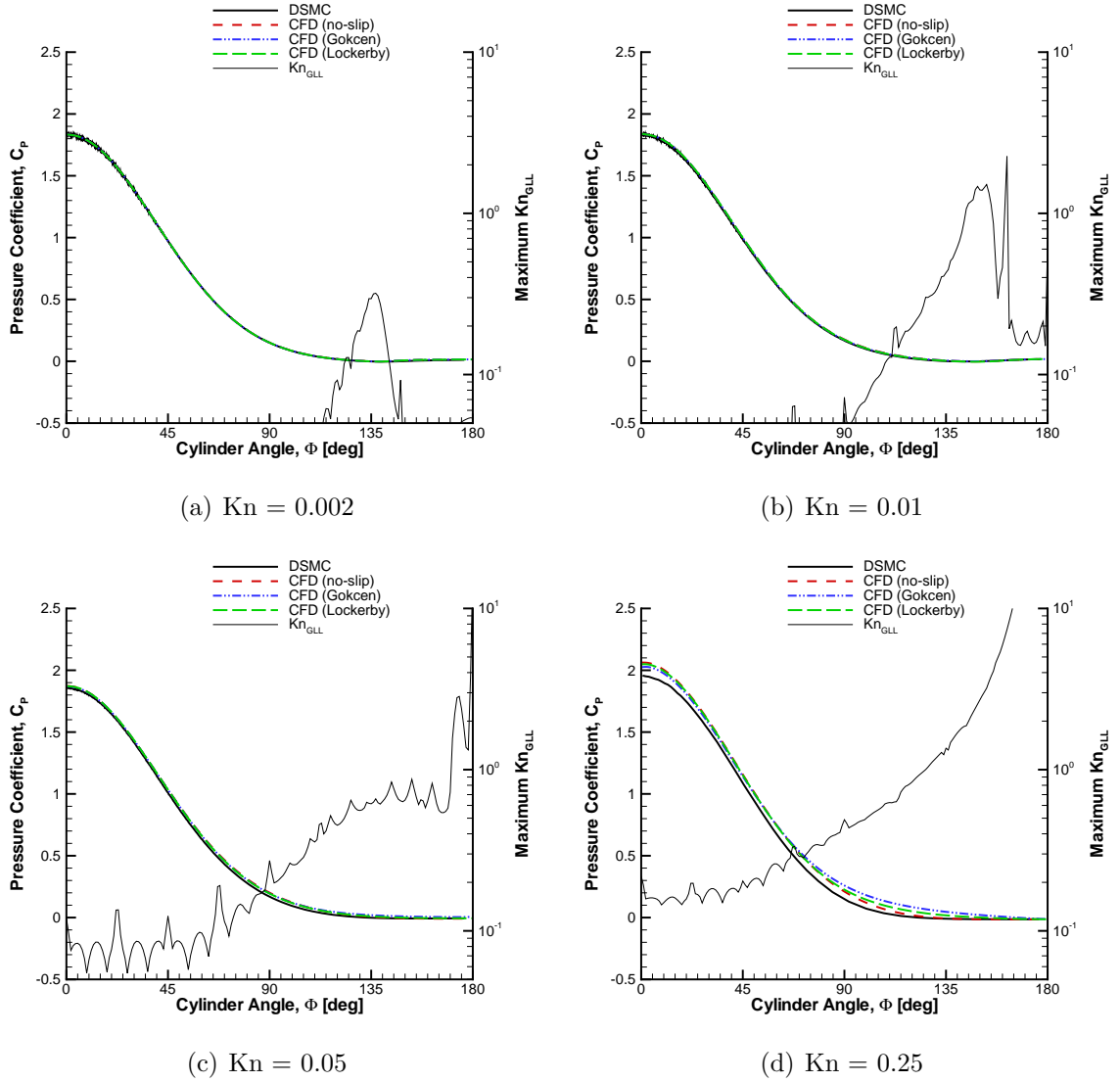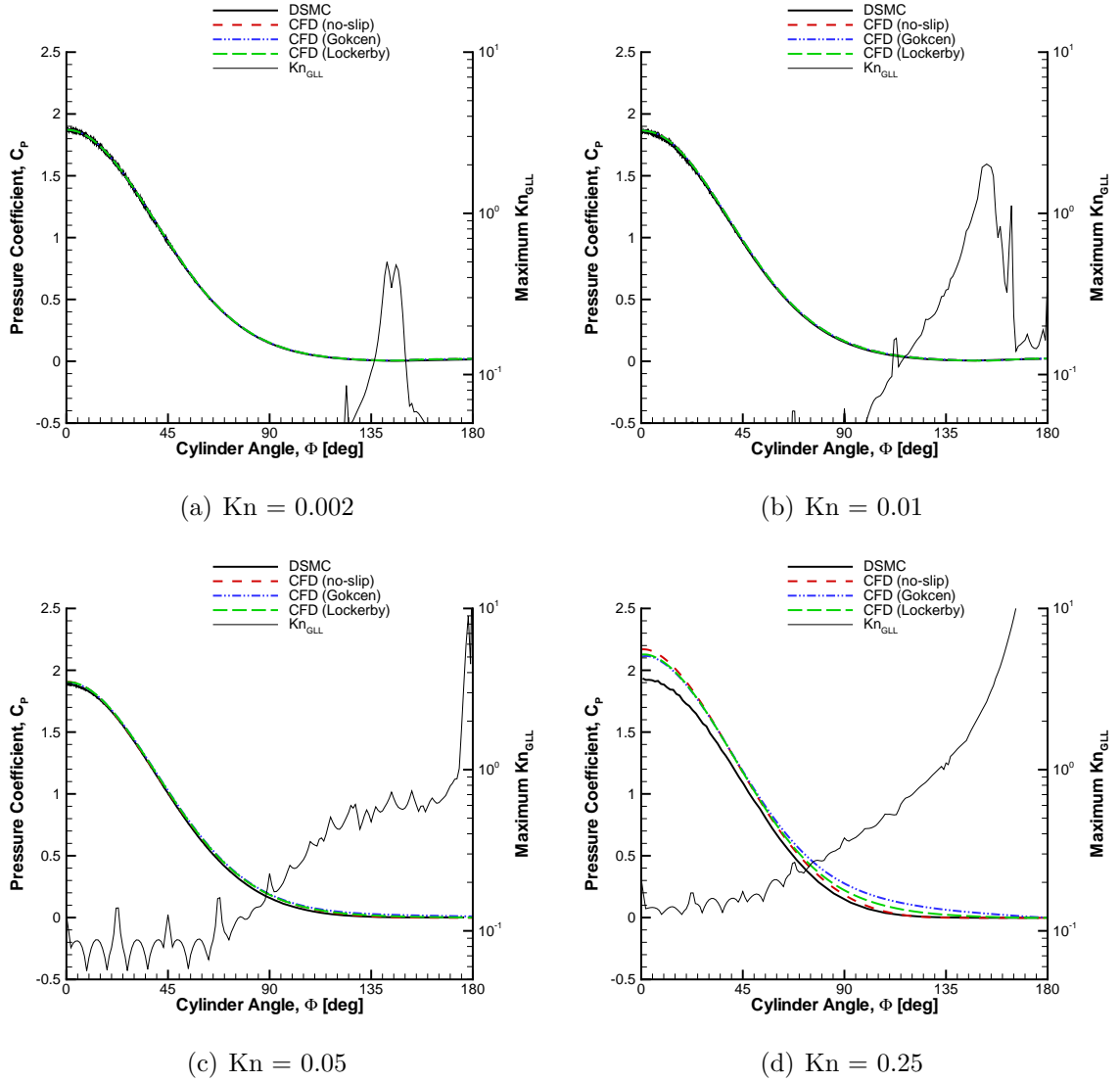
Figure 4.45: Surface pressure coefficient for a Mach 25 flow of nitrogen about a cylinder. The maximum Kn_{GLL} near the surface is plotted on the right axis. Φ is the angle from the stagnation point.

the results are very similar to those for argon, although CFD diverges more from DSMC as the Knudsen number increases. Nevertheless, the slip boundary conditions greatly improve the agreement, with the Gökçen boundary conditions showing the best agreement with DSMC.

The heat transfer rate distributions are shown in Figures 4.48 and 4.49. Here, the $Kn = 0.002$ cases the current differences of about 3% are reasonable. These results are also very similar the argon cases, with the CFD results diverging from DSMC at the higher Knudsen number conditions and with the Tye 2 slip conditions giving the best agreement.

For $Kn = 0.01$, the total drag predicted by CFD is still within 1% of that predicted by DSMC, for Mach 10, and within 2% for Mach 25, as shown in Table 4.6. The peak heating also differs by about 2% for all cases.

The total drag for the $Kn = 0.05$ case solutions are within 4% of the DSMC case, again with the Gökçen boundary condition showing the best agreement. While the no-slip case predicts a peak heat transfer rate about 9% higher than DSMC, the slip cases show better agreement, with the Gökçen case being within 5%.

For the most rarefied case considered, the peak heat transfer rates differ by as much as almost 30% for the no-slip case at Mach 25, but the Gökçen case shows the best agreement with just over 5% difference at Mach 10 and 8% difference at Mach 25.

4.3.5   Flow Properties Along a Line at $\Phi = 90°$

The solution temperatures (including the translational, rotational, and translational/rotational averaged temperature) are plotted along a line normal to the surface at an angle of 90° as shown in Figures 4.50 and 4.51. Note the increasing
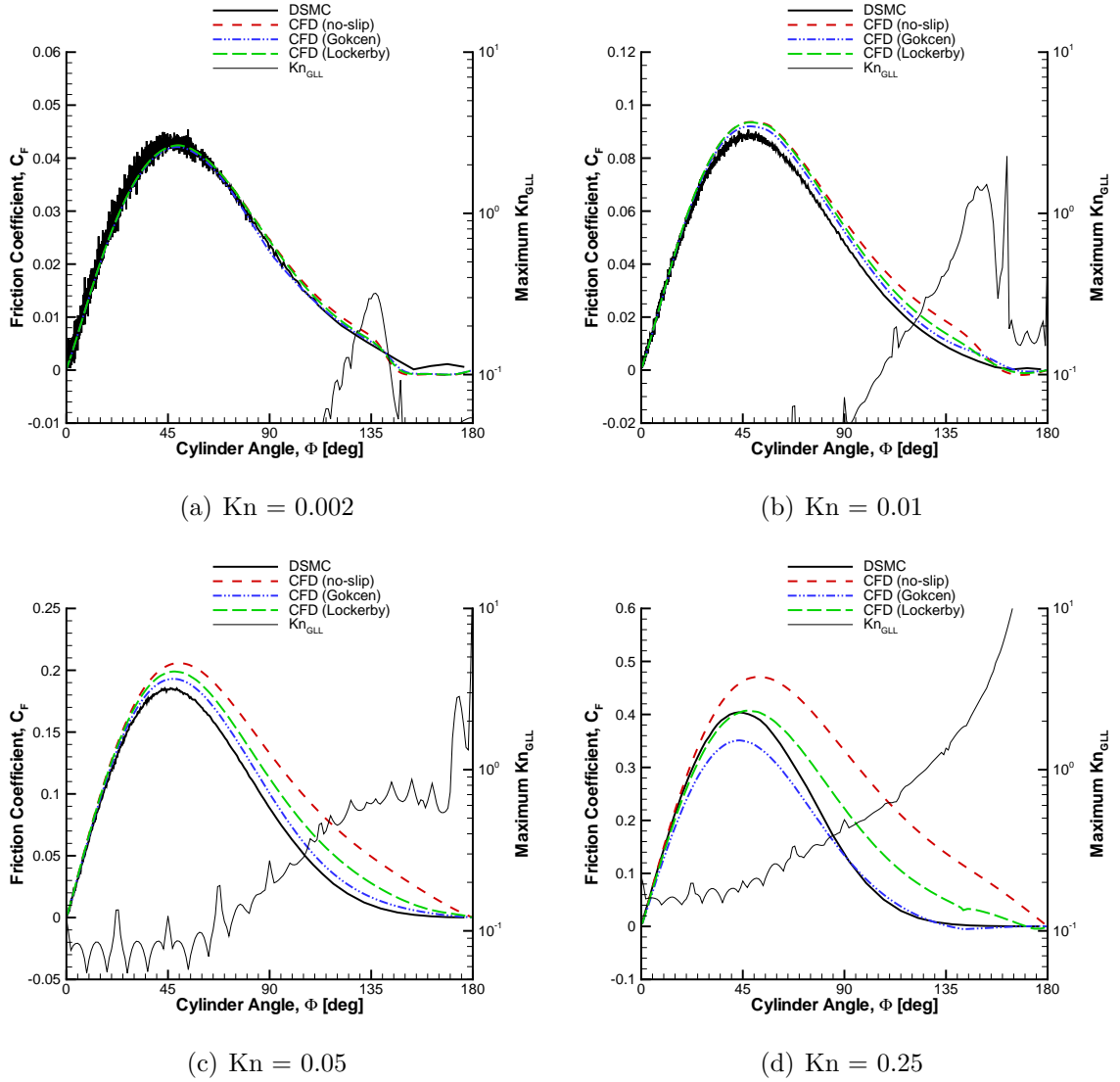
(a) Kn = 0.002

(b) Kn = 0.01

(c) Kn = 0.05

(d) Kn = 0.25

Figure 4.46: Surface friction coefficient for a Mach 10 flow of nitrogen about a cylinder. The maximum Kn_{GLL} near the surface is plotted on the right axis. Φ is the angle from the stagnation point.

(a) Kn = 0.002

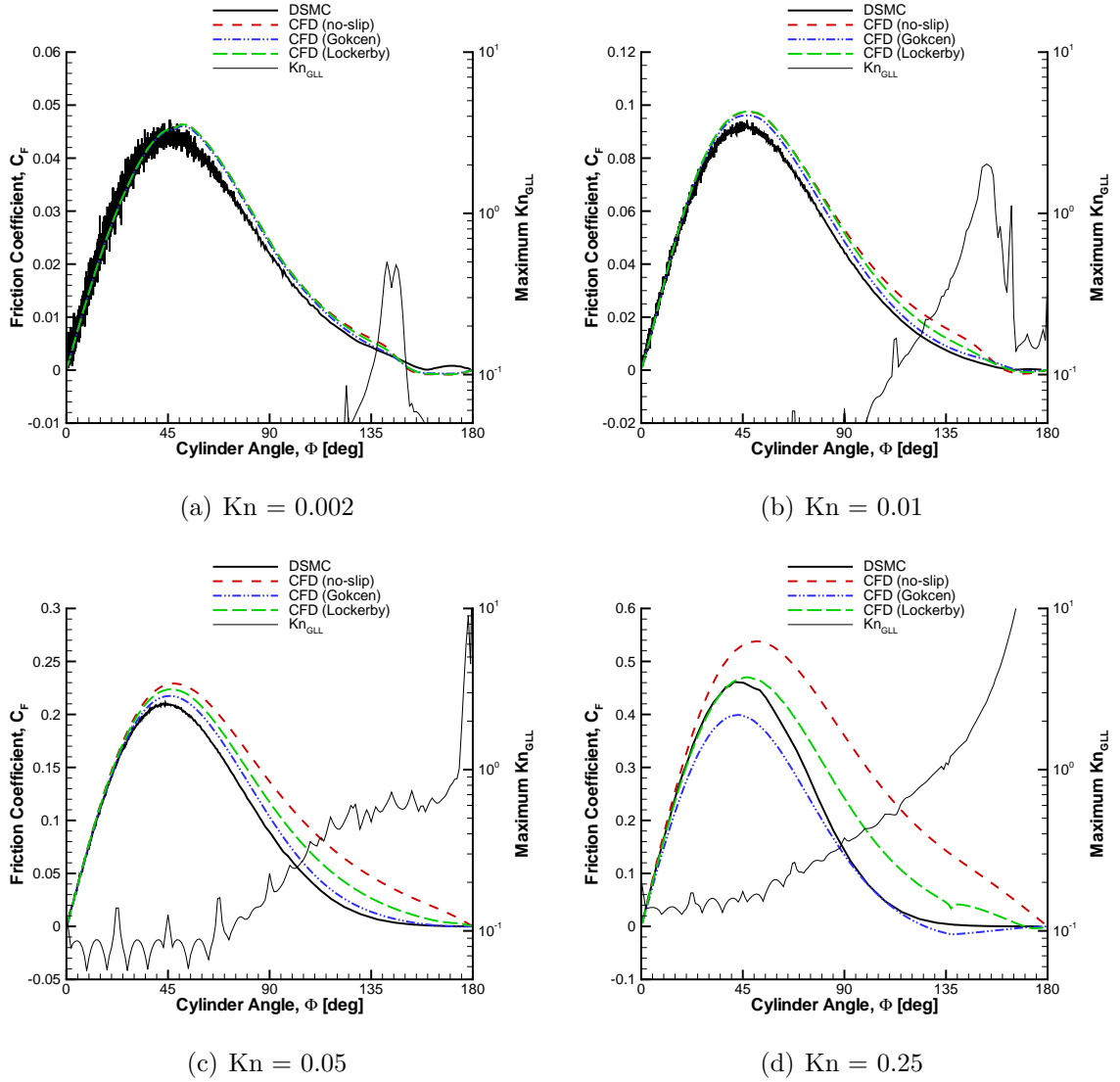(b) Kn = 0.01

(c) Kn = 0.05

(d) Kn = 0.25

Figure 4.47: Surface friction coefficient for a Mach 25 flow of nitrogen about a cylinder. The maximum Kn_{GLL} near the surface is plotted on the right axis. Φ is the angle from the stagnation point.

(a) Kn = 0.002

(b) Kn = 0.01

(c) Kn = 0.05

(d) Kn = 0.25

Figure 4.48: Surface heating coefficient for a Mach 10 flow of nitrogen about a cylinder. The maximum Kn_{GLL} near the surface is plotted on the right axis. Φ is the angle from the stagnation point.

(a) Kn = 0.002

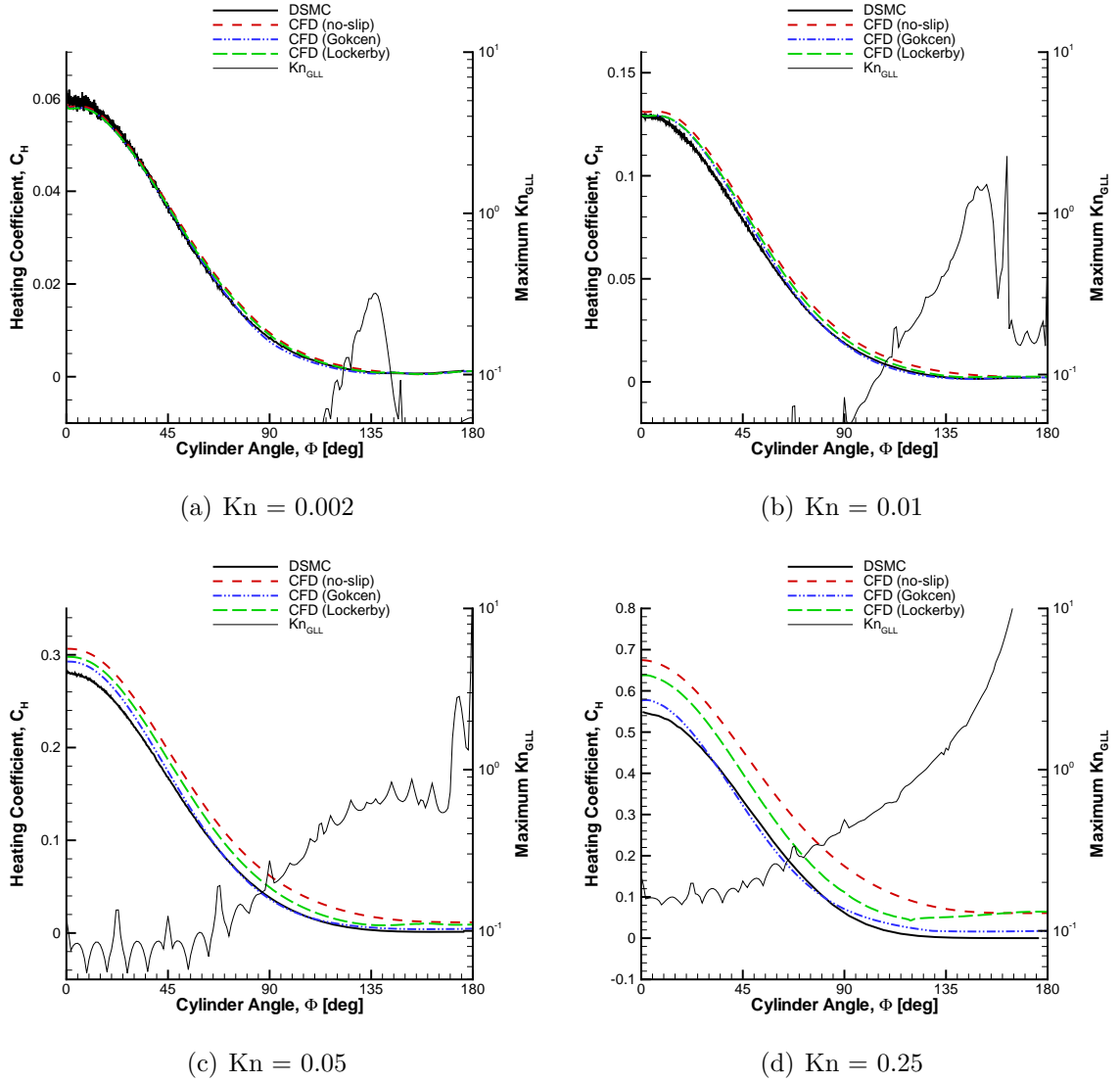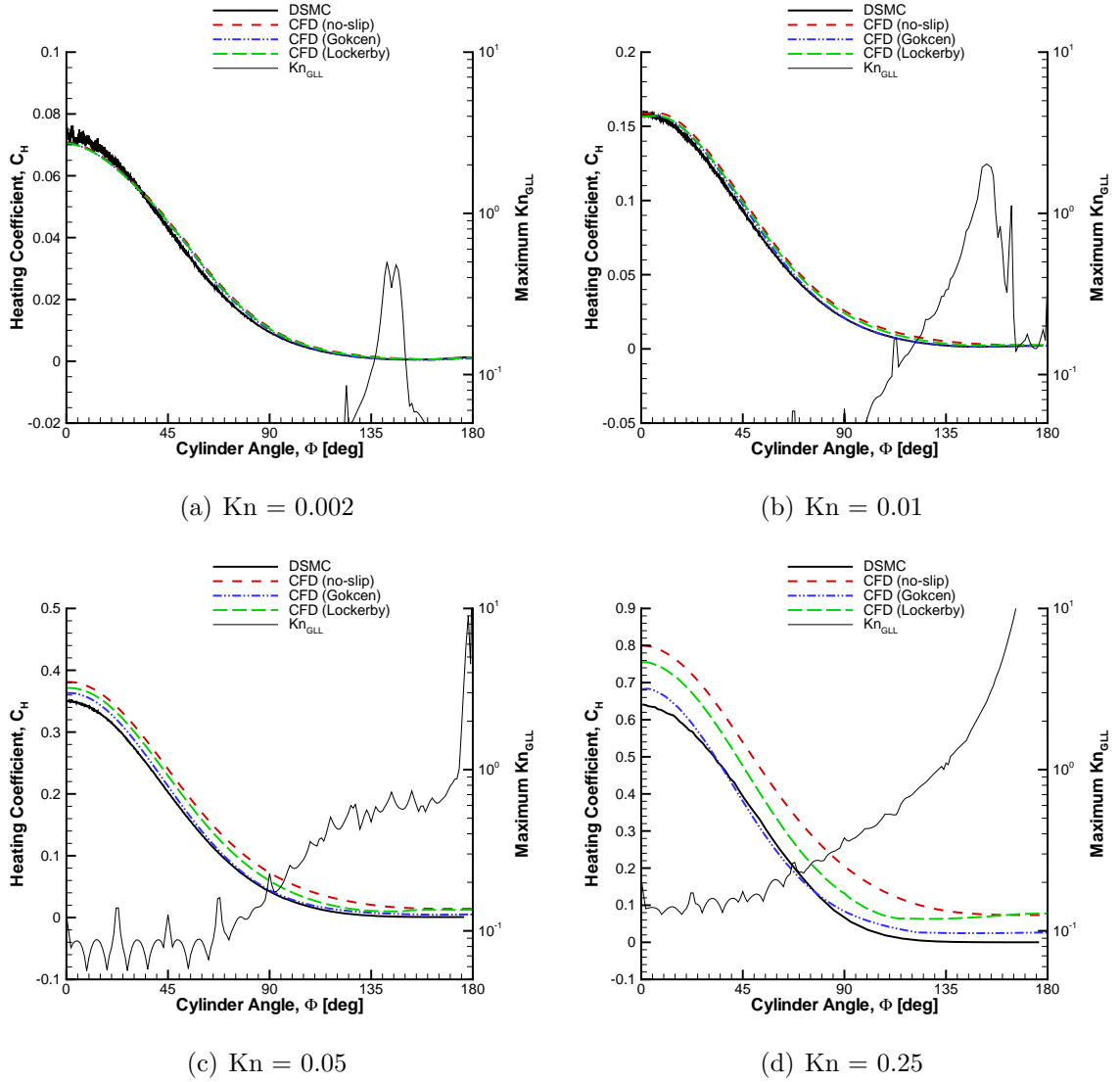(b) Kn = 0.01

(c) Kn = 0.05

(d) Kn = 0.25

Figure 4.49: Surface heating coefficient for a Mach 25 flow of nitrogen about a cylinder. The maximum Kn_{GLL} near the surface is plotted on the right axis. Φ is the angle from the stagnation point.

amount of nonequilibrium as quantified by values of Kn_{GLL} as the Knudsen number increases. Although there is some translational-rotational nonequilibrium, there is reasonable agreement between the Gökçen and Lockerby solutions and DSMC, with the Lockerby solutions being slightly better.

There is also good agreement between the CFD solutions and the DSMC solution for vibrational temperature, shown in Figures 4.52 and 4.53 for most of the cases. The Mach 10, $Kn = 0.25$ case shows good agreement between DSMC and the Gökçen CFD solution, and the Mach 25, $Kn = 0.25$ case shows a very large disagreement between DSMC and all of the CFD solutions. In this case, DSMC shows a significant amount of vibrational excitation away from the wall, while CFD predicts vibrational excitation only due to the wall boundary conditions.

Again, very similar trends are seen with the velocity magnitude, which is plotted along the same line in Figures 4.54 and 4.55. Here, the Gökçen and Lockerby solutions show reasonable agreement for most of the cases, with the Gökçen solution being better at $Kn = 0.25$.

4.3.6 Slip Quantities

The velocity slip for each nitrogen simulation is seen in Figures 4.56 and 4.57. Again, the results are very similar to those obtained for argon. Although there are some differences in the actual peak velocity slip values, the qualitative agreement is very good. Again, note that the Lockerby boundary conditions agree best with the DSMC data because of its use of the correct velocity slip at the wall rather than a fictitious slip, as discussed in Chapter III. Recall that the Gökçen solution was derived specifically to match the wall properties of shear stress and heat flux at the wall rather than to accurately predict the velocity slip and temperature jump at the
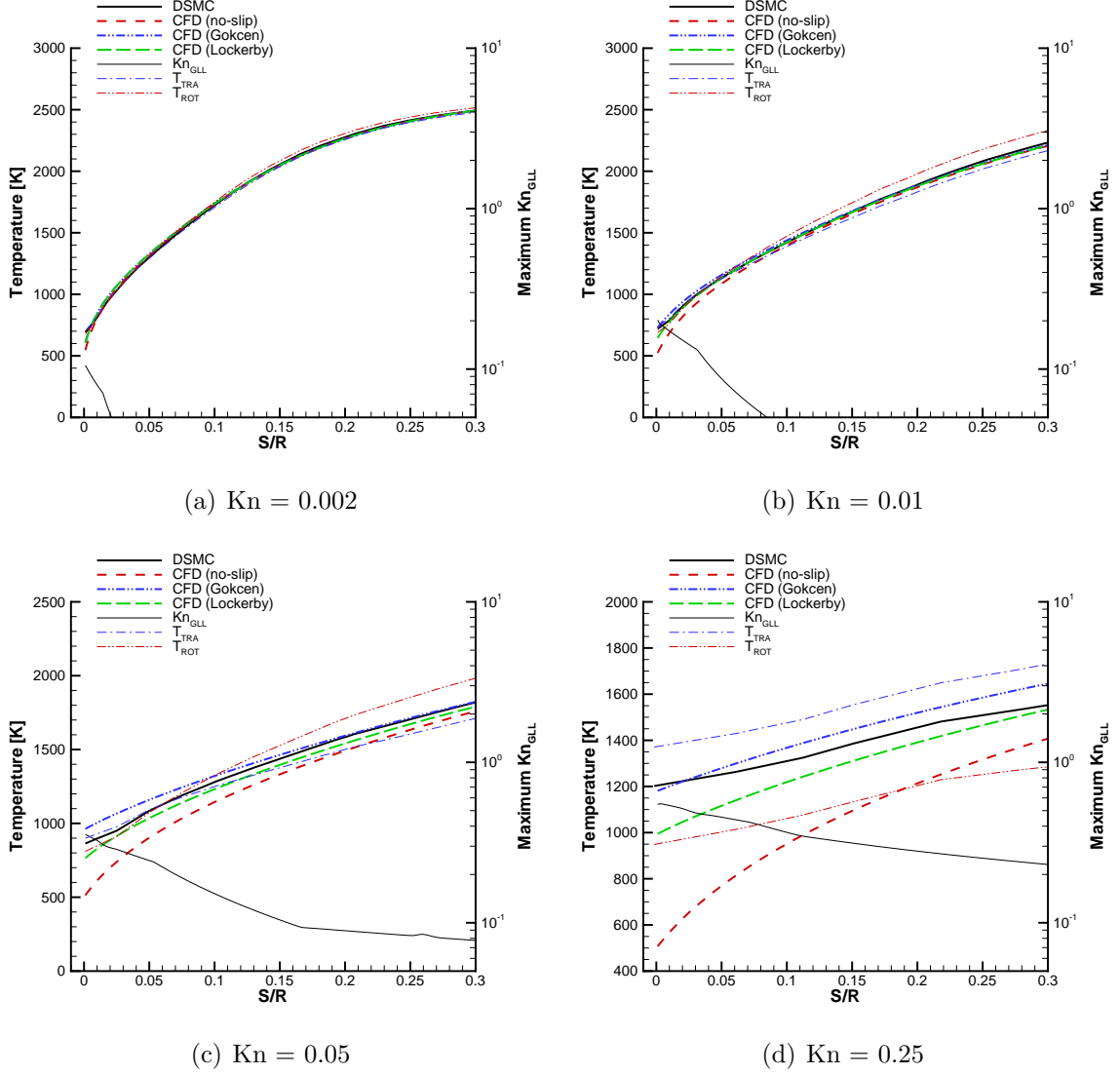
(a) Kn = 0.002

(b) Kn = 0.01

(c) Kn = 0.05

(d) Kn = 0.25

Figure 4.50: Translational/rotational temperatures along a line normal to the body surface at $\Phi = 90°$ for a Mach 10 flow of nitrogen about a cylinder. Distance is normalized by the cylinder radius and Φ is the angle from the stagnation point. The separate translational and rotational temperatures from the DSMC simulations are shown along with the weighted-average temperature. Note that the wall temperature (at $S/R = 0$) is 500 K.

(a) Kn = 0.002

(b) Kn = 0.01

(c) Kn = 0.05

(d) Kn = 0.25

Figure 4.51: Translational/rotational temperatures along a line normal to the body surface at $\Phi = 90°$ for a Mach 25 flow of nitrogen about a cylinder. Distance is normalized by the cylinder radius and Φ is the angle from the stagnation point. The separate translational and rotational temperatures from the DSMC simulations are shown along with the weighted average temperature. Note that the wall temperature (at $S/R = 0$) is 1500 K.
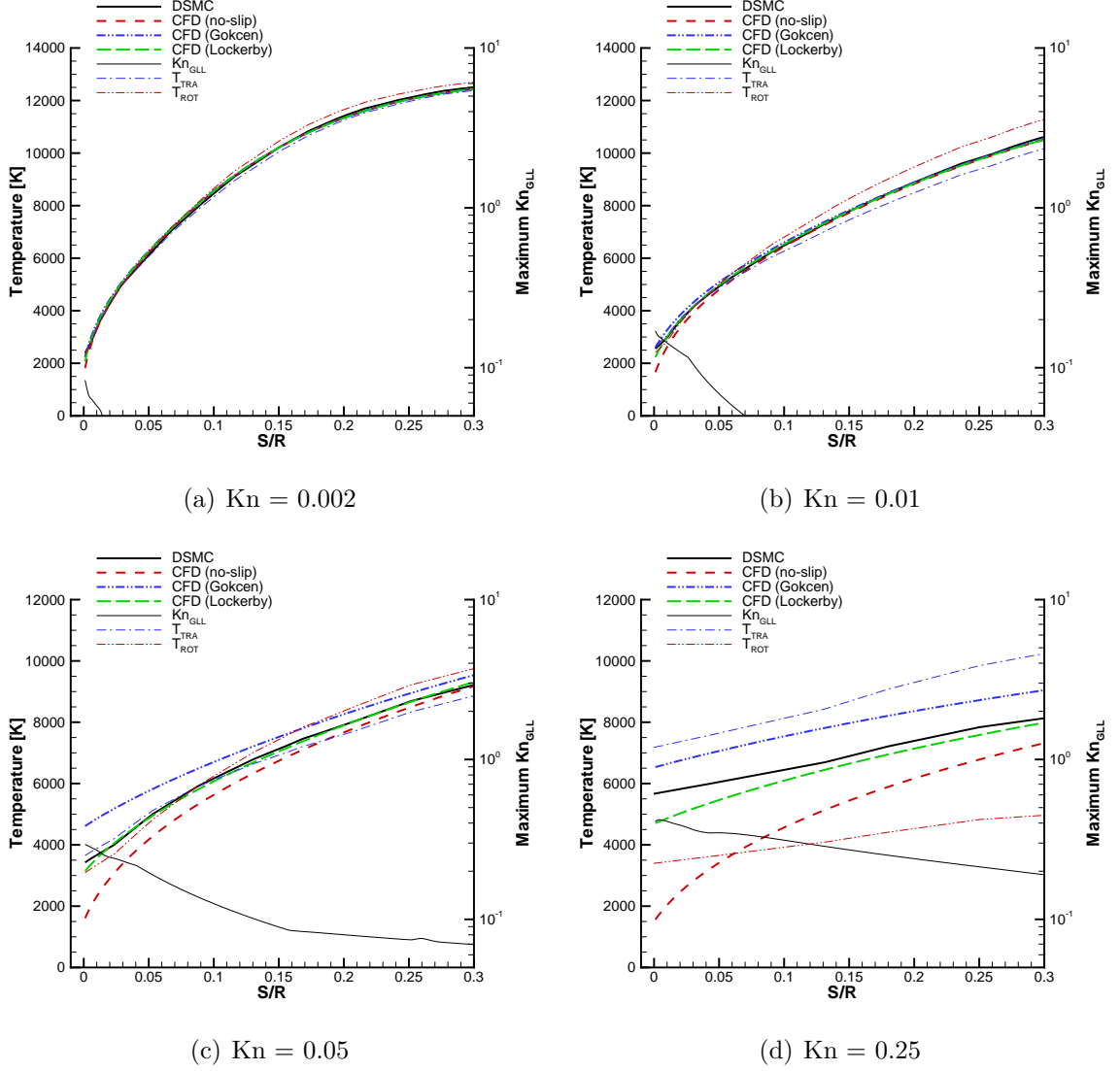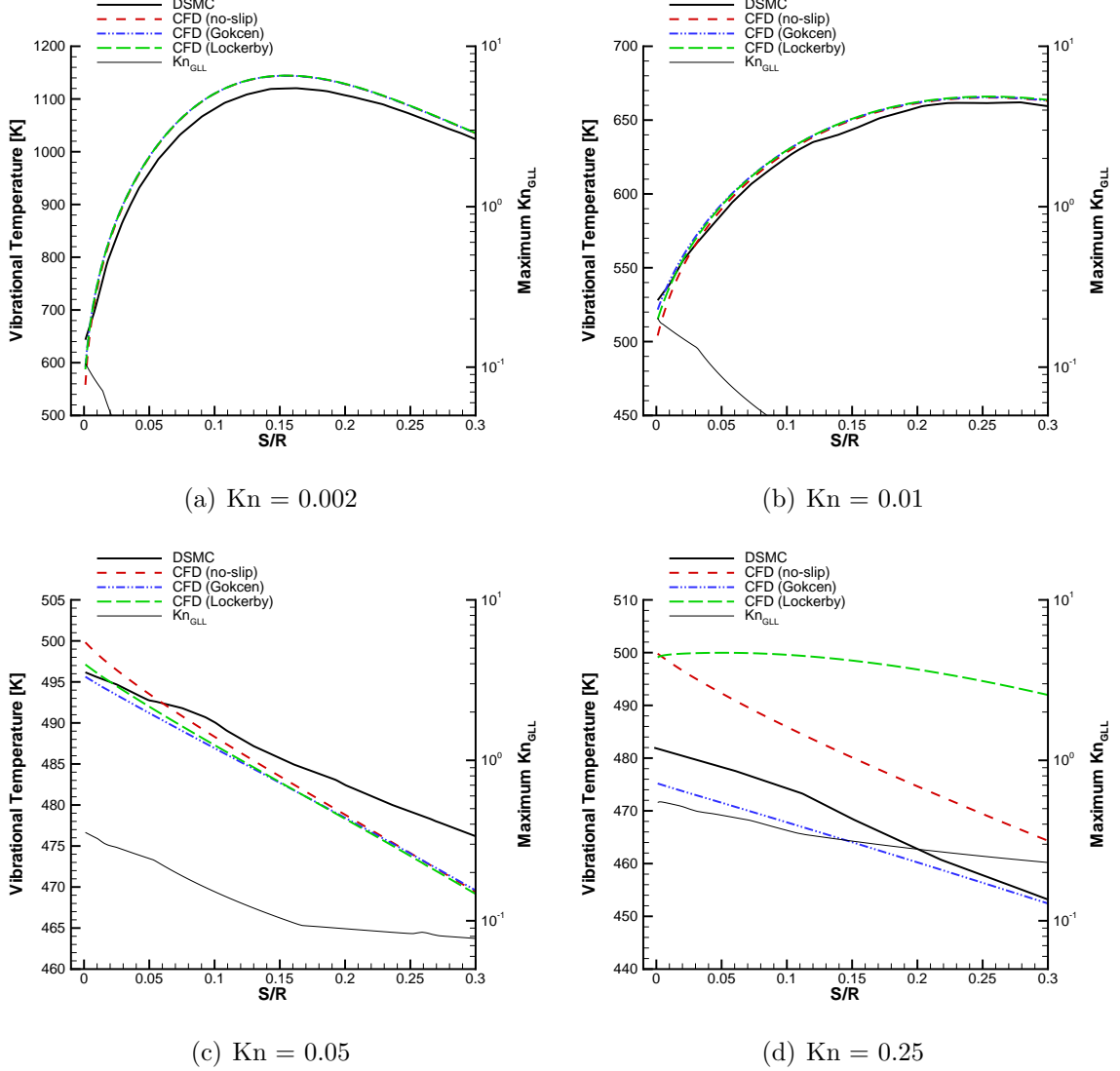
(a) Kn = 0.002

(b) Kn = 0.01

(c) Kn = 0.05

(d) Kn = 0.25

Figure 4.52: Vibrational temperature along a line normal to the body surface at $\Phi = 90°$ for a Mach 10 flow of nitrogen about a cylinder. Distance is normalized by the cylinder radius and Φ is the angle from the stagnation point. Vibrational temperature decreases away from the wall for the higher Knudsen number; vibrational activation is due only to the wall boundary conditions, where the vibrational temperature is 500 K.
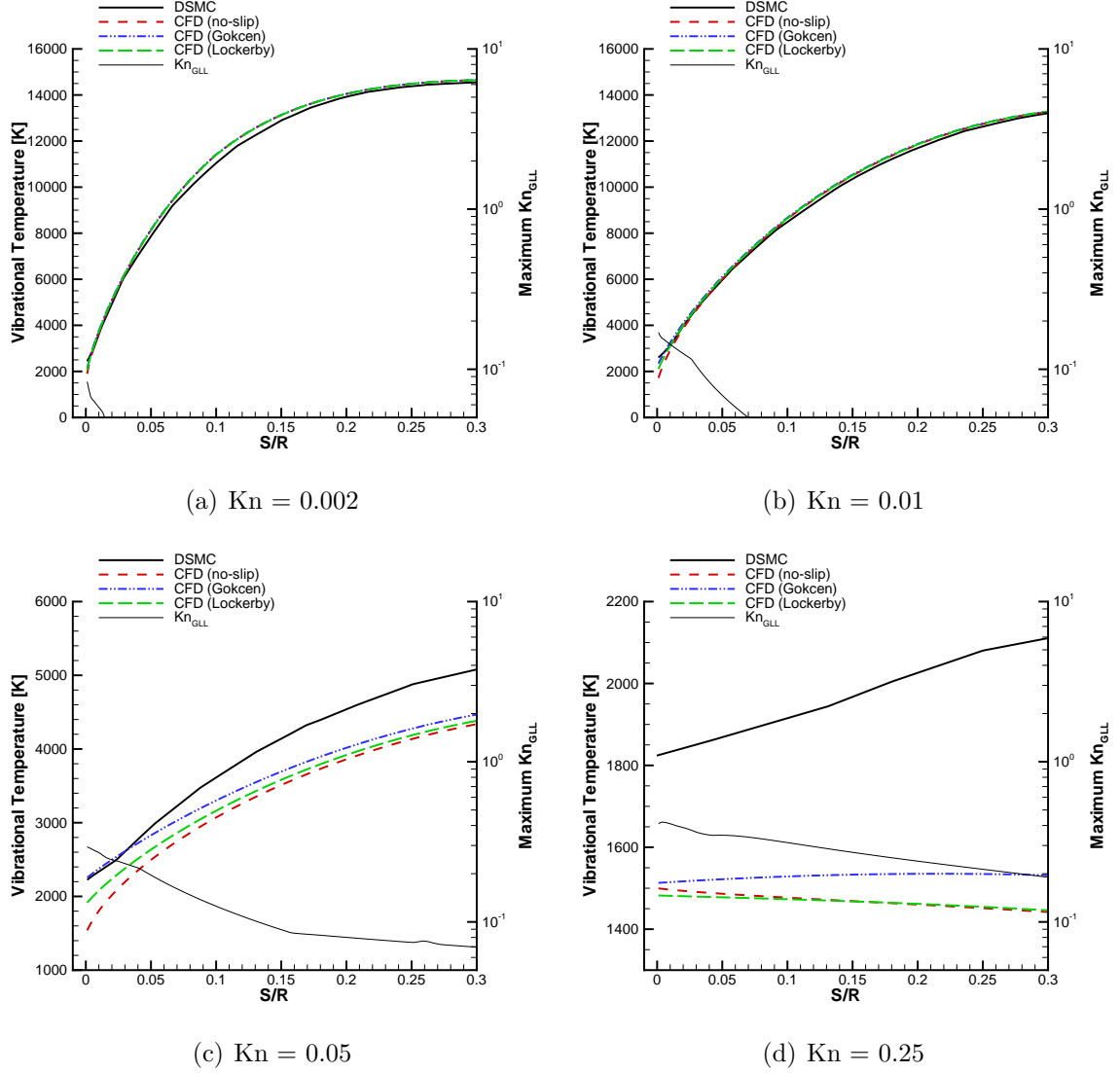
(a) Kn = 0.002

(b) Kn = 0.01

(c) Kn = 0.05

(d) Kn = 0.25

Figure 4.53: Vibrational temperature along a line normal to the body surface at $\Phi = 90°$ for a Mach 25 flow of nitrogen about a cylinder. Distance is normalized by the cylinder radius and Φ is the angle from the stagnation point. None of the CFD solutions agree well with DSMC at Kn = 0.25; the vibrational temperature away from the wall in the CFD cases are near the wall temperature of 1500 K, while DSMC predicts increased vibrational activation further from the wall.
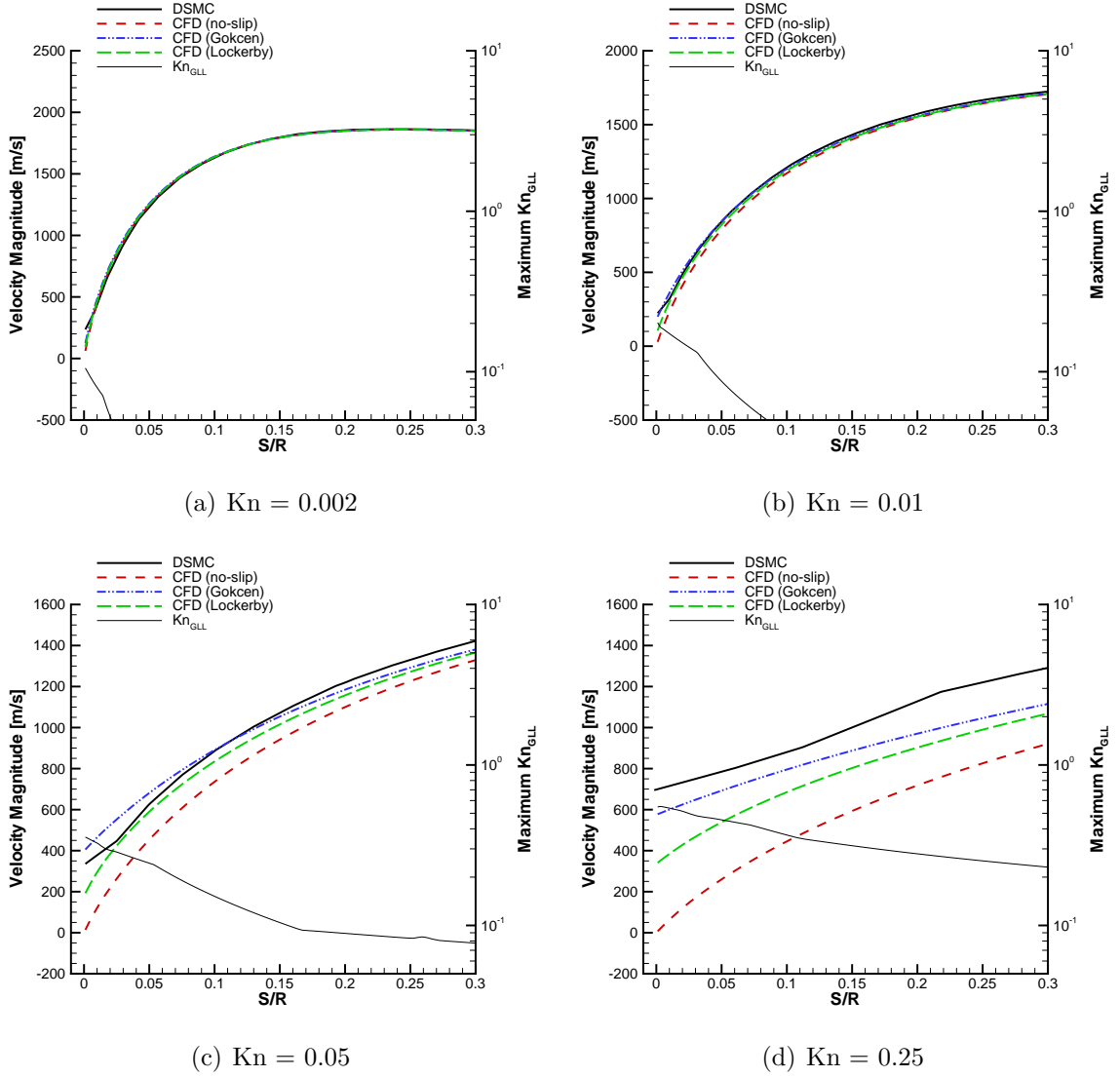
(a) Kn = 0.002

(b) Kn = 0.01

(c) Kn = 0.05

(d) Kn = 0.25

Figure 4.54: Velocity magnitude along a line normal to the body surface at $\Phi = 90°$ for a Mach 10 flow of nitrogen about a cylinder. Distance is normalized by the cylinder radius and Φ is the angle from the stagnation point. Note the non-zero velocity slip at the wall (at $S/R = 0$).
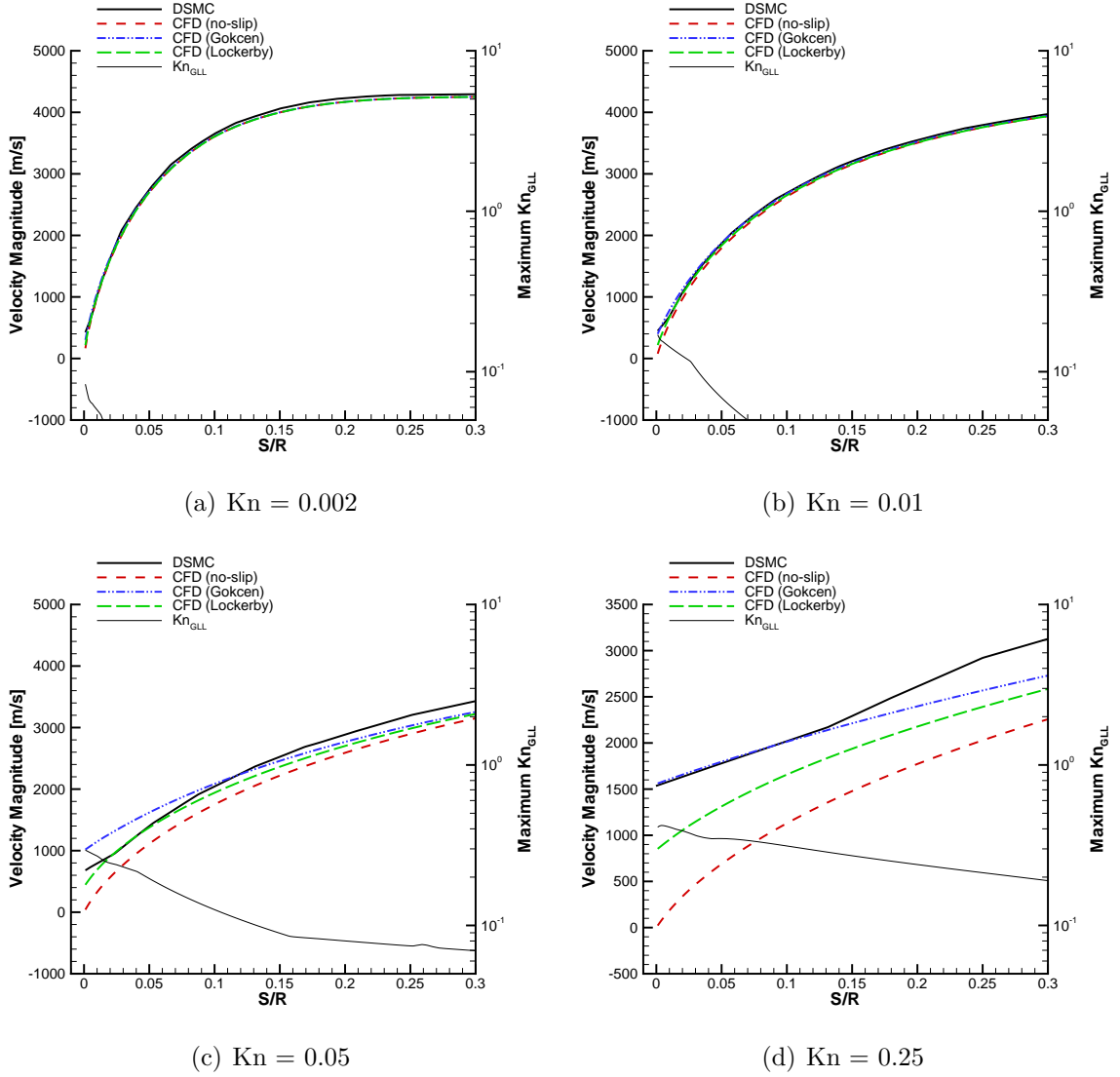
(a) Kn = 0.002

(b) Kn = 0.01

(c) Kn = 0.05

(d) Kn = 0.25

Figure 4.55: Velocity magnitude along a line normal to the body surface at $\Phi = 90°$ for a Mach 25 flow of nitrogen about a cylinder. Distance is normalized by the cylinder radius and Φ is the angle from the stagnation point. Note the non-zero velocity slip at the wall (at $S/R = 0$).

wall.

The temperature jump is plotted in Figures 4.58 and 4.59. Here, the DSMC translational/rotational averaged temperature jump is shown along with the actual translational and rotational temperature jumps (with the exception of the $Kn = 0.002$ case, for which the rotational temperature jump data is unavailable), and compared to the CFD temperature jump. It is interesting to note the amount of translational-rotational nonequilibrium present at the surface as seen in the differences between the translational and rotational temperature jumps. Again, there is fair agreement at the lower Knudsen numbers. The differences are very pronounced at the highest Knudsen numbers, with the Gökçen cases showing a nearly 500% difference at the stagnation point, and the Lockerby cases show the best agreement.

The vibrational temperature jump for each simulation (with the exception of the $Kn = 0.002$ case, for which the vibrational temperature jump is not available) is plotted in Figures 4.60 and 4.61. Qualitatively, the vibrational temperature jump curves look similar to the translational/rotational temperature jump curves.

For the Mach 10, $Kn = 0.01$ and $Kn = 0.05$ cases, there is reasonable agreement between CFD and DSMC, notwithstanding the statistical scatter present in the DSMC data. The large scatter is due to the small number of particles with a significant amount of vibrational energy, which is expected in a flow with the relatively low temperatures. For the Mach 10, $Kn = 0.25$ case, the Lockerby CFD case agrees well in the fore-body region, but predicts a positive vibrational temperature jump in the wake while DSMC predicts a negative vibrational temperature jump. Incidently, the negative vibrational temperature jump also supports the conclusion that the vibrational energy present in the flow at the most rarefied conditions is due to the wall boundary conditions.
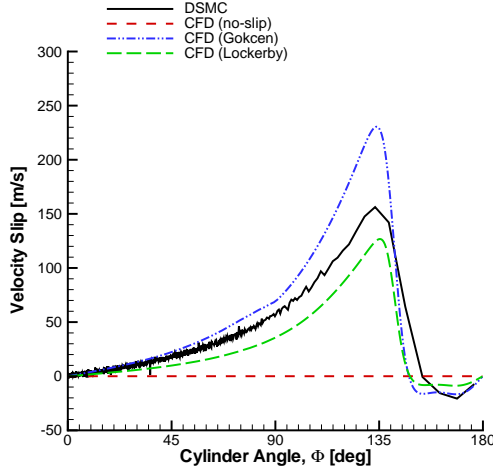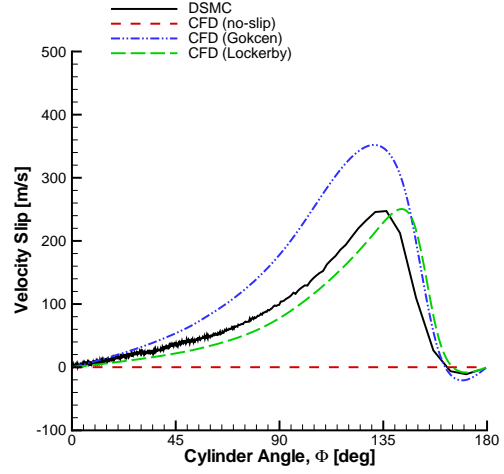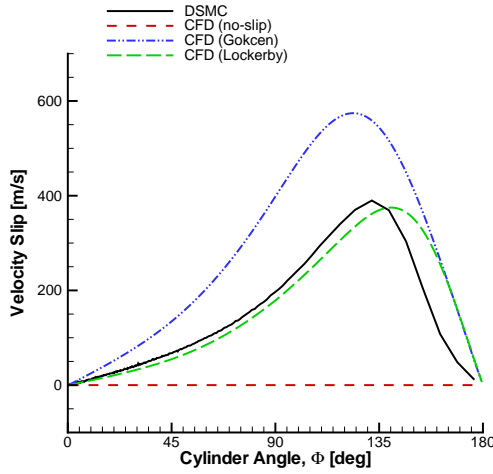
(a) Kn = 0.002

(b) Kn = 0.01

(c) Kn = 0.05

(d) Kn = 0.25

Figure 4.56: Velocity slip for a Mach 10 flow of nitrogen about a cylinder. Φ is the angle from the stagnation point.
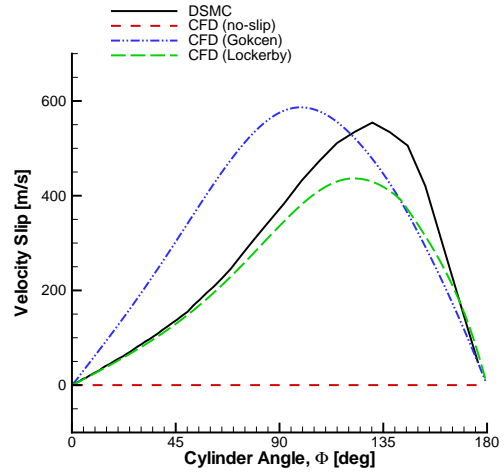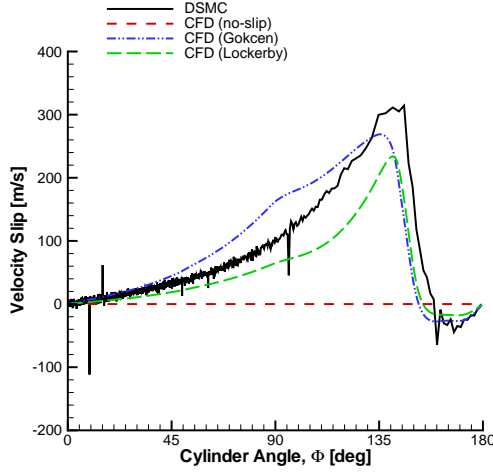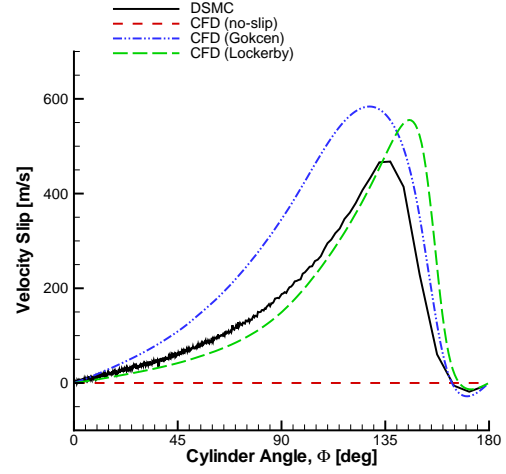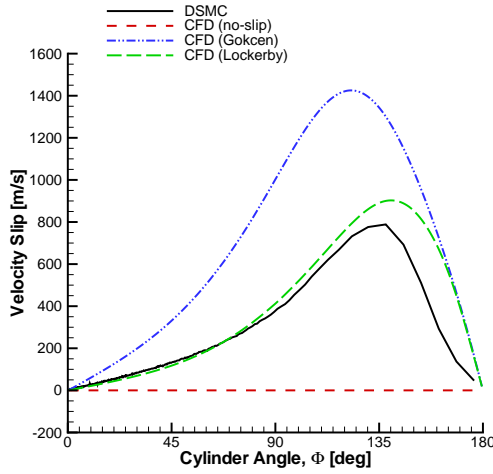
(a) Kn = 0.002

(b) Kn = 0.01

(c) Kn = 0.05

(d) Kn = 0.25

Figure 4.57: Velocity slip for a Mach 25 flow of nitrogen about a cylinder. Φ is the angle from the stagnation point.
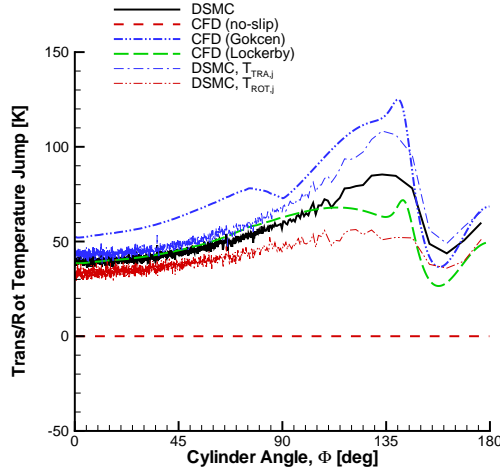
(a) Kn = 0.002

(b) Kn = 0.01

(c) Kn = 0.05
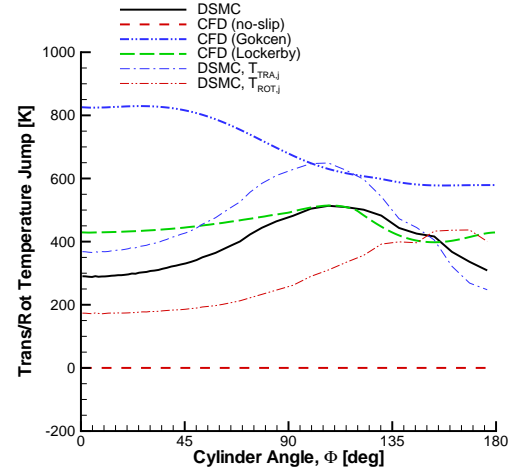
(d) Kn = 0.25

Figure 4.58: Translational/rotational temperature jump for a Mach 10 flow of nitrogen about a cylinder. Separate translational and rotational temperature jumps from DSMC are plotted as well as the average temperature jump. Φ is the angle from the stagnation point.
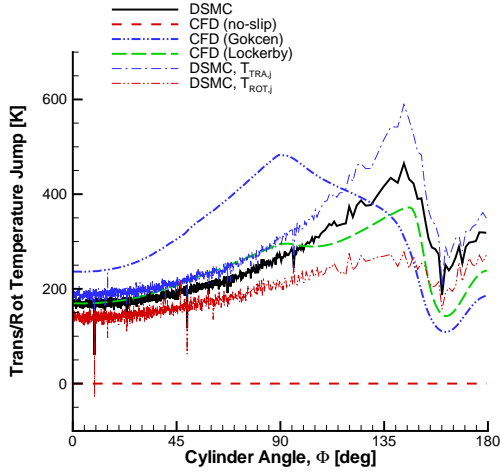
(a) Kn = 0.002
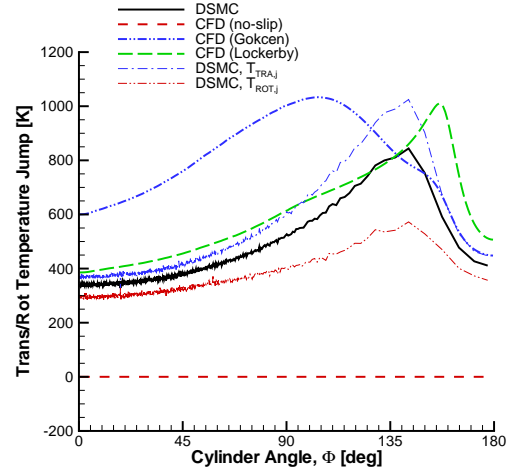
(b) Kn = 0.01
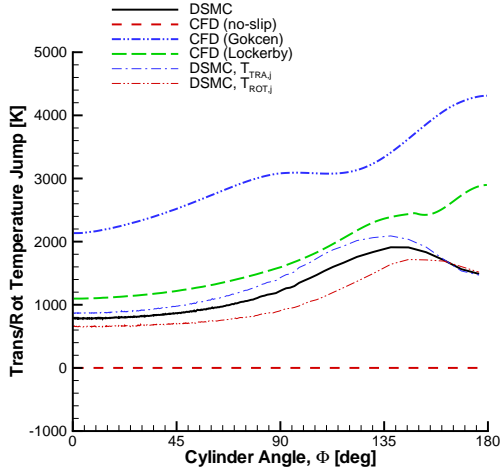
(c) Kn = 0.05
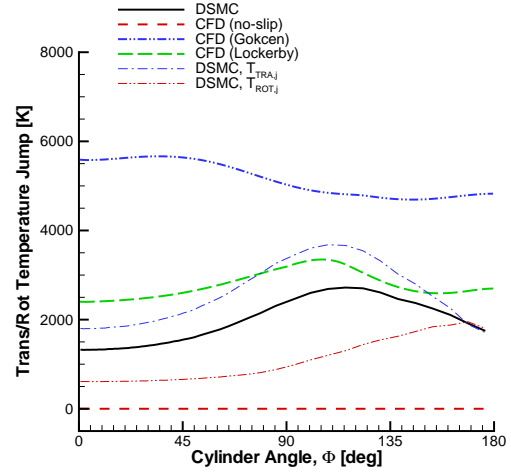
(d) Kn = 0.25

Figure 4.59: Translational/rotational temperature jump for a Mach 25 flow of nitrogen about a cylinder. Separate translational and rotational temperature jumps from DSMC are plotted as well as the average temperature jump. Φ is the angle from the stagnation point.

(a) Kn = 0.002

(b) Kn = 0.01
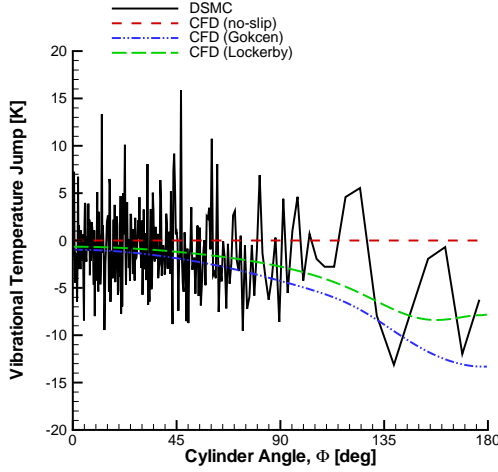
(c) Kn = 0.05
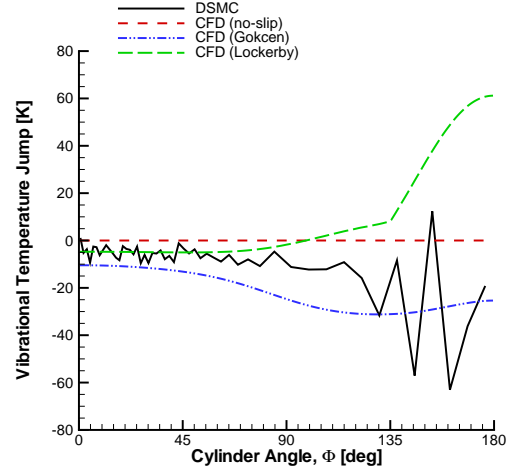
(d) Kn = 0.25

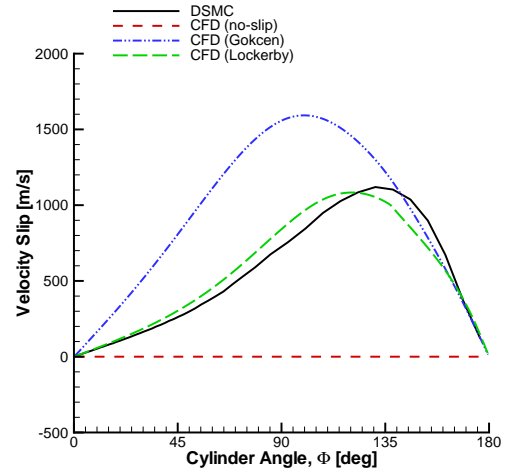Figure 4.60: Vibrational temperature jump for a Mach 10 flow of nitrogen about a cylinder. Φ is the angle from the stagnation point. There are statistical fluctuations in the DSMC data due to the low vibrational collision probability at the lower temperatures.
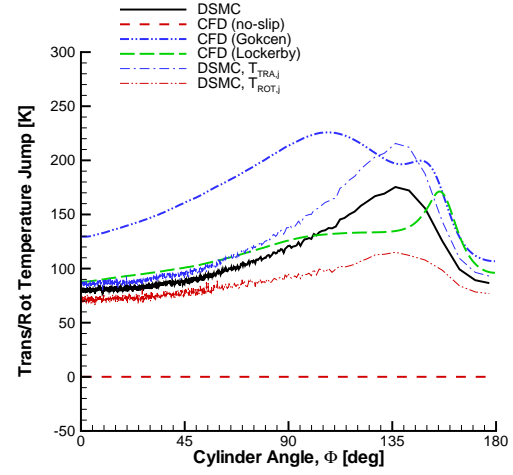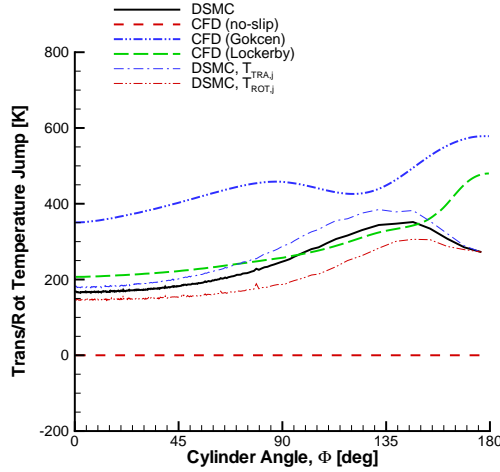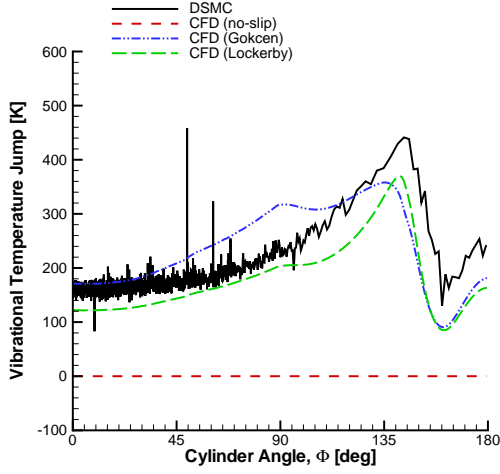
(a) Kn = 0.002
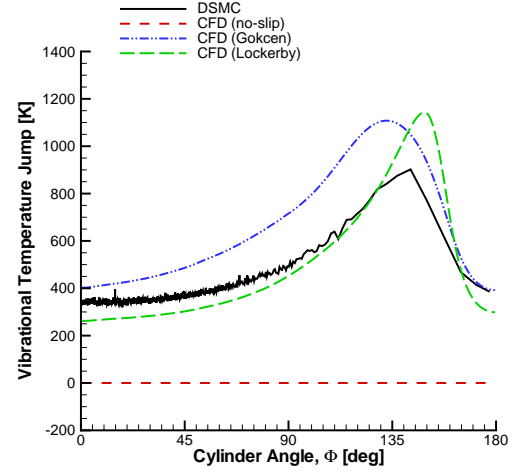
(b) Kn = 0.01
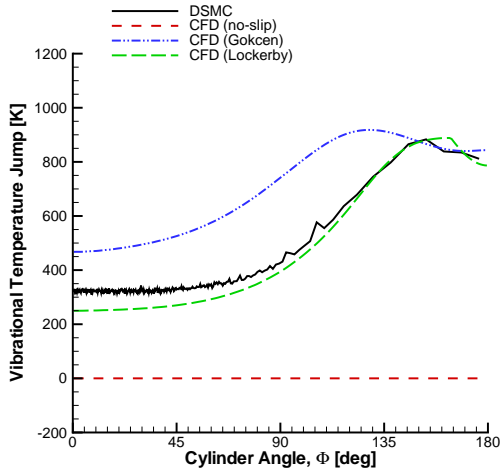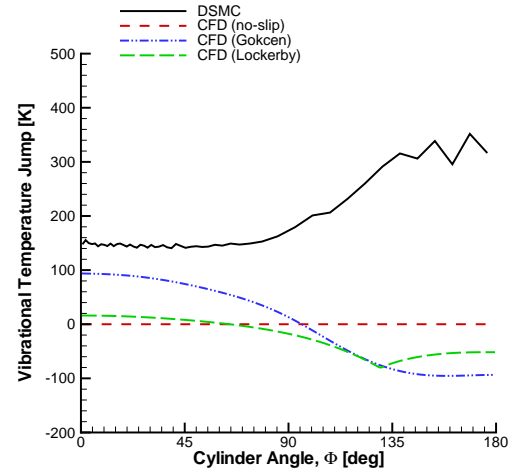
(c) Kn = 0.05

(d) Kn = 0.25

Figure 4.61: Vibrational temperature jump for a Mach 25 flow of nitrogen about a cylinder. Φ is the angle from the stagnation point.

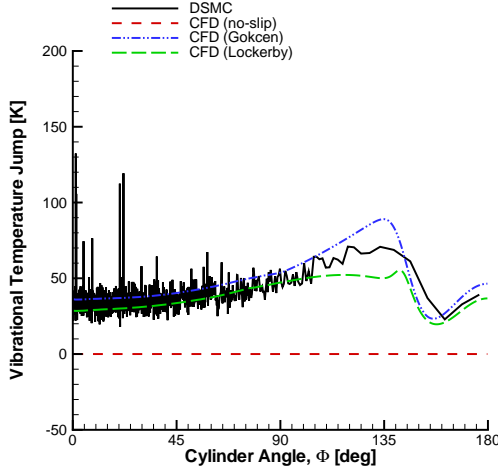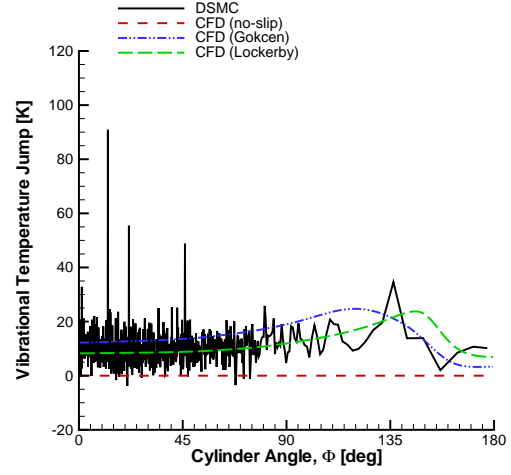The Mach 25, Kn = 0.01 and Kn = 0.05 cases also show very reasonable agreement between the simulations, with the Lockerby cases being very close to the DSMC solutions. However, neither of the CFD slip cases are able to accurately predict the vibrational temperature jump in the Kn = 0.25 case.

4.3.7   Computational Details

The computational details for the nitrogen simulations are given in Table 4.8.

4.4   Summary—Hypersonic Flow about a Cylinder

Comparison of CFD and DSMC results for the flow of argon about a cylinder show that the surface properties of pressure, shear stress and heat transfer rates are very similar for the lower Knudsen number flows where the continuum hypothesis is valid, as expected, while the results diverge in the higher Knudsen number cases. The surface pressure is least affected by continuum breakdown, as quantified by the gradient-length local Knudsen number, among those properties investigated, and seems to be affected only by continuum breakdown as the shock and boundary layer merge in the highest Knudsen number flows. The shear stress is most influenced by nonequilibrium effects. The addition of slip velocity and temperature jump boundary conditions greatly improve the agreement at higher Knudsen numbers. Several different types of slip boundary conditions are examined, and the best agreement for the surface properties is obtained when using the generalized slip conditions proposed by Gökçen [29]. With these boundary conditions, the differences in total drag and peak heat flux predicted by CFD and DSMC increase from less than 1% at $Kn_\infty = 0.002$ to around 5% at $Kn_\infty = 0.25$.

For the case of a simple gas, the higher velocities associated with a Mach 25 flow do not seem to increase the difference between the CFD and DSMC predictions.

Table 4.8: Computational details for a flow of nitrogen about a cylinder. Total CPU time is the wall time multiplied by the number of CPUs.

Mach 10

Kn_∞	DSMC				
	Cells	Particles	Time Steps	CPUs	Total CPU Time*[hours]
0.002	120,309	70.9×10^6	400,000	64	7,296
0.01	102,755	39.4×10^6	300,000	32	2,847
0.05	35,421	12.4×10^6	200,000	16	460
0.25	18,402	6.2×10^6	200,000	8	221
Kn_∞	CFD				
	Cells		Iterations	CPUs	Total CPU Time*[hours]
0.002	80,000		25,000	8	300
0.01	40,000		25,000	8	150
0.05	40,000		25,000	8	150
0.25	40,000		25,000	8	150

Mach 25

Kn_∞	DSMC				
	Cells	Particles	Time Steps	CPUs	Total CPU Time*[hours]
0.002	102,626	75.1×10^6	420,000	64	8,319
0.01	71,997	37.7×10^6	300,000	32	2,734
0.05	22,523	13.1×10^6	200,000	16	508
0.25	18,395	6.2×10^6	200,000	8	243
Kn_∞	CFD				
	Cells		Iterations	CPUs	Total CPU Time*[hours]
0.002	50,000		45,000	8	328
0.01	40,000		25,000	8	150
0.05	40,000		25,000	8	150
0.25	40,000		25,000	8	150

* Approximate

Although the extent of the region where the continuum breakdown parameter exceeds the critical value of 0.05 is larger at the higher Mach number, the predicted surface properties with the Gökçen slip boundary conditions still remain well under 5% for all but the $Kn_\infty = 0.25$ case, where the peak heat transfer rates and total drag predictions are within 6%.

The best agreement for the actual slip values is obtained with the Lockerby [49] slip conditions. While the Lockerby slip conditions attempt to predict the actual value of the velocity slip and temperature jump, the Maxwell slip conditions use a higher velocity slip at the wall in order to increase accuracy in flow properties further from the wall. The Gökçen slip conditions were derived to accurately predict the wall properties of shear stress and heat flux as the Knudsen number increases, rather than the actual slip values.

Although there is a significant amount of nonequilibrium between the different thermal modes (translational, rotational and vibrational) when considering a flow of nitrogen, the trends are largely similar to those noted when considering a simple gas with no internal degrees of freedom. The pressure and shear stress are least sensitive to the nonequilibrium effects, while the heat transfer rate is most sensitive. Total drag differences between CFD (with the best slip boundary conditions) and DSMC remain under 3%, while peak heat flux differences are less than 8%.

It is also shown that as the Knudsen number increases, the percentage of total drag due to friction forces (versus pressure) increases as well. Differences in drag due to skin friction also tend to be larger than differences in predicted drag due to pressure; thus the larger errors at the higher Knudsen numbers is due mostly to errors in skin friction prediction.

Differences in flow property prediction is generally concentrated in the Knudsen

layer, defined here as the region of the flow 10 mean free paths or less from the wall surface.

CHAPTER V

Hypersonic Flow about a Wedge

5.1 Introduction

The previous chapter considered the case of a hypersonic blunt body. This chapter now considers the flow about a wedge with a sharp leading-edge. The cylinder simulations exhibited a typical blunt-body hypersonic flow with an unattached shock, followed by a high-temperature, low velocity region termed the shock layer. Regions of high nonequilibrium were found in the shock, the boundary layer and the wake. A sharp leading-edge body, on the other hand, is characterized by an attached shock, and supersonic velocities throughout the flow (with the exception of the boundary layer). Regions of high nonequilibrium are expected near the leading-edge and in the boundary layer and wake.

The wedge considered here has a 10-deg half-angle; the height of the base is 12-inches, equivalent to the diameter of the cylinder previously considered.

The inflow boundary conditions are the same as those for the cylinder; that is, the inflow Mach numbers are 10 and 25, and the free stream density of the flow is varied such that several different regimes are considered, from the continuum through the transitional to the rarefied regime, as shown in Table 4.1. The global Knudsen number is calculated based on the wedge base height, again using the hard-sphere

model for the mean free-path.

The other relevant boundary conditions are also as shown in Table 4.2.

As with the cylinder, surface and flow field properties for this flow are presented from two different computational approaches. First, CFD results are obtained using the LeMANS code. Previous simulations showed that the Gökçen slip conditions [29] gives the best agreement with DSMC; therefore, this chapter will present only CFD simulations computed using the Gökçen boundary conditions.

As with the cylinder, a mesh-independence study is conducted in each case to determine the final mesh resolution used. For the cylinder it was determined that the wall-normal spacing had the most effect on mesh-independence of the surface properties. For the wedge, mesh refined near the leading edge in the wall-parallel direction also has a large effect on the surface properties, due to the large gradients in that area. For the wedge, in addition to the wall-normal mesh refinement, the number of nodes near the leading edge is successively doubled. A mesh-independent solution is defined as one for which the total drag and peak heat transfer rate change by 1% or less when using the more refined mesh.

Second, DSMC results are provided from the MONACO code for the same flow conditions. Again, the mesh used for the final solution is adapted such that the cell sizes are on the order of one mean free path or smaller, with the exceptions of the $Kn = 0.002$ and $Kn = 0.01$ cases (where the subcell method is used to select particles for collisions to ensure physical accuracy [4]). The flow near the leading-edge exhibits an extremely high amount of nonequilibrium. Thus, the mesh around the leading-edge in each case is adapted such that the cell size is about 10-40% of a mean free path in order to sufficiently resolve the flow details. Example meshes for both DSMC and CFD for the different flow regimes are shown in Figure 5.1. In the
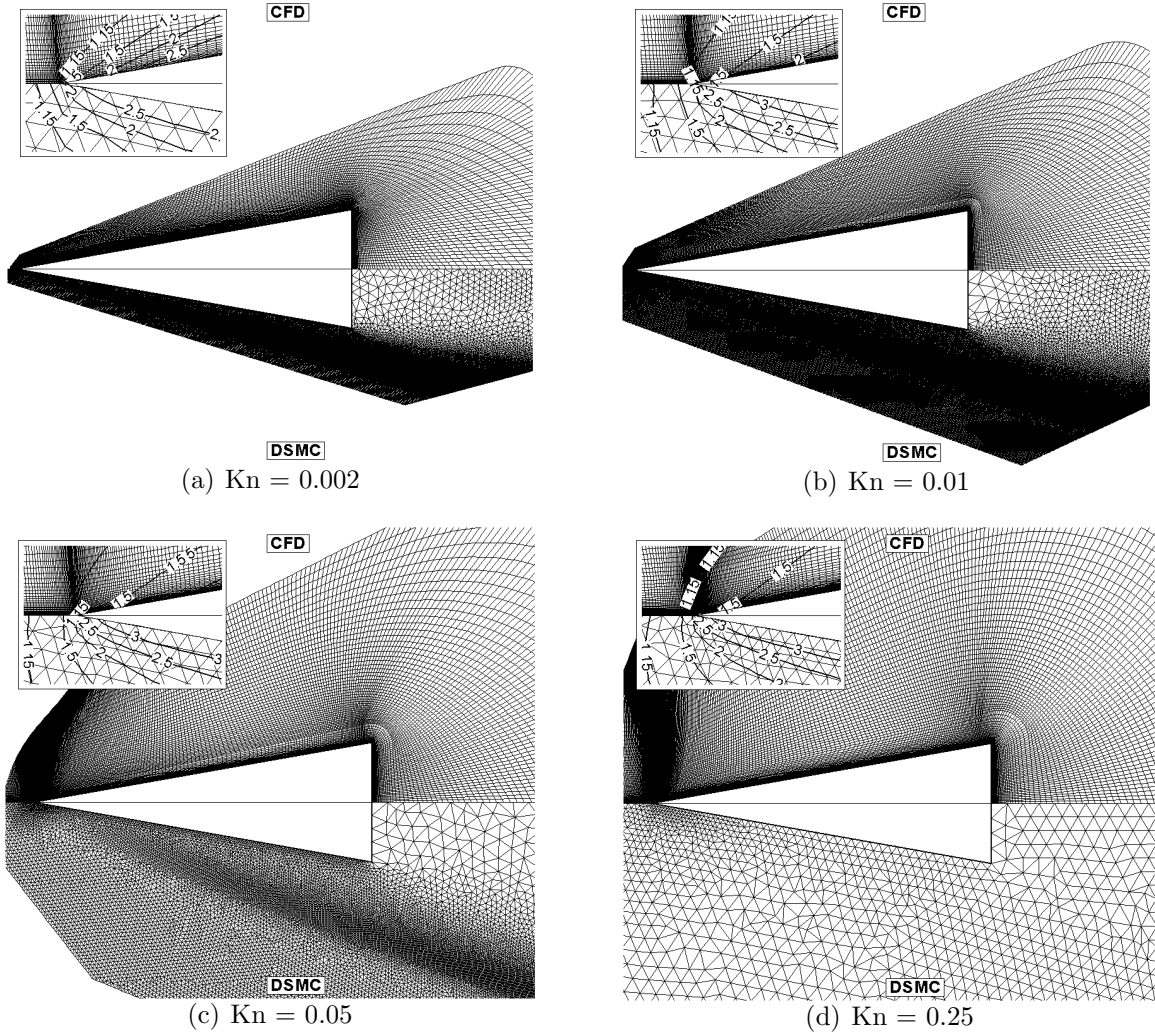
Figure 5.1: Example meshes for DSMC and CFD for the flow about a wedge. In the inset, density ratio contours are plotted with the mesh, giving an idea of the mesh resolution across the shock.

inset plots, density ratio contours are plotted with the mesh in a detailed view of the leading edge, giving an idea of the mesh resolution across the shock.

As before, the DSMC solutions are assumed to be the more correct solutions.

In the results that follow, the surface properties are presented in terms of non-dimensional coefficients, as defines in Eqs. 4.2 - 4.4. The surface properties in each case are plotted as a function of the distance, S, along the wedge surface, normalized by the length, L, of the top surface. Thus, $S/L = 1$ is the location of the wedge

Table 5.1: Total drag for flow of argon about a wedge.

Kn$_\infty$	Mach 10			Mach 25		
	Drag/Length [N/m] (% Difference)					
	DSMC	CFD		DSMC	CFD	
0.002	38.89	39.42	(1.4%)	252.3	257.2	(1.9%)
0.01	13.66	14.22	(4.1%)	92.74	99.86	(7.7%)
0.05	5.091	5.639	(10.8%)	34.39	40.13	(16.7%)
0.25	1.709	2.051	(20.0%)	10.35	13.91	(34.4%)

shoulder and the beginning of the wake of the flow.

Along with the surface properties, the maximum value of Kn$_{\mathrm{GLL}}$ at the surface (based on the CFD solution) is plotted in each case.

5.2 Argon

The flow of argon about the wedge is considered first. Table 5.1 summarizes the total drag predicted by CFD and DSMC. There is reasonable agrement at the lowest Knudsen number, with less than 2% difference for both Mach 10 and Mach 25. However, as the flow becomes more rarefied, the differences increase, with the maximum differences of 20% for Mach 10 and over 34% for Mach 25 seen for the Kn = 0.25 cases.

Figure 5.2 illustrates the percentage of total drag due to pressure and friction forces, for both DSMC and CFD. It is significant to note that as the Knudsen number increases, the percentage of total drag due to friction increases from about 50% at Kn = 0.002 to over 80% at Kn = 0.25 for Mach 10. For Mach 25, an even larger portion of the total drag is due to friction forces—nearly 60% at Kn = 0.002 to almost 90% at Kn = 0.25. This is contrasted with the cylinder in the previous chapter where friction forces accounted for, at most, 20% of the total drag (at Kn = 0.25); the vast
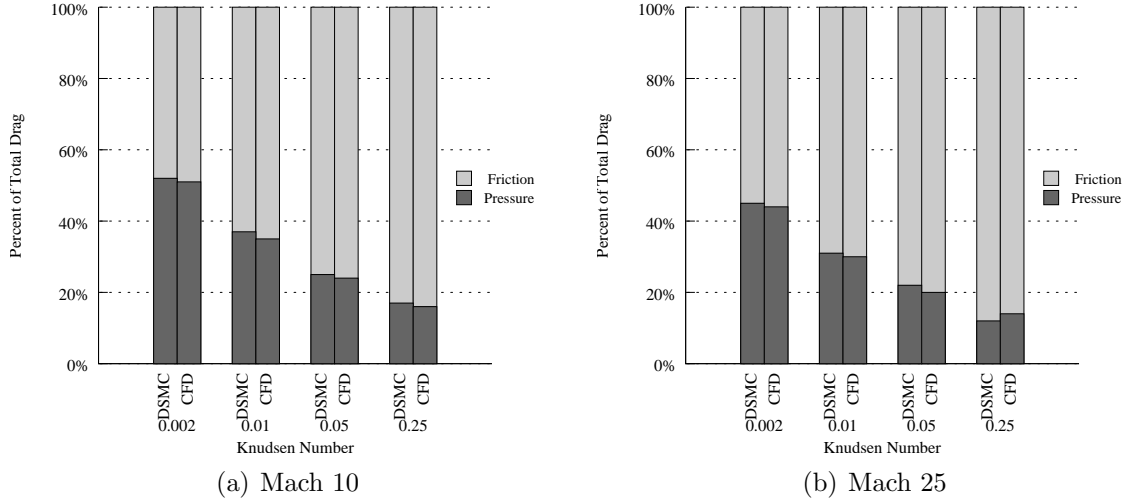
Figure 5.2: Percentage of total drag due to pressure and friction for flow of argon about a wedge. In contrast to the cylinder cases, here friction forces account for most of the drag.

majority of the drag was due to pressure forces. It is also significant to note, as shown in Figure 5.3, that the difference in predicted total drag between CFD and DSMC is due mostly to the differences predicted in the friction forces, as was also the case with the cylinder.

In all cases, CFD overpredicts the total drag. Although these CFD simulations make use of the Gökçen slip conditions (which gave very reasonable results for total drag in the case of the cylinder), the differences in total drag predictions here are similar in magnitude to the disagreement produced when using the no-slip boundary conditions in the case of the cylinder. This increased disagreement for the wedge is simply due to the fact that a larger percentage of the total drag is due to friction forces, and the shear stress is more sensitive to continuum breakdown due to rarefaction than is pressure; hence there is more disagreement in the total drag predictions for the wedge than there was for the cylinder.

The peak heat transfer rate predicted by CFD and DSMC is summarized in Table 5.2, and the differences are shown graphically in Figure 5.4. Here the differences
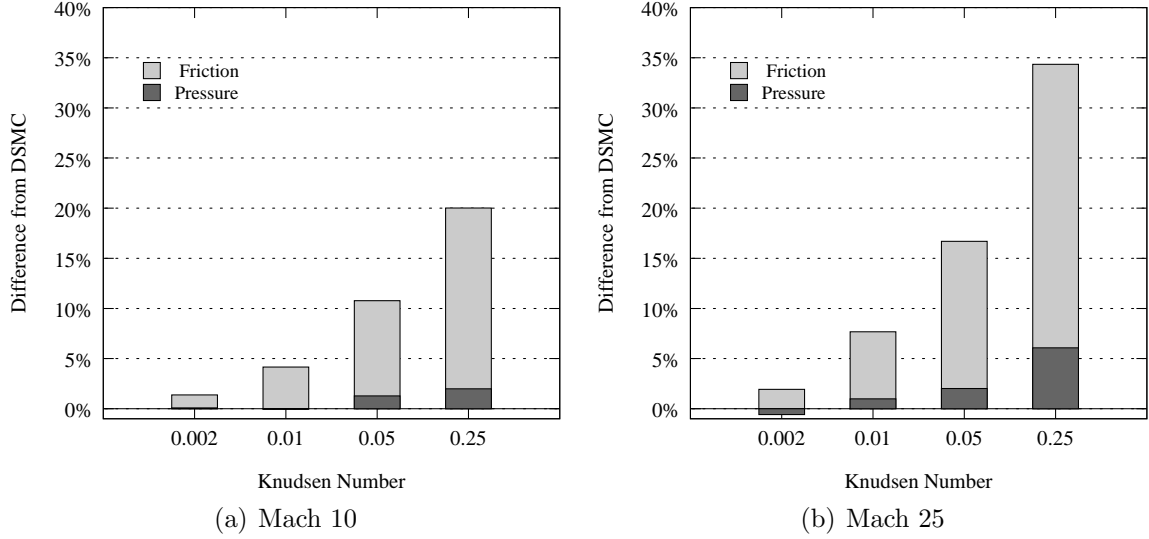
Figure 5.3: Total drag difference from DSMC predicted by CFD for flow of argon about a wedge.

between CFD and DSMC for all but the most rarefied cases are near 70%. It will be shown below that for the Kn = 0.25 cases the peak heating is predicted by CFD to occur at the shoulder of the wedge rather than at the leading edge for these cases— the differences in peak heating at the leading edge is 100%. In all cases, CFD also underpredicts the maximum heat flux. These differences are significantly larger than were seen with the cylinder, and this is the most striking difference between surface predictions of a blunt body compared with those of a sharp-leading edge body. It will also be shown below that DSMC predicts a very high temperature region at the leading edge in all cases; CFD is unable to match these flow conditions due to the large effects of nonequilibrium present near the leading edge.

5.2.1 Continuum Breakdown

As before, the breakdown parameter is calculated using both the CFD and the DSMC solutions according to Equation 3.26. For the case of a wedge in a hypersonic flow of a simple gas, breakdown of the continuum hypothesis is expected in regions of

Table 5.2: Peak heat transfer rate for flow of argon about a wedge. The large differences between CFD and DSMC are due to the failure of CFD to predict the high temperatures at the leading edge.

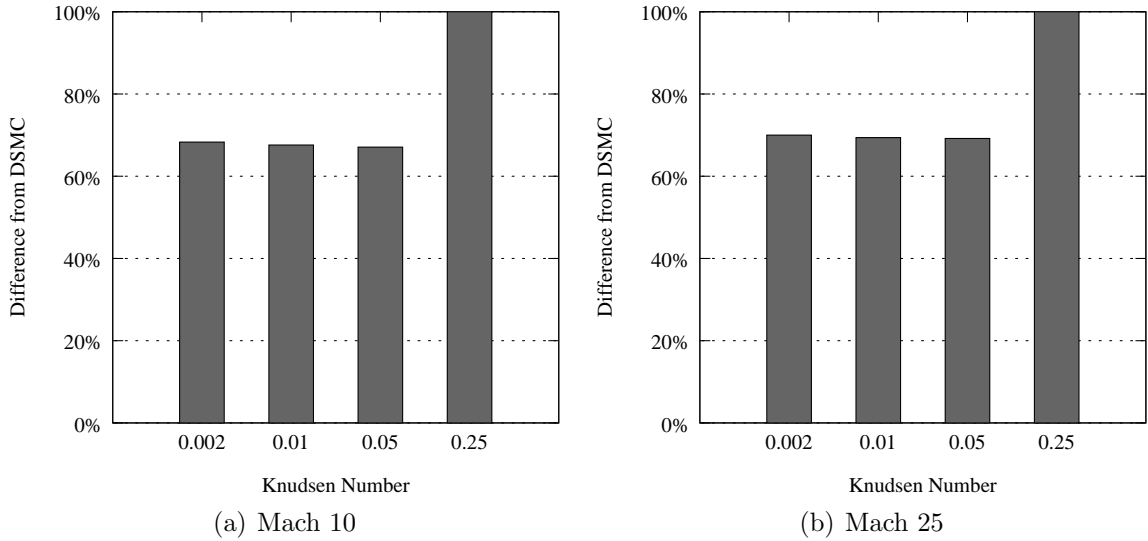| Kn_∞	Mach 10			Mach 25		
	Peak Heating [kW/m^2] (% Difference)					
	DSMC	CFD		DSMC	CFD	
0.002	239.5	76.03	(-68.3%)	3807.	1143.	(-70.0%)
0.01	47.48	15.38	(-67.6%)	754.2	231.1	(-69.4%)
0.05	9.451	3.109	(-67.1%)	151.0	46.50	(-69.2%)
0.25	1.902	1.247	(-100.0%)	31.76	26.04	(-100.0%)

(a) Mach 10   (b) Mach 25

Figure 5.4: Peak heat transfer rate difference from DSMC predicted by CFD for flow of argon about a wedge. The large differences in peak heating are due to the failure of CFD to predict the high temperatures at the leading edge.

high gradients (such as the shock and boundary layer, and especially near the leading edge) and in regions of rarefaction (such as the wake). The amount of continuum breakdown is again expected to increase as the gas flow becomes more rarefied.

The maximum Kn_{GLL} for each case is plotted in Figures 5.5 and 5.6. The detail of the flow near the leading-edge is shown in the inset. In these figures, the maximum gradient length local Knudsen number is computed from the DSMC (top) and CFD (bottom) solutions. The light gray regions correspond to $Kn_{GLL} < 0.05$, dark gray regions correspond to $Kn_{GLL} < 1.0$, and black regions correspond to $Kn_{GLL} > 1.0$. Notice that the minimum value of Kn_{GLL} for the black regions is an order of magnitude greater than those shown for the cylinder; therefore, the amount of nonequilibrium represented by the black portions in Figures 5.5 and 5.6 is much greater than in those regions represented by black in Figures 4.6 and 4.7.

For the Kn = 0.002 cases, there is a significant amount of nonequilibrium (as quantified by a breakdown parameter value exceeding 0.05, and represented by dark gray) present in the shock, the boundary layer and the wake. The size of this region of nonequilibrium grows as the flow becomes rarefied, until it encompasses nearly the entire computational domain at Kn = 0.25. This is very similar to what was seen in the flow around the cylinder. Note, however, the large amount of nonequilibrium near the leading-edge, as shown in the inset of Figures 5.5 and 5.6, and near the shoulder of the wedge as the flow expands into the wake. As the flow becomes more rarefied, these regions of severe nonequilibrium grow larger. It will be seen below that the region of high nonequilibrium near the leading-edge has a much more significant impact on the surface property predictions, even for the cases that are within the continuum regime, than does the wake region.

Figure 5.5: Kn_{GLL} field for a Mach 10 flow of argon about a wedge. The light gray regions correspond to $Kn_{GLL} < 0.05$, dark gray regions correspond to $Kn_{GLL} < 1.0$, and black regions correspond to $Kn_{GLL} > 1.0$. Note that the minimum value of Kn_{GLL} for the black regions is an order of magnitude greater than those for the cylinder
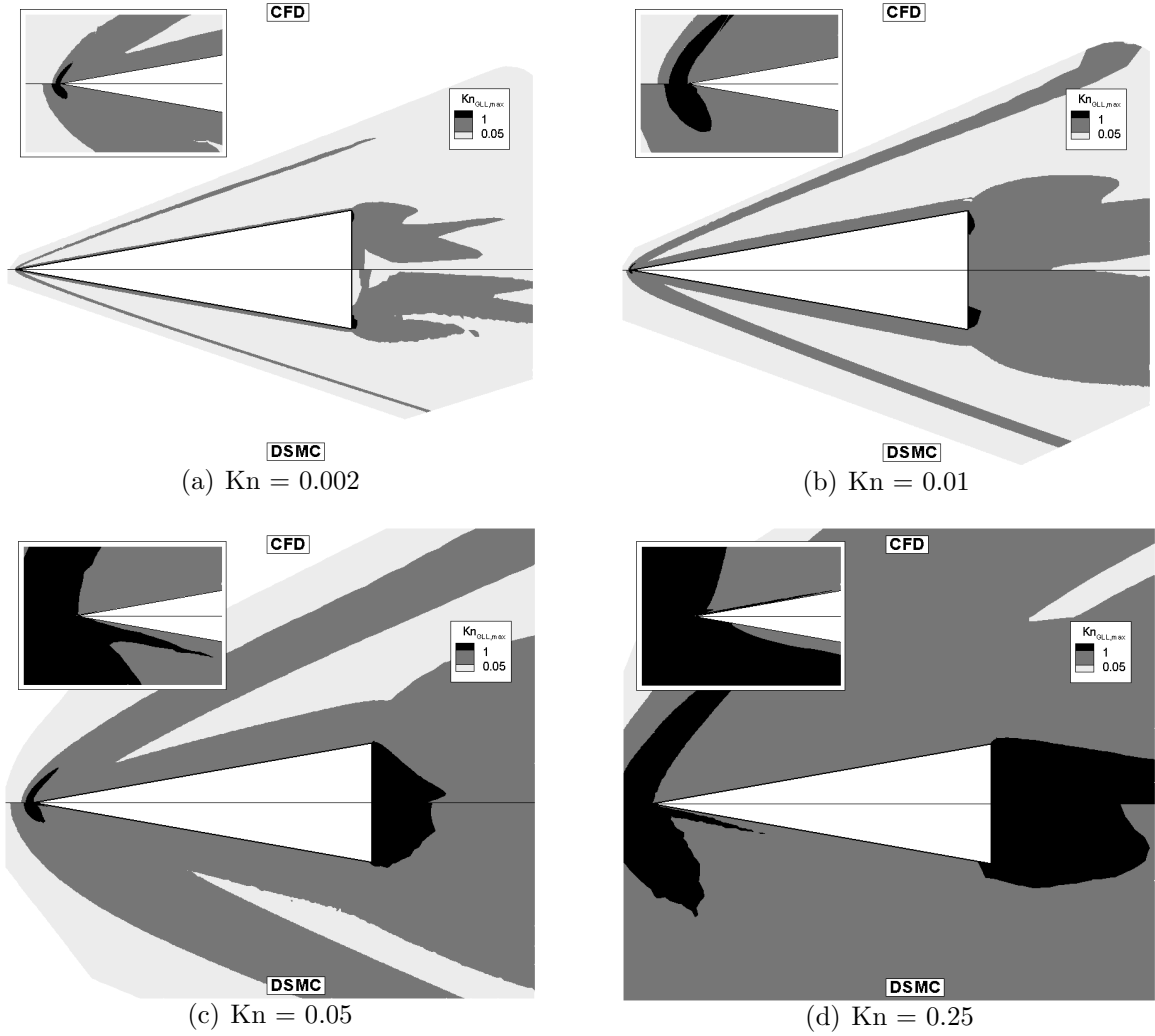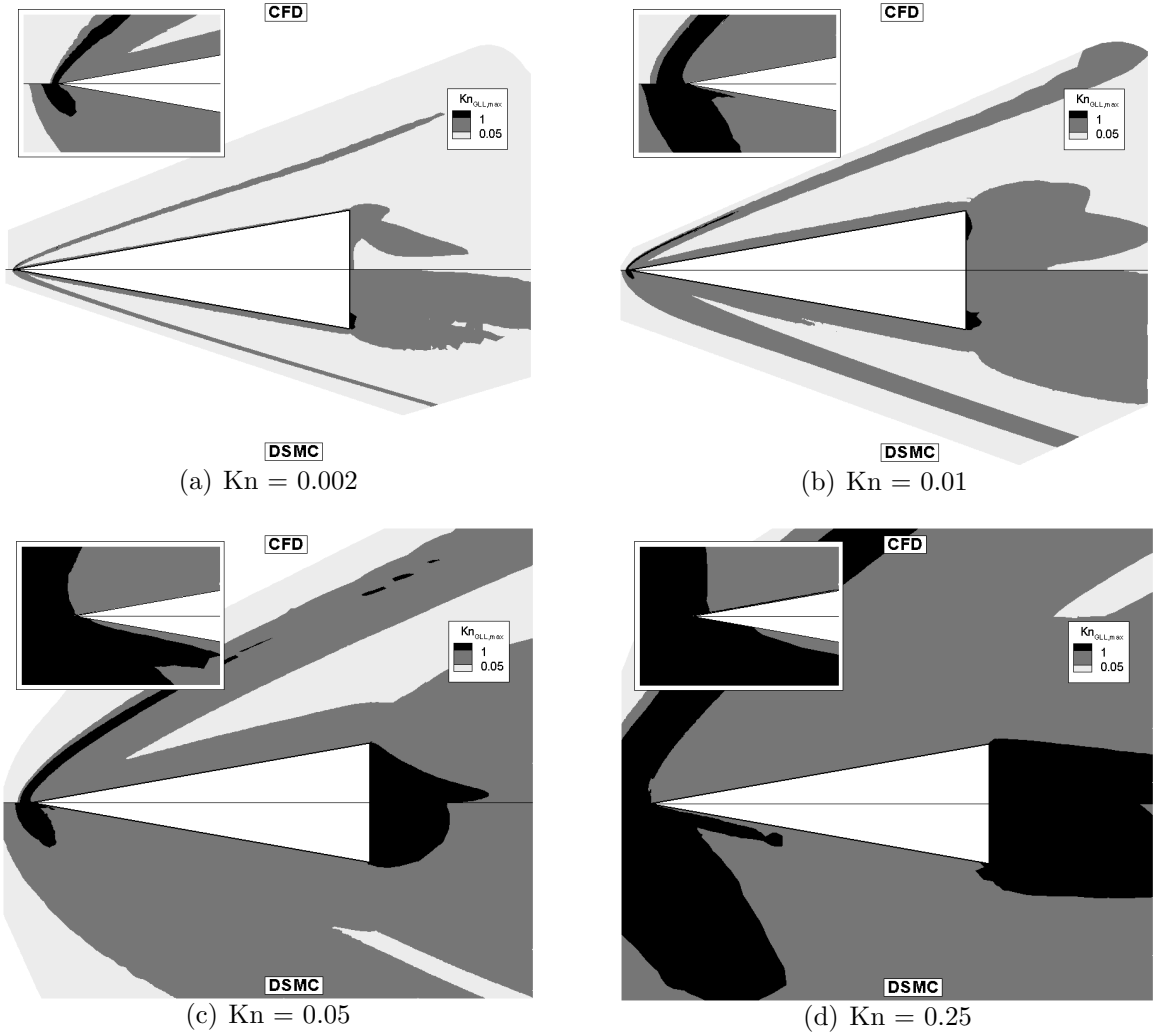
Figure 5.6: Kn_{GLL} field for a Mach 25 flow of argon about a wedge. The light gray regions correspond to $Kn_{GLL} < 0.05$, dark gray regions correspond to $Kn_{GLL} < 1.0$, and black regions correspond to $Kn_{GLL} > 1.0$. Note that the minimum value of Kn_{GLL} for the black regions is an order of magnitude greater than those shown for the cylinder.

5.2.2   Flow Field Properties

The density ratio fields, where the density is normalized by the free stream density, are shown in Figures 5.7 and 5.8. The thin shock present at Kn = 0.002 becomes more diffuse as the Knudsen number increases and there is a low density region in the wake, causing breakdown of the continuum hypothesis. As the Mach number increases from Mach 10 to Mach 25, there is little qualitative difference in the density contours, although the amount of compression through the shock is higher at the higher velocity, as shown by the higher density ratio (a maximum density ratio of about 4.5 for Mach 25 compared to about 3.2 for Mach 10 at Kn = 0.002). DSMC also predicts a higher density near the wedge surface. This is most clearly seen in the leading-edge details and at the higher Knudsen numbers.

The temperature fields predicted by both CFD and DSMC can be seen in Figures 5.9 and 5.10. The temperature field predicted by both methods seems to agree in the majority of the computational domain for Kn = 0.002, Kn = 0.01 and even Kn = 0.05, with some differences in the wake. However, near the leading edge (see insets), DSMC predicts a much higher temperature than CFD (the peak temperatures are about 3,000-3,400 K for Mach 10 and 16,000-20,000 K for Mach 25). For Kn = 0.002, the DSMC temperature at the leading edge is about 40% higher than the CFD temperature, and the peak DSMC temperature is about 15% higher than the peak CFD temperature. As the Knudsen number increases, the difference in temperature at the leading edge increases to nearly 50% for Kn = 0.25. Although DSMC always predicts the peak temperature to be at the leading edge, CFD predicts a higher temperature in the wake for these most rarefied cases. It is clear that CFD cannot accurately predict the temperature gradients near the leading edge even for the highest density cases, causing a large difference in the predicted heat transfer rates.

(a) Kn = 0.002

(b) Kn = 0.01

(c) Kn = 0.05

(d) Kn = 0.25

Figure 5.7: Density ratio field for a Mach 10 flow of argon about a wedge.

(a) Kn = 0.002

(b) Kn = 0.01

(c) Kn = 0.05

(d) Kn = 0.25
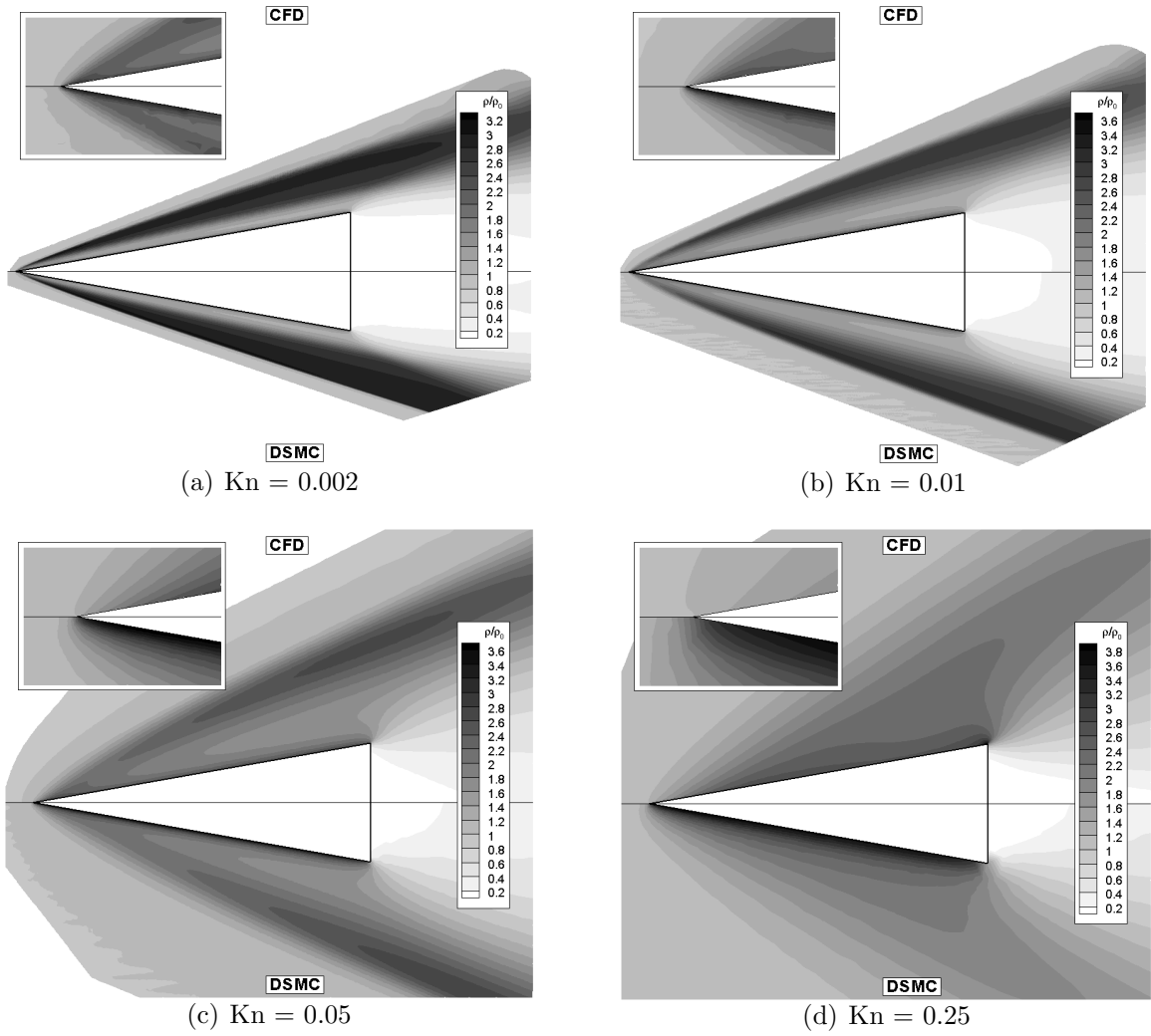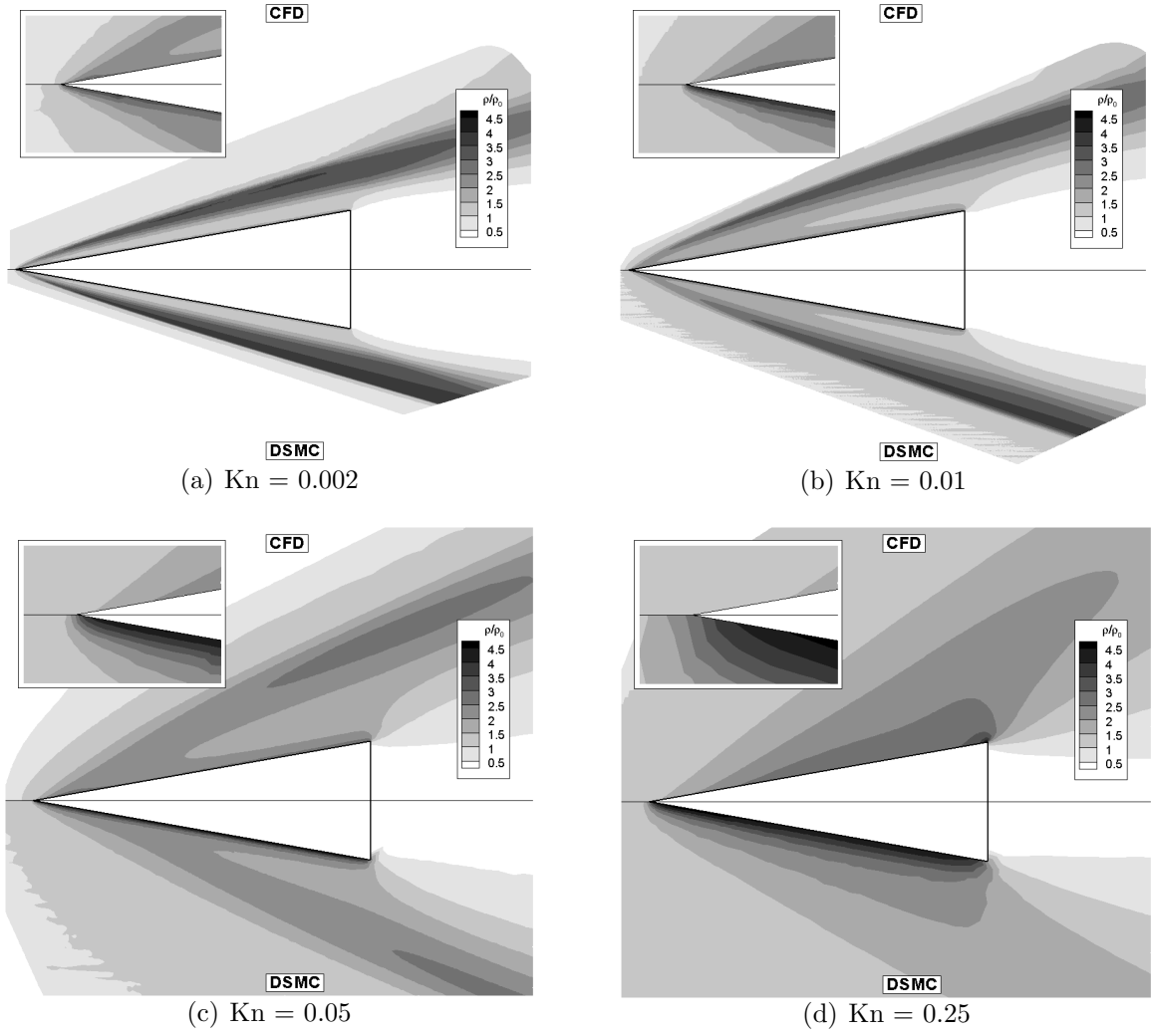
Figure 5.8: Density ratio field for a Mach 25 flow of argon about a wedge.
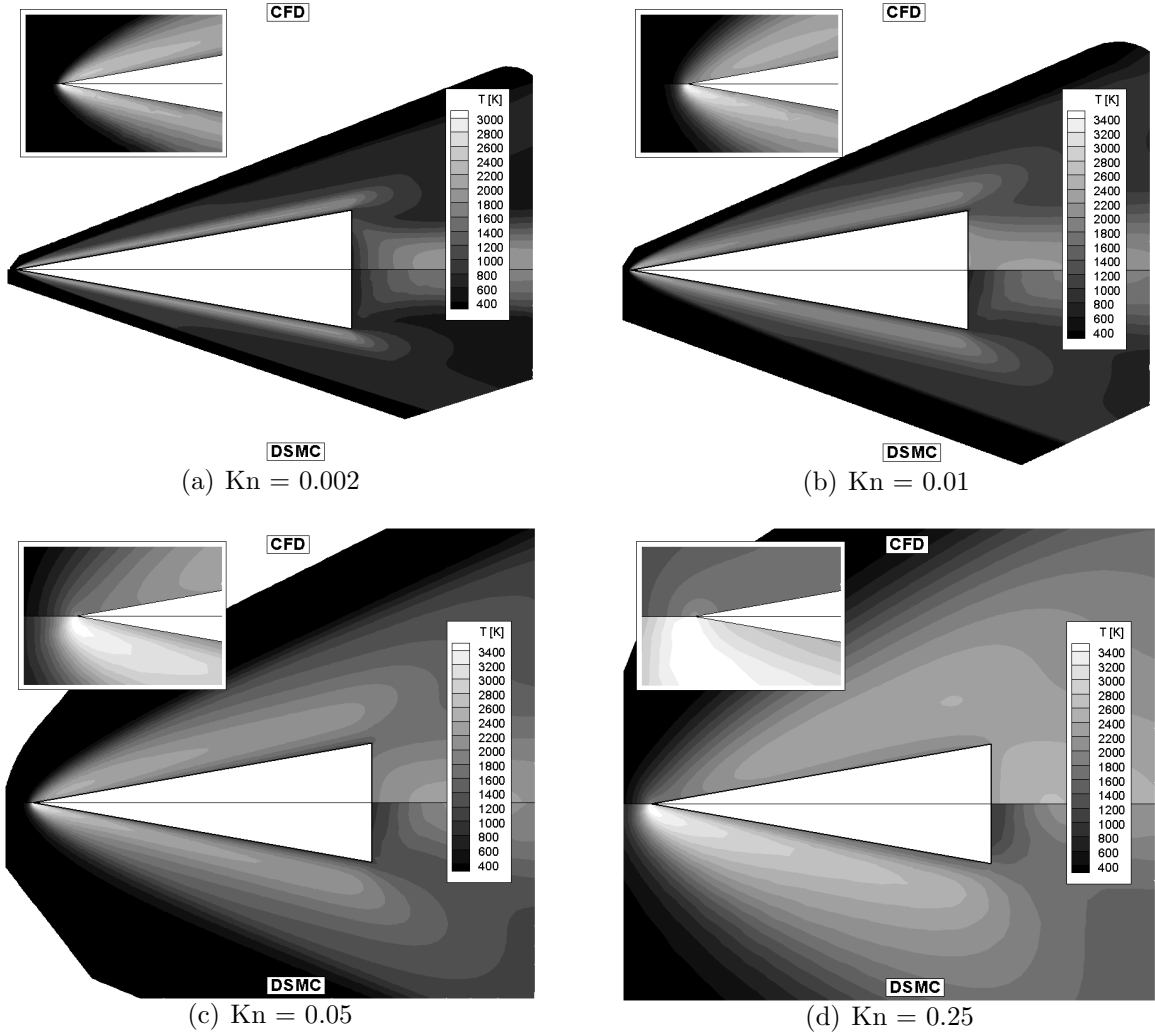
Figure 5.9: Temperature field for a Mach 10 flow of argon about a wedge. DSMC predicts a much higher temperature than CFD near the leading edge (inset). Note that CFD predicts a higher temperature in the wake than near the leading edge for Kn = 0.25, while DSMC predicts a maximum temperature at the leading edge.

(a) Kn = 0.002

(b) Kn = 0.01

(c) Kn = 0.05

(d) Kn = 0.25

Figure 5.10: Temperature field for a Mach 25 flow of argon about a wedge. DSMC predicts a much higher temperature than CFD near the leading edge (inset). Note that CFD predicts a higher temperature in the wake than near the leading edge for Kn = 0.25, while DSMC predicts a maximum temperature at the leading edge.

5.2.3   Surface Properties

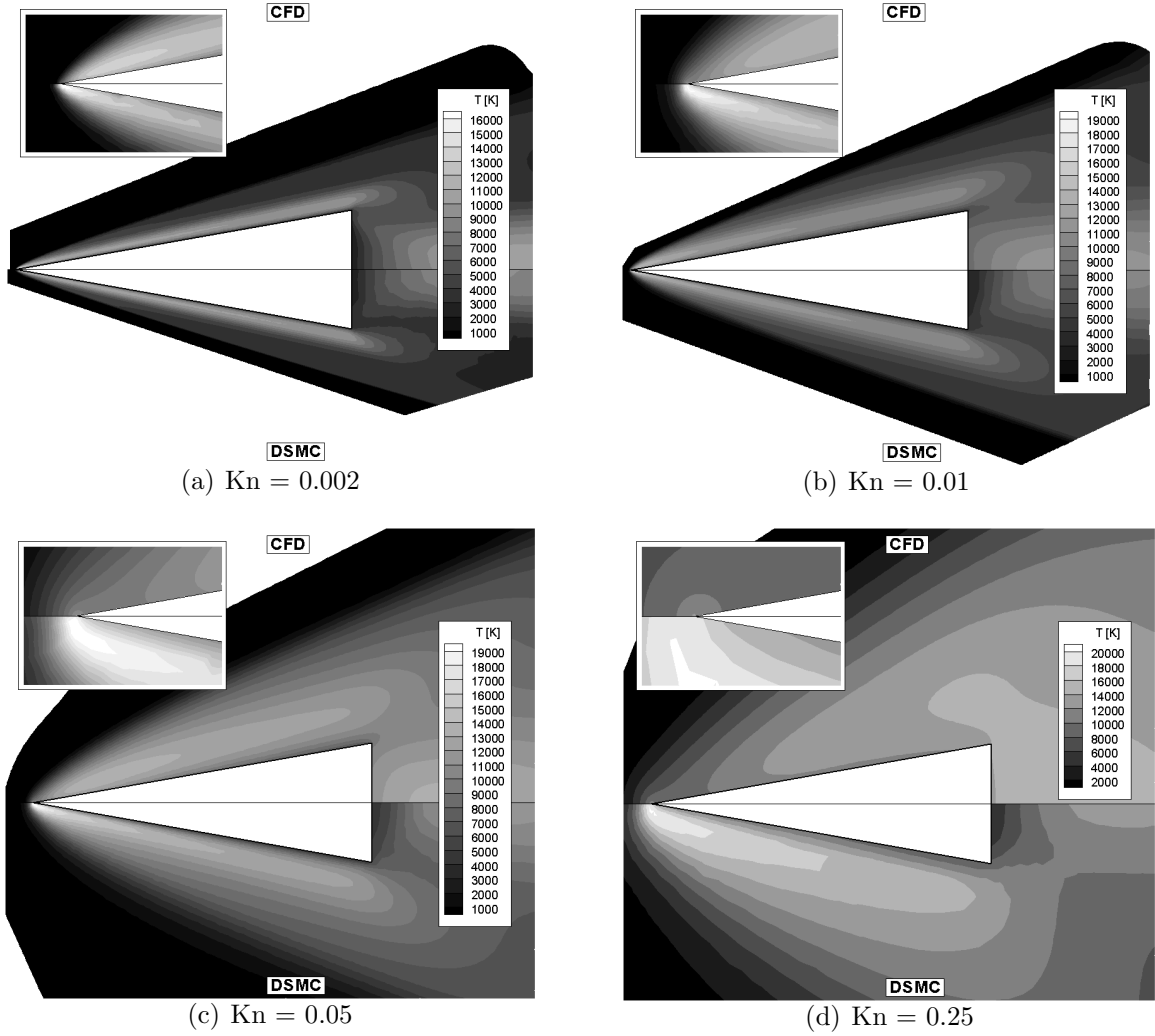The surface property distributions (pressure, shear stress and heat flux) for each case are now examined. The surface pressure, in the form of a pressure coefficient, is shown in Figures 5.11 and 5.12. For the blunt-body, the surface pressure was the least sensitive to nonequilibrium of all the surface properties; for the wedge, however, there are significant differences in the pressure distributions, even at Kn = 0.002. Although there are significant levels of nonequilibrium in the wake as well as at the leading edge, as shown by Figures 5.5 and 5.6, the pressure is affected primarily at the leading edge. The overall CFD pressure distribution agrees qualitatively with DSMC for all but the Kn = 0.25 case, but the peak pressure at the leading edge is overpredicted by CFD. The distributions also start to differ in the wake for Kn = 0.05 and Kn = 0.25, with CFD predicting a large spike in the pressure at $S/L = 1$ as the flow begins to expand into the wake. In all cases, CFD tends to overpredict the pressure, hence there is some effect of the pressure on the overall overprediction of total drag by CFD, although this effect is not as great as that of shear stress, as was shown in Figure 5.3.

The shear stress on the wedge surface is seen in Figures 5.13 and 5.14. Here, there is a large spike in the CFD shear stress right at the leading edge that is not shown in the figures. The maximum friction coefficient at that point is annotated in each case. This peak ranges from a fairly low value of 0.43 for Mach 25, Kn = 0.002 (which is not much different from the peak DSMC value) to a maximum of 41.3 for Mach 25, Kn = 0.25 (compared to about 0.36 for DSMC). Other than this peak at the leading edge, there are fewer differences in the shear stress than there were for the pressure. However, the total drag is affected most by the friction forces. This apparent paradox is explained by noting again the much larger effect that shear stress

(a) Kn = 0.002

(b) Kn = 0.01

(c) Kn = 0.05

(d) Kn = 0.25

Figure 5.11: Surface pressure coefficient for Mach 10 flow of argon about a wedge. The maximum value of Kn_{GLL} near the surface plotted on the right axis. The distance along the surface (including the base), S, is normalized by the top surface length, L.

(a) Kn = 0.002

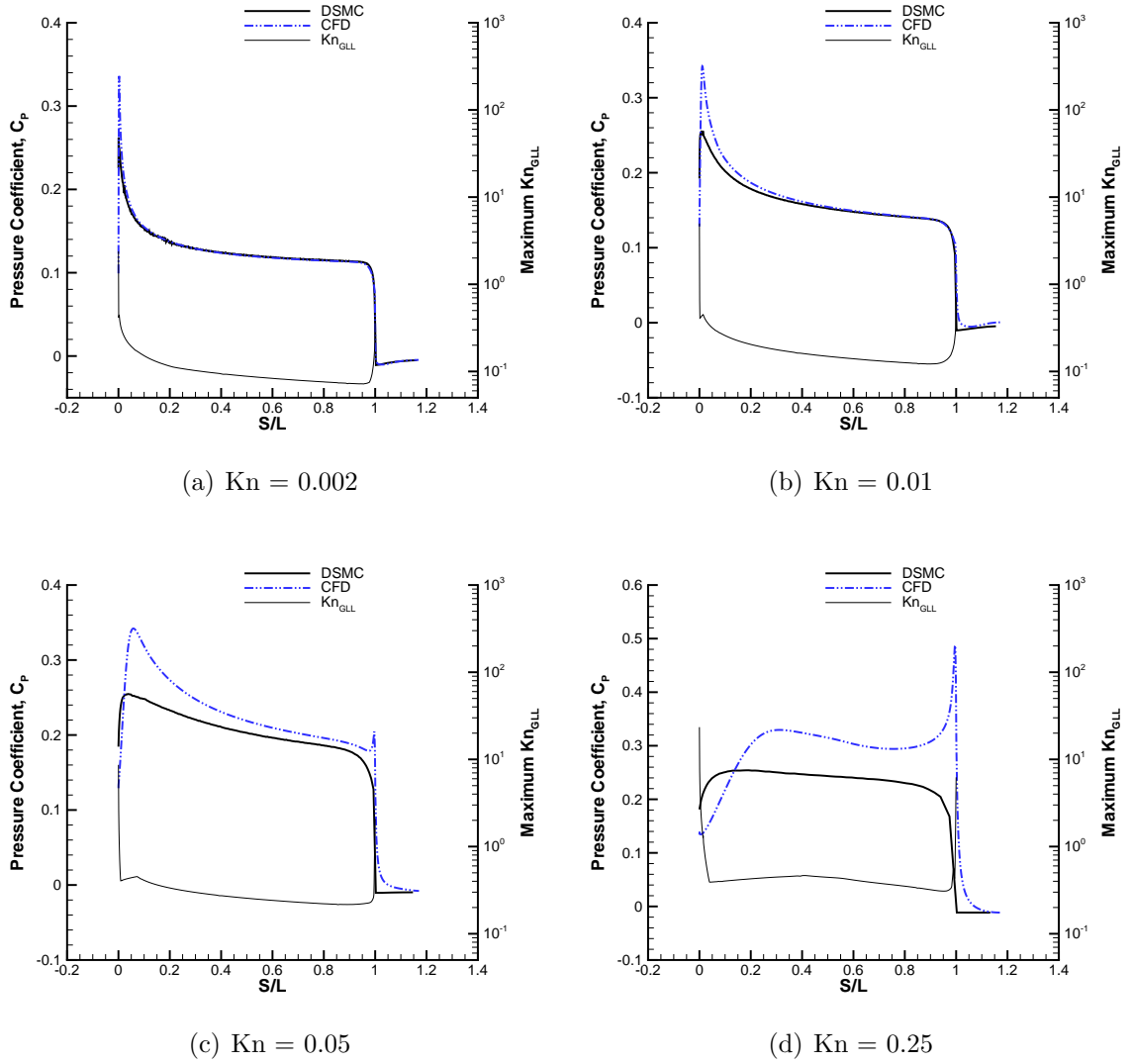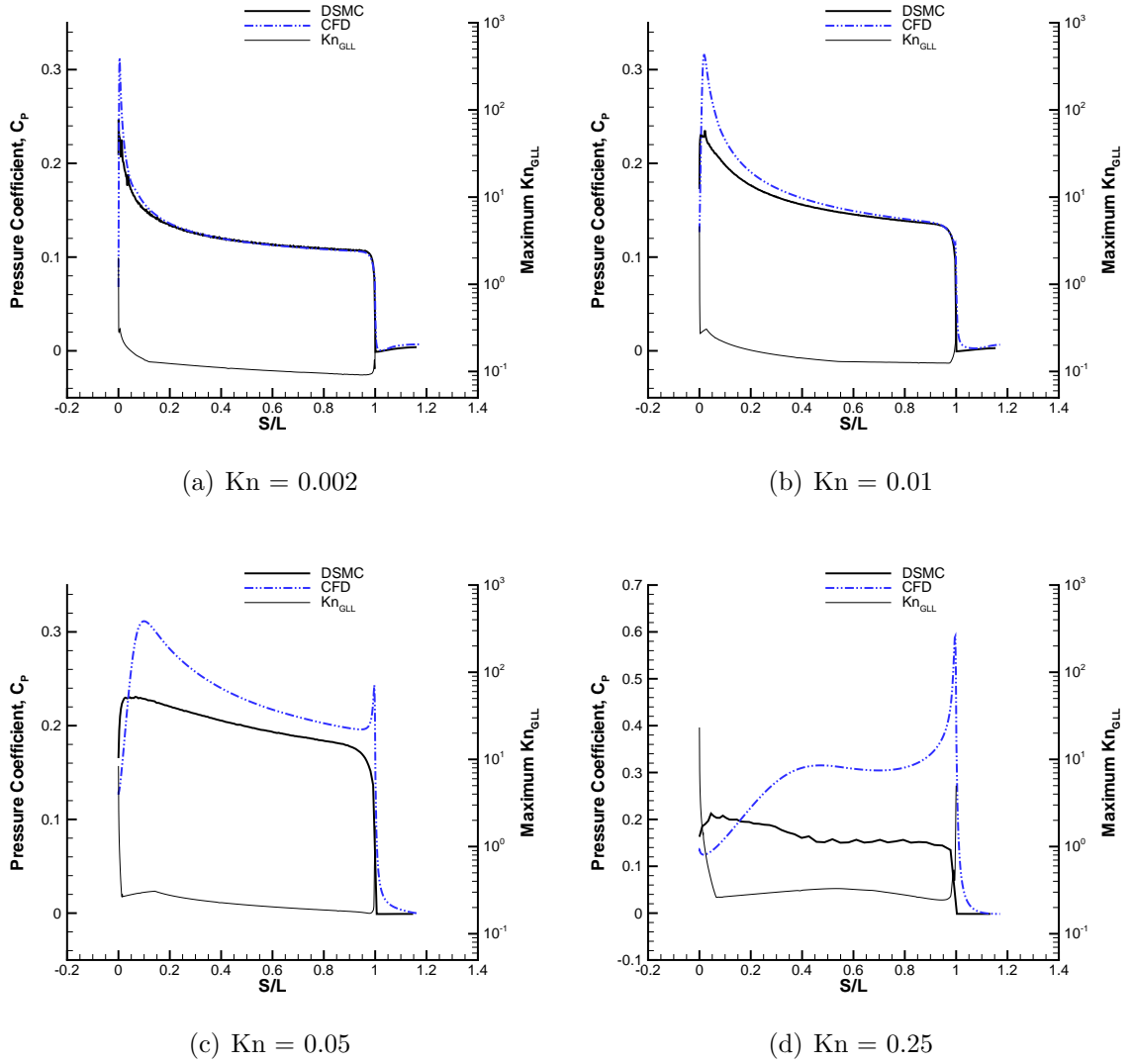(b) Kn = 0.01

(c) Kn = 0.05

(d) Kn = 0.25

Figure 5.12: Surface pressure coefficient for Mach 25 flow of argon about a wedge. The maximum value of Kn_{GLL} near the surface plotted on the right axis. The distance along the surface (including the base), S, is normalized by the top surface length, L.

has on the total drag as seen in Figure 5.3.

The peak at the leading edge does not have any significant effect on the total drag due to the small surface area on which the friction force acts. Figures 5.15 and 5.16 compare the accumulated total drag along the wedge surface due to both friction and pressure forces. The accumulated total drag along the surface is calculated by summing the drag from the leading edge up to each point along the surface, thus the total drag is shown at about $S/L = 1.2$. The locations where there are large differences between the CFD and DSMC drag predictions are seen where the distance between the two lines on the plots increases. Thus, the differences in friction drag for Kn = 0.002 and Kn = 0.01 occur along the first 20% of the wedge surface. For Kn = 0.05, the area where the difference accumulates most is in the first 40-50% of the wedge surface; and for Kn = 0.25, the differences accumulate mostly between 20% and 80% of the wedge length. Note that the peak in friction coefficient at the leading edge has no significant impact on the total drag. Figures 5.15 and 5.16 also demonstrate that:

- The contribution of friction forces to the total drag increases as the density decreases.

- There is no contribution to total drag due to friction forces in the wake.

- Pressure forces on the base of the wedge (in the wake) decrease the total drag.

- There is little disagreement in the predictions of total drag due to pressure forces for most cases.

Fairly significant disagreement in shear stress prediction for Kn = 0.05 and Kn = 0.25 is also seen at $S/L = 1$ at the sharp angle between the top wedge surface and the base.

(a) Kn = 0.002

(b) Kn = 0.01

(c) Kn = 0.05

(d) Kn = 0.25

Figure 5.13: Surface friction coefficient for Mach 10 flow of argon about a wedge. The maximum value of Kn_{GLL} near the surface plotted on the right axis. The distance along the surface (including the base), S, is normalized by the top surface length, L.

(a) Kn = 0.002

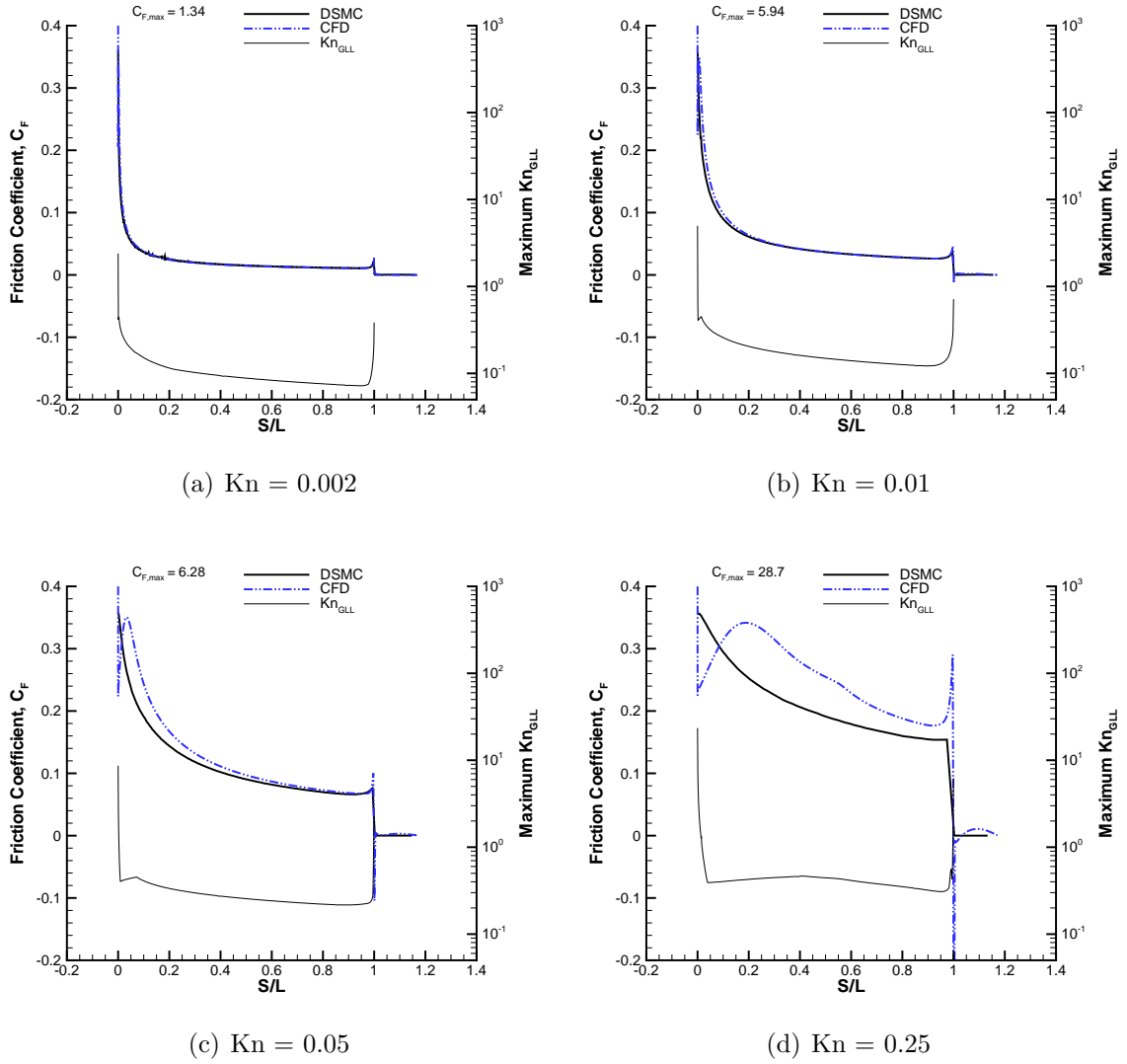(b) Kn = 0.01

(c) Kn = 0.05

(d) Kn = 0.25
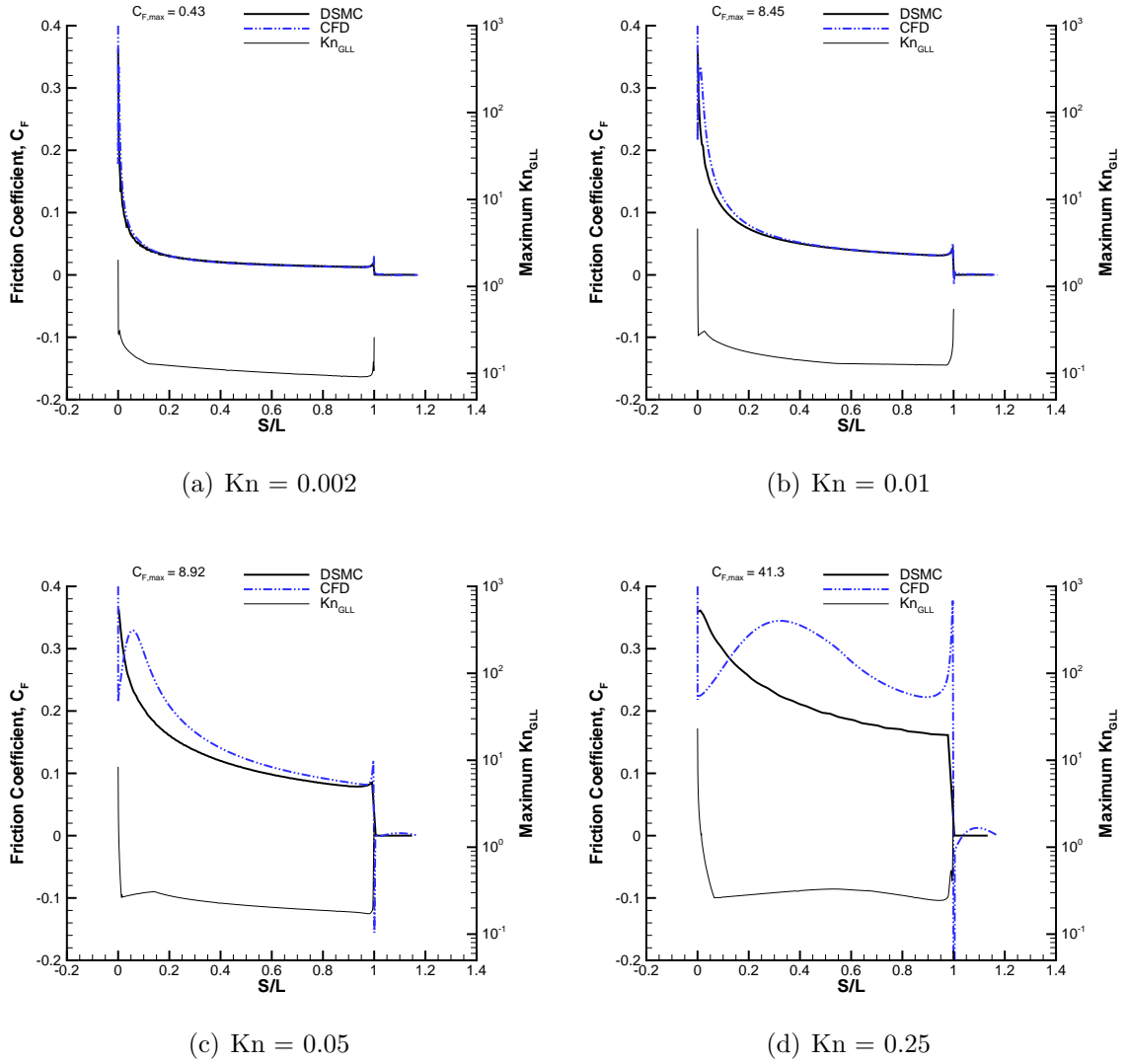
Figure 5.14: Surface friction coefficient for Mach 25 flow of argon about a wedge. The maximum value of Kn_{GLL} near the surface plotted on the right axis. The distance along the surface (including the base), S, is normalized by the top surface length, L.

(a) Kn = 0.002
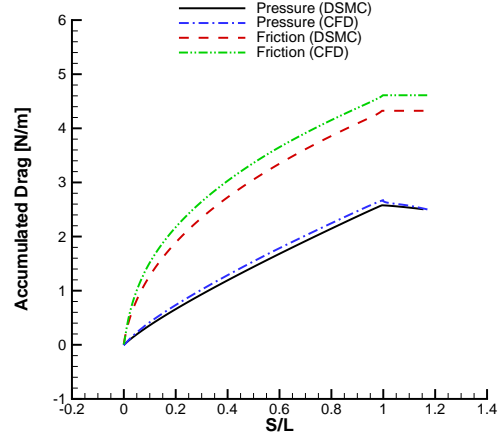
(b) Kn = 0.01
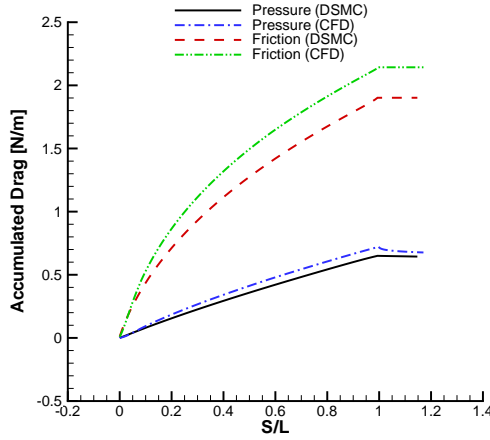
(c) Kn = 0.05

(d) Kn = 0.25

Figure 5.15: Contributions of pressure and skin friction forces to accumulated total drag for a Mach 10 flow of argon about a wedge. The distance along the surface (including the base), S, is normalized by the top surface length, L.

(a) Kn = 0.002
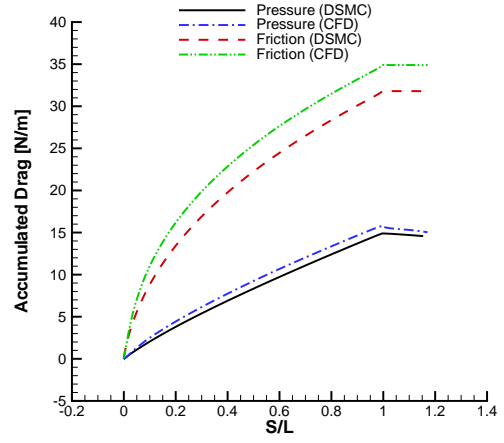
(b) Kn = 0.01
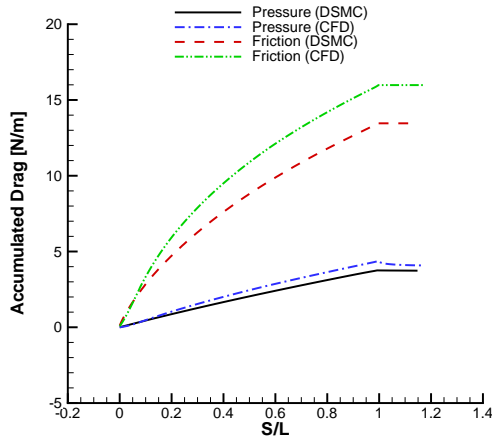
(c) Kn = 0.05
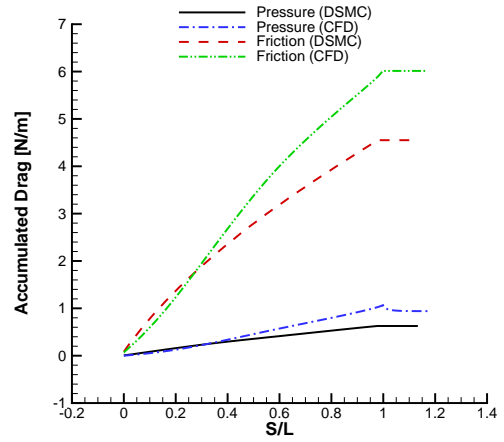
(d) Kn = 0.25

Figure 5.16: Contributions of pressure and skin friction forces to accumulated total drag for a Mach 25 flow of argon about a wedge. The distance along the surface (including the base), S, is normalized by the top surface length, L.

The heat transfer rate distributions are shown in Figures 5.17 and 5.18. Previously, it was shown that DSMC predicts a temperature as much as 40% higher than CFD at the leading edge. The inability of CFD to model the flow at the leading edge has a large effect on the heat flux. Although the qualitative agreement is good at Kn = 0.002, DSMC predicts a heating coefficient of nearly 0.19, while CFD predicts a much lower heating coefficient of about 0.07. As the Knudsen number increases, the DSMC peak heating coefficient remains at about 0.19 - 0.20, while the CFD peak heating coefficient remains near 0.05 - 0.06. Thus, the difference in heating rate is around 70% for most of the cases. For Kn = 0.25, CFD predicts a peak heating rate at the shoulder, with no heating predicted at the leading edge. The actual error in heating rate prediction, then, is much greater than the 35% and 18% cited in Table 5.2 and shown in Figure 5.4.

5.2.4 Slip Quantities

The velocity slip along the wedge surface is shown in Figures 5.19 and 5.20. In all cases, CFD predicts a peak velocity slip of about 2000 m/s (for Mach 10) and about 5000 m/s (for Mach 25) near the leading edge, while DSMC predicts a maximum velocity slip of about 700 m/s (for Mach 10) and about 1100 m/s (for Mach 25). Past the leading edge, the velocity slip is very quickly reduced to a nearly constant finite value until the wedge shoulder, where a sharp increase is seen. For Kn = 0.002 Kn = 0.01 and even Kn = 0.05 to some extent, CFD qualitatively agrees fairly well with DSMC. However, for Kn = 0.25 this agreement worsens considerably. The locations where the disagreement is most apparent, at and near the leading edge, are also the locations where the shear stress distributions differ the most. Thus, there is a good correlation between velocity slip disagreement and shear stress disagreement.

(a) Kn = 0.002

(b) Kn = 0.01

(c) Kn = 0.05

(d) Kn = 0.25
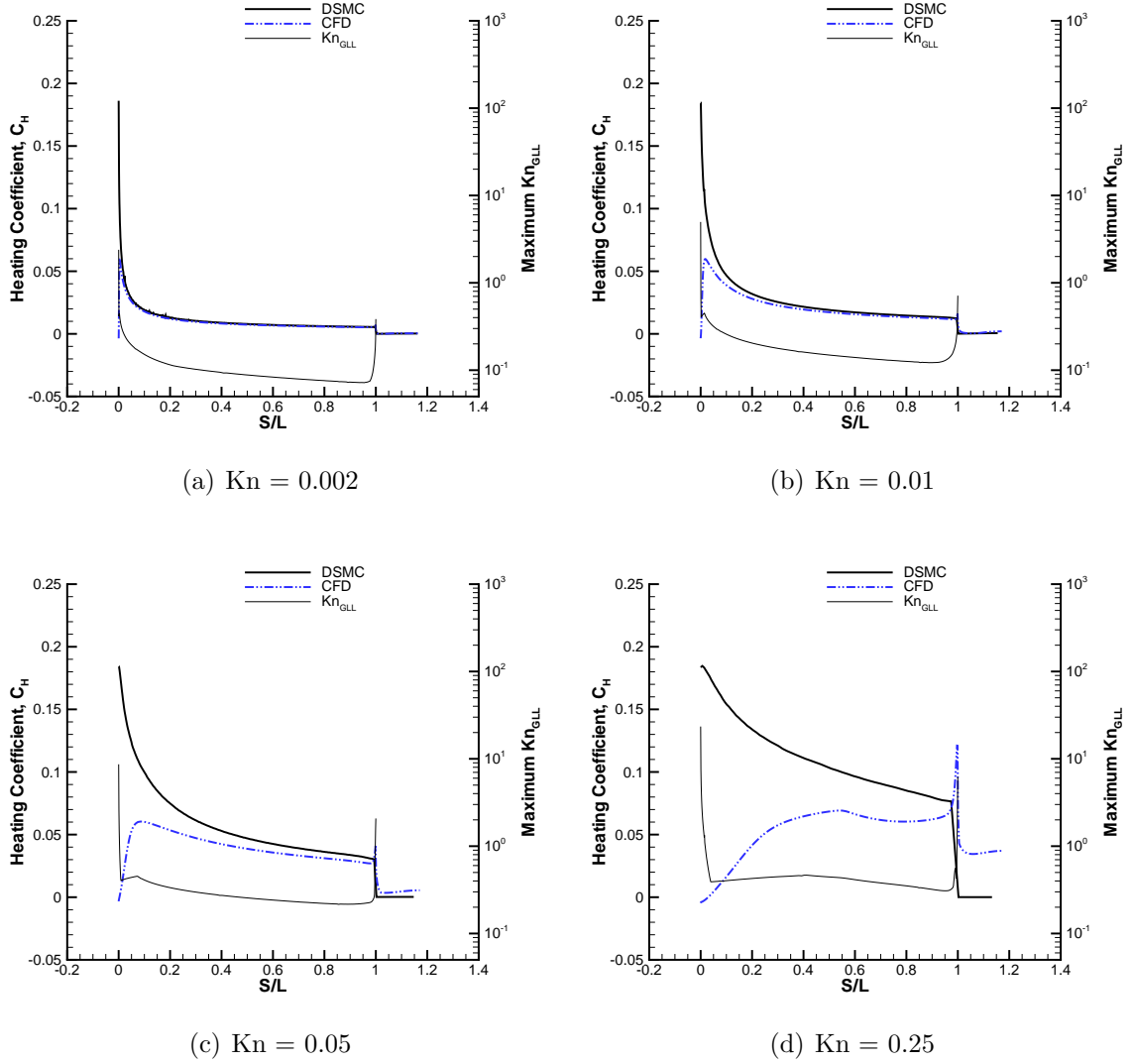
Figure 5.17: Surface heating coefficient for Mach 10 flow of argon about a wedge. The maximum value of Kn_{GLL} near the surface plotted on the right axis. The distance along the surface (including the base), S, is normalized by the top surface length, L.
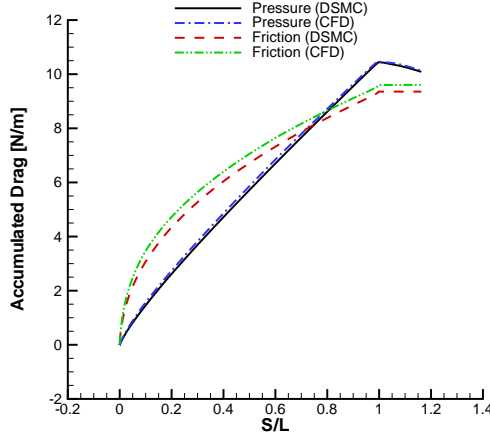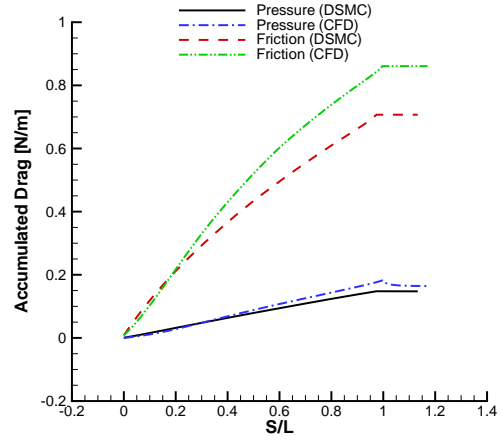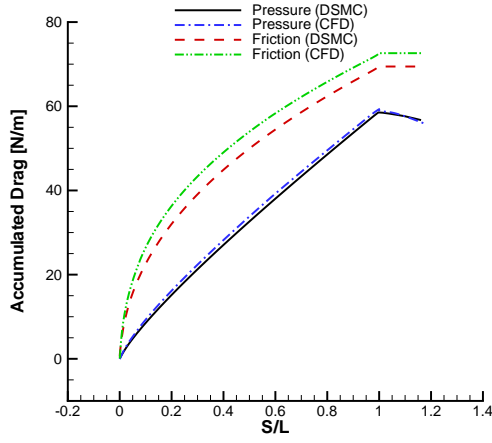
(a) Kn = 0.002

(b) Kn = 0.01

(c) Kn = 0.05

(d) Kn = 0.25
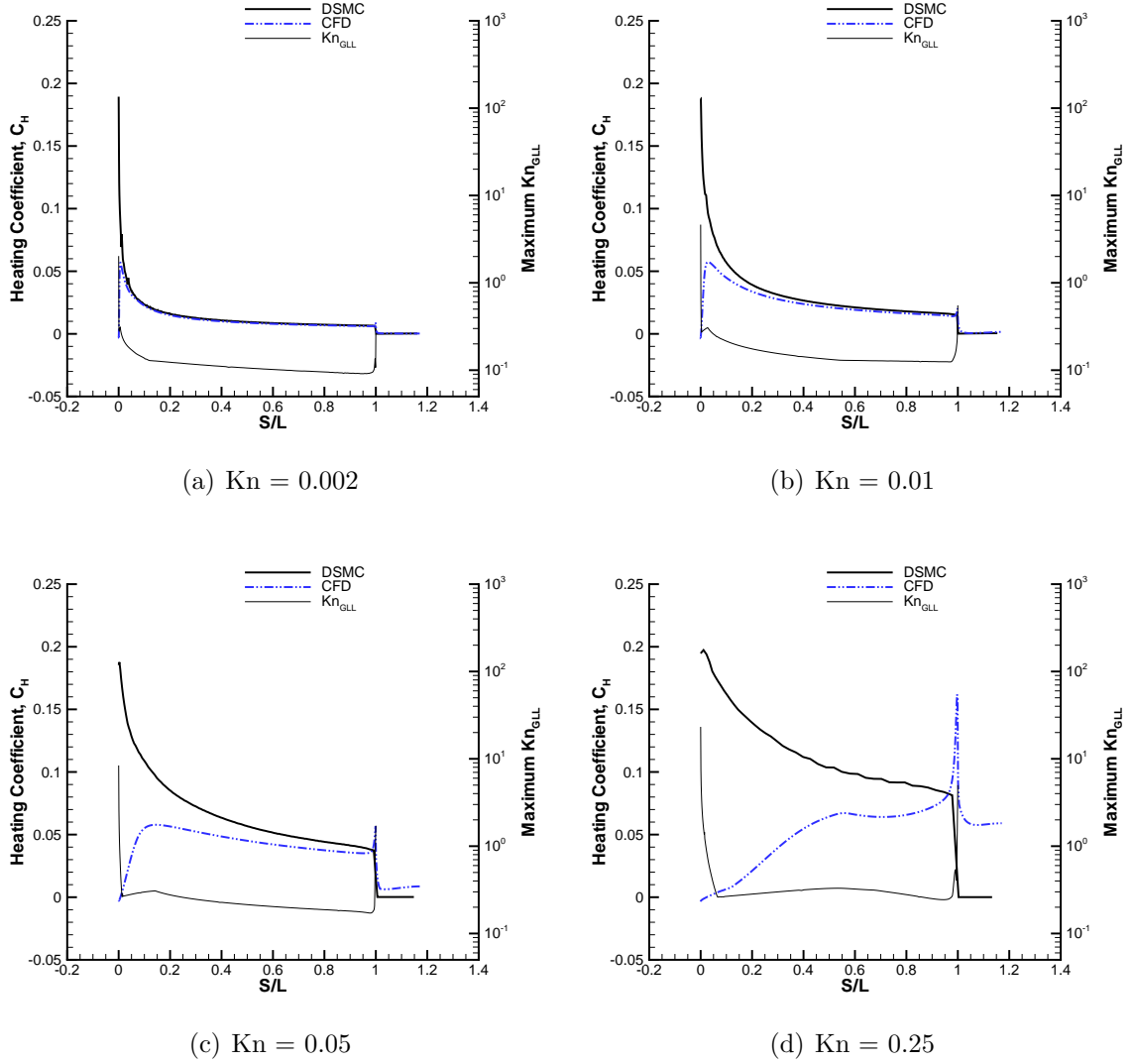
Figure 5.18: Surface heating coefficient for Mach 25 flow of argon about a wedge. The maximum value of $\mathrm{Kn_{GLL}}$ near the surface plotted on the right axis. The distance along the surface (including the base), S, is normalized by the top surface length, L.
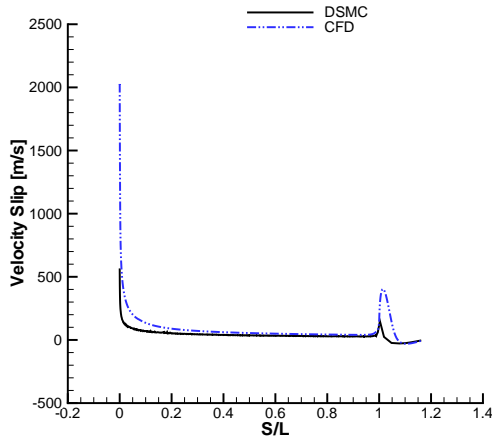
(a) Kn = 0.002
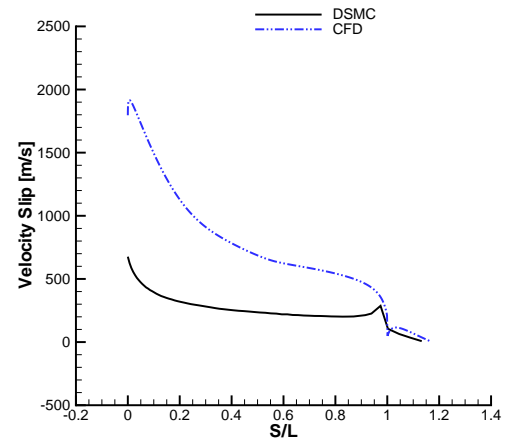
(b) Kn = 0.01

(c) Kn = 0.05

(d) Kn = 0.25

Figure 5.19: Velocity slip for a Mach 10 flow of argon about a wedge. The distance along the surface (including the base), S, is normalized by the top surface length, L.
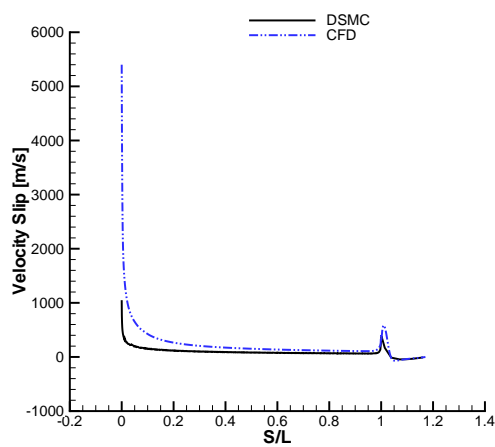
(a) Kn = 0.002
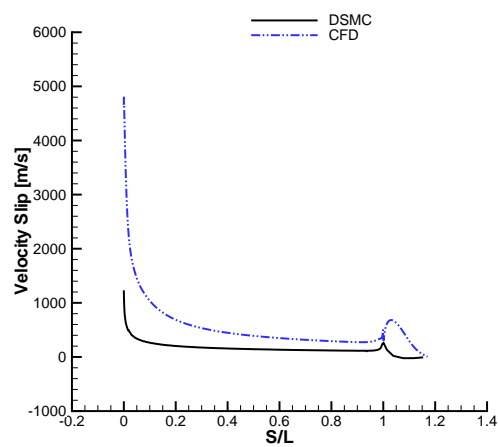
(b) Kn = 0.01
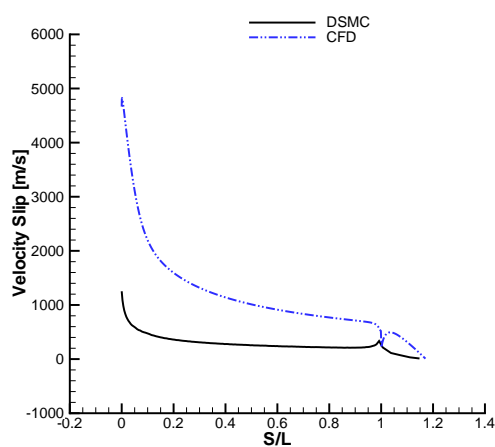
(c) Kn = 0.05
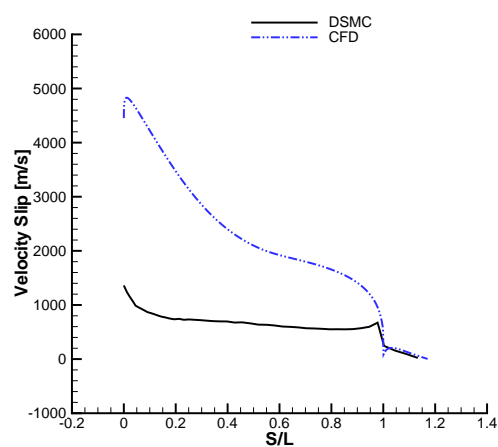
(d) Kn = 0.25

Figure 5.20: Velocity slip for a Mach 25 flow of argon about a wedge. The distance along the surface (including the base), S, is normalized by the top surface length, L.

The temperature jump is shown in Figures 5.21 and 5.22. The DSMC profile of temperature jump is very similar to that for velocity slip; the temperature jump is highest at the leading edge, with a gradual decrease to an almost constant value and a slight bump around the wedge shoulder. The peak temperature jump predicted by DSMC is between about 2000-2200 K (for Mach 10) and 10000-11000 K (for Mach 25). CFD agrees fairly well for Kn = 0.002, but shows large disagreements for all other cases, particularly in the wake. The CFD peak temperature jump is not much different from that of DSMC, especially for the Mach 25 cases. There does not seem to be any strong correlation between the temperature jump agreement and the disagreement between heat transfer rates.

5.2.5   Computational Details

The computational details for the simulations of a hypersonic flow of argon about a wedge discussed in this section are shown in Table 5.3.
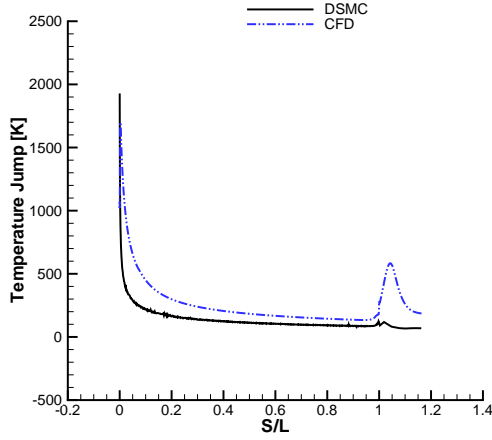
(a) Kn = 0.002
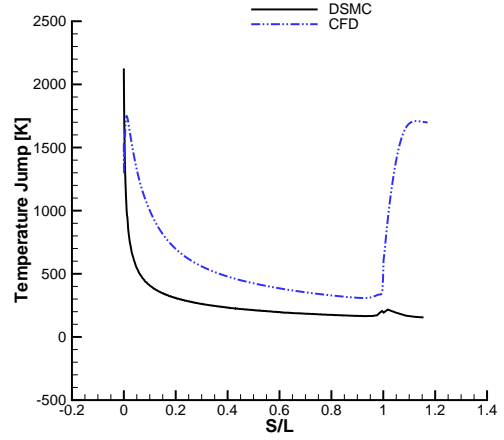
(b) Kn = 0.01
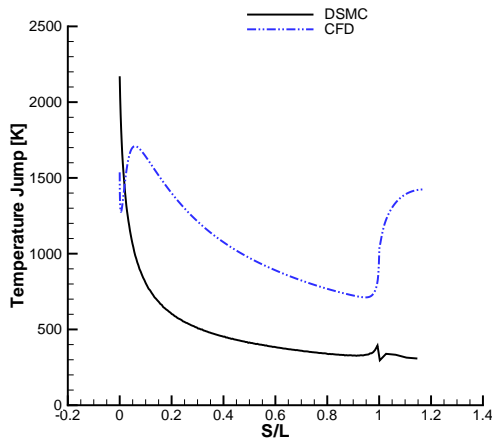
(c) Kn = 0.05
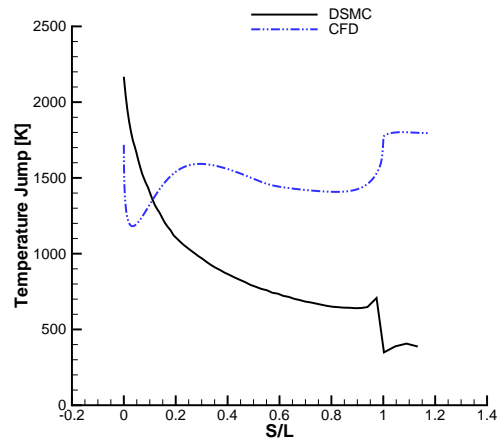
(d) Kn = 0.25

Figure 5.21: Temperature jump for a Mach 10 flow of argon about a wedge. The distance along the surface (including the base), S, is normalized by the top surface length, L.
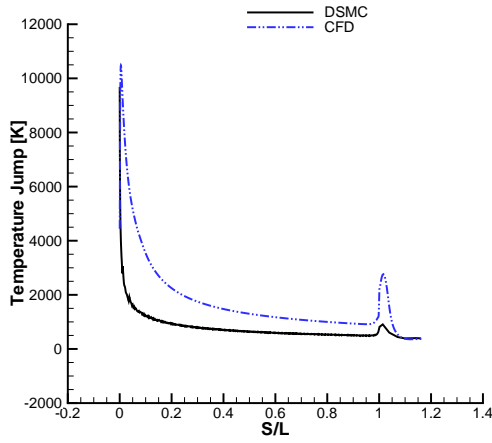
(a) Kn = 0.002
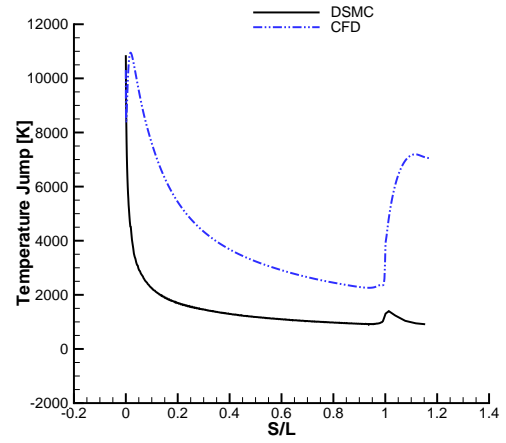
(b) Kn = 0.01
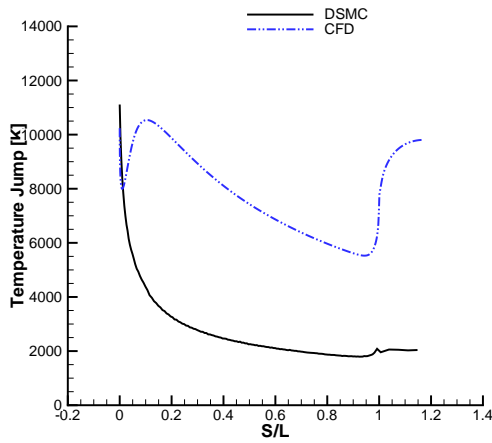
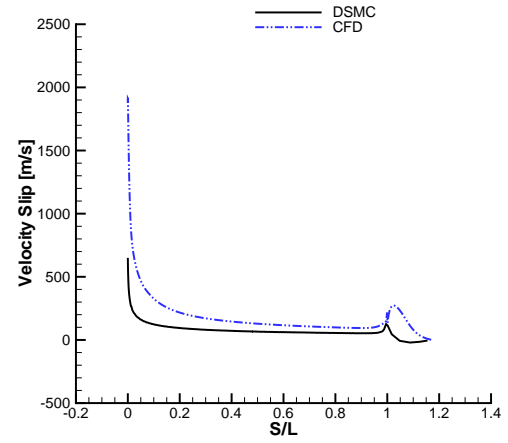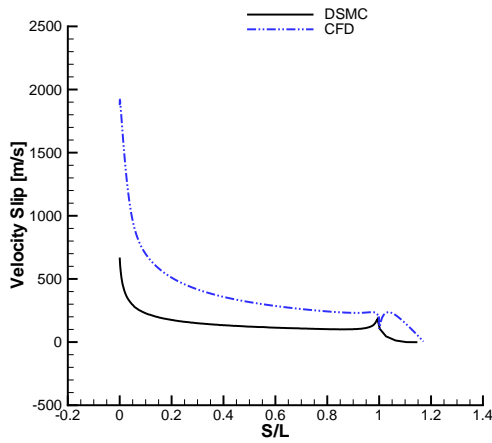(c) Kn = 0.05
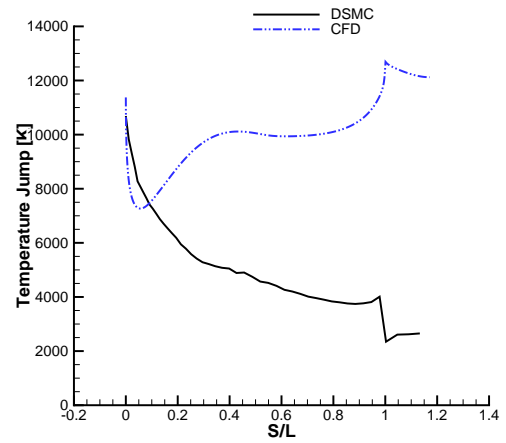
(d) Kn = 0.25

Figure 5.22: Temperature jump for a Mach 25 flow of argon about a wedge. The distance along the surface (including the base), S, is normalized by the top surface length, L.

Table 5.3: Computational details for a flow of argon about a wedge. Total CPU time is the wall time multiplied by the number of CPUs.

Mach 10

Kn_∞	DSMC				
	Cells	Particles	Time Steps	CPUs	Total CPU Time*[hours]
0.002	187,036	50.7×10^6	260,000	32	3,072
0.01	155,126	47.6×10^6	200,000	32	2,220
0.05	26,329	9.6×10^6	200,000	8	636
0.25	8,083	5.3×10^6	200,000	4	159
Kn_∞	CFD				
	Cells		Iterations	CPUs	Total CPU Time*[hours]
0.002	25,200		30,000	8	56
0.01	25,200		20,000	8	38
0.05	28,400		30,000	8	64
0.25	30,175		30,000	8	66

Mach 25

Kn_∞	DSMC				
	Cells	Particles	Time Steps	CPUs	Total CPU Time*[hours]
0.002	107,421	32.4×10^6	360,000	32	3,494
0.01	94,596	24.2×10^6	200,000	16	1,275
0.05	19,398	4.2×10^6	200,000	4	125
0.25	6,110	5.3×10^6	200,000	4	162
Kn_∞	CFD				
	Cells		Iterations	CPUs	Total CPU Time*[hours]
0.002	29,050		30,000	8	60
0.01	25,200		30,000	8	66
0.05	28,400		30,000	8	60
0.25	30,175		30,000	8	80

* Approximate

Table 5.4: Total drag for flow of nitrogen about a wedge.

Kn$_\infty$	Mach 10			Mach 25		
	Drag/Length [N/m] (% Difference)					
	DSMC	CFD		DSMC	CFD	
0.002	29.92	30.34	(1.4%)	183.8	189.9	(3.3%)
0.01	10.48	10.86	(3.6%)	67.82	72.34	(6.7%)
0.05	3.946	4.255	(7.8%)	26.10	29.03	(11.2%)
0.25	1.364	1.547	(13.4%)	8.488	10.05	(18.4%)

5.3   Nitrogen

The flow of nitrogen about the wedge is now considered. Table 5.4 summarizes the total drag predicted by CFD and DSMC. Again, there is reasonable agrement at the lowest Knudsen number, with less than 2% difference for Mach 10, but with a little more than 3% for Mach 25. As the flow becomes more rarefied, the differences increase, although the maximum differences of about 13% and 18% at Kn = 0.25 are lower than that seen with argon.

Figure 5.23 again illustrates the percentage of total drag due to pressure and friction forces, for both DSMC and CFD. The amount of drag due to friction again ranges from around 50% for Mach 10, Kn = 0.002, to about 90% for Mach 25, Kn = 0.25. A slightly larger percentage of the drag is due to friction at the higher velocity, as was seen with argon, and the contribution of friction forces to the total drag also increases with increasing Knudsen number. It is also shown in Figure 5.24, that the difference in predicted total drag between CFD and DSMC is due mostly to the differences predicted in the friction forces. Note, however, that the differences due to pressure drag are much lower than was the case with argon; for instance, the argon case for Mach 25, Kn = 0.25 case had a difference of over 5% in the pressure drag prediction (see Figure 5.3), while the currently considered cases
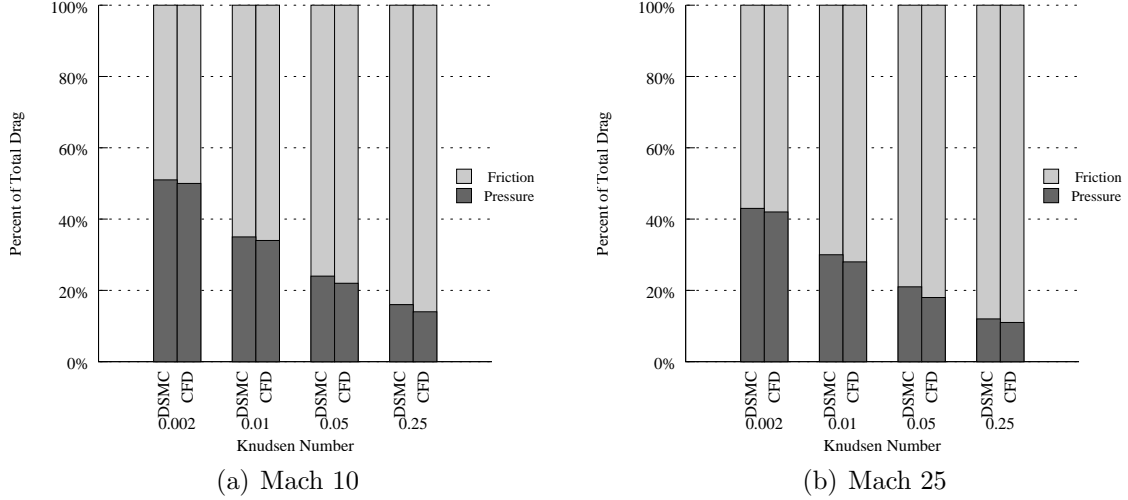
Figure 5.23: Percentage of total drag due to pressure and friction for flow of nitrogen about a wedge. In contrast to the cylinder cases, here friction forces account for most of the drag.

show a maximum of only about 2% for the same Mach and Knudsen numbers. The pressure drag differences for the Mach 10 nitrogen cases are insignificant.

Peak heating rates for the nitrogen cases are summarized in Table 5.5, and illustrated graphically in Figure 5.25. Similar to the argon cases, the error in peak heating is about 70% for most cases, and decreases to about 40% and 25% for Mach 10 and Mach 25, respectively. Again, though, the decrease in peak heating differences is due to CFD's prediction of peak heating occurring at the wedge shoulder rather than at the leading edge—the actual error at the leading edge is nearly 100%.

5.3.1 Continuum Breakdown

Again, the breakdown parameter is calculated using both the CFD and the DSMC solutions according to Equation 3.26. Continuum breakdown is expected near the leading edge and in the wake, as was the case for the flow of argon, with the degree of nonequilibrium increasing with increasing Knudsen number.

The maximum Kn_{GLL} for each case is plotted in Figures 5.26 and 5.27, with
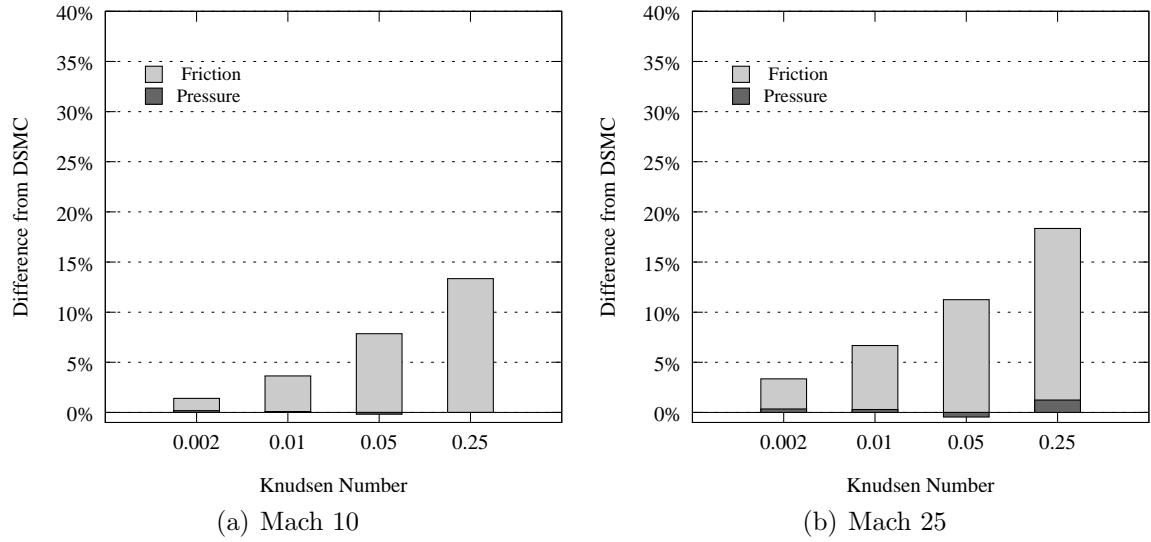
Figure 5.24: Total drag difference from DSMC predicted by CFD for flow of nitrogen about a wedge.

Table 5.5: Peak heat transfer rate for flow of nitrogen about a wedge. The large differences between CFD and DSMC are due to the failure of CFD to predict the high temperatures at the leading edge.

Kn_∞	Mach 10			Mach 25		
	Peak Heating [kW/m^2] (% Difference)					
	DSMC	CFD		DSMC	CFD	
0.002	209.7	56.76	(-72.9%)	3333.	869.5	(-73.9%)
0.01	41.84	11.46	(-72.6%)	663.1	172.9	(-73.9%)
0.05	8.329	2.308	(-72.3%)	132.8	36.62	(-72.4%)
0.25	1.694	1.032	(-39.1%)	27.31	20.89	(-23.5%)

(a) Mach 10   (b) Mach 25
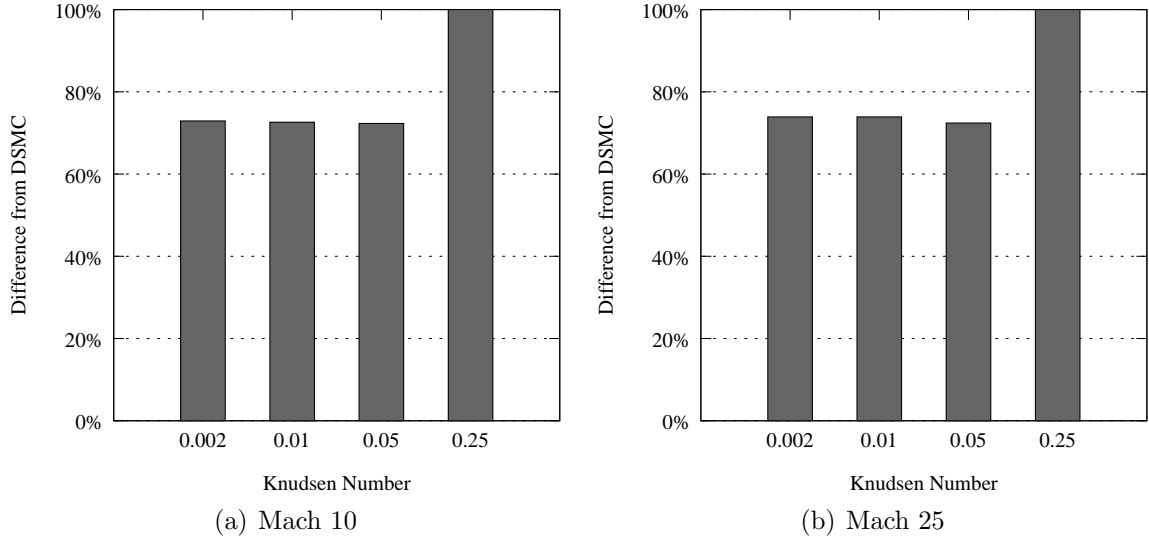
Figure 5.25: Peak heat transfer rate difference from DSMC predicted by CFD for flow of nitrogen about a wedge. The large differences in peak heating are due to the failure of CFD to predict the high temperatures at the leading edge.

the detail of the leading edge in the inset of each frame. The maximum gradient length local Knudsen number is computed from the DSMC (top) and CFD (bottom) solutions. As before, the light gray regions correspond to $Kn_{GLL} < 0.05$, dark gray regions correspond to $Kn_{GLL} < 1.0$ and black regions correspond to $Kn_{GLL} > 1.0$.

The locations and values of the breakdown parameter are very similar to what was seen for argon. A large degree of nonequilibrium is predicted near the leading edge and the wedge shoulder, and as the flow becomes more rarefied, the regions where the continuum breakdown parameter exceeds the critical value of 0.05 grow until nearly all of the computational domain is expected to require DSMC for accurate modeling.

5.3.2 Flow Field Properties

The density ratio fields, where the density is normalized by the free stream density, are shown in Figures 5.28 and 5.29. The density ratio results are very similar
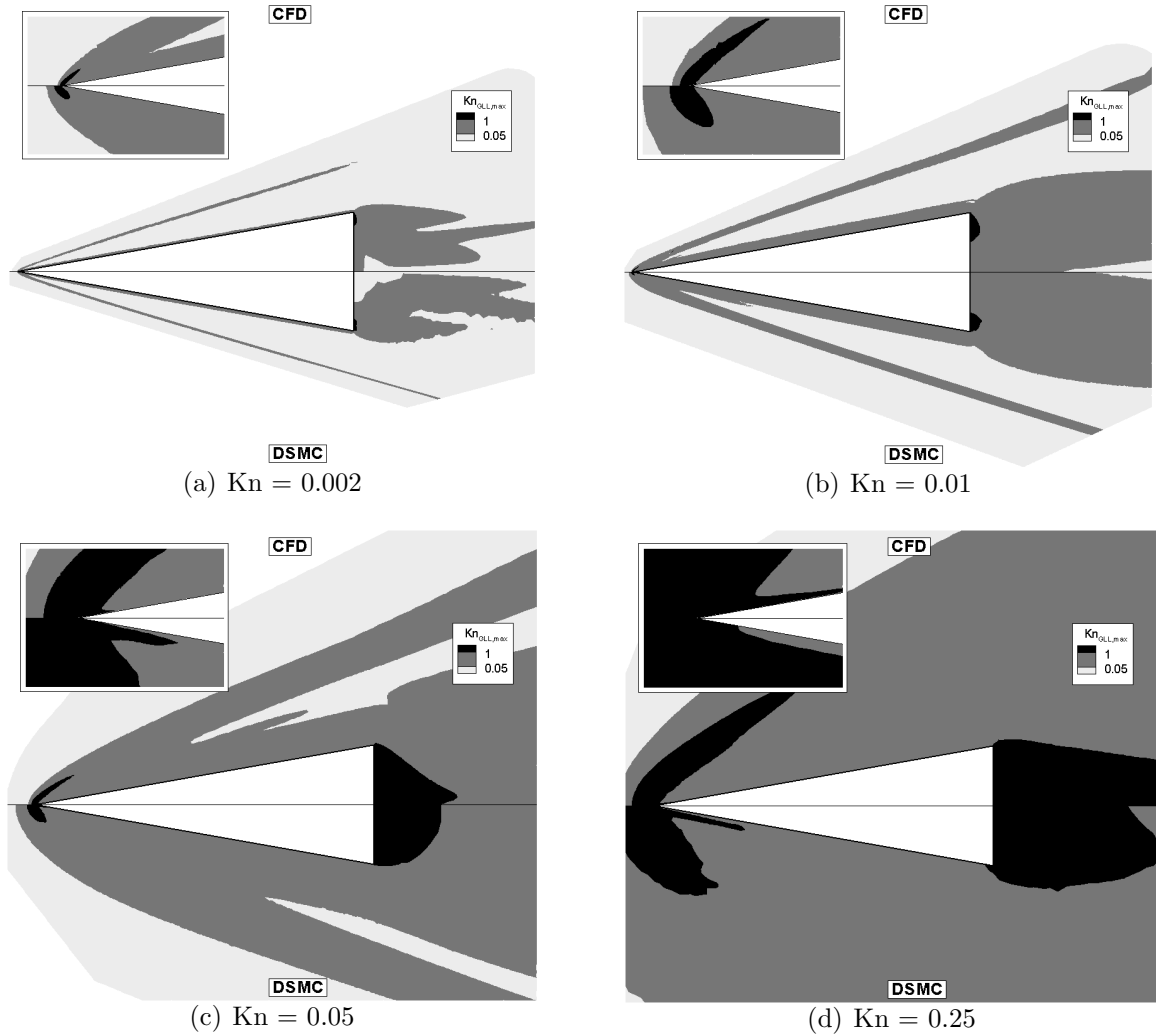
Figure 5.26: Kn_{GLL} field for a Mach 10 flow of nitrogen about a wedge. The light gray regions correspond to $Kn_{GLL} < 0.05$, dark gray regions correspond to $Kn_{GLL} < 1.0$, and black regions correspond to $Kn_{GLL} > 1.0$. Note that the minimum value of Kn_{GLL} for the black regions is an order of magnitude greater than those for the cylinder.
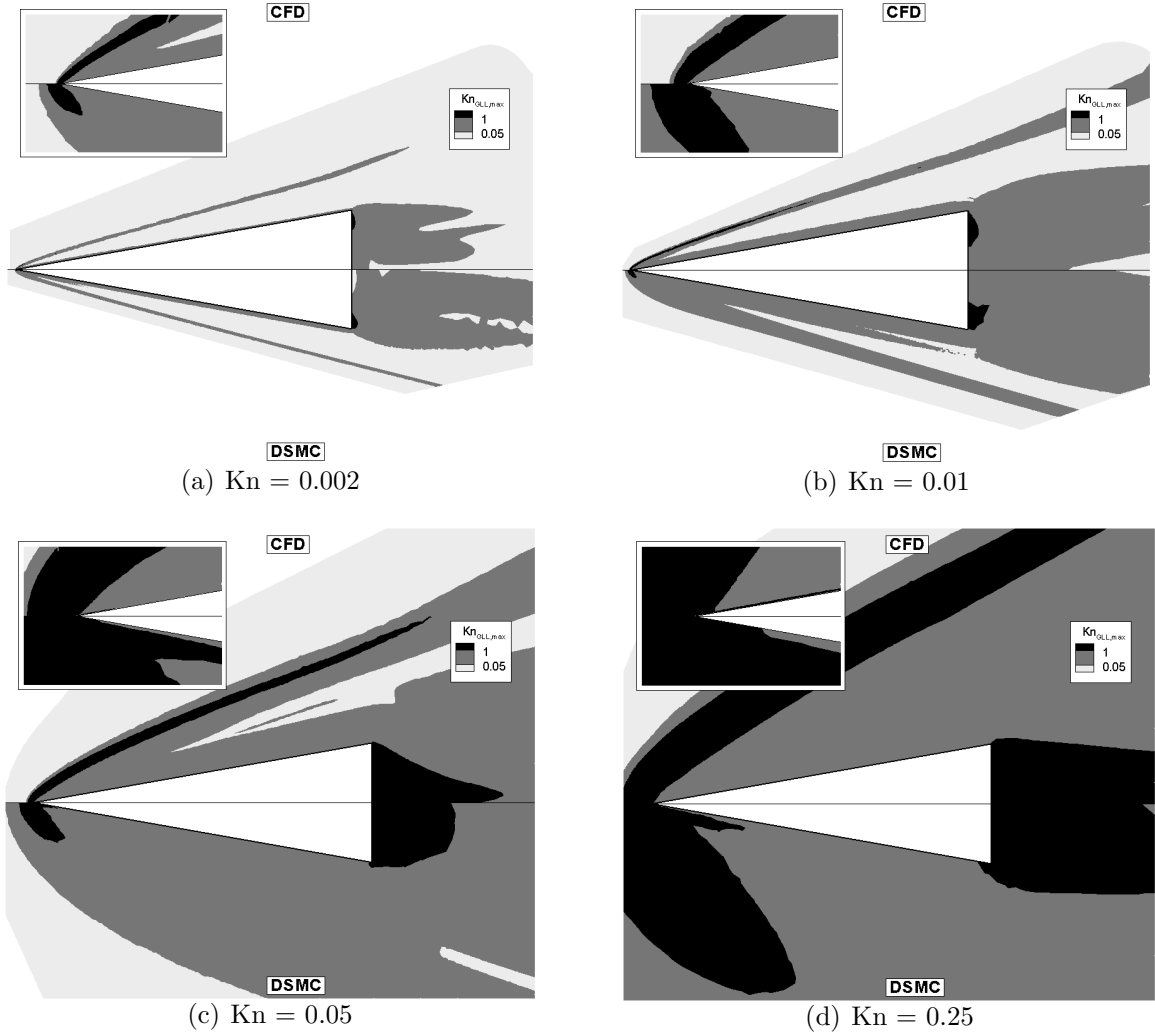
Figure 5.27: Kn$_{GLL}$ field for a Mach 25 flow of nitrogen about a wedge. The light gray regions correspond to Kn$_{GLL}$ < 0.05, dark gray regions correspond to Kn$_{GLL}$ < 1.0, and black regions correspond to Kn$_{GLL}$ > 1.0. Note that the minimum value of Kn$_{GLL}$ for the black regions is an order of magnitude greater than those for the cylinder.
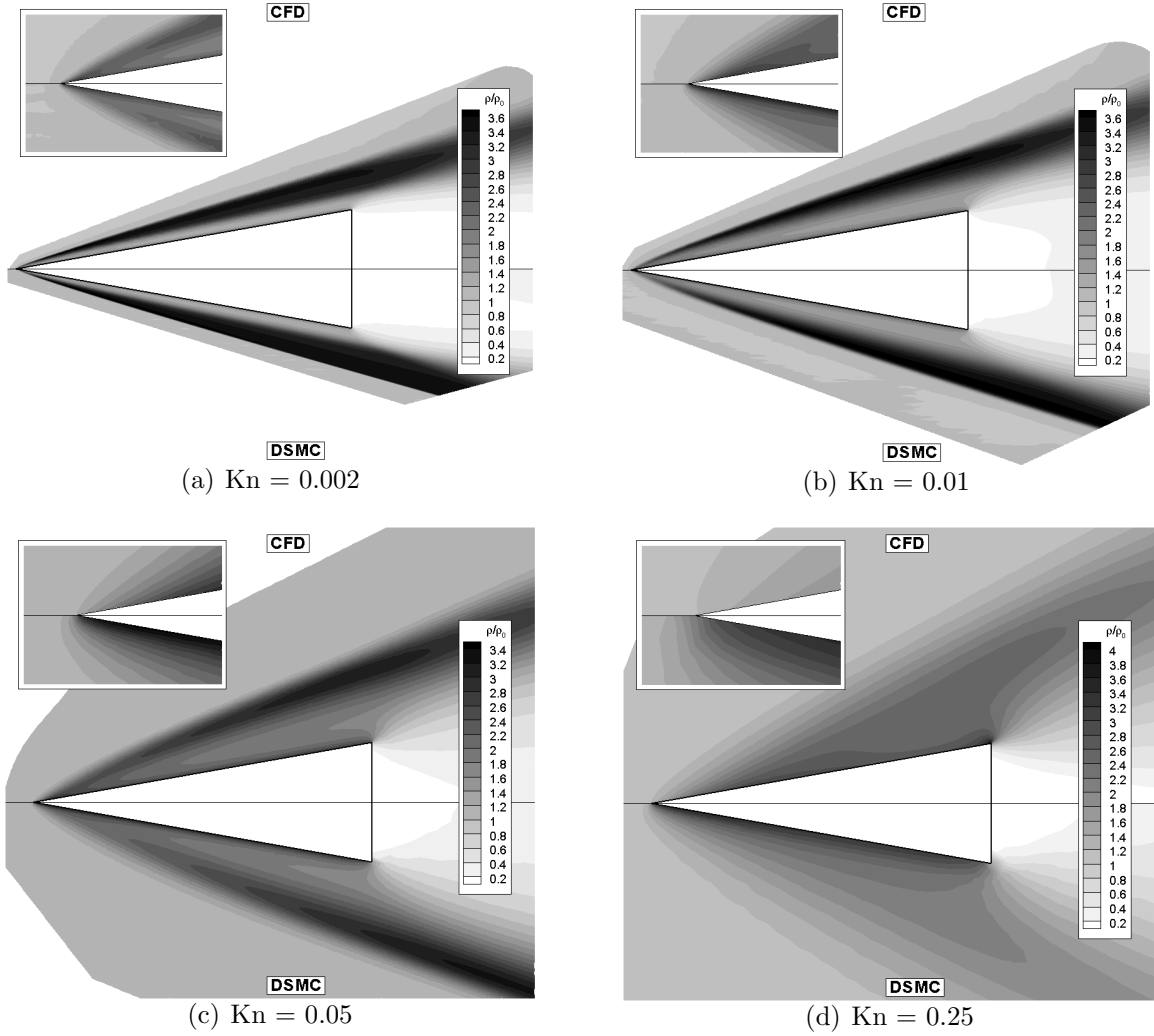
Figure 5.28: Density ratio field for a Mach 10 flow of nitrogen about a wedge.

to those for argon, with the exception that nitrogen achieves a higher compression ratio through the shock; the maximum density ratio is about 3.8 for Mach 10 and about 5 for Mach 25. The shock here is not normal (as with the cylinder), and the compression ratio is not as high as theoretically possible; nevertheless, a diatomic gas can be compressed more than a monatomic gas. DSMC again predicts a higher density near the wedge surface, as seen in the leading-edge details and at the higher Knudsen numbers.

The translational/rotational temperature fields predicted by both CFD and DSMC

(a) Kn = 0.002

(b) Kn = 0.01

(c) Kn = 0.05

(d) Kn = 0.25
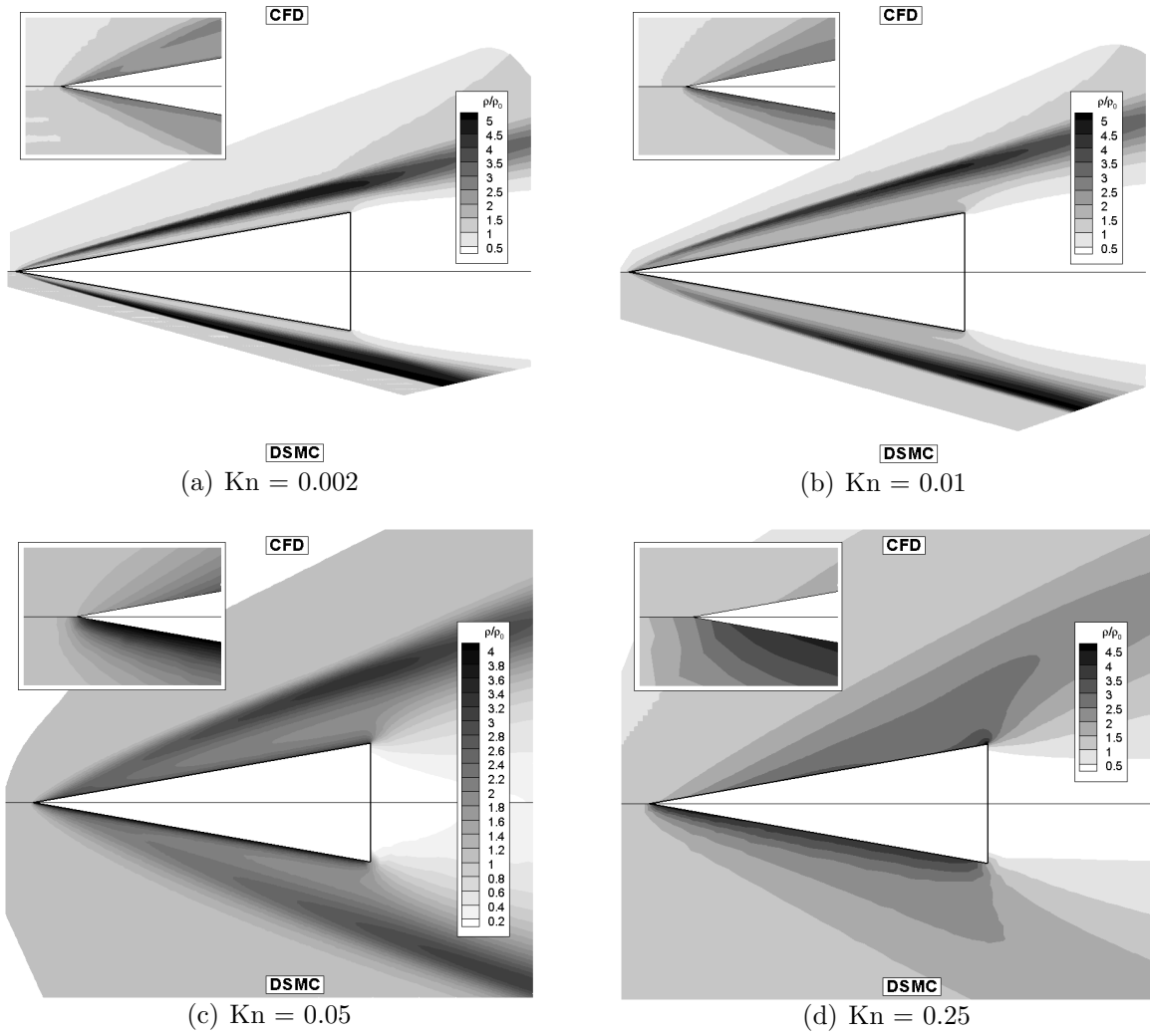
Figure 5.29: Density ratio field for a Mach 25 flow of nitrogen about a wedge.

can be seen in Figures 5.30 and 5.31. Again, the area of most concern is near the leading edge where DSMC predicts a higher temperature than does CFD. Although the peak temperatures in the nitrogen flows are lower than those in the argon flows (around 1,700-1,900 K for Mach 10 and 9,000-10,000 K for Mach 25), CFD again underpredicts the temperature by about 40-50%. Similarly to argon, DSMC always predicts the peak temperature to be at the leading edge, while CFD predicts a higher temperature in the wake for these most rarefied cases.

Due to the additional internal energy modes present in a diatomic gas such as nitrogen, a vibrational temperature is also modeled for the wedge. The vibrational temperature fields are shown in Figures 5.32 and 5.33. For Mach 10, the maximum vibrational temperature is near the wall temperature of 500 K, again indicating (along with the relatively low translational/rotational temperatures of approximately 2,000 K) that the vibrational modes are only activated due to the wall boundary conditions. The effects of the CFD temperature jump conditions are seen in Figure 5.32 as the vibrational temperature does not attain the wall temperature of 500 K right at the leading edge.

The Mach 25 cases do exhibit some vibrational excitation due to elevated temperatures; the peak vibrational temperature is about 1,800 K for the Mach 25, $Kn = 0.002$ case. Here it is also seen that DSMC predicts a higher level of vibrational activation than does CFD. This is most likely due to the method used to adjust the DSMC vibrational collision probability to match the theoretical vibrational collision probability, as explained in Chapter III. Recall that the DSMC vibrational collision probability is multiplied by a correction factor based on the maximum translational temperature seen in the flow field. Here, the maximum translational temperatures are approximately 10,000 K, and a correction factor of 1.43 is used (see Table 3.2).
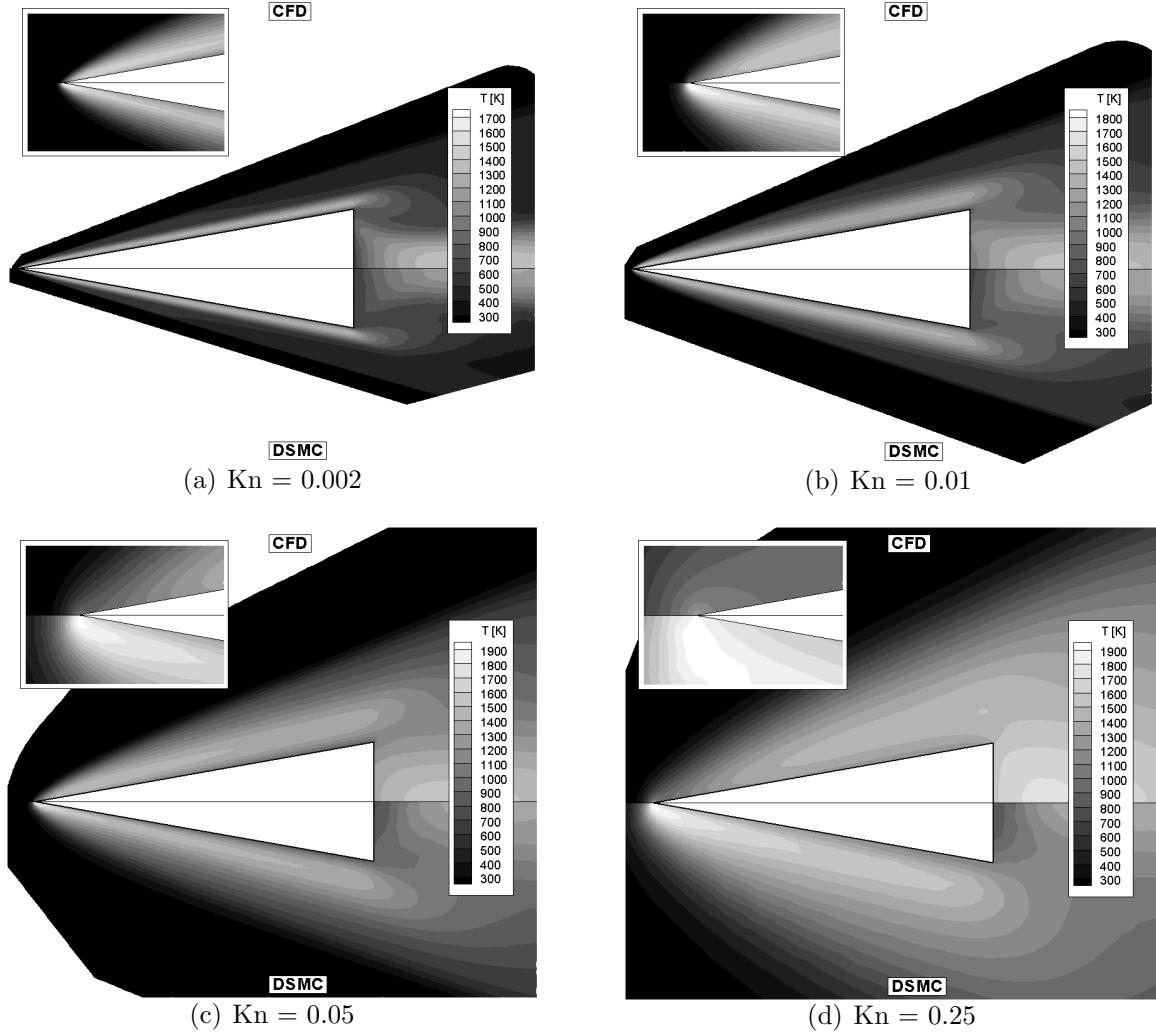
Figure 5.30: Translational/rotational temperature field for a Mach 10 flow of nitrogen about a wedge. DSMC predicts a much higher temperature than CFD near the leading edge (inset). Note that CFD predicts a higher temperature in the wake than near the leading edge for Kn = 0.25, while DSMC predicts a maximum temperature at the leading edge.

(a) Kn = 0.002

(b) Kn = 0.01

(c) Kn = 0.05

(d) Kn = 0.25
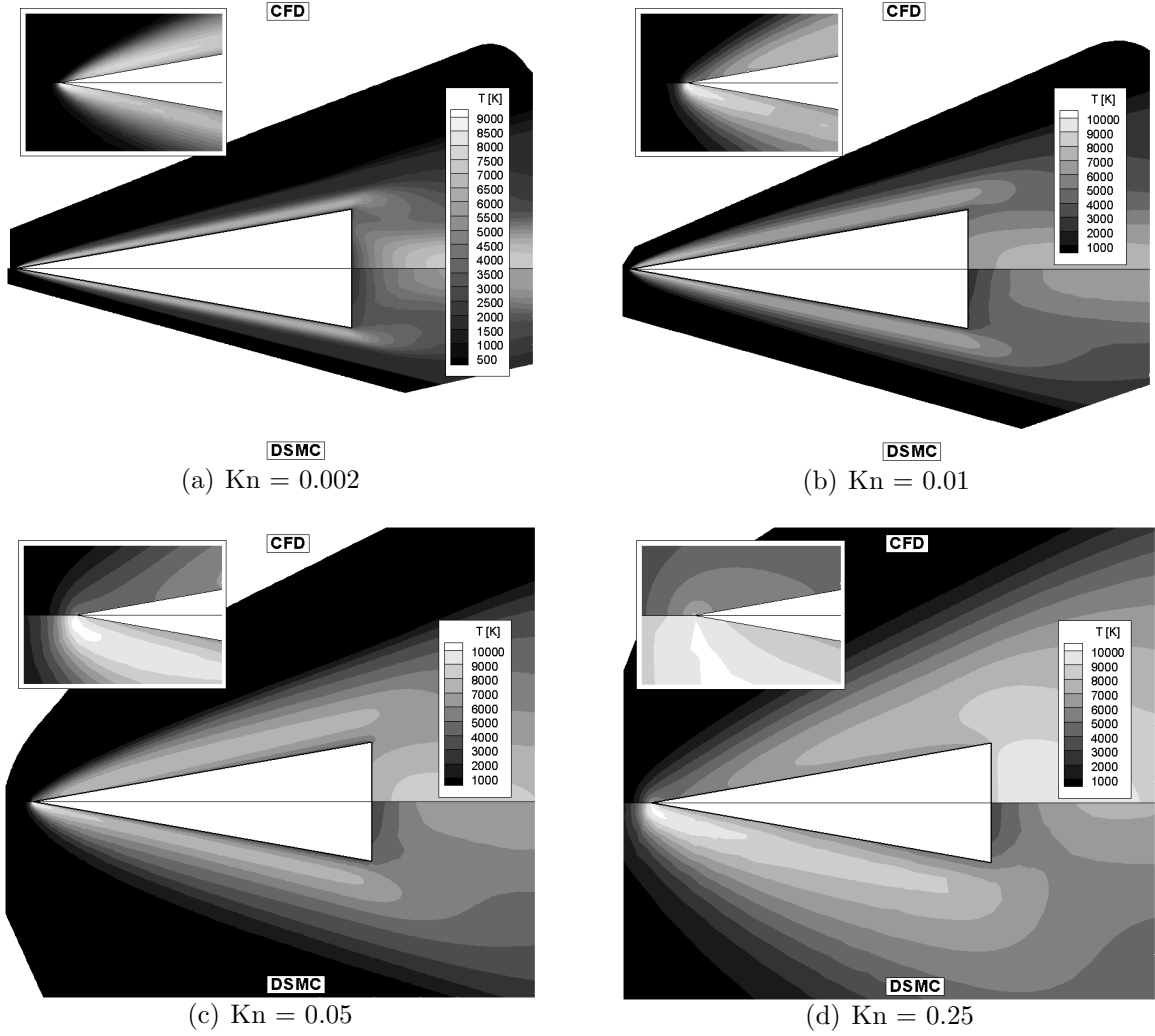
Figure 5.31: Translational/rotational temperature field for a Mach 25 flow of nitrogen about a wedge. DSMC predicts a much higher temperature than CFD near the leading edge (inset). Note that CFD predicts a higher temperature in the wake than near the leading edge for Kn = 0.25, while DSMC predicts a maximum temperature at the leading edge.
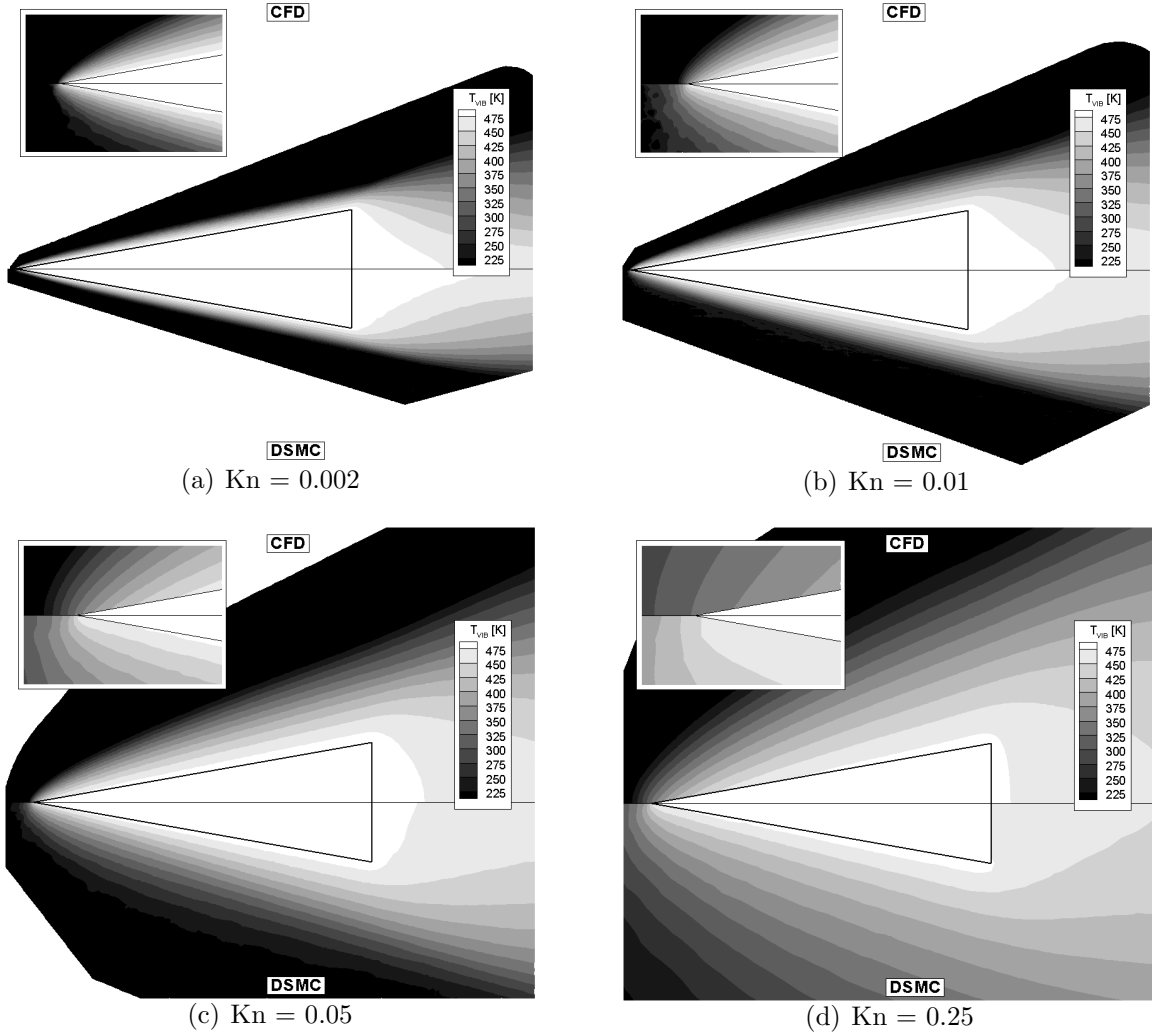
Figure 5.32: Vibrational temperature field for a Mach 10 flow of nitrogen about a wedge. Note that the vibrational activation is due to the wall vibrational temperature of 500 K.

However, the maximum vibrational temperatures are not near the leading edge of the wedge, but further back along the surface where the translational/rotational temperatures are much lower, around 4,000-5,000 K. The DSMC vibrational collision probability for temperatures in that range are higher than the theoretical model (again see Table 3.2 and Figure 3.2); thus the correction factor should be smaller than unity (around 0.79), rather than larger. Nevertheless, vibrational temperature differences do not seem to affect the surface properties significantly.

(a) Kn = 0.002

(b) Kn = 0.01

(c) Kn = 0.05

(d) Kn = 0.25
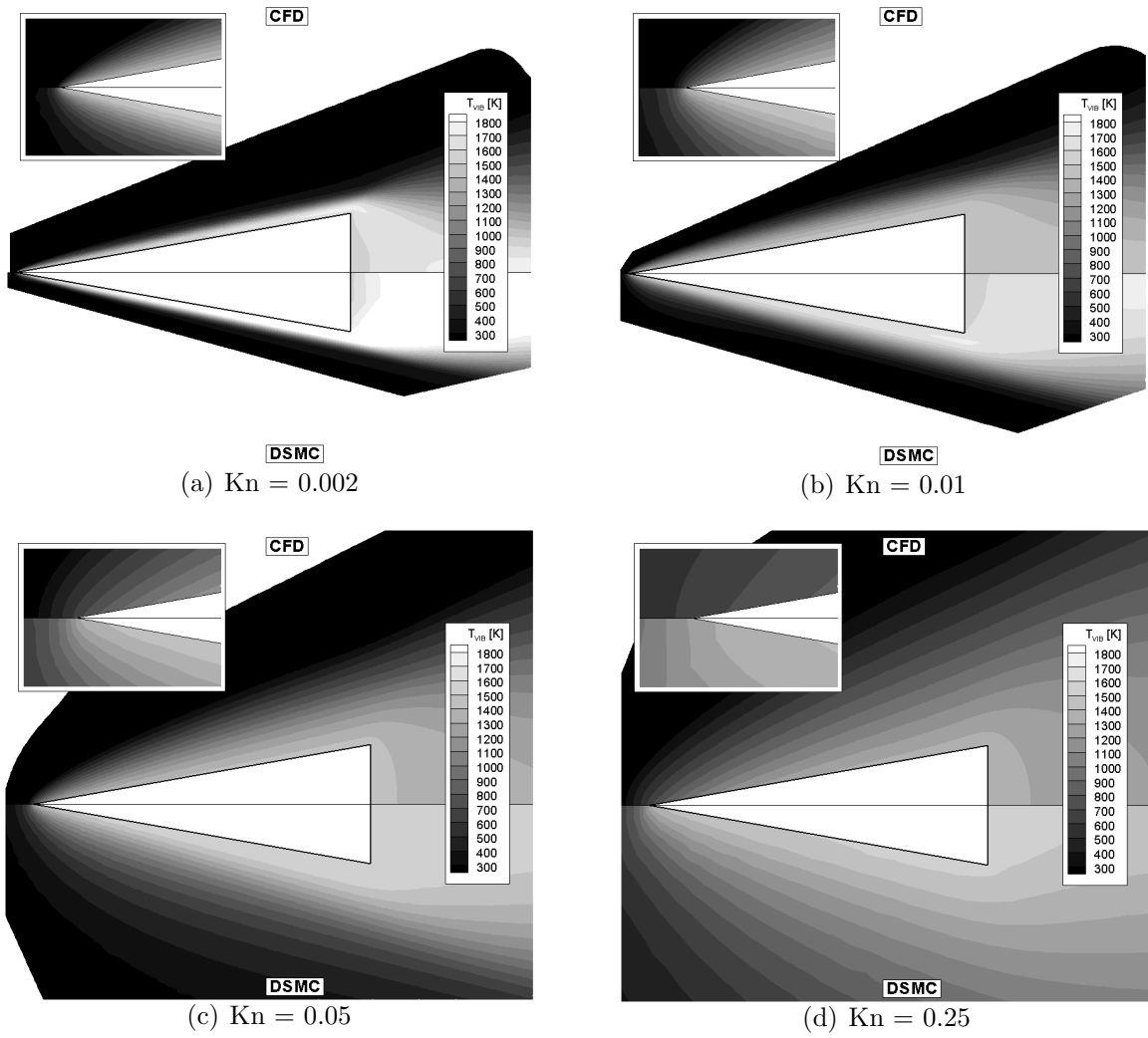
Figure 5.33: Vibrational temperature field for a Mach 25 flow of nitrogen about a wedge. Note that the wall vibrational temperature is 1500 K.

5.3.3 Surface Properties

The surface property distributions (pressure, shear stress and heat flux) for each of the cases are now examined. The surface pressure, in the form of a pressure coefficient, is shown in Figures 5.34 and 5.35. The overall CFD pressure distribution agrees qualitatively with DSMC for all but the Kn = 0.25 case, but the peak pressure at the leading edge is overpredicted by CFD. The distributions also start to differ in the wake for Kn = 0.05 and Kn = 0.25, with CFD predicting a large spike in the pressure at $S/L = 1$ as the flow begins to expand into the wake. In all cases, CFD tends to overpredict the pressure and there is some effect of the pressure on the overall overprediction of total drag by CFD, although this effect is not as great as that of shear stress, as was shown in Figure 5.24.

The shear stress on the wedge surface is seen in Figures 5.36 and 5.37. The large spike in the CFD shear stress at the leading edge does not significantly affect the total drag, and the value of this peak is annotated on the plots. Other than this peak at the leading edge, there are fewer differences in the shear stress than there were for the pressure. However, the total drag is affected most by the friction forces. Again, this is explained by noting the much larger effect that shear stress has on the total drag as seen in Figure 5.3.

Figures 5.38 and 5.39 compare the accumulated total drag along the wedge surface due to both friction and pressure forces for the nitrogen cases. Thus, the differences in friction drag for Kn = 0.002 and Kn = 0.01 occur along the first 20% of the wedge surface. For Kn = 0.05, the area where the difference accumulates most is in the first 40-50% of the wedge surface; and for Kn = 0.25, the differences accumulate mostly between 20% and 80% of the wedge length. The same trends are noted here with nitrogen as they were with argon:

(a) Kn = 0.002

(b) Kn = 0.01

(c) Kn = 0.05

(d) Kn = 0.25

Figure 5.34: Surface pressure coefficient for a Mach 10 flow of nitrogen about a wedge. The maximum value of Kn_{GLL} near the surface plotted on the right axis. The distance along the surface (including the base), S, is normalized by the top surface length, L.

(a) Kn = 0.002

(b) Kn = 0.01

(c) Kn = 0.05

(d) Kn = 0.25
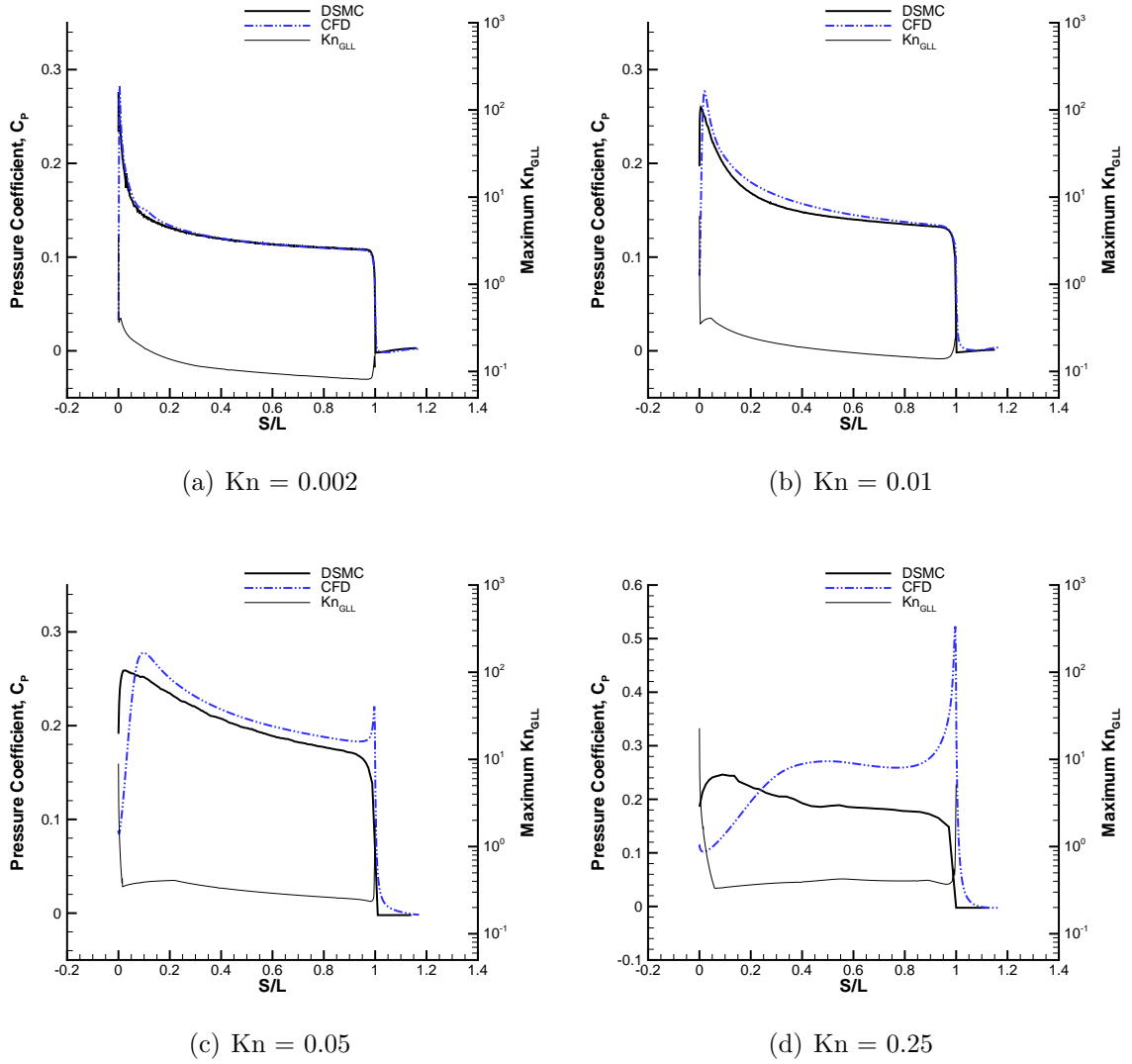
Figure 5.35: Surface pressure coefficient for a Mach 25 flow of nitrogen about a wedge. The maximum value of $\mathrm{Kn_{GLL}}$ near the surface plotted on the right axis. The distance along the surface (including the base), S, is normalized by the top surface length, L.

(a) Kn = 0.002

(b) Kn = 0.01

(c) Kn = 0.05

(d) Kn = 0.25

Figure 5.36: Surface friction coefficient for a Mach 10 flow of nitrogen about a wedge. The maximum value of Kn_{GLL} near the surface plotted on the right axis. The distance along the surface (including the base), S, is normalized by the top surface length, L.

(a) Kn = 0.002

(b) Kn = 0.01
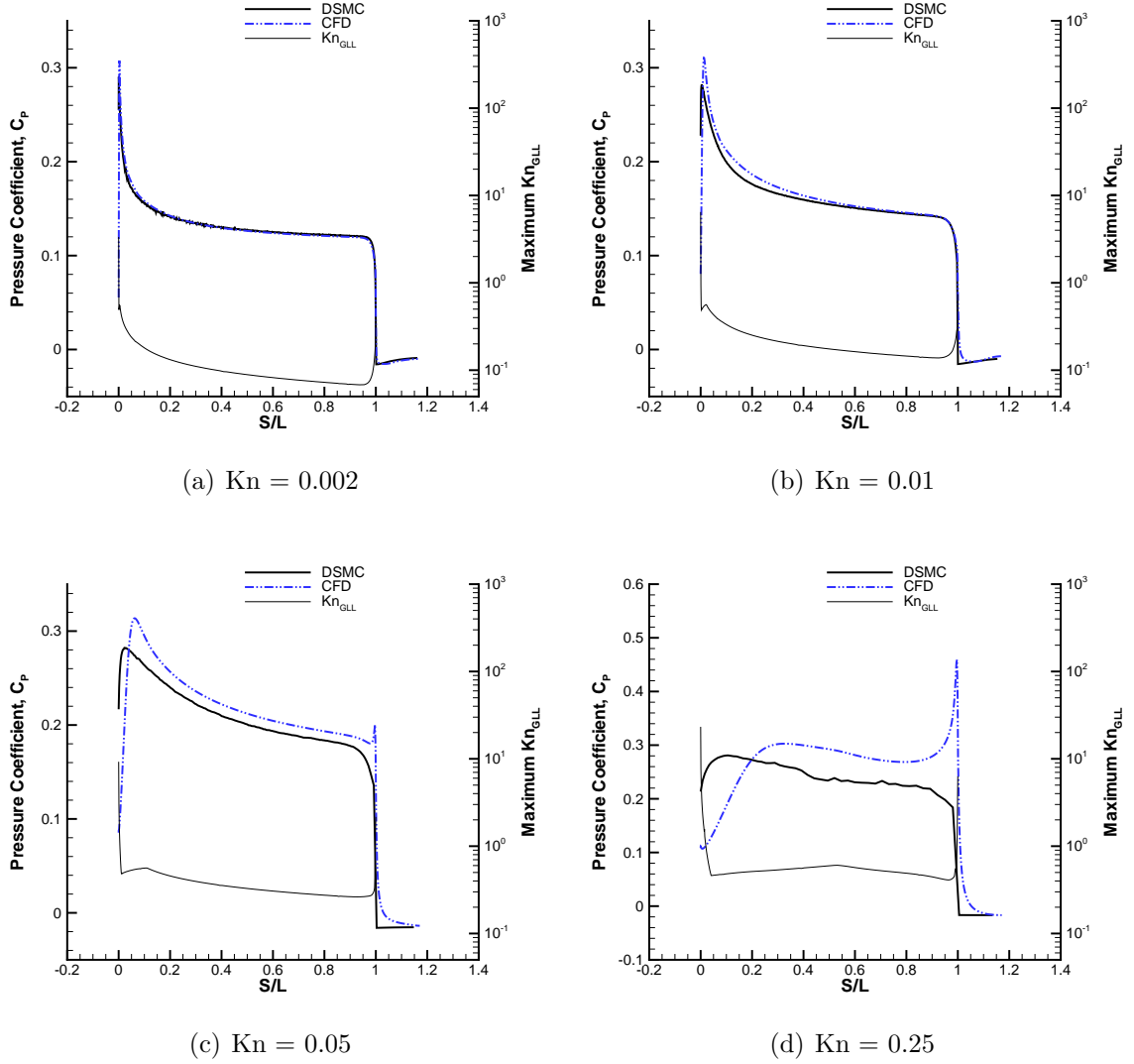
(c) Kn = 0.05

(d) Kn = 0.25

Figure 5.37: Surface friction coefficient for a Mach 25 flow of nitrogen about a wedge. The maximum value of $\mathrm{Kn_{GLL}}$ near the surface plotted on the right axis. The distance along the surface (including the base), S, is normalized by the top surface length, L.

- The large value of skin friction coefficient at the leading edge does not significantly affect the total drag.

- The contribution of friction forces to the total drag increases as the density decreases.

- There is no contribution to total drag due to friction forces in the wake.

- Pressure forces on the base of the wedge (in the wake) decrease the total drag.

- There is little disagreement in the predictions of total drag due to pressure forces for most cases.

Additionally, the good agreement between drag due to pressure, as Figure 5.24 shows, is not due to perfect agreement between the pressure distributions along the entire surface (as discussed above). Instead, the accumulated drag due to pressure does show some differences along the surface, but the final total values happen to agree.

The heat transfer rate distributions are shown in Figures 5.40 and 5.41. Previously, it was shown that DSMC predicts a much higher temperature at the leading edge. The inability of CFD to model the flow at the leading edge again has a large effect on the heat flux. The same general trends with argon are seen here, although a larger heat flux coefficient is predicted for nitrogen. The peak DSMC heating coefficients remain near 0.22, and the peak CFD heating coefficients remain well under 0.1. Thus, the difference in heating rate is also around 70% for most of the cases. For $Kn = 0.25$, CFD predicts a peak heating rate at the shoulder, with no heating predicted at the leading edge. Thus, the actual error in heating rate prediction is much greater than the 40% and 25% cited in Table 5.5 and shown in Figure 5.25.
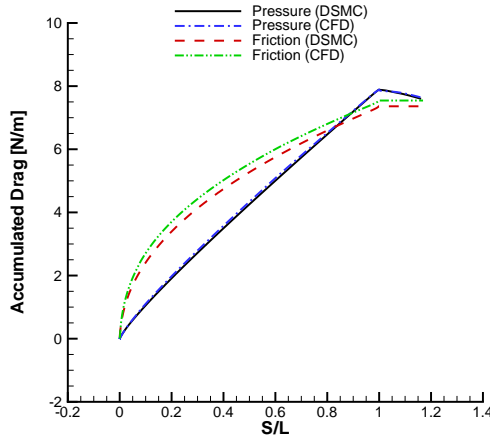
(a) Kn = 0.002
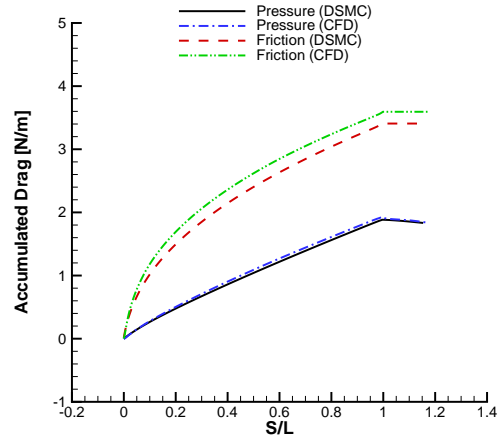
(b) Kn = 0.01
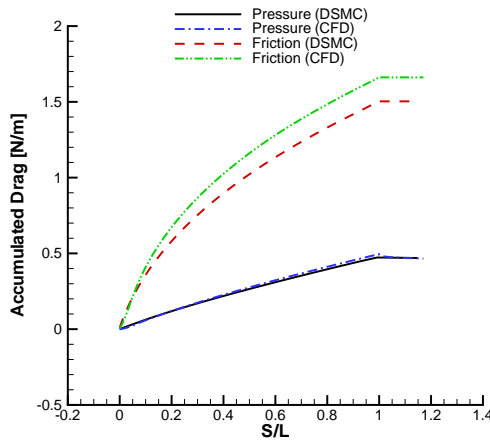
(c) Kn = 0.05
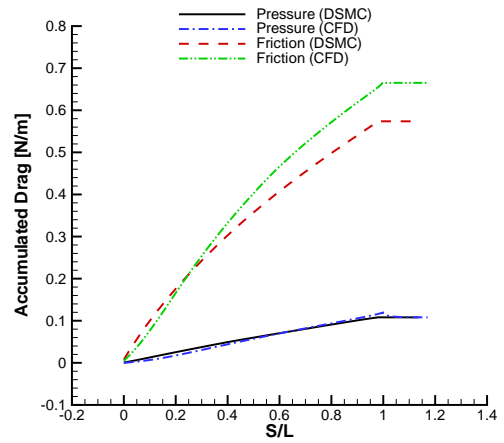
(d) Kn = 0.25

Figure 5.38: Contributions of pressure and skin friction forces to accumulated total drag for a Mach 10 flow of nitrogen about a wedge. The distance along the surface (including the base), S, is normalized by the top surface length, L.

(a) Kn = 0.002

(b) Kn = 0.01

(c) Kn = 0.05

(d) Kn = 0.25

Figure 5.39: Contributions of pressure and skin friction forces to accumulated total drag for a Mach 25 flow of nitrogen about a wedge. The distance along the surface (including the base), S, is normalized by the top surface length, L.

(a) Kn = 0.002

(b) Kn = 0.01

(c) Kn = 0.05

(d) Kn = 0.25
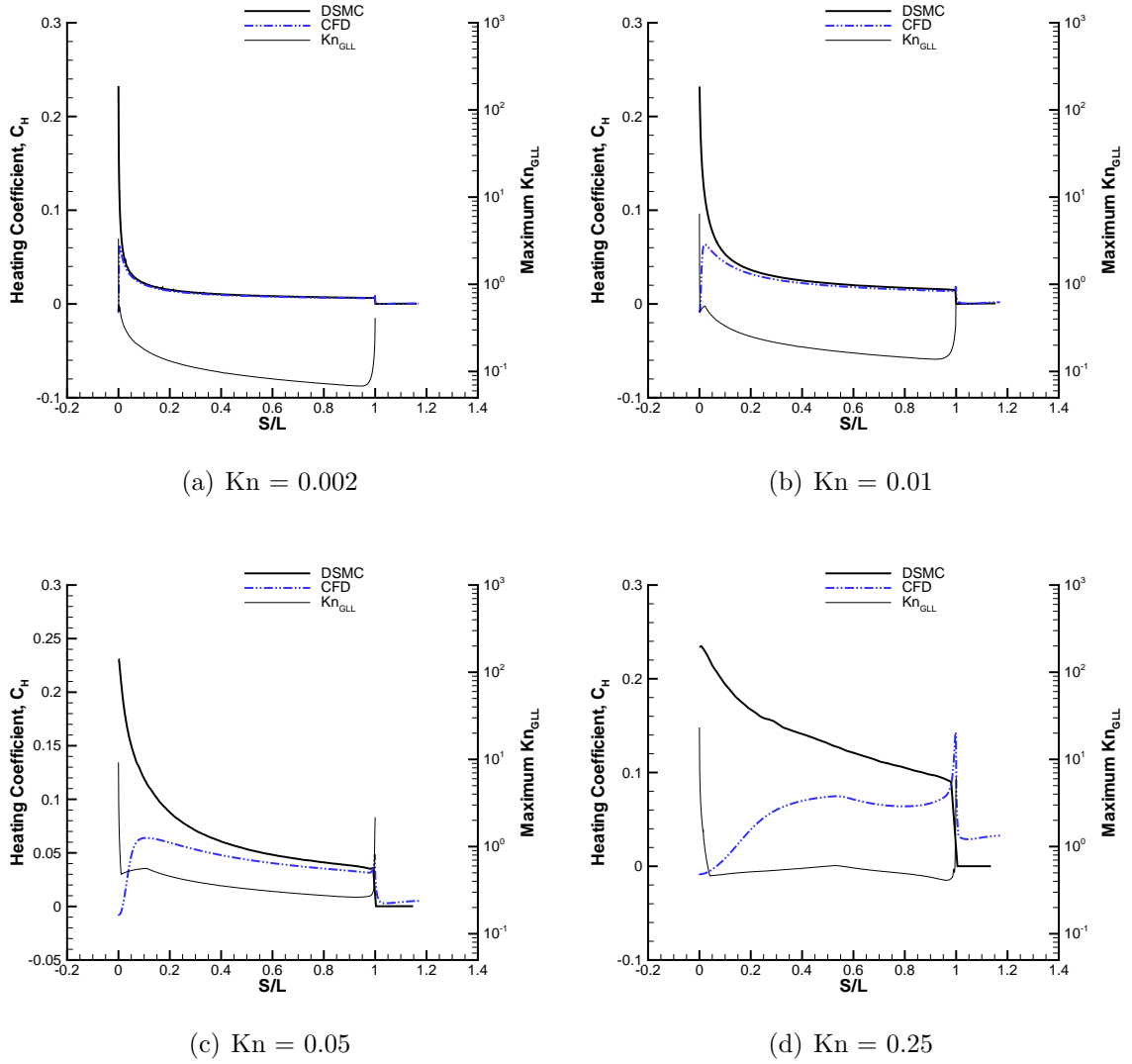
Figure 5.40: Surface heating coefficient for a Mach 10 flow of nitrogen about a wedge. The maximum value of $\mathrm{Kn_{GLL}}$ near the surface plotted on the right axis. The distance along the surface (including the base), S, is normalized by the top surface length, L.
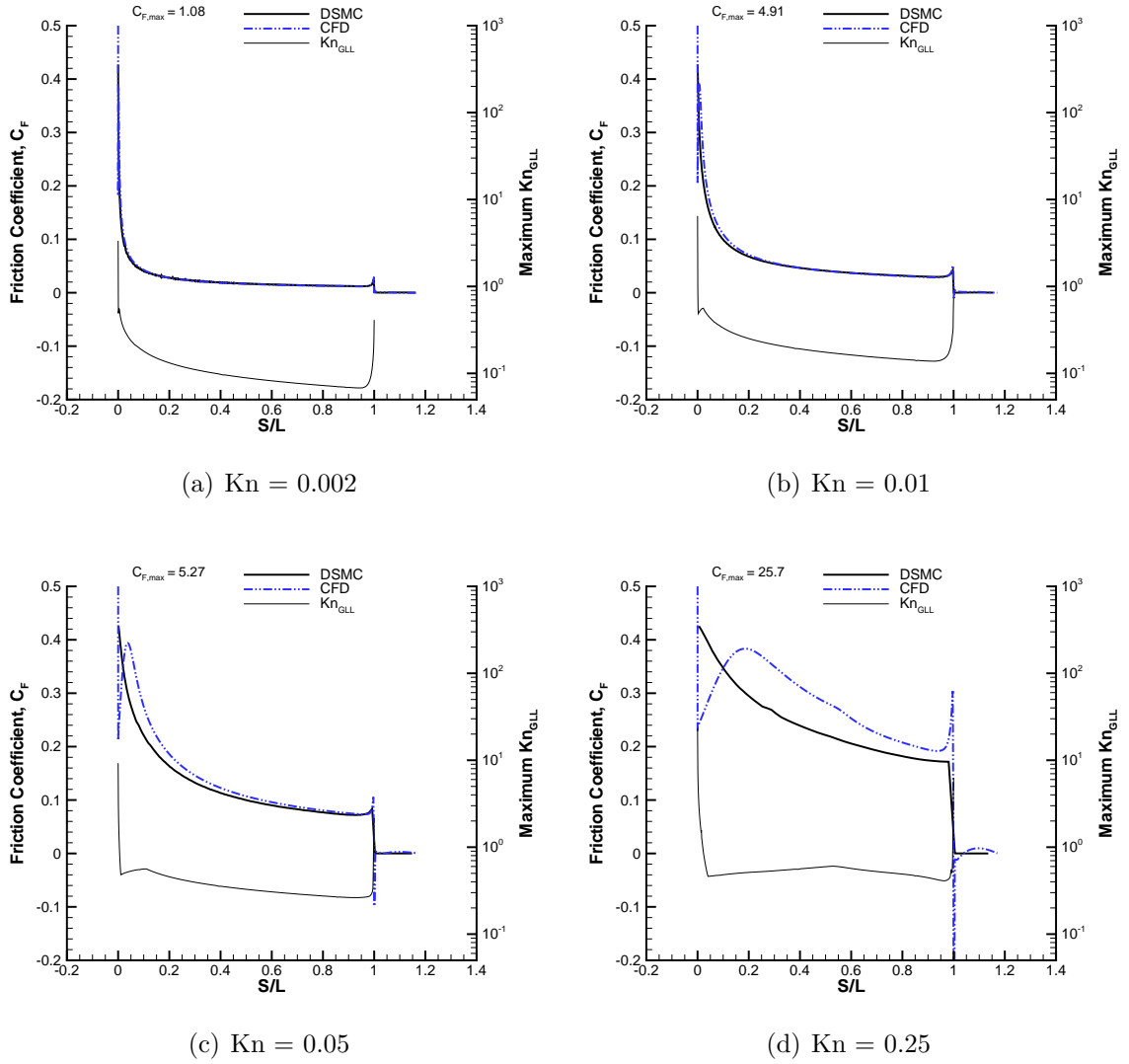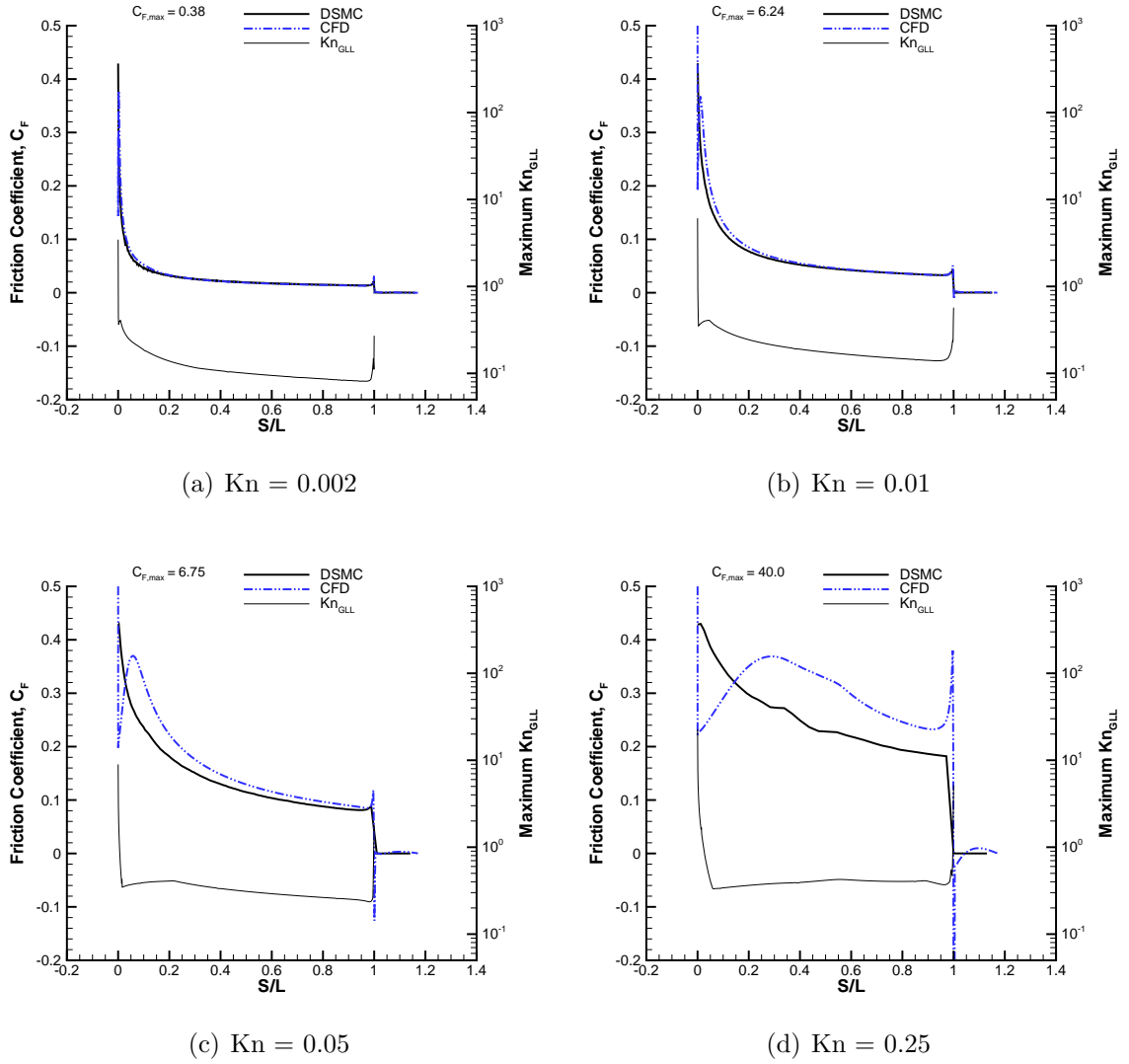
(a) Kn = 0.002

(b) Kn = 0.01

(c) Kn = 0.05

(d) Kn = 0.25
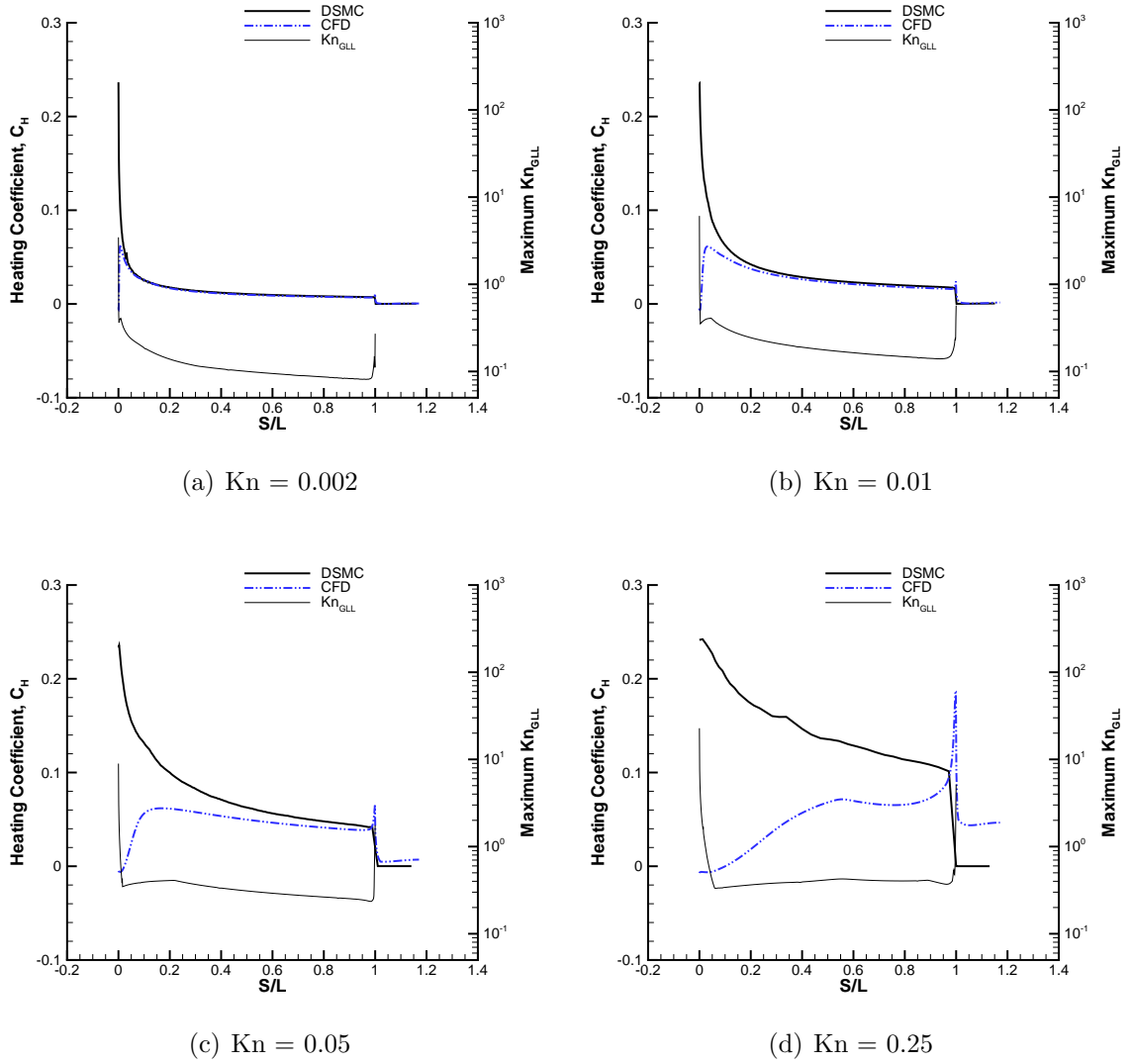
Figure 5.41: Surface heating coefficient for a Mach 25 flow of nitrogen about a wedge. The maximum value of Kn_{GLL} near the surface plotted on the right axis. The distance along the surface (including the base), S, is normalized by the top surface length, L.

5.3.4 Slip Quantities

The velocity slip along the wedge surface is shown in Figures 5.42 and 5.43. Overall, the velocity slip profiles are very similar to those obtained with argon. Here, CFD predicts a peak velocity slip between 2,000-2,500 m/s for Mach 10 and between 5000-6,000 m/s for Mach 25 near the leading edge, while DSMC predicts a maximum velocity slip of about 750 m/s for Mach 10 and about 1,500 m/s for Mach 25. For $Kn = 0.002$, $Kn = 0.01$ and even $Kn = 0.05$ to some extent, CFD qualitatively agrees fairly well with DSMC. However, for $Kn = 0.25$ this agreement worsens considerably. Once again, the locations where the disagreement is most apparent, at and near the leading edge, are also the locations where the shear stress distributions differ the most. Thus, there is a good correlation between velocity slip disagreement and shear stress disagreement.

The translational/rotational temperature jump profiles for the nitrogen flows, shown in Figures 5.44 and 5.45, are qualitatively similar to the temperature jump profiles obtained for argon. Also included here are the translational and rotational temperature jump values from the DSMC simulations. Although the peak translational temperature jump values predicted by DSMC are nearly 2,000 K for Mach 10 and nearly 10,000 K for Mach 25, which are near those predicted for argon, there is significant thermal nonequilibrium and the rotational temperature jump is much lower than the translational temperature jump; at the leading edge, the rotational temperature jump is negative. For $Kn = 0.05$ and $Kn = 0.25$, the translational and rotational temperatures along the surface never do fully equilibrate, although they are closer to equilibrium at the base of the wedge. Nevertheless, CFD agrees moderately well with the averaged translational/rotational temperature jump predicted by DSMC for the lower Knudsen number flows for Mach 10; there is more disagreement
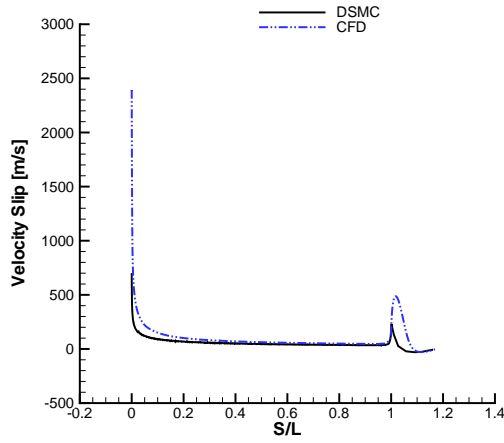
(a) Kn = 0.002
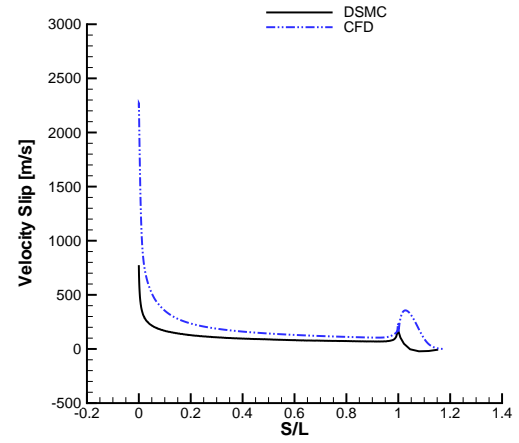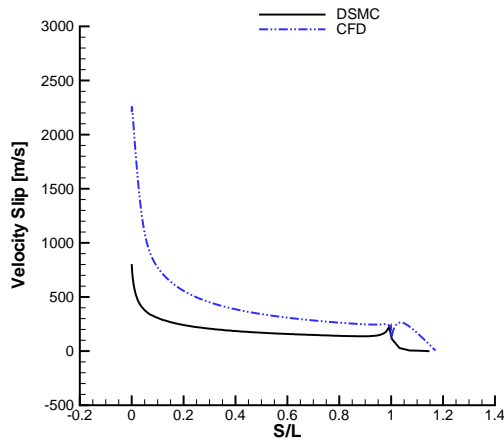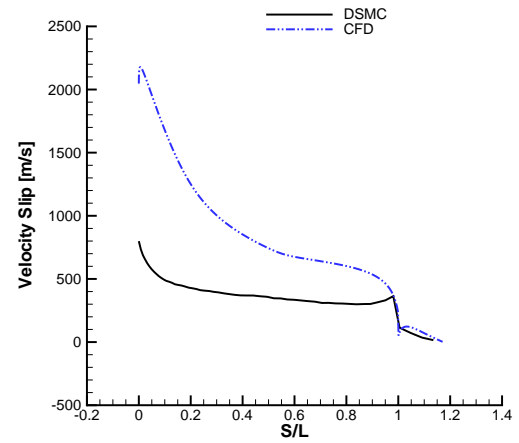
(b) Kn = 0.01

(c) Kn = 0.05

(d) Kn = 0.25

Figure 5.42: Velocity slip for a Mach 10 flow of nitrogen about a wedge. The distance along the surface (including the base), S, is normalized by the top surface length, L.
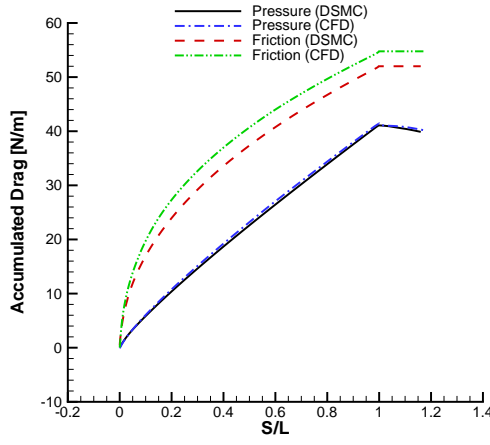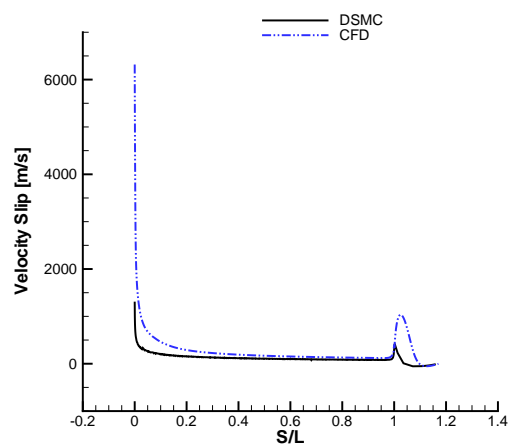
(a) Kn = 0.002
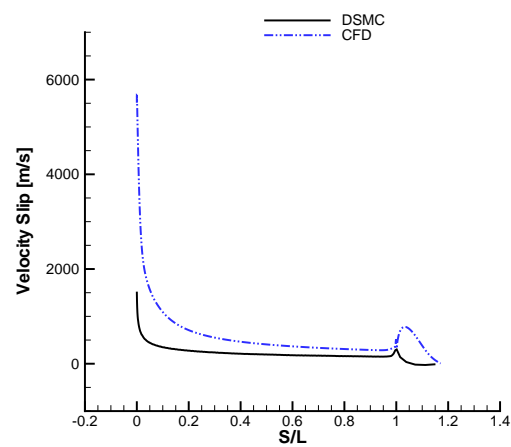
(b) Kn = 0.01
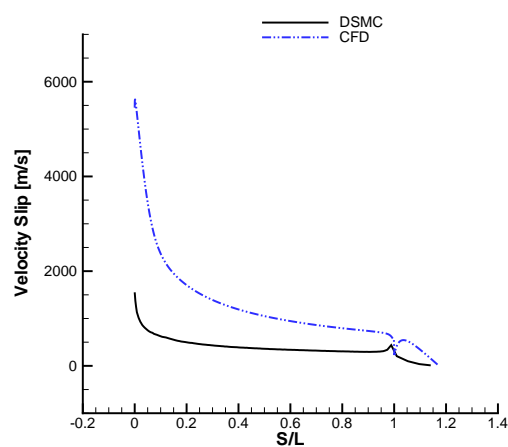
(c) Kn = 0.05
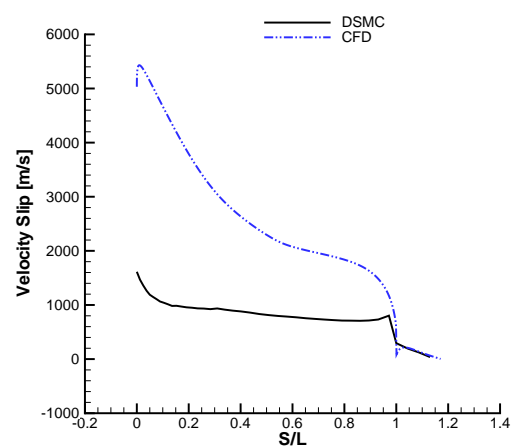
(d) Kn = 0.25

Figure 5.43: Velocity slip for a Mach 25 flow of nitrogen about a wedge. The distance along the surface (including the base), S, is normalized by the top surface length, L.
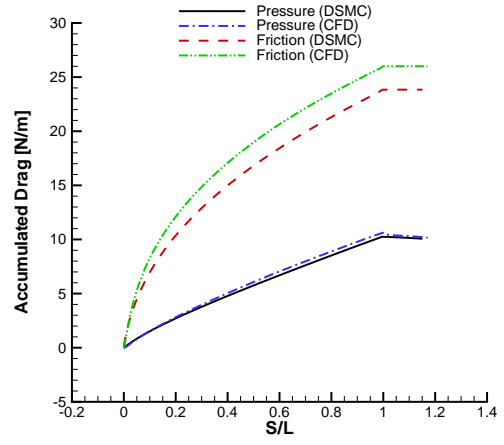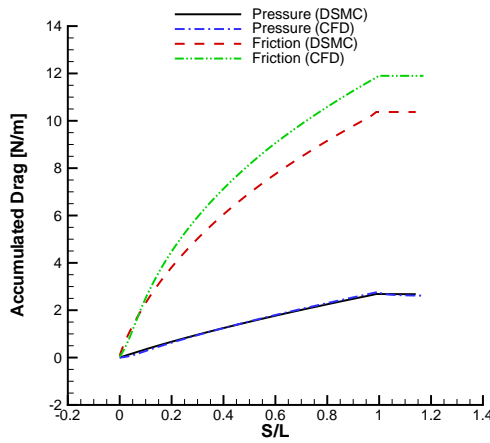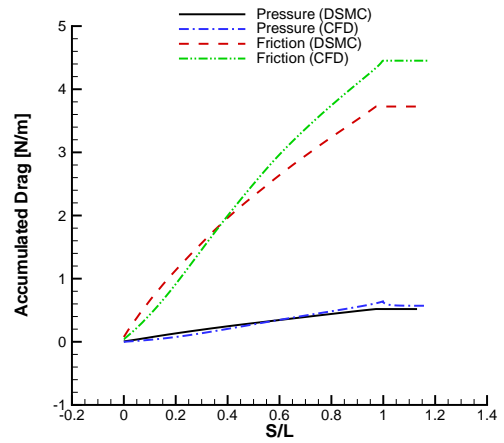
for Mach 25.

The vibrational temperature jump is also seen in Figures 5.46 and 5.47. For Mach 10, there is very little vibrational excitation and the vibrational temperature jump predicted by both methods is near zero, except at the leading edge where CFD overpredicts the amount of vibrational temperature slip. The Kn = 0.25 case is an exception, where DSMC predicts a small, negative, temperature jump value. For Mach 25, the situation is very similar to that for Mach 10, except that the differences between CFD and DSMC are more pronounced for Kn = 0.01 and Kn = 0.05.

5.3.5   Computational Details

The computational details for the simulations of a hypersonic nitrogen flow about a wedge discussed in this section are shown in Table 5.6.

5.4   Summary—Hypersonic Flow about a Wedge

The sharp-leading edge geometry of the wedge leads to additional flow phenomena not seen with the cylinder, which in turn affect the surface property predictions.

The differences in total drag predicted by CFD and DSMC are greater than they were with the cylinder geometry, due to the larger effect of the friction forces on the drag. Additionally, there are greater differences in the pressure profiles along the wedge surface, but the effect on total drag is relatively small (due to the small angle of the surface with the flow).

The amount of nonequilibrium near the leading-edge significantly affects the prediction of temperature gradients, and thus there are significant differences in the heat transfer rate predictions–CFD fails to adequately predict the large heat fluxes near the leading edge of an infinitely-sharp wedge.
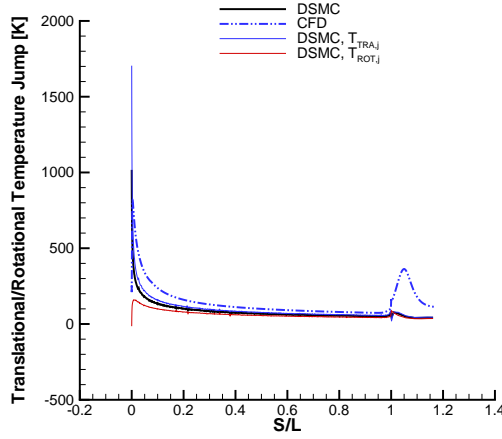
(a) Kn = 0.002
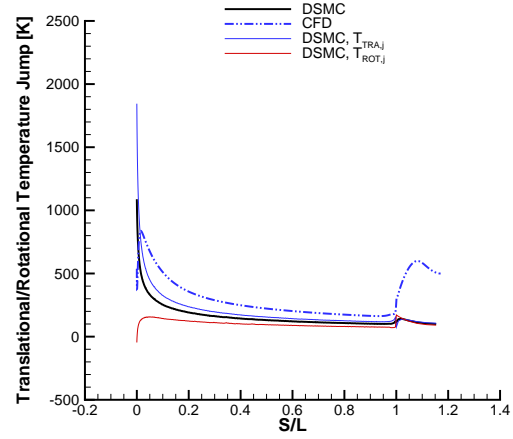
(b) Kn = 0.01
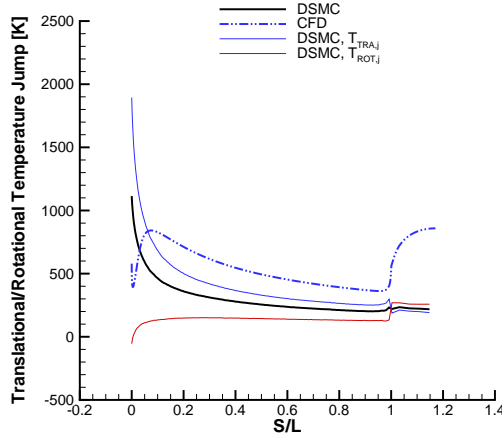
(c) Kn = 0.05
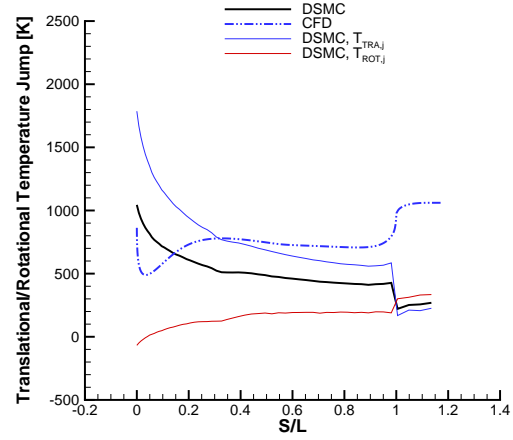
(d) Kn = 0.25

Figure 5.44: Translational/rotational temperature jump for a Mach 10 flow of nitrogen about a wedge. The separate translational and rotational temperature jumps from DSMC are plotted along with the average temperature jump from CFD and DSMC. The distance along the surface (including the base), S, is normalized by the top surface length, L.
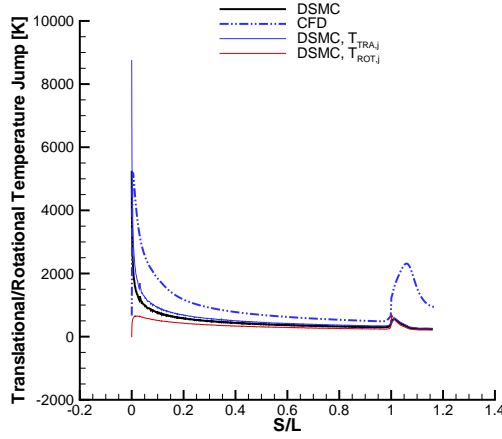
(a) Kn = 0.002
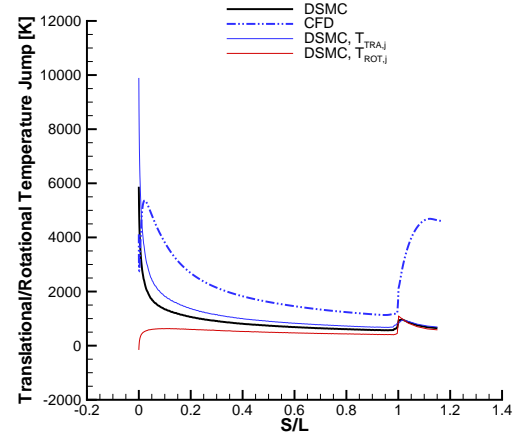
(b) Kn = 0.01
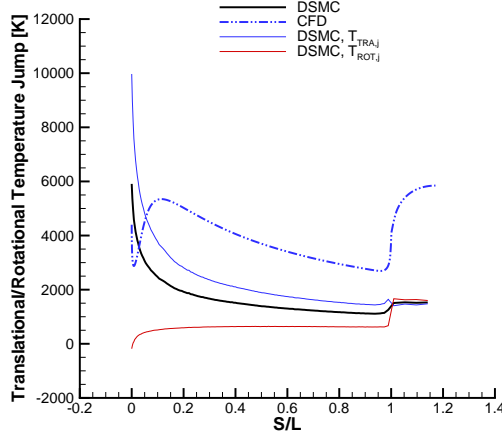
(c) Kn = 0.05
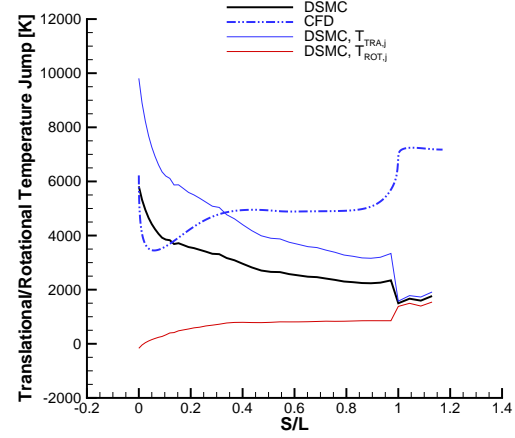
(d) Kn = 0.25

Figure 5.45: Translational/rotational temperature jump for a Mach 25 flow of nitrogen about a wedge. The separate translational and rotational temperature jumps from DSMC are plotted along with the average temperature jump from CFD and DSMC. The distance along the surface (including the base), S, is normalized by the top surface length, L.
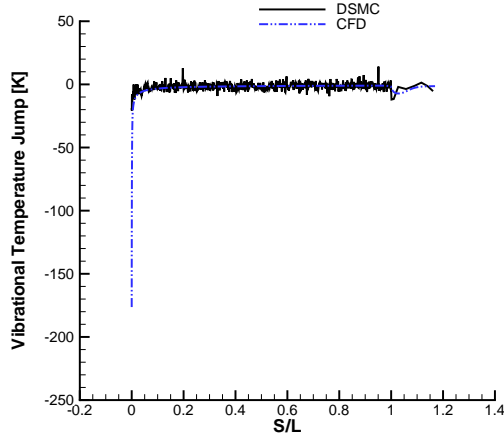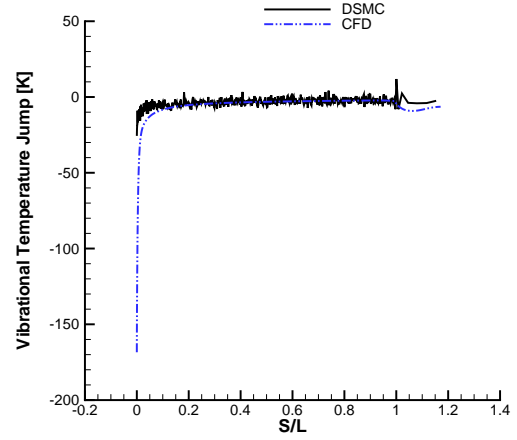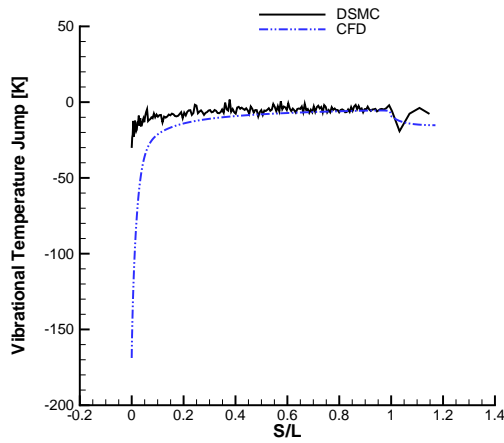
(a) Kn = 0.002
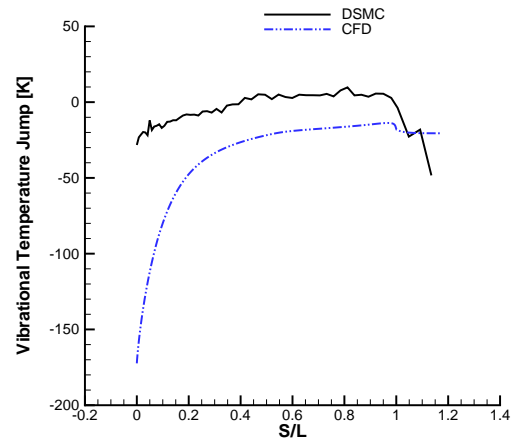
(b) Kn = 0.01

(c) Kn = 0.05

(d) Kn = 0.25

Figure 5.46: Vibrational temperature jump for a Mach 10 flow of nitrogen about a wedge. The distance along the surface (including the base), S, is normalized by the top surface length, L.
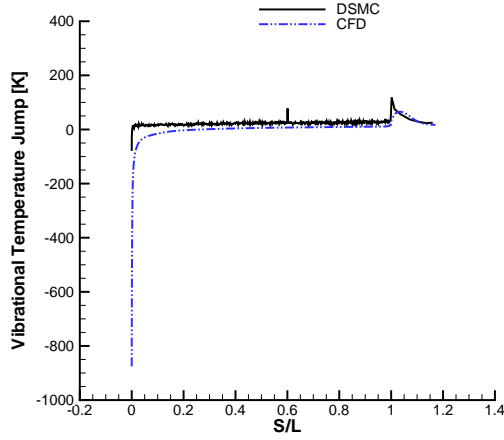
(a) Kn = 0.002
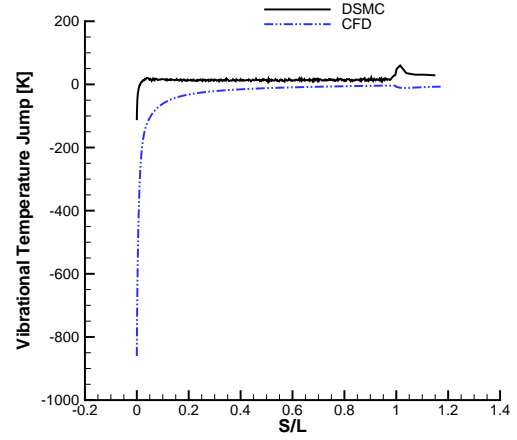
(b) Kn = 0.01
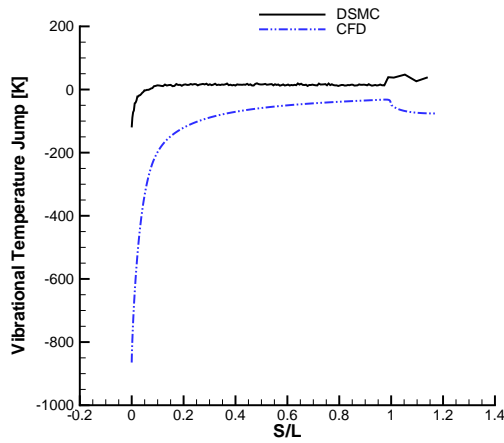
(c) Kn = 0.05
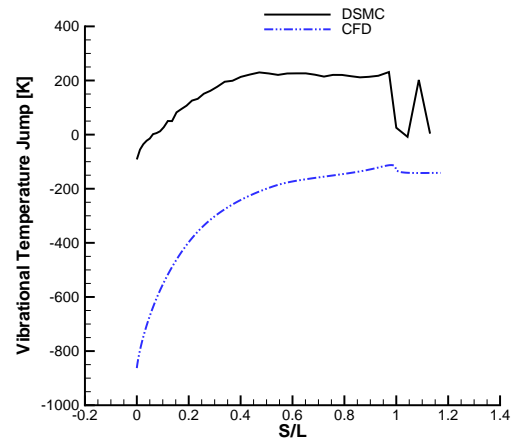
(d) Kn = 0.25

Figure 5.47: Vibrational temperature jump for a Mach 25 flow of nitrogen about a wedge. The distance along the surface (including the base), S, is normalized by the top surface length, L.

Table 5.6: Computational details for a flow of nitrogen about a wedge. Total CPU time is the wall time multiplied by the number of CPUs.

Mach 10

Kn_∞	DSMC				
	Cells	Particles	Time Steps	CPUs	Total CPU Time[*][hours]
0.002	236,351	57.5×10^6	360,000	64	6,483
0.01	215,090	47.9×10^6	250,000	32	1880
0.05	27,615	9.5×10^6	200,000	8	248
0.25	7,137	7.8×10^6	200,000	8	200

Kn_∞	CFD				
	Cells		Iterations	CPUs	Total CPU Time[*][hours]
0.002	25,200		30,000	8	130
0.01	25,200		30,000	8	116
0.05	28,400		30,000	8	126
0.25	30,175		30,000	8	140

Mach 25

Kn_∞	DSMC				
	Cells	Particles	Time Steps	CPUs	Total CPU Time[*][hours]
0.002	168,464	31.7×10^6	350,000	64	3,696
0.01	120,985	28.6×10^6	270,000	32	2,395
0.05	24,632	4.9×10^6	200,000	8	144
0.25	6,041	5.2×10^6	200,000	4	142

Kn_∞	CFD				
	Cells		Iterations	CPUs	Total CPU Time[*][hours]
0.002	29,050		30,000	8	140
0.01	25,200		30,000	8	138
0.05	28,400		30,000	8	128
0.25	30,175		30,000	8	132

[*] Approximate

Again, there are no significant differences between the nitrogen and argon flows, despite the additional presence of thermal nonequilibrium for the diatomic gas.

CHAPTER VI

Comparison with Experiment: Hypersonic Flow over a Flat Plate

6.1 Introduction

The previous chapters focused purely on numerical results, with CFD simulations being compared directly to DSMC simulations. In particular, the walls were assumed to be fully diffusive; that is, the gas molecules colliding with the wall were assumed to accommodate fully to the wall conditions. Hence, an accommodation coefficient of unity was used for the CFD slip boundary conditions. In this chapter, two-dimensional CFD solutions are compared with experimental measurements of a hypersonic flow of nitrogen over a flat plate [21]. Several different values for the accommodation coefficient are evaluated. In addition, the CFD solutions are also indirectly compared to DSMC solutions of the same flow [66]. Thus, the relative accuracy of CFD and DSMC can be evaluated against a realistic flow.

6.2 Background and Experimental Results

The experiment was conducted at the University of Virginia by Cecil and McDaniel [21]. Measurements of the flow were taken using planar laser-induced flourescence (PLIF). A hypersonic flow of nitrogen, with a Mach number of approximately
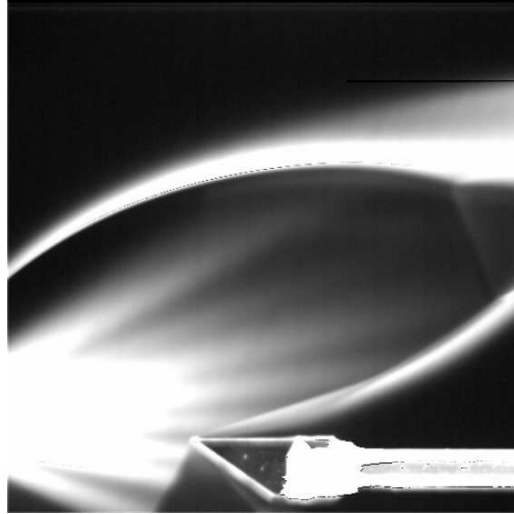
Figure 6.1: PLIF image of hypersonic flow over the flat plate model (from Ref. [21]). The gas expands in a free jet from the left, creating a barrel shock (near the top of the figure). Note the light-colored rays extending from the orifice upstream, showing the radial variation of the velocity. Note also the shock attached to the plate leading edge.

11.9 at the leading edge of the flat plate, was created by expanding an iodine-seeded flow of nitrogen from a settling chamber through a thin, circular orifice and over the model in a continuously evacuated vacuum chamber. A PLIF image of the flow is seen in Figure 6.1. Here, the gas is seen expanding in a free jet from an orifice at the left of the image to the right over the model. The process of expanding the flow through the orifice created a barrel shock (the top portion of which is clearly seen at the top of the figure) terminated by a normal shock (not shown). The expanding flow from the orifice within the barrel shock, where the model was located, was not uniform, but instead varied radially. On the left of the figure, the light-colored rays extending from the orifice upstream of the model shows the radial variation of the velocity. The shock formed by the flow over the model is also clearly shown.

The temperature of the settling chamber was approximately 300 K. Expansion through the orifice reduced the temperature to about 11.5 K near the leading edge

of the model. This temperature is sufficiently low that no vibrational activation is expected.

The density at the leading edge was about 3×10^{-4} kg/m^3, giving a global Knudsen number (based on a hard-sphere mean free path and the flat plate length of 20mm) of about 0.009. This is comparable to the global Knudsen number value of 0.01 for the cases discussed in previous chapters. In those cases, CFD gave decent results for the wedge flow, with the exception of the region near the leading edge where nonequilibrium effects were significant.

Velocity magnitude contours and streamlines from the experimental results are shown in Figure 6.2. Note that the length coordinates, x and y, are nondimensionalized by the diameter, $d = 0.5$ mm, of a small nozzle built into the plate at $x/d = 30$, or, equivalently, $x = 15$ mm. In further experiments, a jet was issued from the nozzle to simulate a reaction control system. The flat plate leading edge is located at $x/d = 0$, and the trailing edge is located at $x/d = 40$. The streamlines in the freestream again illustrate the nonuniform flow due to the source-like nature of the flow expanding from the orifice.

It should also be noted that there is a pocket of very low velocity gas near the trailing edge of the model (between $x/d = 40$ and 50). There is evidence of an adverse pressure gradient at this location that will be discussed in further detail below.

Experimental data for the time-averaged velocity was provided for $y/d = 0$ to 15 at several locations along the plate from $x/d = 0$ to 40 in increments of 5. This corresponds to $y = 0$ to 7.5 mm and $x = 0$ to 20 mm in increments of 2.5 mm. The uncertainties of the U and V-velocity components were estimated to be on the order of 50 m/s and 30 m/s, respectively [21].
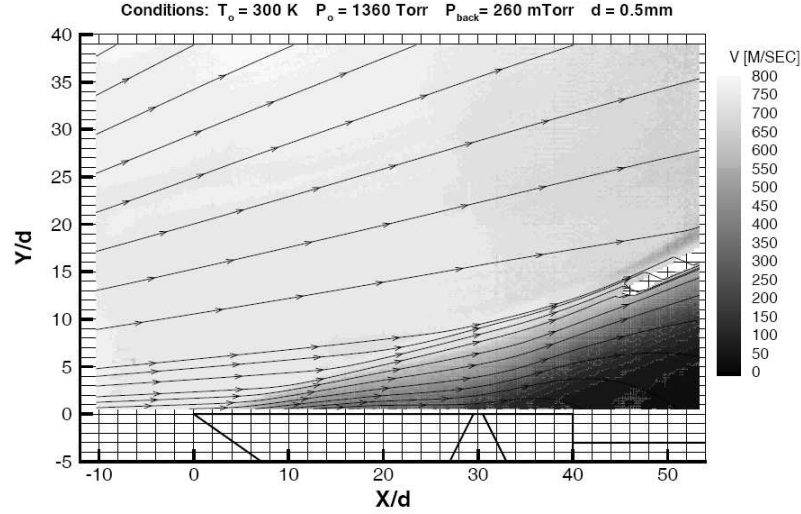
Figure 6.2: Measured velocity contours and streamlines on the centerplane of the hypersonic flow over a flat plate (from Ref. [21]). A small nozzle is built into the plate at $x/d = 30$. Note the radial variation in velocity upstream of the flat plate, and the pocket of low velocity gas near the trailing edge at $x/d = 40$.

6.3 Computational Results: DSMC

Padilla and Boyd[66] conducted DSMC simulations of this flow using pure nitrogen and the variable soft-sphere (VSS) DSMC model [4]. The nonuniform inflow velocity profiles used for the DSMC case were taken from the experimental data. The temperature and the particle number density were calculated assuming an isentropic expansion from the settling chamber conditions of $T = 300$ K and $p = 1.79$ atm. These inflow boundary conditions are shown in Figure 6.3, where the streamwise, or x-direction, velocity component is U and the wall-normal, or y-direction, velocity component is V. Note that the particle number density has been converted to the mass density. The variation of the V-velocity is particularly important; while the U-velocity varies by only 6 m/s across the inflow boundary, the V-velocity varies by nearly 150 m/s (from about 20 m/s at $y = 0$ mm to about 160 m/s at $y = 7.5$ mm.

(a) Velocity components

(b) Temperature and mass density
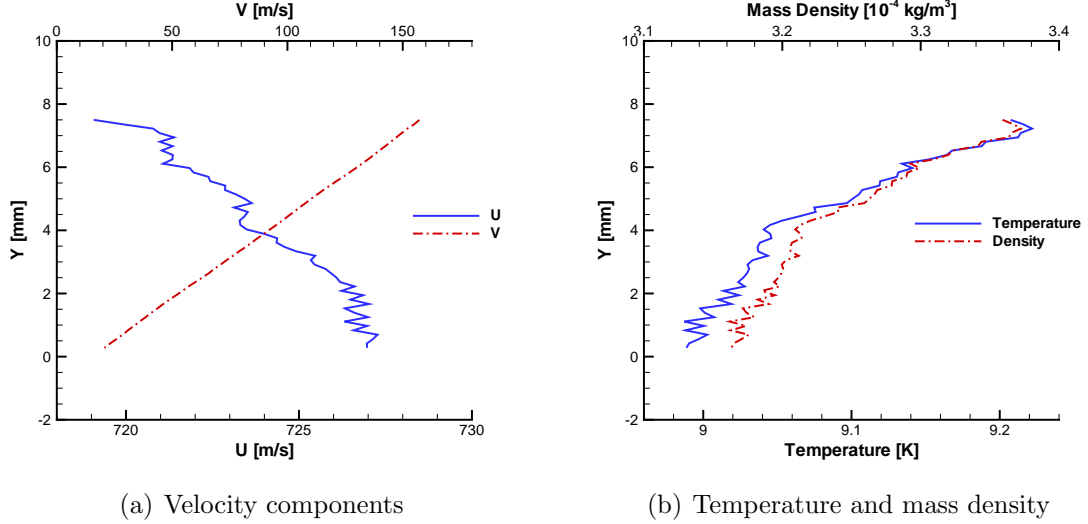
Figure 6.3: Inflow boundary conditions for a hypersonic flow over a flat plate. The inflow boundary conditions for the two-dimensional simulations vary with vertical distance from the plate (y) to match the radial variation of the experimental conditions.

The inflow boundary was set 2 mm upstream of the flat plate leading edge. A wall temperature of 300 K was assumed.

DSMC simulations were computed with two different gas-surface interaction models and tangential momentum accommodation coefficients of 0 to 1.0. The DSMC simulations show that a tangential momentum accommodation coefficient of 1.0 gives the best agreement with the measured data for the streamwise-component of velocity (U), while a tangential momentum accommodation coefficient of 0.75 gives the best overall agreement with the wall-normal component of velocity (V). An average accommodation coefficient of 0.875 gave good overall agreement with the experimental data.

6.4   Computational Results: CFD

CFD solutions are obtained using the Gökçen [29] slip boundary conditions. Simulations performed using the Maxwell and Lockerby's wall-function [49] slip bound-

ary conditions show very similar results, with the exception that the Gökçen slip conditions tend to show a larger slip velocity. This is not unexpected; previous simulations for similar flow conditions (see, for example, Figures 4.54(b) and 4.55(b)) showed that the velocities predicted by all three slip conditions are very similar away from the wall, with the Gökçen simulations predicting the highest slip velocity. The higher slip velocity values predicted by the Gökçen slip conditions agree best with DSMC and the experimental data, for these flow conditions, as will be shown below.

The VHS viscosity, with the values for nitrogen given in Table 3.1, are also used here. Although the DSMC simulations used the VSS model, there are no significant differences expected at the low temperatures encountered. In addition, a test simulation using Blottner's curve fit for the viscosity [7] yielded no discernable difference in the velocity profiles.

The method used here for producing mesh-independent results is somewhat different than that used previously. Earlier studies were mainly concerned with obtaining correct values for the surface properties. Therefore, the surface property values were used to determine when a mesh-independent solution was obtained. It was found that mesh-independent solutions were most sensitive to the node spacing near the wall (for both the wedge and the cylinder cases) and in the streamwise direction (for the wedge case). The objective here, however, is to compare the flow field properties (specifically the velocity components) with the experimental measurements. Therefore, a mesh-independent solution is defined as one for which successively refined meshes produce no discernable differences in the velocity profiles. For this flat plate flow, the flow field properties (especially the V-component of velocity) is very sensitive to the node spacing in the wall-normal direction in the entire flow field, rather than simply near the wall. There is also some sensitivity to the node spacing

in the streamwise direction, especially near the leading edge where the gradients are largest.

In a similar manner to the DSMC simulations, here the accommodation coefficient is varied from 0.5 to 1.0. The computational domain consists of a rectangular area from $y = 0$ to 20 mm and from $x = -2$ to 30 mm.

6.4.1 Flow Field

The contours for the value of the continuum breakdown parameter, Kn_{GLL}, as computed from the CFD solutions for two different accommodation coefficient values ($\sigma = 1.0$ and 0.5), are shown in Figure 6.4, and the density contours are shown in Figure 6.5. It is apparent that the flow is dominated by viscosity effects; in other words, the flow has a large amount of nonequilibrium present, since the transfer of momentum due to velocity gradients is an inherent nonequilibrium process. The largest values of the breakdown parameter are found in the shock region, and, to a lesser extent, the wake. It is interesting to note that the value of the breakdown parameter exceeds the critical value of 0.05 in most of the flow region behind the shock, due to the merging of the shock and the boundary layer. Nevertheless, the CFD solutions do give good agreement with the experimental data in these areas, as shown below.

Reducing surface accommodation from full ($\sigma = 1.0$) to half ($\sigma = 0.5$) effectively reduces the effect of viscosity on the flow field. For full accommodation the shock is stronger, and the compression ratio is higher (with maximum density ratio of about 2.0 compared to 1.7 for half accommodation). In addition, the strong viscous-shock interaction at the leading edge is more apparent for full accommodation, as can be seen by the curvature of the shock in that area. Cecil and McDaniel [21]
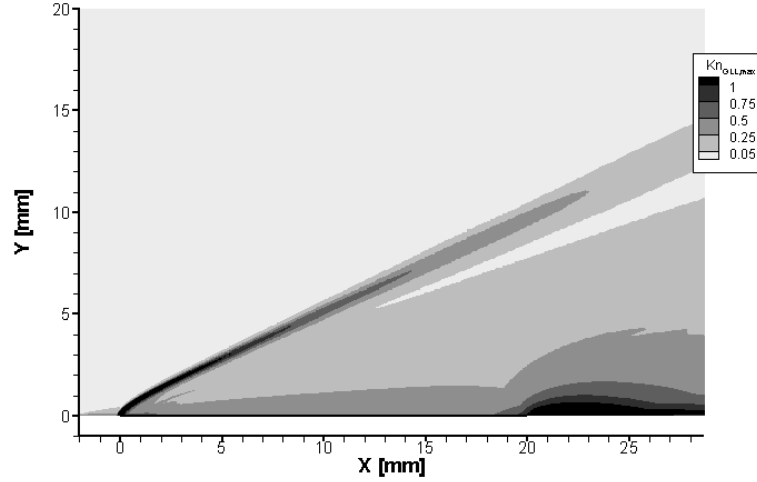
(a) $\sigma = 1.0$
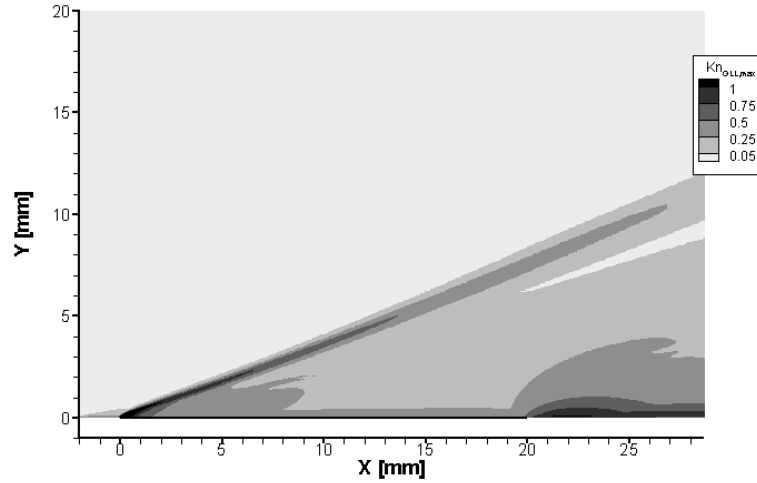
(b) $\sigma = 0.5$

Figure 6.4: Kn_{GLL} field for hypersonic flow over a flat plate. Significant nonequilib-
rium effects are expected at the leading edge and in the wake. Full ac-
commodation increases the viscous effects, increasing the shock strength
and the shock-boundary layer interaction that leads to a curved shock at
the leading edge.
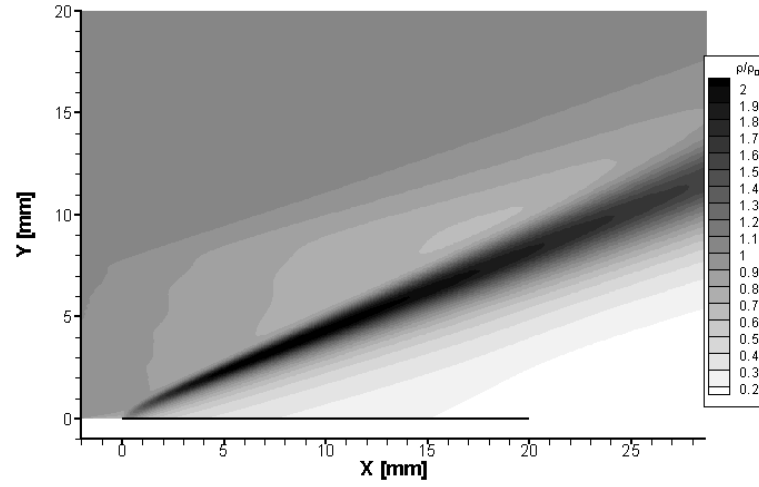
(a) $\sigma = 1.0$
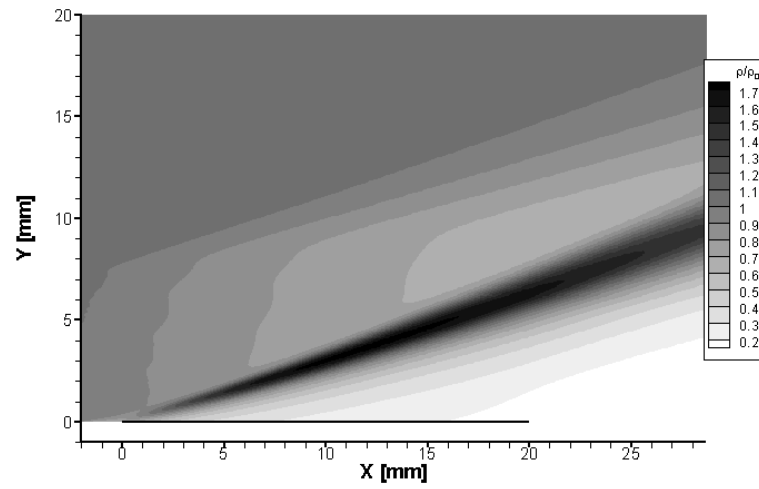
(b) $\sigma = 0.5$

Figure 6.5: Density field for hypersonic flow over a flat plate. Full accommodation increases the viscous effects, increasing the compression across the shock, as well as the shock-boundary layer interaction that leads to a curved shock at the leading edge.

mention that the shock wave angle of 18° far exceeds the value of 4.8° predicted by inviscid theory and that an effective angular displacement of $13 - 14°$ by the boundary layer is necessary to produce the 18° angle. The reduction in shock angle as the accommodation coefficient is reduced also demonstrates the reduced effect of viscosity as surface accommodation is reduced.

One can compare the velocity magnitude contour plots with streamlines from the CFD results in Figure 6.6 with the similar plot of the experimental data in Figure 6.2. First, note that the nonuniform inflow conditions appear to match the experimental results quite well. Also note that the surface accommodation in the experiment appears to be lower than 1.0, as the streamlines near the leading edge in the experimental results are not displaced upward as much as is shown in the numerical results with full accommodation. Finally, note that the computational results do not show the pocket of low velocity at the trailing edge that is apparent in the experimental results. (Recall that $x/d = 40$ is the location of the trailing edge, and is equivalent to $x = 20$ mm.) It appears that whatever causes the low velocity at the trailing edge (perhaps a region of high pressure) also causes the streamlines to be displaced upwards much more in the experimental results than is shown in the numerical results.

6.4.2 Velocity Comparisons

The flow velocity component results from each numerical simulation are compared with the experimental results at several locations along the flat plate. The U-velocity profiles are compared in Figure 6.7 and the V-velocity profiles are compared in Figure 6.8. The U profiles show typical boundary layer behavior, including the non-zero velocity slip at the wall due to the rarefied nature of the flow. The V profiles include
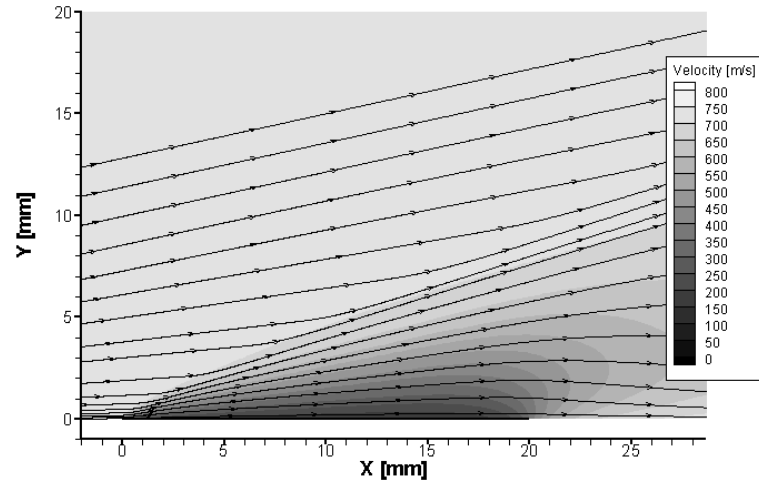
(a) $\sigma = 1.0$
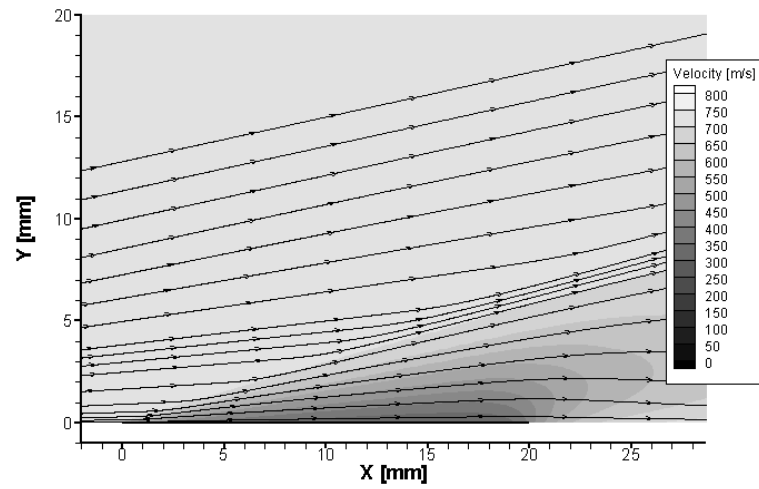
(b) $\sigma = 0.5$

Figure 6.6: Computed velocity magnitude contours and streamlines for hypersonic flow over a flat plate. The half-accommodation results compare more favorably with the experimental results in Figure 6.2.

the effects due to the shock.

The first profiles, at $x = 0$ mm, show good agreement between the experiment and the simulations. Although there is slightly worse agreement in the V-velocity profile as y increases, the numerical results remain well within the estimated level of uncertainty in the experimental data. The disagreement as y increases is most likely due to incomplete inflow boundary condition modeling. The values used were derived from the experimental data, which is limited to values below $y = 7.5$ mm. Although it can be assumed, by looking at the experimental streamlines in Figure 6.2, that the radial component of velocity continues to increase as y increases, the boundary conditions implemented do not assume an increasing value of V as y increases beyond $y = 7.5$ mm (see Figure 6.8(a)). Nevertheless, the boundary conditions used in the simulations are assumed to be adequately correct.

Very near the leading edge, at $x = 1.5$ mm, the flow solution with $\sigma = 0.5$ shows the best agreement with the experiment, for both U and V. Further down the plate, however, up to $x = 12.5$ mm, flow solutions with more surface accommodation, $\sigma = 60$ or 70, agree best for U, while the solutions with $\sigma = 50$ continue to agree best for V. Starting at $x = 15$ mm, the agreement for U progressively worsens, and the experimental U profiles at $x = 17.5$ and 20 mm strongly imply the presence of an adverse pressure gradient. The specific cause of the pressure gradient is not present in the simulations, and it is not surprising to see disagreement in the flow velocity predictions near the trailing edge.

It is not surprising that the lower surface accommodation values agree better nearer to the leading edge; less surface accommodation reduces the affect of viscosity (and increases the velocity slip)—it was shown previously for the wedge that CFD tends to underpredict the value of the velocity slip near the leading edge.
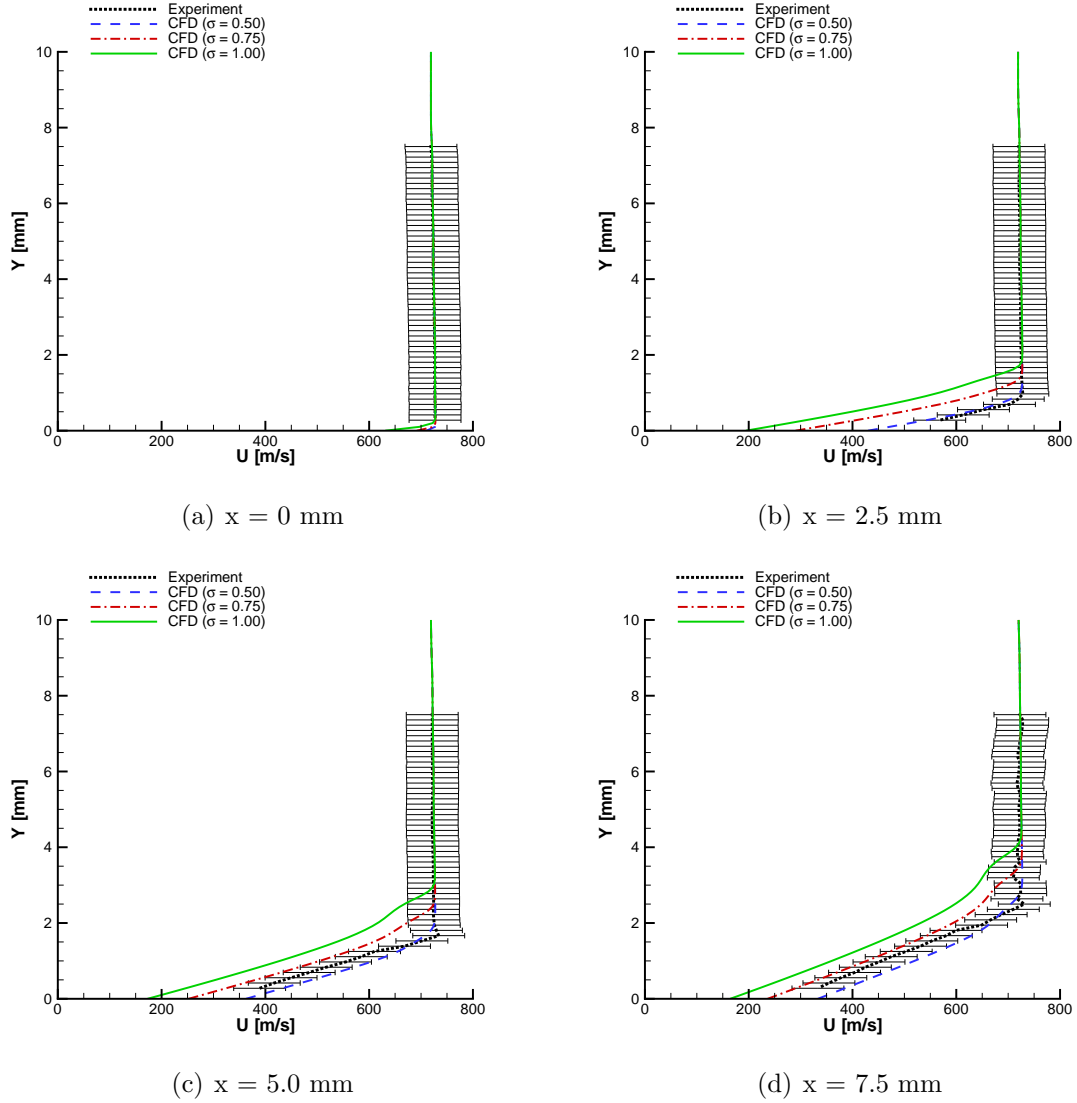
(a) x = 0 mm

(b) x = 2.5 mm

(c) x = 5.0 mm

(d) x = 7.5 mm

Figure 6.7: Velocity component parallel to the surface (U) for a hypersonic flow over a flat plate. All CFD results match the experimental values at the leading edge, confirming that the inflow boundary conditions are correct. Simulations with higher values of surface accommodation match the experimental results best near the leading edge.
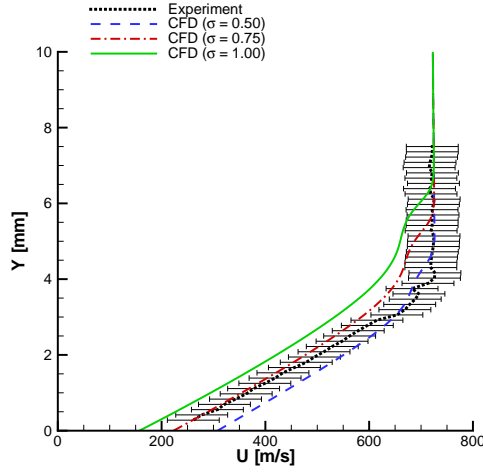
(e) x = 12.5 mm
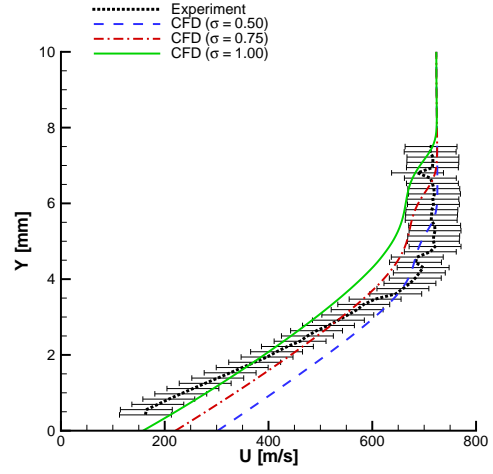
(f) x = 15.0 mm
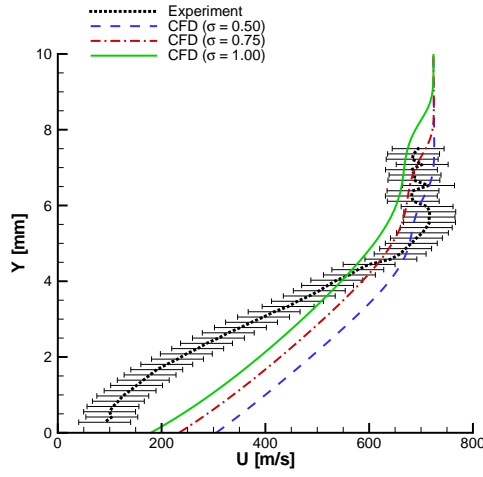
(g) x = 17.5 mm
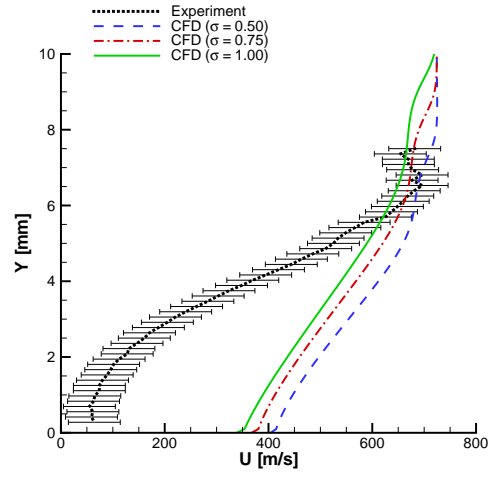
(h) x = 20.0 mm

Figure 6.7: Velocity component parallel to the surface (U) for a hypersonic flow over a flat plate (cont.). Downstream of the leading edge, CFD results with $\sigma = 0.75$ agree best with experiment. The experimental velocity profiles near the trailing edge strongly suggest the presence of an adverse pressure gradient.
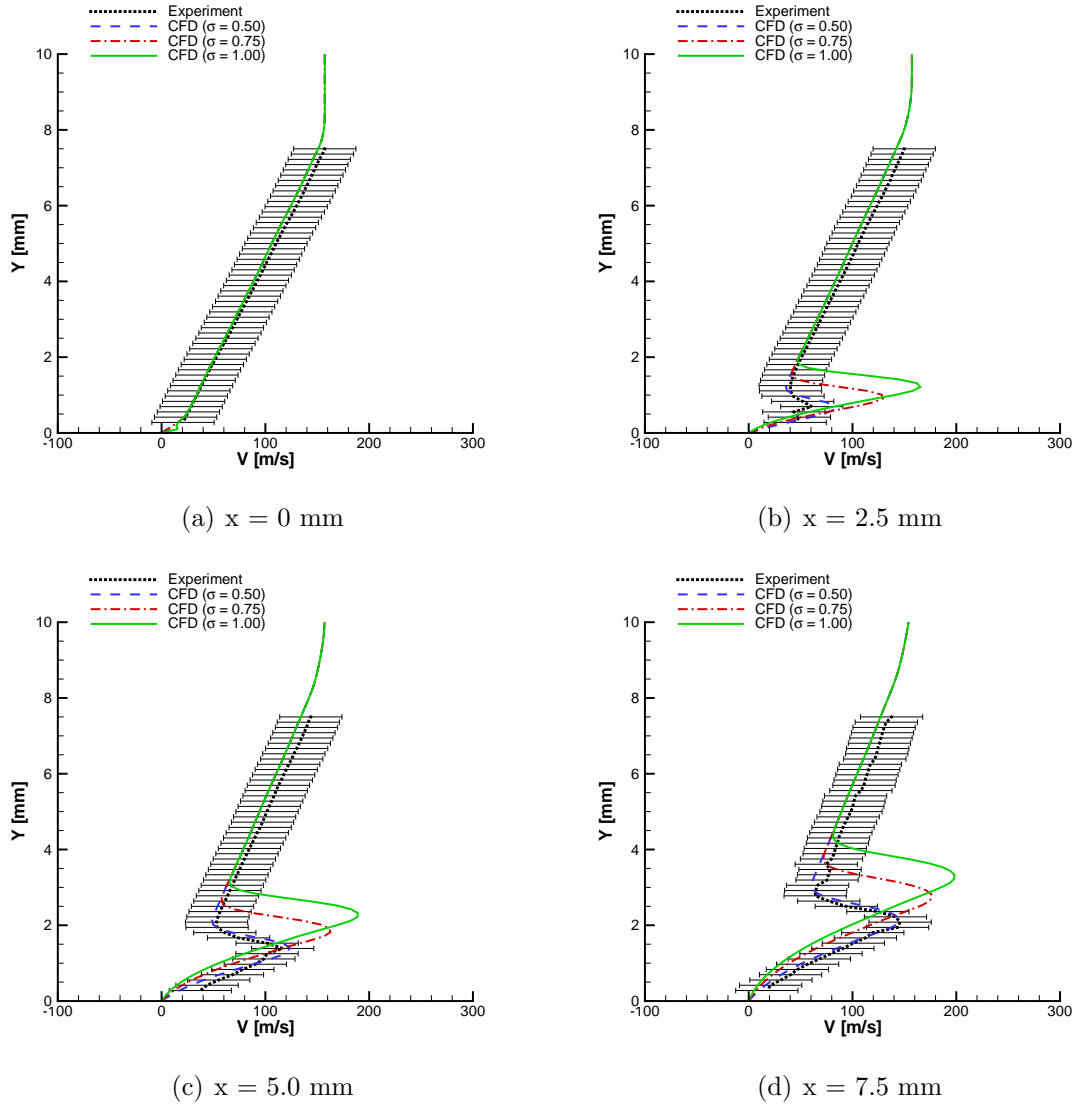
(a) x = 0 mm

(b) x = 2.5 mm

(c) x = 5.0 mm

(d) x = 7.5 mm

Figure 6.8: Velocity component normal to the surface (V) for a hypersonic flow over a flat plate. The inflow boundary conditions match the experimental data where present (below $y = 0.75$ mm). The computed velocity profiles through the shock match the experiment best for $\sigma = 0.5$.
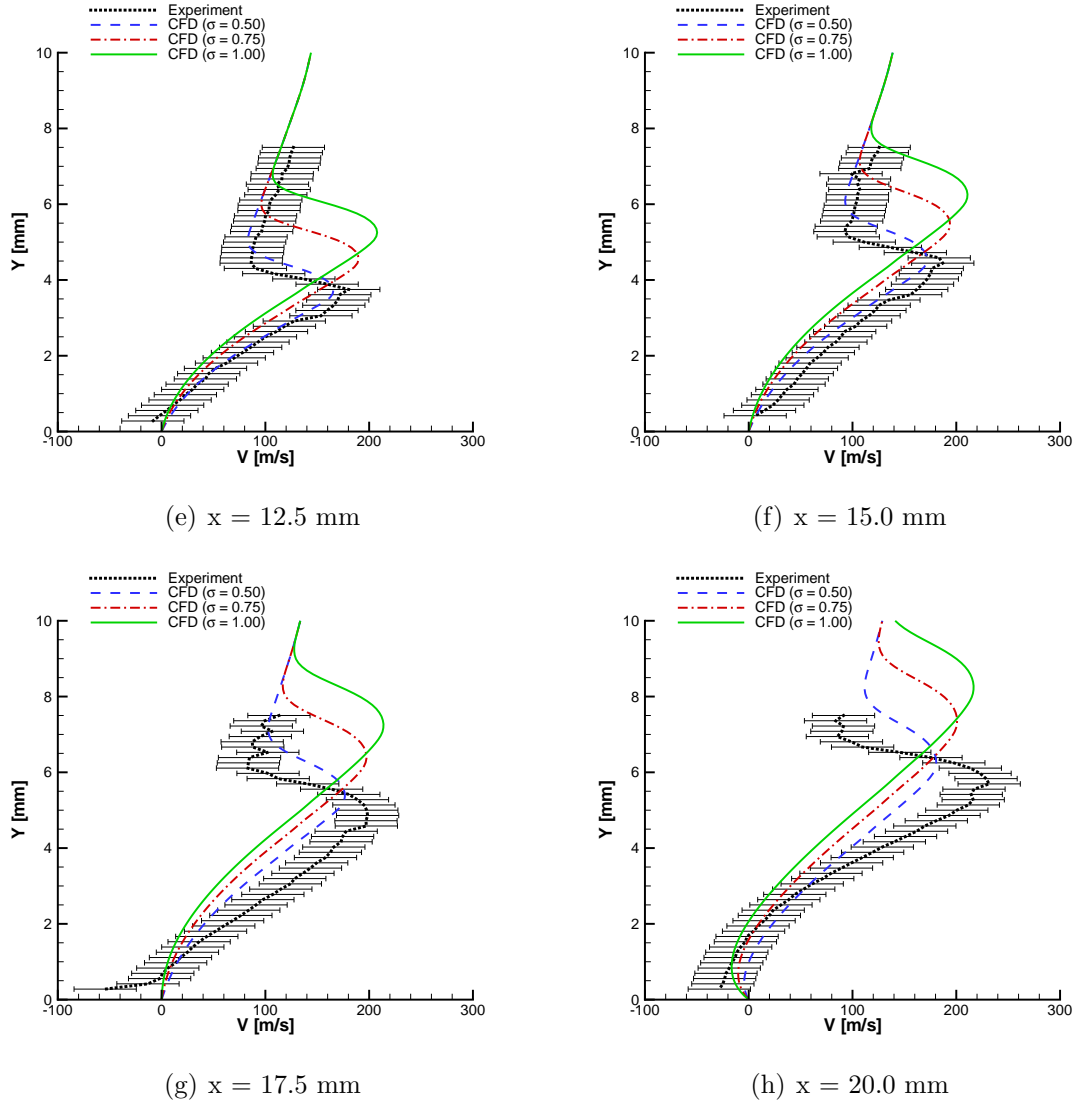
(e) x = 12.5 mm

(f) x = 15.0 mm

(g) x = 17.5 mm

(h) x = 20.0 mm

Figure 6.8: Velocity component normal to the surface (V) for a hypersonic flow over a flat plate (cont.). The computed velocity profiles through the shock match best with experiment for lower values of surface accommodation. Simulation results do not agree well with the experimental values near the trailing edge due to an adverse pressure gradient in the experimental results.

(a) Pressure
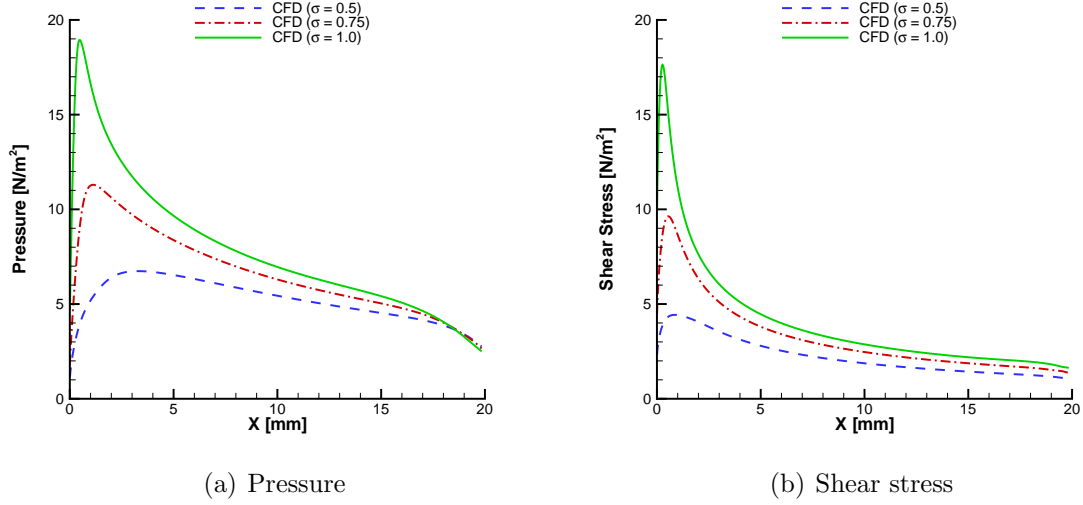
(b) Shear stress

Figure 6.9: Surface pressure and shear stress for a hypersonic flow over a flat plate. Decreasing the surface accommodation decreases the viscous effects, decreasing the pressure and shear stress.

The previous DSMC results [66] also showed that simulations employing lower values of the accommodation coefficient tended to agree better for the V-velocity. However, the DSMC results agreed best for higher levels of surface accommodation ($\sigma_{DSMC} = 1.0$ rather than $\sigma_{CFD} = 70$ for U, and $\sigma_{DSMC} = 0.75$ rather than $\sigma_{CFD} = 0.5$ for V).

6.4.3 Surface Properties

Although there are no experimental results for surface pressure and shear stress, it is instructive to compare the numerical results at the different values of accommodation coefficient. Figure 6.9 compares the surface pressure and shear stress along the flat plate. The profiles are very similar to those for the wedge; a large peak at the leading edge is gradually reduced along the surface. As expected, lower levels of surface accommodation reduce the shear stress on the surface. The surface pressure is also reduced with lower values of surface accommodation as the pressure on a flat plate is due solely to viscous effects.
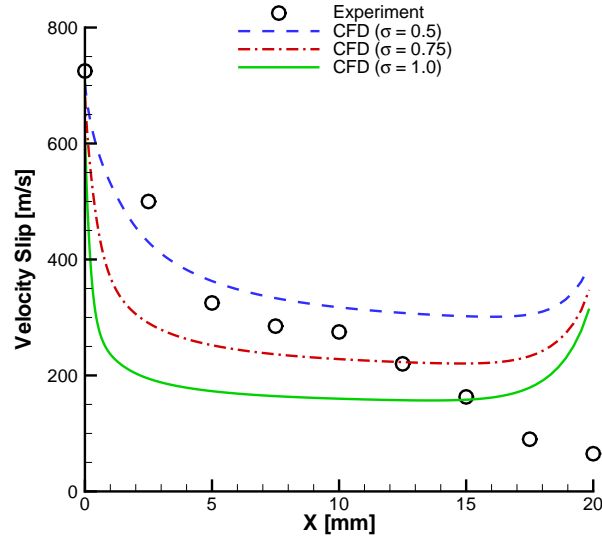
Figure 6.10: Velocity slip for a hypersonic flow over a flat plate. Reduction in sur-
face accommodation increases velocity slip. The large decrease in the
experimental velocity slip near the trailing edge is most likely due to an
adverse pressure gradient.

The experimental values are extrapolated to the surface and plotted with the computational results for velocity slip in Figure 6.10. As the flow progresses along the plate the large value at the leading edge is reduced to an almost constant value. The large reduction in experimental velocity slip near the trailing edge is also due to the adverse pressure gradient. Extrapolating the experimental velocity slip from the U profiles show that near the middle of the plate, at about $x = 10$ mm, the experimental values fall between the flow solutions with $\sigma = 0.75$ and $\sigma = 0.5$.

6.5   Computational Details

The computational details for the simulations of a hypersonic flow of argon about a wedge discussed in this section are shown in Table 6.1.

Table 6.1: Computational details for a hypersonic flow over a flat plate. Total CPU time is the wall time multiplied by the number of CPUs.

Cells	Iterations	CPUs	Total CPU Time[*][hours]
78,375	6,000	8	36

[*] Approximate

6.6 Summary—Hypersonic Flow over a Flat Plate

CFD simulations of a hypersonic flow over a flat plate are compared with experimental results and previously obtained DSMC results. Although there is some evidence of flow separation near the trailing edge of the plate in the experimental results, CFD velocity data agrees fairly well with the experimental data at other locations along the plate. For the velocity component parallel to the flow (U), results obtained using a surface accommodation coefficient value of 0.5 agrees better with the experimental results near the leading edge, while further along the plate an accommodation coefficient value between 0.75 and 1.0 provides best agreement. The lower accommodation value near the leading edge effectively increases the slip velocity; CFD also under-predicted the velocity slip near the leading edge of the wedge. For the wall normal velocity component (V), an accommodation coefficient of 0.5 gives best agreement with experimental data. Previous DSMC simulations showed best agreement with the experimental data for higher values of the accommodation coefficient.

Less surface accommodation significantly decreases the predicted pressure and shear stress near the leading edge.

CHAPTER VII

Conclusions

7.1 Summary

The primary goal of this study was to quantify the difference between DSMC and CFD simulations in determining the effects of different levels of nonequilibrium on the surface properties of pressure, shear stress and heat flux of a body under hypersonic flow conditions.

This detailed computational study of the effects of nonequilibrium on the surface properties of a hypersonic vehicle considered the flow about a cylinder and an infinitely sharp wedge. Several different flow regimes, from the continuum and into the transitional, were considered—free stream Knudsen numbers were 0.002, 0.01, 0.05 and 0.25—with Mach numbers of 10 and 25. The effects of translational nonequilibrium were isolated by considering flows of argon; thermal nonequilibrium effects were included when considering flows of nitrogen over the same bodies at the same flow conditions. Validation of the CFD code, as well as the effect of different levels of surface accommodation, was shown by considering a nitrogen flow over a flat plate and comparing the simulation results with experimental data.

Comparison of CFD and DSMC results for the flow of argon about a cylinder showed that the surface properties of pressure, shear stress and heat transfer rates

were very similar for the lower Knudsen number flows where the continuum hypothesis is valid, as expected, while the results diverged in the higher Knudsen number cases. The surface pressure was least affected by continuum breakdown, as quantified by the gradient-length local Knudsen number, among those properties investigated, and seemed to be affected only by continuum breakdown as the shock and boundary layer merged at the highest Knudsen number flow. The shear stress was most influenced by nonequilibrium effects. The addition of slip velocity and temperature jump boundary conditions greatly improved the agreement between CFD and DSMC at higher Knudsen numbers. Several different types of slip boundary conditions were examined, and the best agreement appears to be obtained when using the generalized slip conditions proposed by Gökçen [29]. With these boundary conditions, the differences in total drag and peak heat flux predicted by CFD and DSMC ranged from less than 1% at Kn = 0.002 to around 5% at Kn = 0.25.

For the case of a simple gas, the higher velocities associated with a Mach 25 flow did not seem to increase the differences between the CFD and DSMC predictions. Although the extent of the region where the continuum breakdown parameter exceeded the critical value of 0.05 was larger at the higher Mach number, the predicted surface properties with the slip boundary conditions still remained well under 5% for all but the Kn = 0.25 case, where the peak heat transfer rates and total drag predictions were within 6%.

Although there was a significant amount of nonequilibrium between the different thermal modes (translational, rotational and vibrational) when considering a flow of nitrogen, the trends were largely similar to those noted when considering a simple gas with no internal degrees of freedom. The pressure and shear stress were least sensitive to the nonequilibrium effects, while the heat transfer rate was most sensitive. Total

drag differences between CFD (with the best slip boundary conditions) and DSMC remained under 3%, while peak heat flux differences were less than 8%.

For the cylinder cases, it was also shown that as the Knudsen number increased, the percentage of total drag due to skin friction forces (versus pressure) increased as well; friction drag accounted for less than 5% of the total drag at Kn = 0.002 to about 20% at Kn = 0.25. Differences in drag due to skin friction also tended to be larger than differences in predicted drag due to pressure; thus the larger errors at the higher Knudsen numbers were due mostly to errors in skin friction prediction.

Differences in flow property prediction were generally concentrated within about 10 mean free paths of the wall surface, or, in other words, within the Knudsen layer.

The sharp-leading edge geometry of the wedge led to additional flow phenomena not seen with the cylinder, which in turn affected the surface property predictions.

The differences in total drag predicted by CFD and DSMC for the wedge were greater than with the cylinder geometry, due to the larger effect of the friction forces on the drag. Additionally, there were greater differences in the pressure profiles along the wedge surface, but the effect on total drag was relatively small (due to the small angle of the surface with the flow). Total drag differences ranged from less than 2% at Kn = 0.002 to more than 20% at Mach 10 and 34% at Mach 25 at Kn = 0.25. Unlike the cylinder cases, friction forces contributed most to the total drag of the wedge. For Kn = 0.002, friction forces accounted for 50% of the total drag, which increased to nearly 90% for Kn = 0.25. Again, differences in the drag due to friction was much higher than differences in the drag due to pressure.

The amount of nonequilibrium near the leading-edge significantly affected the prediction of temperature gradients, and thus there were significant differences in the heat transfer rate predictions—CFD fails to adequately predict the large heat

fluxes near the leading edge of an infinitely-sharp wedge. Peak heat flux differences were near 70% (and as much as 100%) for the regimes considered.

As with the cylinder, there were no significant differences between the nitrogen and argon flows about the wedge (although drag differences were slightly less with nitrogen, as with the cylinder cases), despite the additional presence of thermal nonequilibrium for the diatomic gas.

CFD simulations of a hypersonic flow over a flat plate were compared with experimental results and previously obtained DSMC results. Several different values for the surface accommodation coefficient were considered, ranging from 0.5 to 1.0. Although there was some evidence of flow separation near the trailing edge of the plate in the experimental results, CFD velocity data agreed fairly well with the experimental data at other locations along the plate. For the velocity component parallel to the flow (U), results obtained using a surface accommodation coefficient value of 0.5 agreed better with the experimental results near the leading edge, while further along the plate an accommodation coefficient value between 0.75 and 1.0 provided the best agreement. The lower accommodation value near the leading edge effectively increased the slip velocity; CFD also under-predicted the velocity slip near the leading edge of the wedge. For the wall normal velocity component (V), an accommodation coefficient of 0.5 gave best agreement with experimental data. Previous DSMC simulations showed best agreement with the experimental data for higher values of the accommodation coefficient.

Less surface accommodation also significantly decreased the predicted pressure and shear stress near the leading edge.

7.2   Contributions

Although there have been some studies comparing CFD and DSMC simulations published in the literature, the current work makes several unique and valuable contributions to the field of computational simulation of hypersonic aerothermodynamics, some of which have been published in References [50, 51, 52]. These contributions are enumerated below.

1. Started with the fundamentals. Many previous studies have compared CFD and DSMC with experimental data. Thus, they have included complex thermochemical nonequilibrium models in the simulation. The present study, as a purely numerical study, has focused primarily on the fundamentals of nonequilibrium behavior and has gradually increased the complexity, starting with a monatomic gas, argon, and progressing to a diatomic gas, nitrogen. The effects of each type of nonequilibrium on the surface properties are then quantified as the complexity increases.

2. Studied many flow regimes, about blunt and sharp bodies. Many of the published studies are limited to a few flow regimes or body geometries. The current work is more comprehensive, considering flow regimes from the continuum and into the transitional regime to quantify the effects of the degree of rarefaction; considering two different flow velocities to quantify the effects of larger Mach number; and considering two types of geometry, a cylinder and a wedge, to quantify differences due to blunt-body phenomena versus sharp leading-edge phenomena.

3. Evaluated the effectiveness of several types of CFD slip boundary conditions and compared the CFD slip values with the DSMC slip values. This research

has evaluated the effectiveness of several CFD slip boundary conditions, including one only recently proposed [49], in predicting the surface properties of a hypersonic vehicle. The actual slip quantities (velocity slip, translational/rotational and vibrational temperature jump) predicted by these boundary conditions are also compared with those extracted from the DSMC simulations for each flow condition, which is unique to this dissertation.

4. Laid the foundation for further studies essential to the design of hybrid methods. Hybrid methods face two basic problems; determining the boundaries between the CFD and DSMC domains and passing information from one domain to the other. This research contributes to both of these areas. The chosen value for the continuum breakdown parameter's effectiveness in predicting differences is shown by comparing the breakdown value with the other flow properties. An effective hybrid design also requires that the different submodels used in both computational methods be equivalent as much as possible; thus information passed between both domains is as equivalent as possible.

5. Showed conclusively that flow property differences near the surface are concentrated in the Knudsen layer. Unique to this dissertation are the results that the differences between CFD and DSMC near the wall are concentrated mainly in the Knudsen layer, defined here as the region of flow 10 mean free paths or less from the wall surface.

7.3   Future Research

The present research is the most complete and systematic study to date to determine the effects of continuum breakdown on the surface properties of a hypersonic

vehicle. However, there are still additional areas in which the work can be expanded.

Geometry

The first area in which to extend this study is the geometry of the hypersonic body. The current work has looked at two-dimensional blunt- and sharp-leading edge bodies, specifically a cylinder and a wedge. It was seen that these two types of geometry yield large differences in the level of agreement between CFD and DSMC predictions of the surface properties, particularly for the peak heat flux. Multi-dimensional effects can be explored by considering axisymmetric bodies such as spheres and cones; fully three-dimensional bodies representative of actual hypersonic vehicles might also yield important information.

O'Brien and Lewis [63] have proposed the use of power-law shaped leading-edges for the blunting of leading-edges while minimizing shock stand-off. The power-law shape can be aerodynamically sharp or blunt, depending on the actual power-law exponent. It was seen in this dissertation that CFD agrees better with DSMC for blunt-bodies, with larger differences for infinitely sharp bodes. Further studies should extend this understanding to power-law shapes.

Chemistry

The research contained in this dissertation was restricted to thermal nonequilibrium only (translational, and rotational/vibrational). At the higher temperatures normally encountered in hypersonic flows, chemical reactions, such as dissociation and recombination, become important. Further research in this area would require an understanding of both forward and backward reactions rates and the methods with which they are modeled in CFD and DSMC. These submodels would need to be as equivalent as possible. The effects of chemical nonequilibrium on the surface

properties of the hypersonic vehicle could then be studied.

Studies that include chemical nonequilibrium would also necessarily consider any linking between vibrational energy activation and dissociation rates, as well as surface catalysis.

Gas Mixtures

While the research presented here has been limited to the consideration of only simple gases consisting of one species, real hypersonic flows typically involve multiple species. Consideration of multiple species, such as oxygen and nitrogen, would require the additional consideration of inter-species diffusion coefficients as well as the definitions of mixture properties versus species properties in both computational methods.

Flow Conditions

The current work has looked at flow conditions ranging from the continuum into the transition regime, at both Mach 10 and Mach 25. It has been seen that the vibrational modes are not largely activated for the Mach 10 flows, and that vibrational nonequilibrium does not affect the surface properties much even at the higher velocities. Additional work might consider higher velocity flows, similar to the Stardust re-entry conditions [12], where vibrational nonequilibrium is expected to be more important. Work in this area might also separate the contributions of translational and vibrational energy modes to the heat flux in the simulations and compare the CFD and DSMC predictions of each component.

Rotational Energy Equation in CFD

The CFD code used here, LeMANS, currently includes a two-temperature model, with one temperature being a combination of the translational and rotational temperatures. Work is currently being performed to implement a separate rotational energy equation into the code. It would be instructive to determine if the additional modeling of rotational nonequilibrium improves the agreement between CFD and DSMC for the nitrogen flows.

Variation of Surface Accommodation

Finally, with the exception of the flat plate flow in Chapter VI, the current research has been limited to considering only full accommodation at the surfaces, for both momentum and energy. For full accommodation, CFD and DSMC tended to agree well at the lower Knudsen numbers. However, it was seen for the flat plate flow that less surface accommodation was required in the CFD simulations to achieve good agreement with the experimental data than was required in the DSMC simulations. Additional studies of the flows about cylinders and wedges might include variation of the amount of surface accommodation, and perhaps independent variation of the momentum and energy accommodation, to determine any additional effects on surface properties.

BIBLIOGRAPHY

BIBLIOGRAPHY

[1] ABE, T. Direct simulation Monte Carlo method for internal-translational energy exchange in nonequilibrium flow. In *Rarefied Gas Dynamics: Theory and Simulations* (1994), B. D. Shizgal and D. P. Weaver, Eds., vol. 159 of *Progress in Astronautics and Aeronautics*, AIAA, pp. 103–113.

[2] ANDERSON, J. D., LEWIS, M. J., AND CORDA, S. Several families of viscous optimized waveriders – a review of waverider research at the university of maryland. In *Proceedings of the First International Hypersonic Waverider Symposium* (1990), University of Maryland.

[3] BIRD, G. A. Breakdown of translational and rotational equilibrium in gaseous expansions. *AIAA Journal 8*, 11 (1970), 1998–2003.

[4] BIRD, G. A. *Gas Dynamics and the Direct Simulation of Gas Flows.* Oxford University Press, Oxford, 1994.

[5] BIRD, G. A. The DS2V/3V program suite for DSMC calculations. In *Rarefied Gas Dynamics* (New York, 2000), M. Capitelli, Ed., AIP Conference Proceedings 762, pp. 541–546.

[6] BIRD, G. A. private communication, Sept. 2006.

[7] BLOTTNER, F. G., JOHNSON, M., AND ELLIS, M. Chemically reacting viscous flow program for multi-component gas mixtures. Tech. Rep. SC-RR-70-754, Sandia Laboratories, Albuquerque, New Mexico, 1971.

[8] BOYD, I. D. Modeling of plasma formation in rarefied hypersonic entry flows. AIAA Paper 2007–0206.

[9] BOYD, I. D. Analysis of rotational nonequilibrium in standing shock waves of nitrogen. *AIAA Journal 28*, 11 (Nov. 1990), 1997–1999.

[10] BOYD, I. D. Analysis of vibrational-translational energy transfer using the direct simulation Monte Carlo method. *Physics of Fluids A 3*, 7 (July 1991), 1785–1791.

[11] BOYD, I. D., CHEN, G., AND CANDLER, G. V. Predicting failure of the continuum fluid equations in transitional hypersonic flows. *Physics of Fluids 7*, 1 (Jan. 1995), 210–219.

[12] BOYD, I. D., TRUMBLE, K., AND WRIGHT, M. J. Nonequilibrium particle and continuum analyses of stardust entry for near–continuum conditions. AIAA Paper 2007–4543.

[13] BOYD, I. D., AND WANG, W.-L. Monte Carlo computations of hypersonic interacting flows. AIAA Paper 2001–1029.

[14] BROWN, S. L. *Approximate Riemann Solvers for Moment Models of Dilute Gases.* PhD thesis, The University of Michigan, 1996.

[15] CAMBEROS, J. A., SCHROCK, C. R., MCMULLAN, R. J., AND BRANAM, R. D. Development of continuum onset criteria with direct simulation Monte-Carlo using Boltzmann's H-Theorem: Review and vision. In *Proceedings of the 9th AIAA/ASME Joint Thermophysics and Heat Transfer Conference* (San Francisco, California, June 2006).

[16] CANDLER, G. V., BOYD, I. D., LEVIN, D. A., MOREAU, S., AND ERDMAN, P. W. Continuum and DSMC analysis of bow shock flight experiments. AIAA Paper 1993–0275.

[17] CANDLER, G. V., NIJHAWAN, S., BOSE, D., AND BOYD, I. D. A multiple translational temperature gas dynamics model. *Physics of Fluids 6*, 11 (Nov. 1994), 3776–3786.

[18] CANDLER, G. V., NOMPELIS, I., AND DRUGUET, M.-C. Navier-Stokes predictions of hypersonic double-cone and cylinder-flare flow field. AIAA Paper 2001–1024.

[19] CANDLER, G. V., NOMPELIS, I., DRUGUET, M.-C., HOLDEN, M. S., WADHAM, T. P., BOYD, I. D., AND WANG, W.-L. CFD validation for hypersonic flight: Hypersonic double–cone flow simulations. AIAA Paper 2002–0581.

[20] CARLSON, H. A. Aerothermodynamic analyses of hypersonic, blunt-body flows. *Journal of Spacecraft and Rockets 36*, 6 (1999), 912–915.

[21] CECIL, E., AND MCDANIEL, J. C. Planar velocity and temperature measurements in rarefied hypersonic flow using iodine LIF. AIAA Paper 2005–4695.

[22] COMEAUX, K. A., CHAPMAN, D. R., AND MACCORMACK, R. W. An analysis of the Burnett equations based on the second law of thermodynamics. AIAA Paper 1995–0415.

[23] DIETRICH, S., AND BOYD, I. D. Scalar and parallel optimized implementation of the direct simulation Monte Carlo method. *Journal of Computational Physics 126*, 2 (1996), 328–342.

[24] FARBAR, E. Testing of vibrational relaxation model in MONACO. Unpublished report, Department of Aerospace Engineering, University of Michigan, Mar. 2007.

[25] FISCKO, K. A., AND CHAPMAN, D. R. Comparison of Burnett, Super-Burnett and Monte Carlo solutions for hypersonic shock structure. In *Rarefied Gas Dynamics: Theoretical and Computational Techniques* (Washington, DC, 1989), E. P. Muntz, D. P. Weaver, and D. H. Campbell, Eds., vol. 118 of *Progress in Astronautics and Aeronautics*, American Institute of Aeronautics and Astronautics, pp. 374–395.

[26] GARCIA, A. L., BELL, J. B., CRUTCHFIELD, W. Y., AND ALDER, B. J. Adaptive mesh and algorithm refinement using direct simulation Monte Carlo. *Journal of Computational Physics 154* (1999), 134.

[27] GILLUM, M. J., AND LEWIS, M. J. Analysis of experimental results on a Mach 14 waverider with blunt leading edges. AIAA Paper 1996–0812.

[28] GNOFFO, P. A. CFD validation studies for hypersonic flow prediction. AIAA Paper 2001–1025.

[29] GÖKÇEN, T., AND MACCORMACK, R. W. Nonequilibrium effects for hypersonic transitional flows using continuum approach. AIAA Paper 1989–0461.

[30] GÖKÇEN, T., MACCORMACK, R. W., AND CHAPMAN, D. R. Computational fluid dynamics near the continuum limit. AIAA Paper 1987-1115.

[31] GOMBOSI, T. I. *Gaskinetic Theory*. Cambridge University Press, 1994.

[32] GREATHOUSE, J. S., KIRK, B. S., LILLARD, R. P., TRUONG, T. H., ROBINSON, P., AND CERIMELE, C. J. Crew exploration vehicle (CEV) crew module shape selection analysis and CEV aeroscience project overview. AIAA Paper 2007–0603.

[33] GUO, K. L., AND LIAW, G. S. Numerical predictions of the transitional flow past blunt bodies. AIAA Paper 2001–0228.

[34] GUO, K. L., LIAW, G. S., AND CHOU, L. C. Numerical predictions of the transitional flow over an elliptic cylinder by the Burnett equations and the DSMC method. AIAA Paper 1999–3457.

[35] HASH, D. B., AND HASSAN, H. A. A decoupled DSMC/Navier-Stokes analysis of a transitional flow experiment. AIAA Paper 1996-0353.

[36] HASH, D. B., AND HASSAN, H. A. Assessment of schemes for coupling Monte Carlo and Navier-Stokes solution methods. *Journal of Thermophysics and Heat Transfer 10*, 2 (1996), 242–249.

[37] HIRSCH, C. *Numerical Computation of Internal and External Flows, Volume 1: Fundamentals of Numerical Discretization*. John Wiley & Sons, 1988.

[38] HIRSCH, C. *Numerical Computation of Internal and External Flows, Volume 2: Computational Methods for Inviscid and Viscous Flows*. John Wiley & Sons, 1990.

[39] INGER, G. R., AND MOSS, J. N. Direct simulation Monte Carlo simulations of hypersonic flows with shock interactions. *AIAA Journal 45*, 8 (Aug. 2007), 2102–2105.

[40] JAIN, A. C., AND HAYES, J. R. Hypersonic pressure, skin friction, and heat transfer distributions on space vehicles: Planar bodies. *AIAA Journal 42*, 10 (Oct. 2004), 2060–2069.

[41] JOU, D., AND PAVÓN, D. Nonlocal and nonlinear effects in shock waves. *Physical Review A 44*, 10 (Nov. 1991), 6496–6502.

[42] JR., C. E. C., AND ENGELUND, W. C. Integrated aeropropulsive computational fluid dynamics methodology for the Hyper-X flight experiment. *Journal of Spacecraft and Rockets 38*, 6 (2001), 836–843.

[43] KATO, H., AND TANNEHILL, J. C. Computation of hypersonic laminar separated flows using an iterated PNS algorithm. AIAA Paper 2001–1028.

[44] KINNEY, D. J., BOWLES, J. V., YANG, L. H., AND ROBERTS, C. D. Conceptual design of a 'SHARP'-CTV. AIAA Paper 2001–1028.

[45] KNIGHT, D. RTO WG 10: Test cases for CFD validation of hypersonic flight. AIAA Paper 2002–0433.

[46] KOURA, K., AND MATSUMOTO, H. Variable soft sphere molecular model for air species. *Physics of Fluids A 4*, 5 (May 1992), 1083–1085.

[47] LEVERMORE, C. D. Moment closure hierarchies for kinetic theories. *Journal of Statistical Physics 83*, 5/6 (1996), 1021–1065.

[48] LOCKERBY, D. A., REESE, J. M., EMERSON, D. R., AND BARBER, R. W. Velocity boundary condition at solid walls in rarefied gas calculations. *Physical Review E 70*, 017303 (2004).

[49] LOCKERBY, D. A., REESE, J. M., AND GALLIS, M. A. Capturing the Knudsen layer in continuum-fluid models of nonequilibrium gas flows. *AIAA Journal 43*, 6 (June 2005), 1391–1393.

[50] LOFTHOUSE, A. J., BOYD, I. D., AND WRIGHT, M. J. Effects of continuum breakdown on hypersonic aerothermodynamics. *Physics of Fluids 19*, 2 (2007), 027105.

[51] LOFTHOUSE, A. J., SCALABRIN, L. C., AND BOYD, I. D. Hypersonic aerothermodynamics analysis across nonequilibrium regimes using continuum and particle methods. AIAA Paper 2007–3903.

[52] LOFTHOUSE, A. J., SCALABRIN, L. C., AND BOYD, I. D. Velocity slip and temperature jump in hypersonic aerothermodynamics. *Journal of Thermophysics and Heat Transfer* (2007). In press.

[53] LUMPKIN, F. E., HAAS, B. L., AND BOYD, I. D. Resolution of differences between collision number definitions in particle and continuum simulations. *Physics of Fluids A 3*, 9 (Sept. 1991), 2282–2284.

[54] MACCORMACK, R. W., AND CANDLER, G. V. The solution of the Navier-Stokes equations using Gauss-Seidel relaxation. *Computers & Fluids 17*, 1 (1989), 135–150.

[55] MARKELOV, G. N., WALPOT, L., AND IVANOV, M. S. Numerical simulation of laminar hypersonic separation using continuum and kinetic approaches. AIAA Paper 2001–2901.

[56] MILLIKAN, R. C., AND WHITE, D. R. Systematics of vibrational relaxation. *Journal of Chemical Physics 39* (1963), 2309–3213.

[57] MONTI, R., FUMO, M. D. S., AND SAVINO, R. Thermal shielding of a reentry vehicle by ultra-high-temperature ceramic materials. *Journal of Thermophysics and Heat Transfer 20*, 3 (2006), 500–506.

[58] MOSS, J. N. DSMC computations for regions of shock/shock and shock/boundary layer interaction. AIAA Paper 2001–1027.

[59] MOSS, J. N., , MITCHELTREE, R. A., DOGRA, V. K., AND WILMOTH, R. G. Hypersonic blunt body wake computations using DSMC and Navier-Stokes solvers. AIAA Paper 1995–2028.

[60] MOSS, J. N., AND BIRD, G. A. Direct simulation of transitional flow for hypersonic reentry conditions. *Journal of Spacecraft and Rockets 40*, 5 (2003), 830–843.

[61] MOSS, J. N., AND BIRD, G. A. Direct simulation Monte Carlo simulations of hypersonic flows with shock interactions. *AIAA Journal 43*, 12 (2005), 2565–2573.

[62] MOSS, J. N., DOGRA, V. K., PRICE, J. M., AND HASH, D. B. Comparison of DSMC and experimental results for hypersonic external flows. AIAA Paper 1995–2028.

[63] O'BRIEN, T. F., AND LEWIS, M. J. Power law shapes for leading-edge blunting with minimal shock standoff. *Journal of Spacecraft and Rockets 36*, 5 (1999), 653–658.

[64] OLYNICK, D. R., TAYLOR, J. C., AND HASSAN, H. A. Comparisons between DSMC and the Navier-Stokes equations for reentry flows. AIAA Paper 1993–2810.

[65] OZAWA, T., ZHONG, J., LEVIN, D. A., BOGER, D., AND WRIGHT, M. Modeling of the stardust reentry flows with ionization in dsmc. AIAA Paper 2007–0611.

[66] PADILLA, J. S., AND BOYD, I. D. Assessment of gas-surface interaction models in DSMC analysis of rarefied hypersonic flow. AIAA Paper 2007–3891.

[67] PADILLA, J. S., AND BOYD, I. D. Assessment of rarefied hypersonic aerodynamics modeling and windtunnel data. AIAA Paper 2006–3390.

[68] PARK, C. *Nonequilibrium Hypersonic Aerothermodynamics*. John Wiley & Sons, 1990.

[69] REUTHER, J. J., KINNEY, D., SMITH, S., KONTINOS, D., GAGE, P., AND SAUNDERS, D. A reusable space vehicle design study exploring sharp leading edges. AIAA Paper 2004–2537.

[70] REUTHER, J. J., PRABHU, D. K., BROWN, J. L., AND WRIGHT, M. J. Compuational fluid dynamics for winged re-entry vehicles at hypersonic conditions. AIAA Paper 2004–2537.

[71] ROVEDA, R., GOLDSTEIN, D. B., AND VARGHESE, P. L. Hybrid Euler/particle approach for continuum/rarefied flows. *Journal of Spacecraft and Rockets 35*, 3 (1998), 258–265.

[72] ROY, C. J., BARTEL, T. J., GALLIS, M. A., AND PAYNE, J. L. DSMC and Navier-Stokes predictions for hypersonic laminar interacting flows. AIAA Paper 2001–1030.

[73] ROY, C. J., GALLIS, M. A., BARTEL, T. J., AND PAYNE, J. L. Navier-Stokes and direct simulation Monte Carlo predictions for laminar hypersonic separation. *AIAA Journal 41*, 6 (2003), 1055–1063.

[74] RUGGERI, T. Breakdown of shock-wave-structure solutions. *Physical Review E 47*, 6 (June 1993), 4135–4140.

[75] SCALABRIN, L. C. *Numerical Simulation of Weakly Ionized Hypersonic Flow Over Reentry Capsules*. PhD thesis, The University of Michigan, 2007.

[76] SCALABRIN, L. C., AND BOYD, I. D. Development of an unstructured Navier-Stokes solver for hypersonic nonequilibrium aerothermodynamics. AIAA Paper 2005–5203.

[77] SCALABRIN, L. C., AND BOYD, I. D. Numerical simulation of weakly ionized hypersonic flow for reentry configurations. AIAA Paper 2006–3773.

[78] SCATTEIA, L., BORRELLI, R., COSENTINO, G., BÊCHE, E., SANS, J.-L., AND BALAT-PICHELIN, M. Catalytic and radiative behaviors of $ZrB_2 - SiC$ ultrahigh temperature ceramic composites. *Journal of Spacecraft and Rockets 43*, 5 (2006), 1004–1012.

[79] SCHWARTZENTRUBER, T. E. *A Modular Particle-Continuum Algorithm for Hypersonic Non-Equilibrium Flows*. PhD thesis, The University of Michigan, 2007.

[80] SCHWARTZENTRUBER, T. E., AND BOYD, I. D. A hybrid particle-continuum method applied to shock waves. *Journal of Computational Physics 215* (July 2006), 402–416.

[81] SCHWARTZENTRUBER, T. E., SCALABRIN, L. C., AND BOYD, I. D. Hybrid particle-continuum simulations of non-equilibrium hypersonic blunt body flow fields. AIAA Paper 2006–3602.

[82] SCHWARTZENTRUBER, T. E., SCALABRIN, L. C., AND BOYD, I. D. A modular particle–continuum numerical method for hypersonic non-equilibrium gas flows. *Journal of Computational Physics 225* (July 2007), 1159–1174.

[83] SHARIPOV, F., AND KALEMPA, D. Velocity slip and temperature jump coefficients for gaseous mixtures. I. Viscous slip coefficient. *Physics of Fluids 15*, 6 (June 2003), 1800–1806.

[84] SHEN, C. *Rarefied Gas Dynamics: Fundamentals, Simulations and Micro Flows.* Springer, 2005.

[85] STEGER, J. L., AND WARMING, R. F. Flux vector splitting of the inviscid gasdynamic equations with application to finite-difference methods. *Journal of Computational Physics 40*, 2 (apr 1981), 263–293.

[86] STREET, R. E. A study of boundary conditions in slip-flow aerodynamics. In *Rarefied Gas Dynamics, Proceedings of the First International Symposium held at Nice* (New York, 1960), F. M. Devienne, Ed., Pergamon Press, pp. 276–292.

[87] SUCCI, S. *The Lattice Boltzmann Equation for Fluid Dynamics and Beyond.* Clarendon Press, 2001.

[88] SUN, Q., CAI, C., BOYD, I. D., CLEMMONS, J. H., AND HECHT, J. H. Computational analysis of high-altitude ionization gauge flight measurements. *Journal of Spacecraft and Rockets 43*, 1 (2006), 186–193.

[89] TANNEHILL, J. C., ANDERSON, D. A., AND PLETCHER, R. H. *Computational Fluid Mechanics and Heat Transfer.* Taylor & Francis, 1997.

[90] TIWARI, S. Coupling of the Boltzmann and Euler equations with automatic domain decomposition. *Journal of Computational Physics 144* (Aug. 1998), 710–726.

[91] TSUBOI, N., YAMAGUCHI, H., AND MATSUMOTO, Y. Direct simulation Monte Carlo method on rarefied hypersonic flow around flat plates. *Journal of Spacecraft and Rockets 41*, 3 (2004), 397–405.

[92] VIJAYAKUMAR, P., SUN, Q., AND BOYD, I. D. Vibrational-translational energy exchange for the direct simulation Monte Carlo method. *Physics of Fluids 11*, 8 (Aug. 1999), 2117–2126.

[93] Vincenti, W. G., and C. H. Kruger, J. *Introduction to Physical Gas Dynamics.* Krieger Publishing Company, 1965.

[94] Wadsworth, D. C., and Erwin, D. A. One-dimensional hybrid continuum/particle simulation approach for rarefied hypersonic flows. AIAA Paper 1990–1690.

[95] Wagner, W. A convergence proof for Bird's direct simulation Monte Carlo method for the Boltzmann equation. *Journal of Statistical Physics 66*, 3-4 (Feb. 1992), 1011–1044.

[96] Walker, S., and Schmisseur, J. D. CFD validation of shock-shock interaction flow fields. AIAA Paper 2002–0436.

[97] Walker, S. P., and Sullivan, B. J. Sharp refactory composite leading edges on hypersonic vehicles. AIAA Paper 2003–6915.

[98] Wang, W.-L. *A Hybrid Particle/Continuum Approach for Nonequilibrium Hypersonic Flows.* PhD thesis, The University of Michigan, 2004.

[99] Wang, W.-L., and Boyd, I. D. Continuum breakdown in hypersonic viscous flows. AIAA Paper 2002–0651.

[100] Wang, W.-L., Boyd, I. D., Candler, G. V., and Nompelis, I. Particle and continuum computations of hypersonic flow over sharp and blunted cones. AIAA Paper 2001–2900.

[101] Weiss, W. Continuous shock structure in extended thermodynamics. *Physical Review E 52*, 6 (Dec. 1995), R5760–R5763.

[102] Whitmore, S. A., and Dunbar, B. J. Orbital space plane: Past, present, and future. AIAA Paper 2003–2718.

[103] Wilke, C. R. A viscosity equation for gas mixtures. *Journal of Chemical Physics 18*, 4 (Apr. 1950), 517–519.

[104] Wilmoth, R. G., LeBeau, G. J., and Carlson, A. B. DSMC grid methodologies for computing low-density, hypersonic flows about reusable launch vehicles. AIAA Paper 1996–1812.

[105] Wright, M. J., Bose, D., Palmer, G. E., and Levin, E. Recommended collision integrals for transport property computations, part 1: Air species. *AIAA Journal 43*, 12 (2005), 2558–2564.

[106] Wright, M. J., and Milos, F. S. Afterbody aeroheating flight data for planetary probe thermal protection system design. *Journal of Spacecraft and Rockets 43*, 5 (2006), 929–943.

[107] WRIGHT, M. J., SINHA, K., OLEGNICZAK, J., CANDLER, G. V., MAGRUDER, T. D., AND SMITS, A. J. Numerical and experimental investigation of double-cone shock interactions. *AIAA Journal 38*, 12 (2000), 2268–2276.

[108] YAMAMOTO, Y., TOTSUKA, A., ISHIYAMA, T., KANEDA, M., YOSHIKURA, H., HOSAKA, Y., KOBAYAKAWA, S., KAMISHIKIRYO, S., AND KINOSHITA, T. Study of complex three-dimensional hypersonic shock interactions for future re-usable space transport system. AIAA Paper 2003–3900.

ABSTRACT

NONEQUILIBRIUM HYPERSONIC AEROTHERMODYNAMICS USING THE
DIRECT SIMULATION MONTE CARLO AND NAVIER-STOKES MODELS

by

Andrew J. Lofthouse

Chair: Iain D. Boyd

This dissertation presents a detailed, computational study quantifying the effects of nonequilibrium on the surface properties of a hypersonic vehicle by comparing Navier-Stokes-based Computational Fluid Dynamics (CFD) and direct simulation Monte Carlo (DSMC) simulation results for the flow about a cylinder and a wedge. Physical submodels contained in both computational methods are ensured to be as equivalent as possible. Translational nonequilibrium effects are isolated by considering a monatomic gas, argon. Thermal nonequilibrium effects are included by considering a diatomic gas, nitrogen. Several different flow regimes are considered, from the continuum into the transitional (freestream Knudsen numbers are 0.002, 0.01, 0.05 and 0.25), with Mach numbers of 10 and 25. Effects on surface properties (total drag and peak heat transfer rate) are quantified at each flow condition. Flow field properties are also compared. Continuum breakdown parameter values are compared with other flow and surface properties.

The effectiveness of several types of CFD slip boundary conditions is evaluated, and the velocity slip and temperature jump (including vibrational temperature jump) values are compared with those extracted from DSMC simulation results. The slip conditions of Gökçen (AIAA Paper 1989-0461) most accurately predict surface properties, while the slip conditions of Lockerby et al. (*AIAA J.* 43(6) (June 2005), 1391-1393) agree best with DSMC slip values.

For flows of argon and nitrogen about a cylinder, CFD total drag predictions remain within 6% of DSMC predictions, and heat flux agreement is 8% or better. For flows about a wedge, total drag differences range between 2% and 34%, mostly due to friction force differences. Peak heating differences are between 70% and 100%; DSMC predicts a much higher temperature near the leading edge than CFD.

Flow property differences near the wall surface are shown to be concentrated primarily in the Knudsen layer. Validation of the CFD code, as well as the effect of various levels of surface accommodation, are shown by considering a nitrogen flow over a flat plate and comparing the simulation results with experimental data.